The Electronic and Vibrational Spectroscopy of Matrix-Isolated Phthalocyanines – Experiment and Theory

A Thesis submitted by

Ciarán Anthony Murray, B.Sc. (Hons.)

to the **National University of Ireland** in fulfilment of the requirements for the Degree of Doctor of Philosophy

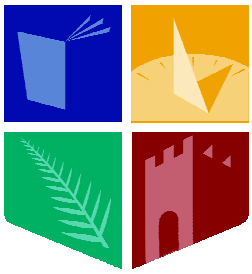

NUI MAYNOOTH

Ollscoil na hÉireann Má Nuad

Based on research carried out in the

Low Temperature Laboratory,

Department of Chemistry,

National University of Ireland, Maynooth.

Research Supervisor: Dr. John G. McCaffrey

Head of Department: Prof. John P. Lowry

Maynooth,
Co. Kildare,
Ireland.

October, 2010

Table of Contents

Declaration

This thesis has not been submitted before, in whole or in part, to this or any other university for any degree, and is, except where otherwise stated, the original work of the author.

Ciarán A. Murray

_____

To my parents – for your never ending love and support

The underlying physical laws necessary for the mathematical theory of a large part of physics and the whole of chemistry are thus completely known, and the difficulty is only that the exact application of these laws leads to equations much too complicated to be soluble. It therefore becomes desirable that approximate practical methods of applying quantum mechanics should be developed, which can lead to an explanation of the main features of complex atomic systems without too much computation.

Paul Dirac (April 1929)

Acknowledgements

I would like to thank my supervisor Dr Sean McCaffrey for all his help, advice and support. I would particularly like to thank him for his patience and guidance throughout the course of my research at the Low Temperature Lab (LTL) in Maynooth. For the introduction to and training in low-temperature chemistry and advanced spectroscopic methods that he has given me and for the discussions on scientific (and non-scientific) matters that we've had, I have been especially grateful for.

I would like to thank Claudine Crépin, Niloufar Shafizadeh, Michel Broquier and everbody at l'Université Paris-Sud, Orsay for the opportunity to collaborate with you during this study. Without your hard work, analysis and thoughtfull discussions, this manuscript would not have been possible. My short but instructive visits to Orsay were very much appreciated. *Merci pour tout*.

To all the postdocs, postgrads and undergraduate students who have worked in the LTL throughout the years. I'd like to thank Owen Byrne (the one and 'Owenly'), who started as a postgrad in our lab the same time as I did; I couldn't ask for a better colleague (despite the awful jokes and puns!). Thank you to Maryanne Ryan and Patrick Lall, for all their assistance and advice and Martin Collier for his probing questions about my work and his willingness to offer solutions.

I would especially like to thank Nadia Dozova who I worked along side for part of this study. She was a joy to work with and a brilliant friend - either discussing laser spectroscopy and DFT calculations in the lab or the qualities of Guinness (I still haven't heard of a ½ pint!), Champions League football and Terry Pratchett books in the Roost. *благодаря*.

I would like to thank Prof. John Lowry and the faculty and staff of the chemistry department for their all help as both an undergraduate and postgraduate student. In particular, I'd like to thank Noel Williams. I cannot praise him highly enough – from finding solutions for problems with the experimental apparatus to setting up

the hardware and software for the computer systems used for calculations. His unassuming and straightforward attitude either in his workshop or on the football pitch was an inspiration.

I would like to thank all the postgrads and postdocs of the department (past and present) for their support and friendship. I'd especially like to thank those you were in my undergraduate class and went on to further their chemistry studies in Maynooth – Claire (a fellow *Conailleach*), Gillian, John, Linda, Owen (he deserves a second mention), Rob and Richard. I'd also like to thank Declan and Dennis (gents), to those who did some research in our lab as undergrads (before moving to the dark-side of electrochemistry!) – Paul, Ken, Anita and Foxy (my computer is still called Catherine!) and *gli Italiani* – Valeria, Enrico, Adelaida and Sinéad (adopted Italian). To *na calíní* upstairs – Alanna, Carol, Laura, Lorna, Louise, Niamh, Róisín, Theresa, Trish and Vickie, and those downstairs – Emer, Keeley, Lynne, Orla Rachel, Saidbhe and Ursala. Not forgetting the lads Ciarán, Colin, Conor, Dean, Gama, John M, Niall (Joey), Niall Maher, Rob D. and Wayne and of course the postdocs Fi, Finno and Ishwar. I know I've probably left some of you out and I apologise, but the department has grown so much over my sojourn here that I could spend the next 50 pages singing all your praises!

I would also like to thank all my extended family (Kincaids and Murrays) and friends (at home in Donegal and down here in Maynooth). Your friendship and support over the years has been very much appreciated, despite the Van Wilder jokes!

Finally, I would like to thank my family. To my parents Ann and Joe - for the life lessons I learnt from you growing up and all the support you have given me (both emotional and financial) over the course of my education, I will be forever grateful. To my siblings, my little bro' Daniel (6' ½", 13 stones) and my baby sis' Mary-Kate (B.A (Hons.), P.G.Dip. (Ed.)), I don't know what sort of example I set for you but I did my best!

Gabh raibh míle maith agaibh go léir.

Abstract

Phthalocyanines (Pcs) are robust macrocyclic tetrapyrrolic molecules having distinctive dark blue to green colours. Despite their importance in industry, their optical spectroscopy has yet to be fully characterised. Low-temperature solids consisting of the rare gases or inert materials like nitrogen offer an ideal environment in which to study these molecules. The resulting spectral bands in inert cryogenic matrices are narrow and well resolved with relatively small shifts from the gas phase values. The aims of the work presented in this thesis are to record the vibrational and luminescence spectroscopy for free-base phthalocyanine (H_2Pc) and zinc phthalocyanine (ZnPc) isolated in various inert low-temperature matrices and with the assistance of extensive theoretical calculations, assign the spectral features observed.

The infrared absorption spectra of matrix-isolated ZnPc and H_2Pc have been recorded in the region from 400 to 4000 cm^{-1} in solid N_2, Ar, Kr and Xe. The isotopomers HDPc and D_2Pc were synthesised in an attempt to resolve the conflicting assignments that currently exist in the literature for the N-H bending modes in H_2Pc spectra. Comparison of the spectroscopic results obtained with isotopic substitution and with predictions from large basis set *ab initio* density functional theory (DFT) calculations, allow identification of the in-plane (IP) bending mode of H_2Pc at 1045 cm^{-1} and the out-of-plane (OP) bending mode at 765 cm^{-1}. The antisymmetric N-H stretching mode observed at ~3310 cm^{-1} in low temperature solids is slightly blue shifted from, but is entirely consistent with the literature KBr data. The vibrational modes of the experimental spectra of H_2Pc and its deuterium isotopomers were correlated using DFT and the ratios of the lighter H atom frequencies to those of their heavier D atom equivalents (ν_H/ν_D) were determined. With the exception the N-H stretches, the recorded H/D isotope shifts in all the N-H vibrations are complex with the IP bending modes exhibiting small ν_H/ν_D ratios (the largest value is 1.089) while one of the observed OP modes has a ν_H/ν_D ratio < 1. DFT results reveal the small ratios arise in particular from strong coupling of the N-H IP bending modes with IP stretching modes of C-N bonds. The unexpected behaviour of ν_H/ν_D ratios is analysed through the examination of the continuous theoretical evolution of the frequencies with the mass of H. A consequence of this frequency increase in the heavier isotopomer is that the

direction of the N-D OP bend is reversed from the N-H OP bend. The Raman scattering data recorded for ZnPc and H_2Pc in KBr discs are also analysed and found to be quite similar and moreover, identical to the visible fluorescence of matrix-isolated Pcs.

The visible absorption, emission and excitation spectra of ZnPc and H_2Pc trapped in Ne, N_2, Ar, Kr and Xe matrices have been recorded. The visible absorption peaks for the Q band of ZnPc and the Q_x and Q_y transitions of H_2Pc have revealed matrix shifts from the gas phase values and distinct sites of isolation. The spectral positions of the vibronic bands in emission with pulse dye laser excitation for both Pcs have been identified. A comparison of the fluorescence spectra with Raman spectra in KBr pellets has revealed very strong similarities. This is entirely consistent with the selection rules and points to the occurrence of only fundamental vibrational transitions in the emission spectra corresponding to those in the ground state. This favourable comparison between Raman and fluorescence spectra has allowed the vibronic modes of ZnPc and H_2Pc coupling to the electronic emission to be assigned using DFT calculated vibrational spectra. A mirror symmetry between the vibronic structures of ZnPc has been observed in emission and excitation, indicating similar geometries in the ground and excited states. The vibrational modes of ZnPc in the excited state have therefore been assigned using the same DFT Raman vibrations determined for the ground state. For the excitation spectra of H_2Pc, the mirror symmetry with emission has been seen to breakdown after ~950 cm^{-1} due the onset of the higher energy Q_y state absorption. A matrix dependence has been found for the Q_x-Q_y energy splitting varying from 916 cm^{-1} in Xe and 985.3 cm^{-1} in Ar. In a comparison of the H_2Pc excitation and emission spectra recorded in this work and those previously reported for D_2Pc, a tentative assignment of the vibrational mode in the Q_x state coupling to the Q_y has been made using DFT to a weakly Raman active mode of B_{1g} symmetry consisting of an in-plane bending motion of the central N-H bonds.

The vertical excitation energies and oscillator strengths of H_2Pc and ZnPc as well as those of free-base and zinc tetraazaporphyrin (TAP), tetrabenzoporphyrin (TBP) and porphine (P) have been calculated with linear-response time-dependent DFT utilizing the B3LYP hybrid functional and 6-311++G(2d,2p) basis set. The theoretical results for the lowest energy transition have been compared to

experimental data and have been found to correctly predict many of the trends apparent for these molecules. One of the major discrepancies that has been observed between the TD-DFT and experimental transition energies was the underestimation of the theoretically determined Q_x-Q_y splitting of H_2Pc and the relative intensities of these bands.

Laser induced fluorescence spectroscopy of H_2Pc and ZnPc phthalocyanines trapped in rare gas and nitrogen matrices reveals a quite unexpected phenomenon with a moderate increase in the laser intensity. For these molecules in all matrices, except for ZnPc in Xe, a huge increase in the intensity of a one particular emission band has been observed when pumping the $S_1 \leftarrow S_0$ transition. The band involves a vibrational mode of the ground state, located at 1550 and 1525 cm^{-1} for H_2Pc and ZnPc, respectively. This vibration has been assigned in both phthalocyanines using DFT to the most intense Raman active mode involving an out-of-phase stretching of the C-N-C bonds in the tetrapyrrole ring. Many of the characteristics of amplified emission (AE) are exhibited by this vibronic transition and the threshold conditions have been investigated. In light of the success of the DFT Raman spectra to correctly predict both the positions and relative intensities of the vibronic emission bands of H_2Pc and ZnPc, the optimized geometries, vibrational frequencies and Raman scattering intensities have been calculated for a selection of other structurally related tetrapyrrolic molecules and their potential for exhibiting AE assessed. Excitation scans recorded for the AE band show greatly enhanced site selectivity compared to what is obtained in normal fluorescence excitation scans.

Chapter I: Introduction

I.1 Phthalocyanine and Porphyrins

Porphyrins have been often called the 'colours of life'[1] - from the bright green chlorophyll responsible for photosynthesis in plants to the crimson red haemoglobin in red blood cells used to transport oxygen through the blood vessels of animals (Figure I.1). The name porphyrin comes from the Greek *πορφύρα* meaning purple, the colour of some porphyrins like hæmatoporphyrin and porphine, the parent molecule of this important group of chemicals[2]. Phthalocyanines are synthetic analogues of porphyrins and are structurally related. Like porphyrins, they are strongly coloured ranging from dark blue to green. They are robust molecules, with stability to high temperatures and UV light and are insoluble in most solvents except in strong acids or when functionalised with sulfonate groups. Despite their low solubility, phthalocyanines are one of the most important pigments produced for use in paints and dyes accounting 25 % of all pigments synthesised world wide[3].

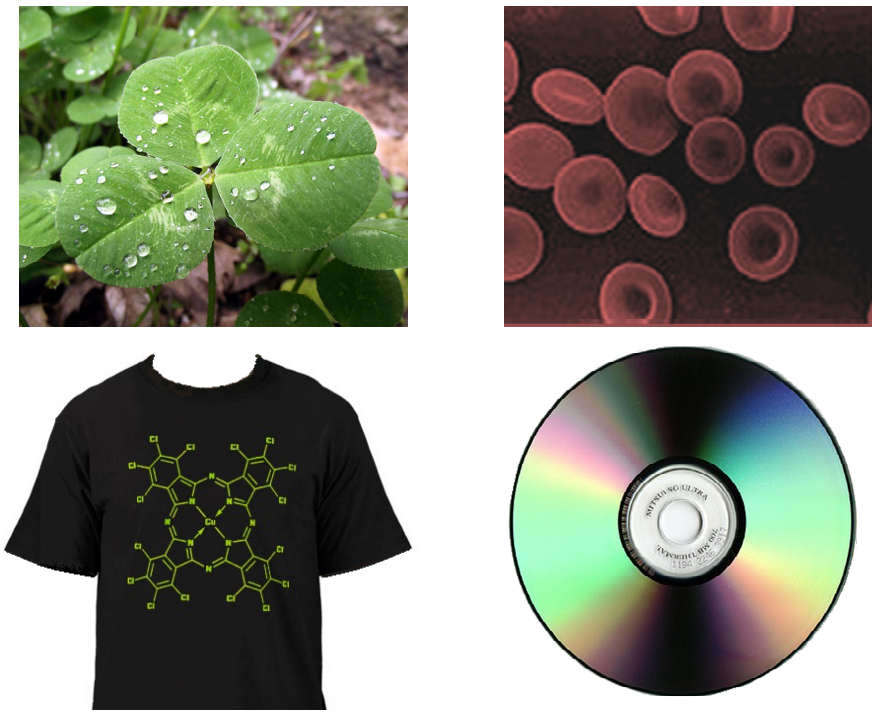

Figure I.1: Brightly coloured tetrapyrrole pigments. The top two pictures show examples of naturally occuring porphyrins - a green clover leaf containing chlorophyll and red blood cells containing hæmoglobin. The bottom pictures show two of the uses for synthetic phthalocyanine - as a pigment in printing inks for clothing and as a dye medium on CD-R disks[4].

I.1.I The Structure of Phthalocyanines and Porphyrins

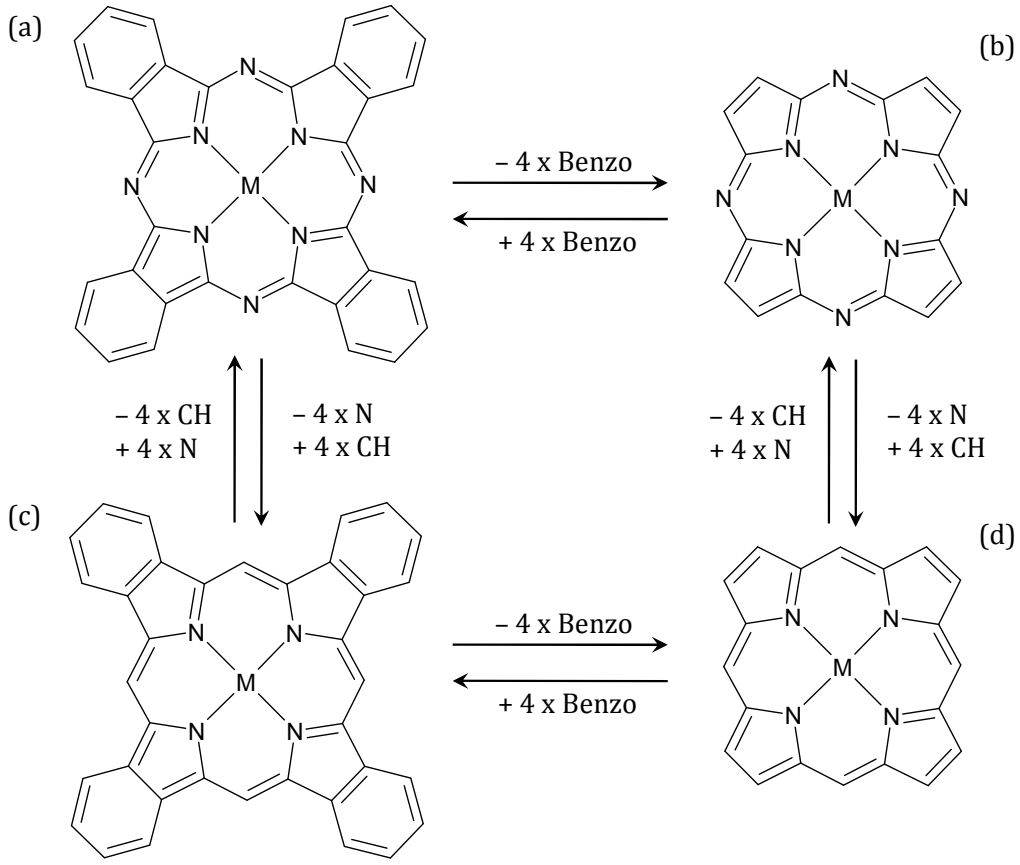

Figure I.2: Comparison of the molecular structures of porphyrins (where M is a metal cation or 2 H atoms). The aza porphyrins, (a) phthalocyanine and (b) tetraazaporphyrin differ from each other by the addition of 4 benzo annulations. Their equivalent methine porphyrins (c) tetrabenzoporphyrin and (d) porphine are derived by exchanging the 4 meso N atoms for CH groups.

Structurally, phthalocyanines are macrocyclic molecules consisting of four pyrrole subunits with benzo annulations (forming an isoindole like ring structure), linked by four nitrogen aza bridging groups to form a sixteen member ring. The phthalocyanine anion (Pc^{2-}) may act as a tetra-dentate ligand, complexing with most metals through the four nitrogen atoms of the pyrrole subunits forming a metallo-phthalocyanine ($M(n)Pc^{n-2}$). The phthalocyanine anion may also bond to two protons, again at the nitrogen atoms on the pyrrole subgroups at the centre of the cavity, forming free-base phthalocyanine (H_2Pc) or to small metal cations for example in Li_2Pc and Na_2Pc[5]. The simplest porphyrin, porphine, is a similar macrocyclic tetrapyrrole whose structure consists of four pyrrole subunits bridged by CH methine groups. Like phthalocyanine, either two hydrogen atoms (forming H_2P) or a metal atom (forming MP) may be bound to the pyrrole nitrogens at centre of the ring cavity. The structural similarities can clearly be seen between the two classes of molecules by comparing the addition of benzo annulations to

porphine to form tetrabenzoporphyrin (TBP) or by replacing the CH bridging groups to form tetraazaporphyrin (also called porphyrazine or TAP) shown in Figure I.2. Phthalocyanines and porphyrins are aromatic fulfilling Hückel's rule being both planar and having 4n+2 electrons in a conjugated π system[6].

I.1.II Phthalocyanine Synthesis

Phthalocyanines were first discovered by accident by four chemists, Dandridge, Drescher, Dunworth and Thomas, working for Scottish Dyes Ltd. at Grangemouth in 1928[1,7]. At the Scottish plant, phthalamide (a colourless solid important in the manufacture of dye molecules like indigo) was being synthesised from phthalic anhydride and ammonia in iron pots when a blue coloured contaminant was noticed. Earlier in 1927, a similar blue compound had been obtained by de Diesbach in Germany by reacting phthalodinitrile with a copper salt[8]. Analysis in Scotland of the blue 'contaminant' found that it was an iron containing complex that was highly stable and insoluble in most solvents. Further research using different metals, including copper, lead to Scottish Dyes Ltd. (until 2008 known as ICI) patenting copper phthalocyanine as the very successful Monastral Blue pigment in 1928. It was not until a few years later that Sir Patrick Linstead at Imperial College, London established the reactivity and structures of both metallo and free-base phthalocyanine[9-14] and recognised that earlier reports from 1907[15] and onwards of similar blue-green insoluble compounds had also been phthalocyanines. It was Linstead who coined the name phthalocyanine, a combination of phthalo, from the precursors it was synthesised from, and cyanine, from the Greek κύανος meaning 'dark blue'[2,9]. The unusual spelling of phthalo ultimately comes from naphthalic acid, which was mistakenly thought to be structurally related to naphthalene until its correct structure was recognised and the name shortened to phthalic acid[2].

Numerous synthetic routes exist for both free-base and metallo phthalocyanine[7,16-18]. Four examples of the reaction schemes for the synthesis of metallo-phthalocyanines are give in Figure I.3. Scheme (I) is similar to the synthesis proposed by Linstead and patented by ICI, using phthalonitrile, copper and $CuCl_2$. In this reaction the Cl^- counter ion acts as a nucleophile, initiating the reaction. Scheme (II) uses diimidoisoindole as a precursor though this molecule is prepared from phthalonitrile and is less common in industry than scheme (I).

Scheme (III) uses reagents phthalic anhydride and urea (as a non-volatile source of nitrogen) with ammonium molybdate as a catalyst. Due to the low cost of materials, this method is preferred for the production of bulk quantities of phthalocyanines for use in cheap dyes and pigments. A more expensive but synthetically more flexible method often used in laboratories is scheme (IV) which uses nitrobenzene and 2-cyanobenzamide as easily functionalised precursors[17]. In some mechanisms, the metal cation can act as a template in the cyclotetramerisation of the metallo-phthalocyanines. Free-base phthalocyanines may be prepared by treatment of weakly complexed metallo-phthalocyanines with strong acids[10,16,17] or directly using some of the precursors used in metallo-phthalocyanine and other reagents like bases and reducing agents[16].

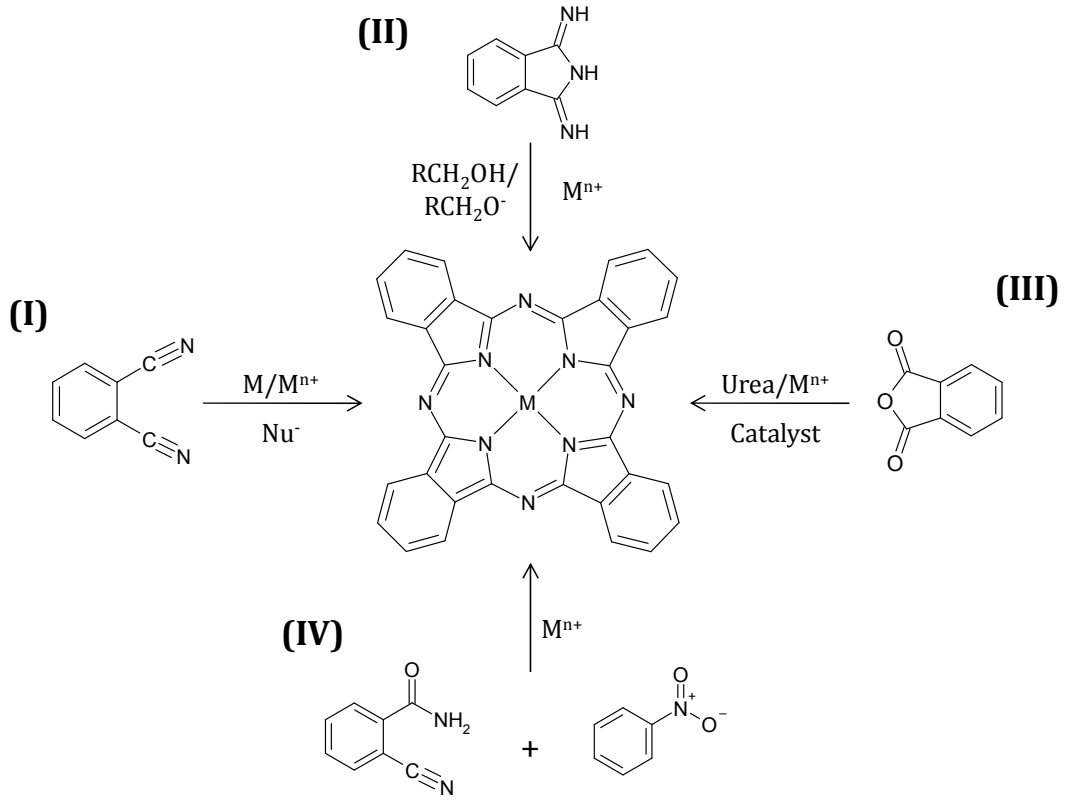

Figure I.3: Examples of synthetic routes to metal phthalocyanines (MPc). The organic precursors are in scheme (I), phthalonitrile, in scheme (II), diiminoisoindole, in scheme (III), phthalic anhydride and scheme (IV), 2-cyanobenzamide and nitrobenzene. All schemes are conducted in the presence of a metal salt, M^{n+}. Scheme (I) is also conducted in the presence of the free metal M and a nucleophile, Nu^-, which is often the counter ion to M^{n+}. The catalyst in scheme (III) is ammonium molybdate.

I.1.III Visible absorption of phthalocyanine and porphyrins – The four-orbital model

One of the most recognisable qualities of phthalocyanines and porphyrins is their colour. Unlike other organo-metallics, the primary origin of absorption bands in the visible spectral region appears to come from electronic transitions in the

macrocyclic ring and not the metal centre. For example, free-base phthalocyanine is a dark blue colour while free-base porphine is a dark red to purple colour. With their strong visible colours and similar structures it is surprising to see how different the UV-Vis absorption spectra of both molecules look. Porphyrins have a strong absorption band in the near-UV (called the Soret or B band) with weakly allowed Q (or quasi-allowed) bands in the visible region. Depending on the symmetry of the molecule, the Q bands can show splitting. D_{4h} symmetry metallo-porphyrins having one single Q band (with often intense vibronic absorption bands) and D_{2h} free-base porphyrins with two Q bands, a lower energy Q_x and a higher energy Q_y. Phthalocyanines, though with similar spectral absorption positions to porphyrins, have the most intense absorption bands in the red spectral region corresponding to the Q bands in porphyrins and weaker absorption bands in the UV region. The label 'Q band' is intended for the porphyrins but is actually inappropriate for the phthalocyanines as it is stronger than the Soret bands. Though the visible transitions of phthalocyanines are not quasi but fully allowed, the Q label is commonly used to show the relationship between these transitions and those in other porphyrin derivatives.

The first successful theoretical model to describe the absorption properties of porphyrins and phthalocyanines is the "Four-Orbital Model" proposed by Martin Gourterman[19-21] in the 1960's. He used a combination of extended Hückel theory, with a linear combination of atomic orbitals treatment of the molecular orbitals (LCAO-MO), to predict the orbital energies and Configuration Interaction (CI) to predict the orbital contributions to the electronic transitions in porphyrins. In his model, Gouterman considered only transitions between the two lowest unoccupied molecular orbitals (LUMOs) and two highest occupied molecular orbitals (HOMOs) which were found to be π orbitals. The two LUMO orbitals, c_1 and c_2, are considered degenerate (as in metallo-porphyrins (MP)) and, as an initial approximation, the HOMO orbitals, b_1 and b_2, are considered accidentally degenerate ("P^{2-}" Figure I.4). Applying the CI method to the four single electron transitions of these orbitals (b_1c_1, b_1c_2, b_2c_1 and b_2c_2) two pairs of degenerate electronic state transitions were determined-

$$B_y = \tfrac{1}{2}(b_1c_1 + b_2c_2),\ B_x = \tfrac{1}{2}(b_1c_2 + b_2c_1),$$
$$Q_y = \tfrac{1}{2}(b_1c_1 - b_2c_2),\ Q_x = \tfrac{1}{2}(b_1c_2 - b_2c_1). \qquad \text{(I.1)}$$

In the first pair (B_y and B_x in I.1), the orbital contributions are combined positively and the transition dipole moments of the contributions are added together to produce a strongly allowed transition at higher energies. These have been assigned to the Soret band. In the second pair (Q_y and Q_x in I.1), the orbital combinations combine negatively resulting in the transition dipole moments for the individual contributions cancelling and the transitions become forbidden. By lifting the degeneracy of the HOMOs slightly, the orbital coefficients in Q_y and Q_x do not cancel completely and the transitions become weakly allowed, correctly predicting the weaker, lower energy Q bands observed in metallo-porphyrins (see MP in Figure I.4). In free-base porphine, the degeneracy of the LUMO c_1 and c_2 orbitals is lifted (H_2P in Figure I.4) resulting in different energy B_y and B_x bands and different energy Q_y and Q_x bands. The non-degeneracy of the LUMO orbitals explains the splitting of the Q bands seen in free-base porphyrins.

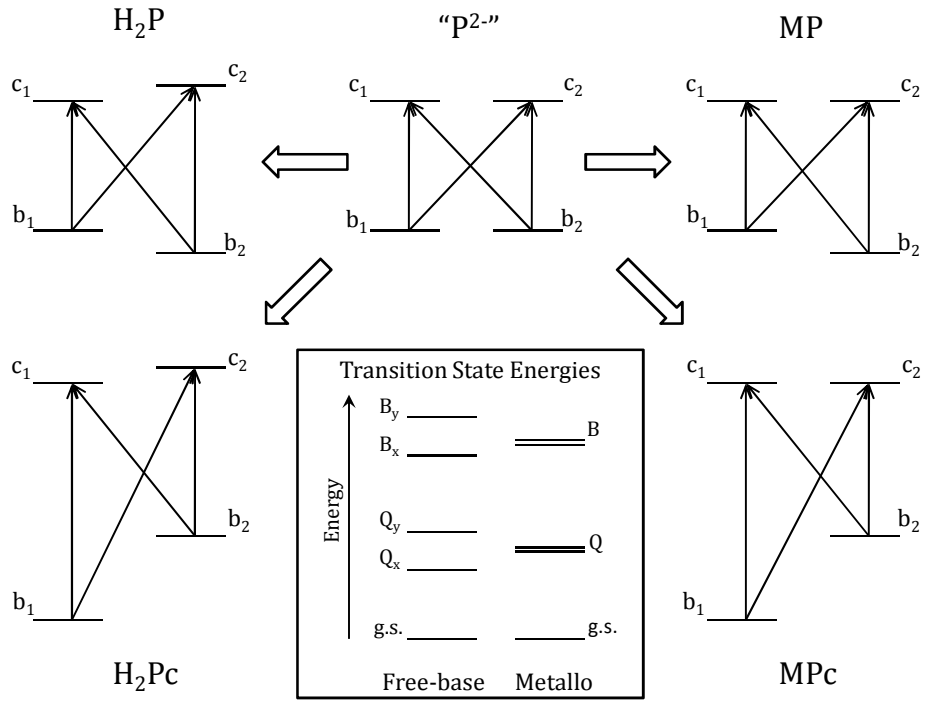

Figure I.4: Gouterman 4-orbital model for both free-base (H_2) and metallo (M) porphine (P) and phthalocyanine (Pc). "P^{2-}" represents the preliminary model where the HOMO b_1 and b_2 orbitals and LUMO c_1 and c_2 are considered degenerate. Shown inset are the relative energies of the various B and Q states.

The four-orbital model may also be applied to phthalocyanines. Replacing the meso-carbons with nitrogen atoms and attaching benzene rings to the pyrrole subunits has a considerable effect on the molecular orbitals. Of the two occupied MOs considered, the b_1 orbital has significant orbital coefficients at the meso positions. The more electronegative nitrogen atom greatly lowers the energy of the b_1 orbital relative to the b_2 orbital. The addition of the nitrogen atom likewise

reduces the energy of both LUMOs. The benzene rings also lower the energy of all four orbitals but again more so for the b_1 orbital (MPc in Figure I.4). This has the effect of lowering the energy of the Q transitions and reducing the contributions from the b_1c_1 and b_1c_2 single orbital transitions in the CI equations. Consequentially, the Q transitions become dominated by the b_2c_1 or b_2c_2 transitions with very large transition dipole moments and are strongly allowed. A splitting in the Q_y and Q_x transitions of H_2Pc is again due to the loss of degeneracy of the c_1 and c_2 orbitals comparable to the splitting in H_2P. Though the Soret B bands of phthalocyanine may be predicted using this method, more modern theoretical approaches (e.g. TD-DFT[22]) have shown that the breakdown of the four-orbital model is so severe that no equivalent mixing of the orbitals involved in the Q transitions is seen for transitions that are predicted in the UV.

I.2 Matrix-Isolation (MI)

According to IUPAC, matrix-isolation refers to the isolation of a reactive or unstable species by dilution in a solid matrix made of an inert material. The matrix is usually co-condensed with the species of interest onto an optical substrate at low temperatures to preserve its structure for identification by spectroscopic means[23]. The expression is most commonly used to refer to the technique of trapping an atom or molecule, called the guest species, in rare gas (Ne, Ar, Kr, Xe) or other inert gas (e.g. N_2) solids, known as the host, at cryogenic temperatures. Reactive molecular gases (e.g. CO, CH_4) may also be used as a host material to investigate the low temperature reactivity of the guest species. In addition, the matrix-isolation technique (MI) may be applied to the investigation of a stable or relatively un-reactive guest species.

Matrix-isolation has its ultimate origins in the development of methods to liquefy gases, pioneered by Michael Faraday and Humphry Davy in the early 19th century[24]. Experiments in the 1850s by James Joule and William Thompson (later Lord Kelvin) found that the adiabatic expansion of gases (i.e. expansion of a gas into a vacuum without the addition of heat) resulted in the cooling of the gas, leading to an effective experimental pathway to lower cryogenic temperatures. The Joule-Thompson effect was used by Cailletet and Pictet in the 1870s to liquefy O_2, N_2 and CO, work which would go on to inspire the chemist James Dewar's subsequent interest in low temperature research. Cryogenic techniques were

further developed by Dewar, who succeeded first in liquefying and then solidifying hydrogen in 1897 and 1899. Nearly a decade later at the University of Leiden, Belgium, Kamerlingh Onnes achieved the landmark goal of liquefying helium, an objective also shared by Dewar. An order from Guinness Breweries, Dublin in 1892 to develop and install a CO_2 liquefaction plant[25], lead to the construction by Carl von Linde in 1895 of the first closed cycle refrigeration unit based on the Joule-Thompson effect and allowed the large-scale liquefaction and separation and distillation of air into its components, including the rare gases.

The first experiments that would be recognised today as matrix-isolation were performed by Vegard at Leiden in the 1920s who investigated the luminescence of condensed gases with electron bombardment and x-ray irradiation[26-29]. Notable discoveries by Vegard included the first observation of the A $^3\Sigma_u^+$—X $^1\Sigma_g^+$ triplet phosphorescence of N_2 and what would be later assigned to the 557.7 nm ^{1}S—^{1}D forbidden transition of atomic oxygen[30]. In the 1940s Gilbert Lewis and co workers reported the UV-Vis absorption spectra of aromatic compounds in low temperature glasses. Though the trapping media used were glasses of organic solvents which have many disadvantages, including reactivity with the guest species and strong absorption in the infrared spectral region, the experiments conducted by Lewis at Berkeley shared many of the qualities and objectives of matrix-isolation[31,32]. In the next decade, the development of matrix-isolation was furthered by Norman and Porter who reported the optical spectra of free radicals and atoms trapped in organic glasses[33,34]. It was not until Pimentel and co-workers in the 1950s that solid rare gases were adapted as a host medium which allowed the systematic study of free radicals[35-38]. He recognised the advantages of using inert gases as a trapping medium including chemical inertness, a tendency to form clear glasses and transparency over a very broad spectral region, from the deep ultra-violet to the infrared. Although the lowest temperature initially attainable by Pimentel and co-workers was only 72 K, limiting the gas matrices available, it was their group that coined the phrase “matrix isolation”[39] and technological developments over the following decades have allowed the technique to be regularly applied to temperatures of 4 K and below.

Matrix-isolation (MI) was originally developed as a convenient way of trapping a reactive species for spectroscopic analysis in an inert environment for long time periods, which may be short lived in conventional solvents and solids or

difficult to achieve in high concentrations in the gas phase. The range of spectroscopic techniques and molecular and atomic species studied by MI has increased to encompass many fields of chemical investigation. In practice, the technique of matrix-isolation involves the simultaneous deposition of a small amount of guest species in the gas phase along with a copious amount of host gas onto a cold spectroscopic substrate. In constructing a MI experimental set-up, some practical requirements must be considered[40-42]. In order to ensure a rigid inert gas solid and reduce diffusion, both of the guest and of the host species, samples must be deposited onto the substrate cooled to below one third of the melting point of the gas being used[42]. For the commonly used matrix gases N_2, Ar, Kr and Xe these temperatures are 19, 25, 35 and 48 K respectively and for Ne and H_2 even lower temperatures of 7.3 and 4.2 K. To reach and maintain these low temperatures, the cryogenic assembly must be placed under a high vacuum (typically 10^{-6} mbar or below), preventing heat transfer through diffusion and eliminating contamination of the sample from atmospheric gases. If the guest sample is a solid or a low volatile liquid, a suitable, controlled vaporisation method must be chosen, for example electron bombardment, laser ablation, resistive heated ovens etc., and the heat transfer from the vapour source minimised.

I.2.I Inert Gas Solids and Sites of Isolation

The use of low temperatures and rigid inert gas solids ensure simpler vibrational and electronic spectra. The low temperatures at which the sample is maintained mean that only the lowest electronic and vibrational states are populated and no 'hot bands' (transitions from thermally populated excited states) are seen. The rigid host matrix in which the guest molecule resides limits rotation of most molecules and removes the rotational progressions observed in gas phase vibrational and electronic spectra. Some smaller molecules like SO_2 and H_2O exhibit hindered rotations, sometimes called librations, which are observed as a simple splitting pattern of the vibrational absorption bands[41]. With their chemical inertness and wide spectral transparency from the far-infrared to the vacuum ultraviolet, solid rare gases make ideal host materials. Nitrogen shares many of these properties, with a similar broad spectral transparency range and low reactivity to many chemical species (a notable exception being its reactivity to some metal atoms and complexes). Despite the inertness of these gases,

spectroscopic band splitting and energy shifts relative to the band origins observed in the gas phase are seen in MI samples due to host-guest interactions. It is therefore important to understand the structure of the inert gas solids and how the guest molecules reside within the crystal lattice of the solids.

All the rare gases have spherical ground states with full outer electron shells. On condensation, they form simple close packing structures with face centred cubic (fcc) arrangements of O_h symmetry (Figure I.5). The dominant forces between the atoms in a rare gas solid are the van der Waals forces and are maximised by each atom achieving the highest coordination possible to its nearest neighbours. Two stable forms of solid nitrogen exist, below 35.6 K, an α form, and above this temperature, a β form[42]. At higher temperatures in β-N_2, the molecules have some rotation and behave as spheres, adopting a hexagonal closed packed structure. At lower temperatures this rotation is reduced and the molecules in α-N_2 act more like cylinders adopting a packing structure derived from cubic closed packing. As nitrogen solids used in matrix isolation are deposited and maintained at temperatures below 35.6 K, only the α form should exist. Within an fcc lattice, each atom has 12 nearest neighbours at a distance of *R* and 6 next nearest neighbours at a distance of *a*. The distance *a* is the lattice parameter which defines the size of the unit cell. The nearest neighbour distance *R* is related to *a* by the simple geometric ratio, $R = a/\sqrt{2}$.

Face Centred Cubic (fcc) unit cell

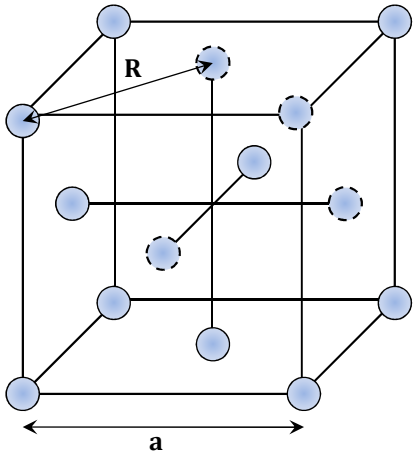

Figure I.5: Sketch of face cubic packing (fcc) unit cell showing the lattice points occupied by atoms or molecules in crystal structures. The lattice parameter, *a*, and nearest neighbour distance, *R*, are also shown where the distance $R = a/\sqrt{2}$.

Small guest or dopant species (e.g. atoms, ions or smaller molecules) may be trapped in a limited number of positions or occupation sites within the host lattice. For very small species isolated in inert gas solids, especially in Kr and Xe with relatively large lattice parameters of 5.644 and 6.131 Å, an atom or molecule may occupy one of two interstitial sites. The tetrahedral interstitial site is found at the centre of a tetrahedral arrangement of atoms (an example of which is found at the centre of the four 'dashed' atoms in Figure I.5) while the larger octahedral interstitial site is found at the centre of the unit cell in Figure I.5. The more commonly occurring sites are substitutional sites where the dopant replaces one or more host atoms or molecules within the matrix. The simplest examples of these are the single substitutional site where one host species is removed and replaced with a guest atom or molecule or the tetrahedral substitutional site where 4 atoms forming a tetrahedral are removed and replaced with a single dopant species. It should be noted that a molecule or atom may occupy multiple thermally stable sites and even thermally unstable sites on deposition. The number of thermally unstable sites may be reduced by the process of annealing. In annealing, the sample is slowly heated to approximately half the melting point of the solid and then allowed to slowly cool back down, permitting the guest and host atoms/molecules to diffuse into the thermally most stable arrangements. This technique also increases the crystallinity and optical clarity of the solid.

Thus far only small, spherical sites have been discussed which are capable of containing relatively small sized dopant species. Larger molecule occupation sites involve the displacement of multiple host atoms/molecules in different spatial arrangements in order to allow the guest molecule to fit within the crystal lattice structure. Obviously the number of possible combinations of host atoms/molecules surrounding the guest molecule has increased greatly compared to the situation seen for smaller guest species. Even with careful sample preparation and annealing, identifying the precise shape and size of the thermally stable sites occupied by a larger molecule can be very difficult and due to the imperfections in the host lattice and the possible orientations of the molecule within the site cage.

I.2.II Matrix effects

The initial goals of matrix isolation were to create a non-interacting environment, without external interactions, in which to spectroscopically observe a guest species. However, it was quickly realised that the matrix environment does have an effect on the vibrational and electronic spectra, perturbing the bands relative to the gas phase. The general terms for these perturbations are matrix effects and can be divided into three often related categories: matrix splitting, matrix shifting and matrix broadening. In order to account for these effects, it is important to understand the interactions between rare gas atoms and inert molecules which both allow them to form crystals at low temperatures and interact with guest species in a matrix.

Rare gas atoms and neutral homogeneous diatomic molecules like N_2 have closed full outer electron shells and no permanent dipole moments. Electronic systems around atoms or molecules are dynamic leading to weak instantaneous dipole moments, where at one moment in time the electron density may not be uniformly distributed around the nuclei of the species. For an isolated atom or molecule the perpetual movement of the electron density will result in an average dipole moment equal to zero.

However, if for example an atom A at a certain time has an instantaneous dipole moment $_A$, this can generate an electric field, $E = \alpha\mu_A/r^3$. This electric field can polarise a neighbouring atom B at a distance r from A, inducing a dipole moment $_B = \alpha\mu_A/r^3$, where α is the polarizablity of atom B[43]. The two dipoles will attract each other, lowering the energy between them. The dipole moment $_B$ can of course polarise its neighbours, inducing further dipole moments and creating a force of attraction. Even when atom A's electron distribution changes with time, the new dipole moment it creates, with a different direction and magnitude, will induce a similar change in polarity of it neighbour B, synchronising the change in polarity between the atoms throughout the system (e.g. atoms in a solid matrix). This synchronisation means that the overall dipole moment of the atoms does not average to zero creating a force of attraction between the atoms. This interaction of induced-dipoles is called the London (or dispersion) Interaction and is dominant at longer distances. At shorter distances electrostatic repulsion forces generated from the overlap of the electron clouds of the atoms, violating the Pauli exclusion principle and raising the energy. Similar interactions are seen for neutral

molecules with no permanent dipole moments. Together these forces make up the van der Waals interactions which may be expressed using the Lennard-Jones potential[43],

$$U_{L-J} = \frac{C_{12}}{r^{12}} - \frac{C_6}{r^6} \quad \text{(I.2)}$$

where, the C_{12} terms describe the repulsive energy and the C_6 terms describe the dispersive energy. These repulsive and attractive forces from the matrix host have an effect on the vibrational and electronic spectra of polyatomic molecules trapped in inert gas solids[44].

I.2.III Matrix effects and vibrational spectra

For a diatomic molecule, the vibrations may be modelled using the simple classical harmonic approximation where the potential energy curve of the vibration, *V*, is given as

$$V = \frac{1}{2}k(r - r_e) \quad \text{(I.3)}$$

where *k* is the force constant and *r* is the displacement of the atoms from the equilibrium bond length r_e. (For an description of the quantum mechanic harmonic oscillator, see Chapter III). When the molecule is placed within a rigid cage of size *D* made of inert atoms or molecules, it is reasonable to modify the potential energy curve in Equation I.3 with terms to account for both the repulsive and attractive forces[42]. Using the repulsive term from Lennard-Jones potential curve, the vibrational energy is now given by,

$$V_{repulsive} = \frac{1}{2}k(r - r_e) + C_{12}/(D - r)^{12}. \quad \text{(I.4)}$$

This increase in the potential energy has the effect of decreasing the bond of the molecule in the matrix and increasing the force constant leading to a higher energy vibrational frequency relative to the truly isolated gas phase molecule[42]. Similarly the attractive forces may be included in the vibrational potential energy curve giving,

$$V_{attractive} = \frac{1}{2}k(r - r_e) - C_6/(D - r)^6. \quad \text{(I.5)}$$

The lowering of the potential energy of the vibration has the opposite effect to the repulsive forces, increasing the equilibrium bond length, lowering the force constant and decreasing the vibrational frequency. The differences between the vibrational frequencies from the gas phase to those observed in matrices due to host/guest interactions are called matrix shifts.

Using the model just described for the effect of van der Waals interactions on vibrational frequencies, the matrix shift of a vibrational mode is dependent on both the polarizability of the host and the cage size. The variation in the polarizability of different host materials can be used to explain the extent of matrix shift seen for the same molecule in a variety of inert gas solids. For example xenon has a much larger polarizability volume of 4.044 $Å^3$ than argon with a polarizability of 1.6411 $Å^3$ and generally exhibits a larger matrix shift[45]. The cage size depends on the site size the molecule occupies in the matrix and how constrained the molecule is within the site. Molecules in larger sites will have reduced guest/host interactions compared to smaller sites. The existence of multiple sites of isolation is one of the explanations for matrix splitting of spectroscopic bands and is called in this context 'site splitting'. The other reasons for the splitting of vibrational bands are due to Fermi resonance (a property intrinsic to the molecule but may not be resolved in gas phase spectra due to rotational broadening) and the reduction of the symmetry of the molecule due to slight changes to the geometry of the molecule in a matrix.

The matrix shifts seen for polyatomic molecules with multiple vibrational modes are more complex but are subjected to similar attractive and repulsive interactions seen in diatomics. Some vibrational bands of a molecule may be blue-shifted indicating repulsive forces from the cage while others of the same molecule are red-shifted indicating attractive forces. The extent of the matrix shift is dependent on many factors. The position of the atoms involved in a vibration and the direction of their displacement during a vibration relative to the cage can determine the extent of matrix shift. For example, matrix IR spectra show a large difference between parallel vibrations with sharp line-shapes and perpendicular vibrations with broad line-shapes (cf. the IR spectrum of dimethyl zinc in argon[46]). The polarizability of a bond can also be a factor with a particularly polarisable bond shifting more than a less polarisable one. With the existence of multiple sites of isolation, the site size and the orientation of the molecule within a site will determine the magnitude of matrix shift and the magnitude of the splitting. The dependence of the matrix shift on the position of the individual bonds of a molecule and the matrix cage allows identification of some isomers that may not be easily distinguishable in other media (e.g. in solution, gas phase or halide salt disks).

I.2.IV Matrix effects in electronic spectra

Taking the case of an atom in the gas phase as an example, electronic absorption (or excitation) occurs from the ground state E_0 to an excited state E_1 with an excitation energy $\Delta E\ (Ex.) = E_1 - E_0$. In the absence of any interactions with other atoms or molecules, E_1 relaxes via emission to E_0, with an emission energy $\Delta E(Em.) = \Delta E(Ex.)$, as depicted in the energy level diagram on the left of Figure I.6. When placed into a crystal lattice of an inert gas matrix, matrix shifts and site effects are observed in the luminescence spectra. Interactions between the host material with ground state orbitals and particularly with the more diffuse (that is to say the more spatially extended) excited state orbitals will have the effect of perturbing the orbital energies. This in turn will shift the excitation and emission energies of the molecule depending on the level of repulsion between the host and excited state. However, one of the most important differences between gas and solid phase spectra is the interaction between the electronic levels of a dopant species and the vibrations (or phonons) of the crystals lattice.

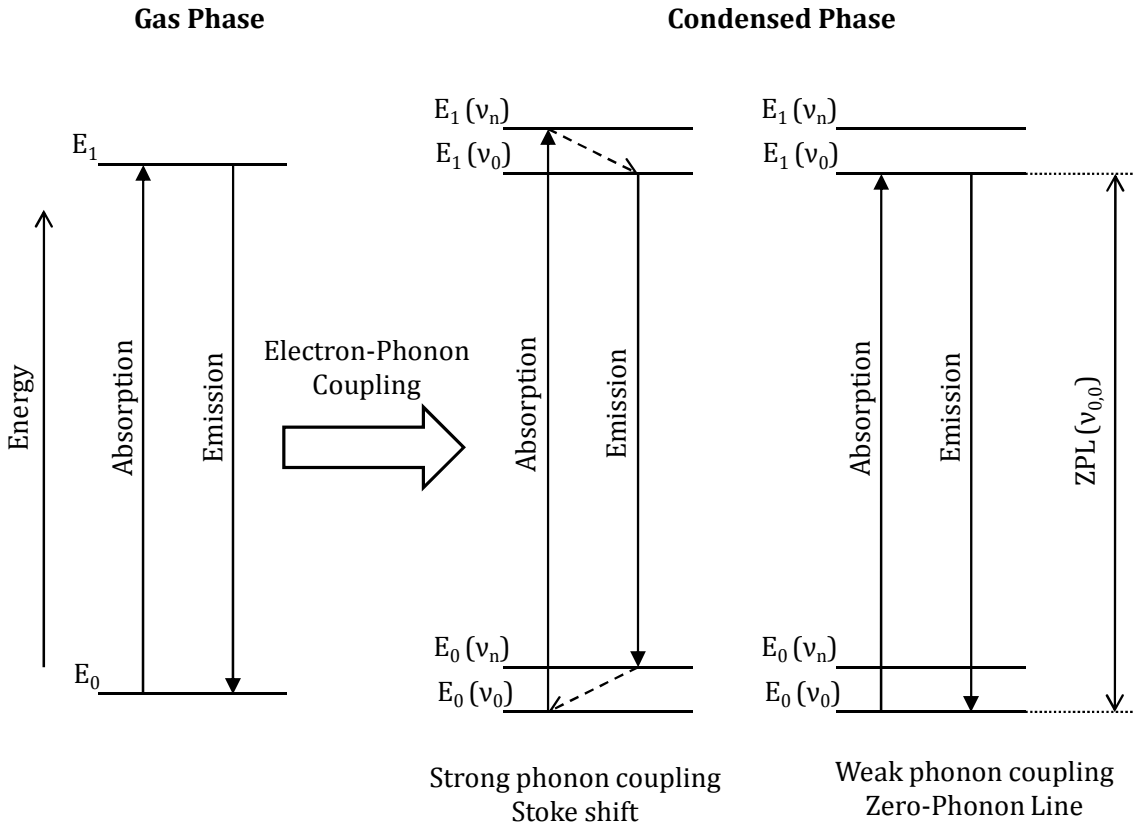

Figure I.6: A comparison between the interactions of a luminescent species in the gas and condensed phase. E_0 and E_1 represent the ground and excited electronic states of the species and ν represent the vibronic interactions in the ground and excited states induced by electron-phonon coupling. The right hand panel in this figure depicts the case of a luminescent centre in the solid where weak electron-phonon coupling ($S \approx 0$) exists.

This electron-phonon coupling can have the effect of both broadening the spectral bands and shifting the excitation and emission frequencies. In the energy level diagram in the centre of Figure I.6, excitation occurs from the ground state $E_0(v_0)$ to the phonon coupled excited state $E_1(v_n)$. This transition is obviously higher in energy than ΔE *(Ex.)* in the gas phase. From $E_1(v_n)$, fast non-radiative relaxation occurs to $E_1(v_0)$ followed by emission to the phonon coupled ground state level $E_0(v_n)$. Finally, non-radiative relaxation occurs from $E_0(v_n)$ to $E_0(v_0)$. By comparing the transition energies, ΔE *(Ex.)* $= E_1(v_n) - E_0(v_0)$ is now greater than ΔE *(Em.)* $= E_1(v_0) - E_0(v_n)$. The difference between ΔE *(Ex.)* and ΔE *(Em.)* is equal to the sum of the non radiative energies and is called the Stokes shift. Coupling to multiple phonons will produce a wide phonon side band in excitation and broadening of the emission line shapes. In cases where coupling between the phonons and electronic states is weak, (due to weak interactions with the host and unfavourable Franck-Condon factors) intense and well resolved zero-phonon lines (ZPLs) will be seen in excitation and the Stokes shift will be minimal (energy level diagram on right of Figure I.6). Phonon coupling is also observed in IR and Raman vibrational spectra but the effect on the lineshapes and positions is usually very small.

Even in cases where sharp ZPLs with low intensity phonon side bands are known to exist, absorption and emission line shapes may still appear broad relative to gas phase spectra. This inhomogeneous broadening is due to the overlap of the ZPLs of molecules or atoms in different matrix environments. Using laser induced fluorescence (LIF), well resolved, site selective spectra may be obtained in both excitation and emission. For polyatomic molecules, the matrix shifts of the vibrations discussed previously will have a slight effect on the electronic spectra, changing the zero-point energies of both ground and excited states from those in the gas phase. The positions of the vibronic bands will also change from those observed in the gas phase, with comparable shifts to those in vibrational spectra obtained using IR absorption and Raman scattering methods.

Matrix isolation is not unique in its site selectivity properties. For example, Shpol'skii matrices[47] consist of low temperature organic glasses doped with a molecule for spectroscopic analysis. Site effects like those observed in inert gas matrices for example matrix shifts from the gas phase and sharp zero-phonon line and phonon side bands apparent. The solvents used for the host are typically

simple alkanes or planar aromatic alkenes that have been selected to match the size of the guest species. Though Shpol'skii matrices are not suitable for infrared studies, due to the strong absorptions of the vibrational modes of the organic host, the vibronic bands in emission and excitation are narrow and well resolved.

The site effects described in the previous sections are seen in most MI experiments but their effect is relatively minor. There is a minimal perturbation of the spectral positions of the vibrational and electronic transitions of molecules in rare and inert gas low temperature matrices relative to the truly isolated gas phase environments. This allows the matrix isolation technique to be a convenient method of recording narrow line width IR and Raman spectra and, with the assistance of monochromatic laser fluorescence, the recording of site specific luminescence spectra with sharp zero-phonon lines. By comparing the host-guest bond lengths, lattice parameters and matrix shifts and splitting seen in experimental spectra along with theoretical calculations, the site occupancy of a molecule or atom in various hosts may be determined. For example, the site occupancy of a small sodium atom[48], medium sized aromatic naphthalene molecule[49] or even a large tetrapyrrole like porphine[50] may be made by comparison of experimental optical spectroscopy results with molecular dynamics (MD) pair potential or other theoretical calculations.

I.3 Spectroscopy of matrix-isolated phthalocyanines

As a result of the widespread interest in porphyrins and phthalocyanines, a vast literature exists (including the now twenty volume *The Porphyrin Handbook*[51,52]) with the optical properties of these important molecules having been studied in a wide range of different environments. Because of their very large extinction coefficients and great stability, the phthalocyanines (Pcs) are used as commercial dyes[53], but in recent times several novel applications such as photoconductors[54], as nonlinear optical materials[55] or as photosensitisers in laser cancer therapy[56] are now emerging. Phthalocyanines have also been proposed as photo-receptors in dye-sensitized solar cells (DSSC) for light energy harvesting, though issues of solubility and aggregation are still to be resolved[57]. Free-base porphyrins and phthalocyanines have also been used as models for intramolecular tautomerization, where the tautomeric forms involving the migration of the two central N bound H atoms may be observed.

The current study concerns the optical spectroscopy of two phthalocyanines – free-base phthalocyanine (H_2Pc) and zinc phthalocyanine (ZnPc). FT-IR spectra of these molecules in various low temperature matrices were recorded along with Raman scattering results KBr disks. Theoretical calculations using density function theory (DFT) were conducted in order to help assign the vibrational bands observed in the experimental results. Visible absorption and emission spectra using lamp excitation were recorded for both H_2Pc and ZnPc in low temperature inert gas solids. Laser-induced fluorescence (LIF) is very well suited for studies of these molecules due to the close match between their strong absorptions in the visible spectral region and the output of tuneable dye lasers. High resolution excitation and emission spectra were recorded using pulsed laser dye laser excitation, resulting in well resolved vibronic bands. Due to similar selection rules for the vibronic transitions and Raman active modes of H_2Pc and ZnPc, the DFT and experimental Raman results were used to help assign these vibronic bands. The unusual occurence of amplified emission was found in the most intense vibronic band of both H_2Pc and ZnPc in different inert gas host matrices. Possible reasons for this nonlinear optical phenomenon were investigated.

I.3.I IR and Raman spectroscopy of H_2Pc and ZnPc

The purpose of the vibrational spectroscopy conducted in this work was to provide assignments for the ground state vibrational modes of H_2Pc (D_{2h} symmetry) and ZnPc (D_{4h} symmetry). Indeed a complete vibrational analysis, involving comparison with narrow line experimental data, has not yet been made for these molecules. Matrix-IR absorption spectroscopy, isotope substitution, Raman spectroscopy and high-level DFT calculations were used to conduct a complete vibrational analysis of zinc and free-base phthalocyanine.

While several infrared studies have been presented for H_2Pc[58,59] and ZnPc[60] in KBr discs and in Nujol, no previously published reports for the low temperature IR spectra of these molecules currently exist. Despite numerous infrared studies of H_2Pc which have been published, the assignments of several vibrational modes remain uncertain, especially in the case of the N-H In-Plane Bending (NH-IPB) mode. This vibrational mode has been assigned to bands at 1006 cm^{-1} and 1539 cm^{-1} in experimental work[58,59]. Theoretical calculations of the infrared and Raman

active vibrations for H_2Pc[61] and ZnPc[62] have also been published. The most detailed vibrational analysis to-date of H_2Pc has been done by Zhang *et al.*[61], who conducted a DFT calculation utilising the B3LYP functional and a 6-31G* basis set.

An important aspect of the visible spectroscopy of H_2Pc which has not yet been resolved is the location of the origin of the S_2 (Q_y) state. In the gas phase the vibronic structure present in the excitation spectra is so complex in the onset region of the Q_y state that the band origin of this state has not yet been identified[63-65]. Extreme spectral congestion arises in the region where the v=0 level of the Q_y state overlaps the vibrationally excited levels of the Q_x (S_1) state rendering visual identification of the origin impossible. Due to the similar energy splitting between the Q_x and Q_y states in matrix spectra and the assumed transition energy of the N-H in-plane bending vibration, this mode is considered to be important in the coupling between the two electronic states[66]. Since the vibrational modes in the ground S_0 state and the first excited Q (S_1) state are very similar[67] , vibrational assignments in the ground state are essential for analysing the complex vibronic structure in the electronic excitation spectra. As a precursor to the analysis of the excitation and emission spectra, an analysis of the fundamental vibrational modes was required.

Investigation of the infrared spectra of H_2Pc and its isotopomers using the matrix-isolation technique allowed conclusive identification of the NH-IPB mode. The IR spectra obtained under these conditions are those of isolated molecules and are largely free of bands arising from interactions present in phthalocyanine aggregates. Moreover, because of the low temperatures used, the thermal population of the lowest frequency modes of the Pcs which are known to exist, were almost completely eliminated. Large basis set DFT calculations were performed on ZnPc and the three isotopic forms of H_2Pc (H_2Pc, D_2Pc and HDPc) in order to assign the observed vibrational modes. When correlating the vibrational modes of the molecules, an inverted isotopic shift was observed between H_2 and D_2Pc. These unusual numerical results were examined with vibrational frequency calculations using sub-amu increments (that is atomic mass units below one) for the hydrogen atoms and were found to derive from avoided crossings of the vibrational frequencies when going from H_2Pc to D_2Pc. These calculations were essential for assignments of the vibrational modes present in both Raman scattering and visible fluorescence spectra recorded with excitation of Q states of matrix-isolated Pcs.

I.3.II Visible spectroscopy of H_2Pc and ZnPc

The electronic spectroscopy of both H_2Pc and ZnPc molecules in the gas phase[68,69], in low-temperature jets[63,70], in He droplets[65,71] and in thin films[72] have been reported. These two molecules have also been studied in cryogenic matrices: either in Shpol'skii organic matrices[67,73,74] or isolated in the solid rare gases[66,75-77]. Although the first absorption spectra of matrix-isolated porphyrins and their synthetic analogues—the phthalocyanines—were reported nearly forty years ago by Bajema *et al.*[77] the behaviour of this important class of molecules isolated in the solid rare gases is still not fully characterised. A notable exception is the recent work by Waluk and co-workers on the spectroscopy[78] and isolation[79] of porphyrins and related molecules in rare gas matrices. In addition, several groups[80,81] have analysed the vibronic structure on the S_1 state of several porphyrins and phthalocyanines in Spol'skii matrices.

The most recent laser-induced fluorescence (LIF) excitation spectra of zinc and free-base phthalocyanine under jet-cooled conditions have been investigated by Plows and Jones[70]. In spite of numerous gas phase studies of H_2Pc, the band origin of the Q_y (S_2) state still has not been determined. This is due to spectral congestion arising from overlap in this region by high frequency modes of the Q_x (S_1) state (Figure I. 7). Matrix-isolation spectroscopy affords an ideal opportunity to identify the true band origin since spectra recorded under these conditions are free of any rotational structure and solvent-shifts induced by the solid rare gases are very small due to very weak interactions with these inert hosts. Moreover, the results obtained under these inert conditions can then be directly compared with predictions obtained from theoretical methods. For the aforementioned reasons, an investigation of the visible spectroscopy of H_2Pc and ZnPc isolated in inert gas solids was undertaken.

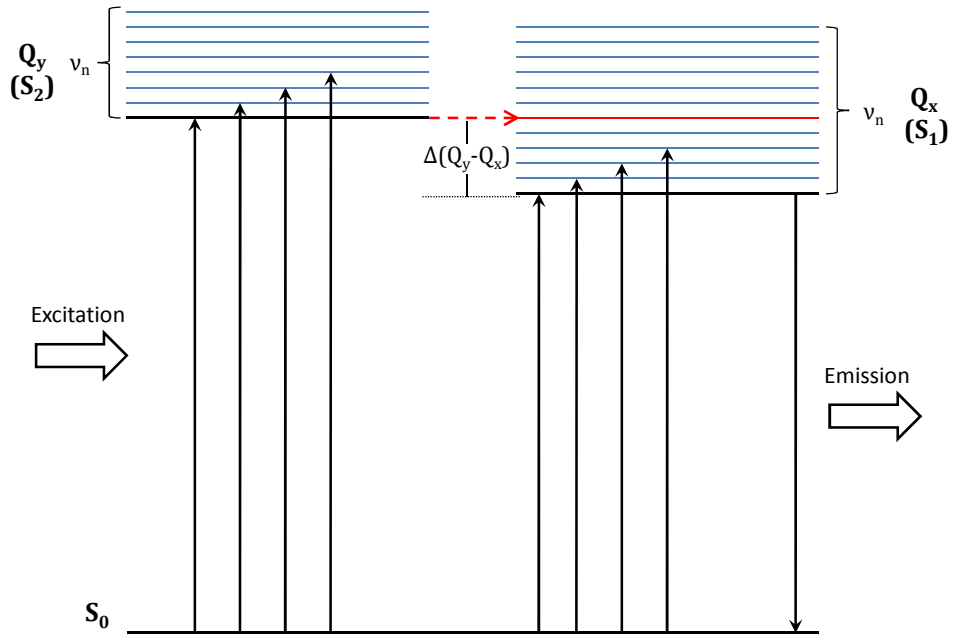

Figure I. 7: Schematic of excitation from ground state S_0 of H_2Pc to the vibronic excited states of $Q_x(S_1)$ and $Q_y(S_2)$ and emission from the $\nu = 0$ vibrational level of Q_x via non-radiative decay. Coupling of the Q_y state to a vibrational mode of Q_x is indicated by the dashed arrow.

ZnPc has been extensively studied in Ar matrices[76,82-84], revealing sharp vibronic bands in both emission and excitation spectra. Like the porphyrins, the phthalocyanines have a propensity of forming dimers and aggregates in more concentrated matrix samples. As demonstrated in the systematic matrix study of Williamson and co-workers[76] on ZnPc and by Lucia *et al.* on CuPc[85], these species absorb to the red of the sharp 0-0 monomer transitions. The content of aggregate species was kept to a minimum in the samples prepared in the present study by careful control of the vaporisation temperature and host gas flow. Accordingly the absorption and emission spectra correspond to samples containing well-isolated guest molecules. Visible absorption spectroscopy of matrix-isolated H_2Pc has also been reported before in the literature, first by Bajema *et al.* in Ar, Kr and Xe matrices[77] and in Ar by Lucia *et al.*[85] with later spectral hole-burning experiments by Geissinger and co-workers of H_2Pc in Ar, Kr and Xe[75]. Of pertinence to the current work, are the results reported in 1979 by Bondybey and English[66]. They recorded high resolution visible laser excitation and emission spectra in Ne and Ar matrices of not only H_2Pc but also of its isotopomer D_2Pc. Well resolved vibronic bands were observed in emission up to 1546 cm^{-1} from the 0-0 band of the Q_x transition. In excitation an equivalent vibronic structure was observed up to ~950 cm^{-1} but due to the overlap with the Q_x vibronic bands, the region around the Q_y

transition was found to be highly congested. Some of the vibronic bands were found to shift upon deuteration including, significantly the Q_y band. From this isotopic shift, it may be concluded that the vibronic mode in Q_x state, coupling to the Q_y, involves some N-H motion.

No successful attempts to assign the vibrational modes coupling to the ground and excited states, observed in emission and excitation spectra, has been reported in the literature. As stated by Bondybey and English with regard to the vibrational structure of both states[66], "*Complete vibrational assignment in a molecule with ~350* [sic] *vibrational degrees of freedom is clearly not feasible.*" From comparison of the Raman scattering and visible emission spectra, a clear correlation is seen between the Raman active modes and vibronic bands in emission due to similar group theoretical selection rules. This allowed the Raman active modes calculated with DFT to be used to assign the emission vibronic bands of both H_2Pc and ZnPc. The position of the excitation bands of ZnPc were found to mirror those in emission indicating a similar molecular structure in the excited state and allowed the vibrational assignments made for ground state to be applied to the vibronic transitions found in the excitation spectrum. Similarly, mirroring of the emission and excitation vibronic structure was apparent for H_2Pc up until the Q_y transition. The correlation between the calculated Raman and emission modes, with comparison to the D_2Pc results of Bondybey and English, allowed a *tentative* assignment of the vibrational mode coupling Q_x to the Q_y excited states. The excitation energies of H_2Pc and ZnPc were calculated using TD-DFT and were compared to those calculated for other aromatic tetrapyrroles in order to assess this technique's potential use in the interpretation and definitive assignment of experimental excited states.

I.3.III Amplified Emission (AE) of H_2Pc and ZnPc

While undertaking the laser induced fluorescence experiments of matrix-isolated H_2Pc and ZnPc, an unusually intense vibronic band was observed with slightly increased laser power. This novel solid state effect is noteworthy in that two previous matrix luminescence studies on the phthalocyanines conducted with laser excitation, one by Bondybey and English[66] on H_2Pc and another by Williamson and coworkers[76] on ZnPc in Ar matrices, did not report such an effect. In contrast, stimulated emission has been reported by Sorokin and co-workers[86,87]

for the closely related molecule chloroaluminium phthalocyanine in solution. Significantly, this was achieved with pulsed ruby laser excitation and within a resonator cavity. The possible reasons for the different results of the previous laser matrix studies were investigated by considering the threshold conditions for amplified emission (AE).

The comparison of the ground state vibronic structures in emission and the Raman active vibrational modes of H_2Pc and ZnPc found not only a close match between their spectral positions but also a correlation with their intensities. DFT calculations allowed assignment of the vibronic mode exhibiting AE to the Raman active vibration determined to have the greatest intensity. The success of DFT to predict the vibronic structures of H_2Pc and ZnPc, by way of calculating their Raman spectra, offered an effective theoretical route to predicting the spectral positions and relative intensities of the vibrational modes seen in emission for other molecules. With this in mind, the Raman active vibrational frequencies and scattering activities of structurally similar tetrapyrrolic molecules were calculated using DFT and their potential to exhibit AE assessed.

I.4 Thesis layout

The following section gives a brief outline of the chapters in this thesis.
In Chapter II the experimental methods used will be described including sample preparation and spectroscopic methods. Chapter III will present a background to the theoretical methods used. A description of how the ground state properties (geometries, vibrational frequencies and intensities) were calculated using DFT and the electronic transitions using TD-DFT will be given in addition to a description of the point group symmetry considerations needed for the interpretation of the spectroscopic results. The matrix-isolated FT-IR absorption results for ZnPc, H_2Pc, HDPc and D_2Pc in Ar, Kr, Xe and N_2 will be given in Chapter IV. These results will be assigned using the DFT vibrational modes calculated at the B3LYP/6-311++G(2d,2p) level and correlations made between the modes of the different Pcs. The Raman scattering spectra of these molecules in KBr salt disks will also be presented and assigned. In Chapter V, the visible luminescence results from H_2Pc and ZnPc in various low temperature solids will be given. These will include absorption recorded using tungsten lamp excitation, emission and excitation spectra obtained using laser induced fluorescence and fluorescence

lifetime measurements. The vibronic bands observed will be assigned with the aid of the vibrational analysis given previously in Chapter IV and the TD-DFT excitation energies and oscillator strengths of H_2Pc and ZnPc (as well as those calculated for H_2 and Zn tetraazaporphyrin (TAP), tetrabenzoporphyrin (TBP) and porphine (P)) will be given and compared with experiment. In Chapter VI, amplified emission of H_2Pc and ZnPc will be described and its properties discussed. The potential of AE to occur for both free-base and metallo TAP, TBP and P will be accessed using DFT calculations. Finally, Chapter VII will give a conclusion of the main results presented in the previous chapters.

I.5 References

(1) Milgrom, L. R. *The colours of life: An introduction to the chemistry of porphyrins and related compounds*; Oxford University Press Oxford, 1997.
(2) OED Online; Oxford University Press, March 2008; Vol. 2010.
(3) Löbbert, G. *Phthalocyanines*; Wiley-VCH Verlag GmbH & Co. KGaA, 2000.
(4) Image sources: Clover taken from en.wikipedia.org, red blood cells copyright Nation Institutes of Health (www.NIH.gov), t-shirt design copyright Razzle Inc. (www.razzel.com) and CD-R from Mitsui Chemicals Inc.
(5) Phthalocyanine and Porphyrin Dyes: Sigma-Aldrich online catalogue; Sigma-Aldrich, 2010.
(6) Clayden, J.; Greeves, N.; Warren, S.; Wothers, P. *Organic Chemistry*; Oxford University Press: Oxford, 2001.
(7) Gregory, P. *Journal of Porphyrins and Phthalocyanines* **2000**, *4*, 432.
(8) de Diesbach, H.; von der Weid, E. *Helevtica Chimica Act* **1927**, *10*, 886.
(9) Linstead, R. P. *Journal of the Chemical Society (Resumed)* **1934**, 1016.
(10) Byrne, G. T.; Linstead, R. P.; Lowe, A. R. *Journal of the Chemical Society (Resumed)* **1934**, 1017.
(11) Linstead, R. P.; Lowe, A. R. *Journal of the Chemical Society (Resumed)* **1934**, 1022.
(12) Dent, C. E.; Linstead, R. P. *Journal of the Chemical Society (Resumed)* **1934**, 1027.
(13) Linstead, R. P.; Lowe, A. R. *Journal of the Chemical Society (Resumed)* **1934**, 1031.
(14) Dent, C. E.; Linstead, R. P.; Lowe, A. R. *Journal of the Chemical Society (Resumed)* **1934**, 1033.
(15) Braun, A.; Tcherniac, J. *Berichte der Deutschen Chemischen Gesellschaft* **1907**, *40*, 2709.
(16) McKeown, N. B. The Synthesis of Symmetrical Phthalocyanines. In *The Porphyrin Handbook*; Kadish, K. M., Smith, K. M., Guilard, R., Eds.; Academic Press: San Diego, 2003; Vol. 15.
(17) Eicher, T.; Hauptmann, S. *The Chemistry of Heterocycles: Structure, Reactions, Syntheses and Applications*, 2nd ed.; Wiley-VCH: Weinheim, 2003.
(18) Sharman, W. M.; van Lier, J. E. Synthesis of Phthalocyanine Precursors. In *The Porphyrin Handbook*; Kadish, K. M., Smith, K. M., Guilard, R., Eds.; Academic Press: San Diego, 2003; Vol. 15.
(19) Gouterman, M. *The Journal of Chemical Physics* **1959**, *30*, 1139.
(20) Gouterman, M. *Journal of Molecular Spectroscopy* **1961**, *6*, 138.
(21) Gouterman, M.; Wagnière, G. H.; Snyder, L. C. *Journal of Molecular Spectroscopy* **1963**, *11*, 108.
(22) Nguyen, K. A.; Pachter, R. *Journal of Chemical Physics* **2001**, *114*.
(23) McNaught, A. D.; Wilkinson, A. *IUPAC Compendium of Chemical Terminology*, 2nd ed.; Blackwell Scientific Publications: Oxford, 1997.
(24) Bondybey, V. E.; Savchenko, E. V. *Low Temperature Physics* **2000**, *26*, 629.
(25) *125 Years of Linde: A Chronicle*; Wolfinger, U., Ed.; Linde AG: Wiesbaden, 2004.
(26) Vegard, L. *Royal Academy of Science* **1923**, *176*, 941.
(27) Vegard, L. *Nature* **1924**, *114*, 357.
(28) Vegard, L.; Kamerlingh-Onnes, H.; Keesom, W. H. *Royal Academy of Science* **1925**, *180*, 1084.

(29) Vegard, L. *Annalen der Physik* **1930**, *6*, 487.
(30) Bondybey, V. E.; Smith, A. M.; Agreiter, J. *Chemical Reviews* **1996**, *96*, 2113.
(31) Lewis, G. N.; Lipkin, D.; Magel, T. T. *Journal of the American Chemical Society* **1941**, *63*, 3005.
(32) Lewis, G. N.; Lipkin, D. *Journal of the American Chemical Society* **1942**, *64*, 2801.
(33) Norman, I.; Porter, G. *Nature* **1954**, *174*, 508.
(34) Norman, I.; Porter, G. *Proceedings of the Royal Society of London Series a-Mathematical and Physical Sciences* **1955**, *230*, 399.
(35) Whittle, E.; Dows, D. A.; Pimentel, G. C. *Journal of Chemical Physics* **1954**, *22*, 1943.
(36) Becker, E. D.; Pimentel, G. C. *Journal of Chemical Physics* **1956**, *25*, 224.
(37) Becker, E. D.; Pimentel, G. C.; Vanthiel, M. *Journal of Chemical Physics* **1957**, *26*, 145.
(38) Turner, J. J.; Pimentel, G. C. *Science* **1963**, *140*, 974.
(39) Whittle, E.; Dows, D. A.; Pimentel, G. C. *The Journal of Chemical Physics* **1954**, *22*, 1943.
(40) Ozin, G. A.; Moskovits, M. *Cryochemistry*; John Wiley & Sons: New York, 1976.
(41) Dunkin, I. R. *Matrix-Isolation: A Practical Approach*; Oxford University Press: Oxford, 1998.
(42) Cradock, S.; Hinchcliffe, A. J. *Matrix Isolation*; Cambridge University Press: Cambridge, 1975.
(43) Kittel, C. *Introduction to Solid State Physics*, 7th ed.; John Wiley & Sons: New York, 1996.
(44) Crépin-Gilbert, C.; Tramer, A. *International Reviews in Physical Chemistry* **1999**, *18*, 485.
(45) Huisken, F.; Kaloudis, M.; Vigasin, A. A. *Chemical Physics Letters* **1997**, *269*, 235.
(46) Bracken, V. A.; Legay-Sommaire, N.; McCaffrey, J. G. *The Journal of Physical Chemistry A* **1997**, *101*, 9863.
(47) *Shpol'skii Spectroscopy and Other Site-Selection Methods: Applications in Environmental Analysis, Bioanalytical Chemistry, and Chemical Physics*; John Wiley & Sons: New York, 2000.
(48) Ryan, M.; Collier, M.; Pujo, P. d.; Crépin, C.; McCaffrey, J. G. *The Journal of Physical Chemistry A* **2009**, *114*, 3011.
(49) Crépin, C.; de Pujo, P.; Bouvier, B.; Brenner, V.; Millié, P. *Chemical Physics* **2001**, *272*, 243.
(50) Kyrychenko, A.; Gorski, A.; Waluk, J. *The Journal of Chemical Physics* **2004**, *121*, 12017.
(51) *The Porphyrin Handbook*; Kadish, K. M.; Smith, K. M.; Guilard, R., Eds.; Academic Press: San Diego, 1999; Vol. 1-10.
(52) *The Porphyrin Handbook*; Kadish, K. M.; Smith, K. M.; Guilard, R., Eds.; Academic Press: San Diego, 2003; Vol. 11-20.
(53) Moser, F. H.; Thomas, A. L. *Phthalocyanine Compounds*; Reinhold Publishing Corporation: New York, 1969.
(54) Hanada, T.; Takiguchi, H.; Okada, Y.; Yoshida, Y.; Tanigaki, N.; Yase, K. *Journal of Crystal Growth* **1999**, *204*, 307.
(55) Bredas, J. L.; Adant, C.; Tackx, P.; Persoons, A.; Pierce, B. M. *Chemical Reviews* **1994**, *94*, 243.

(56) Bown, S. G.; Tralau, C. J.; Smith, P. D. C.; Akdemir, D.; Wieman, T. J. *British Journal of Cancer* **1986**, *54*, 43.
(57) Robertson, N. *Angewandte Chemie International Edition* **2006**, *45*, 2338.
(58) Shurvell, H. F.; Pinzuti, L. *Canadian Journal of Chemistry* **1966**, *44*, 125.
(59) Sammes, M. P. *Journal of the Chemical Society-Perkin Transactions 2* **1972**, 160.
(60) Tackley, D. R.; Dent, G.; Smith, W. E. *Physical Chemistry Chemical Physics* **2000**, *2*, 3949.
(61) Zhang, X.; Zhang, Y.; Jiang, J. *Vibrational Spectroscopy* **2003**, *33*, 153.
(62) Tackley, D. R.; Dent, G.; Smith, W. E. *Physical Chemistry Chemical Physics* **2001**, *3*, 1419.
(63) Fitch, P. S. H.; Haynam, C. A.; Levy, D. H. *Journal of Chemical Physics* **1980**, *73*, 1064.
(64) Fitch, P. S. H.; Haynam, C. A.; Levy, D. H. *Journal of Chemical Physics* **1981**, *74*, 6612.
(65) Lehnig, R.; Slipchenko, M.; Kuma, S.; Momose, T.; Sartakov, B.; Vilesov, A. *Journal of Chemical Physics* **2004**, *121*, 9396.
(66) Bondybey, V. E.; English, J. H. *Journal of the American Chemical Society* **1979**, *101*, 3446.
(67) Huang, T. H.; Rieckhoff, K. E.; Voigt, E. M. *Journal of Chemical Physics* **1982**, *77*, 3424.
(68) Eastwood, D.; Edwards, L.; Gouterman, M.; Steinfel.J. *Journal of Molecular Spectroscopy* **1966**, *20*, 381.
(69) Edwards, L.; Gouterman, M. *Journal of Molecular Spectroscopy* **1970**, *33*, 292.
(70) Plows, F. L.; Jones, A. C. *Journal of Molecular Spectroscopy* **1999**, *194*, 163.
(71) Slenczka, A.; Dick, B.; Hartmann, M.; Toennies, J. P. *The Journal of Chemical Physics* **2001**, *115*, 10199.
(72) Stendal, A.; Beckers, U.; Wilbrandt, S.; Stenzel, O.; vonBorczyskowski, C. *Journal of Physics B-Atomic Molecular and Optical Physics* **1996**, *29*, 2589.
(73) Hala, J.; Pelant, I.; Parma, L.; Vacek, K. *Czechoslovak Journal of Physics* **1982**, *32*, 705.
(74) Personov, R. I. *Optika I Spektroskopiya* **1963**, *15*, 61.
(75) Geissinger, P.; Kador, L.; Haarer, D. *Physical Review B* **1996**, *53*, 4356.
(76) Prince, B. J.; Williamson, B. E.; Reeves, R. J. *Journal of Luminescence* **2001**, *93*, 293.
(77) Bajema, L.; Gouterman, M.; Meyer, B. *Journal of Molecular Spectroscopy* **1968**, *27*, 225.
(78) Starukhin, A.; Shulga, A.; Waluk, J. *Chemical Physics Letters* **1997**, *272*, 405.
(79) Kyrychenko, A.; Waluk, J. *Journal of Chemical Physics* **2005**, *123*.
(80) Arabei, S. M.; Egorova, G. D.; Katibnikov, M. A.; Soloviev, K. N.; Shkirman, S. F. *Teoreticheskaya I Eksperimentalnaya Khimiya* **1989**, *25*, 306.
(81) Arabei, S. M.; Galaup, J. P.; Solovyov, K. N.; Donyagina, V. F. *Chemical Physics* **2005**, *311*, 307.
(82) Krausz, E.; Riesen, H.; Schatz, P. N.; Gasyna, Z.; Dunford, C. L.; Williamson, B. E. *Journal of Luminescence* **1995**, *66-67*, 19.
(83) Metcalf, D. H.; VanCott, T. C.; Snyder, S. W.; Schatz, P. N.; Williamson, B. E. *The Journal of Physical Chemistry* **1990**, *94*, 2828.
(84) Van Cott, T. C.; Rose, J. L.; Misener, G. C.; Williamson, B. E.; Schrimpf, A. E.; Boyle, M. E.; Schatz, P. N. *The Journal of Physical Chemistry* **1989**, *93*, 2999.
(85) Lucia, E. A.; Verderame, F. D.; Taddei, G. *The Journal of Chemical Physics* **1970**, *52*, 2307.

(86) Sorokin, P. P.; Lankard, J. R. *IBM Journal of Research and Development* **1966**, *10*, 162.
(87) Sorokin, P. P.; Lankard, J. R.; Hammond, E. C.; Moruzzi, V. L. *IBM Journal of Research and Development* **1967**, *11*, 130.

Chapter II: Experimental Methods

II.1 Introduction

The experimental portion of this work primarily involved the spectroscopy of phthalocyanines isolated in inert gas solids. In this chapter the experimental procedures used in the preparation of the matrix isolated samples and deuterated free-base phthalocyanine will be described. A description of the apparatus and procedures used for recording steady-state and time-resolved spectra will be provided. Finally an account of the Fourier transform infrared (FTIR) spectrometer used in this work will be given as well as a review of the procedures used to convert an interferogram to an IR spectrum.

II.2 Matrix-Isolation Apparatus

The matrix-isolation (MI) apparatus used in this work is shown in Figure II.1. In order to reduce heat exchange and prevent deposition of atmospheric gases, a high vacuum is essential[1,2]. Different pumping systems were used for the FTIR and Ultraviolet/visible (UV-Vis) experiments. The UV-Vis experimental setup achieved a high vacuum using an Edwards E02 *Speedivac* oil diffusion pump backed by an Edwards RV3 rotary pump. An Edwards liquid nitrogen (L-N_2) cold trap was attached to the diffusion pump to reduce contamination of the cryogenic system with diffusion pump oil vapour when cold. An Edwards QSBR quarter swing valve allowed the isolation of the vacuum manifold from the pump system for venting the system up to atmospheric pressures.

The FTIR experimental setup used an Edwards 100/300M *Diffstak* oil diffusion pump with an Edwards E2M-18 rotary backing pump. The *Diffstak* design of this diffusion pump increases the ability of the pump to condense diffusion oil vapour, relative to standard diffusion pump designs, and reduces the need for an L-N_2 cold trap. Isolation of the vacuum manifold from the pump system was achieved using a quarter swing valve integral to the *Diffstak* pump.

Both diffusion pumps require vacuum pressures below 5 x 10^{-3} mbar in order to operate. These pressures were achieved by the rotary backing pumps and were monitored using a Granville-Phillips Series 275 Convectron gauge[3] in the UV-Vis experiment and an Edwards Pirani PRE10K gauge head with an Edwards Pirani

501 gauge readout in the FTIR experiment. Lower vacuum pressures (10^{-3}—10^{-7} mbar) were measured using an Alcatel CF2P Penning gauge. Comparable vacuum pressures were achieved in both setups: 10^{-7} mbar at room temperature and < 10^{-7} mbar following cool-down to cryogenic temperatures.

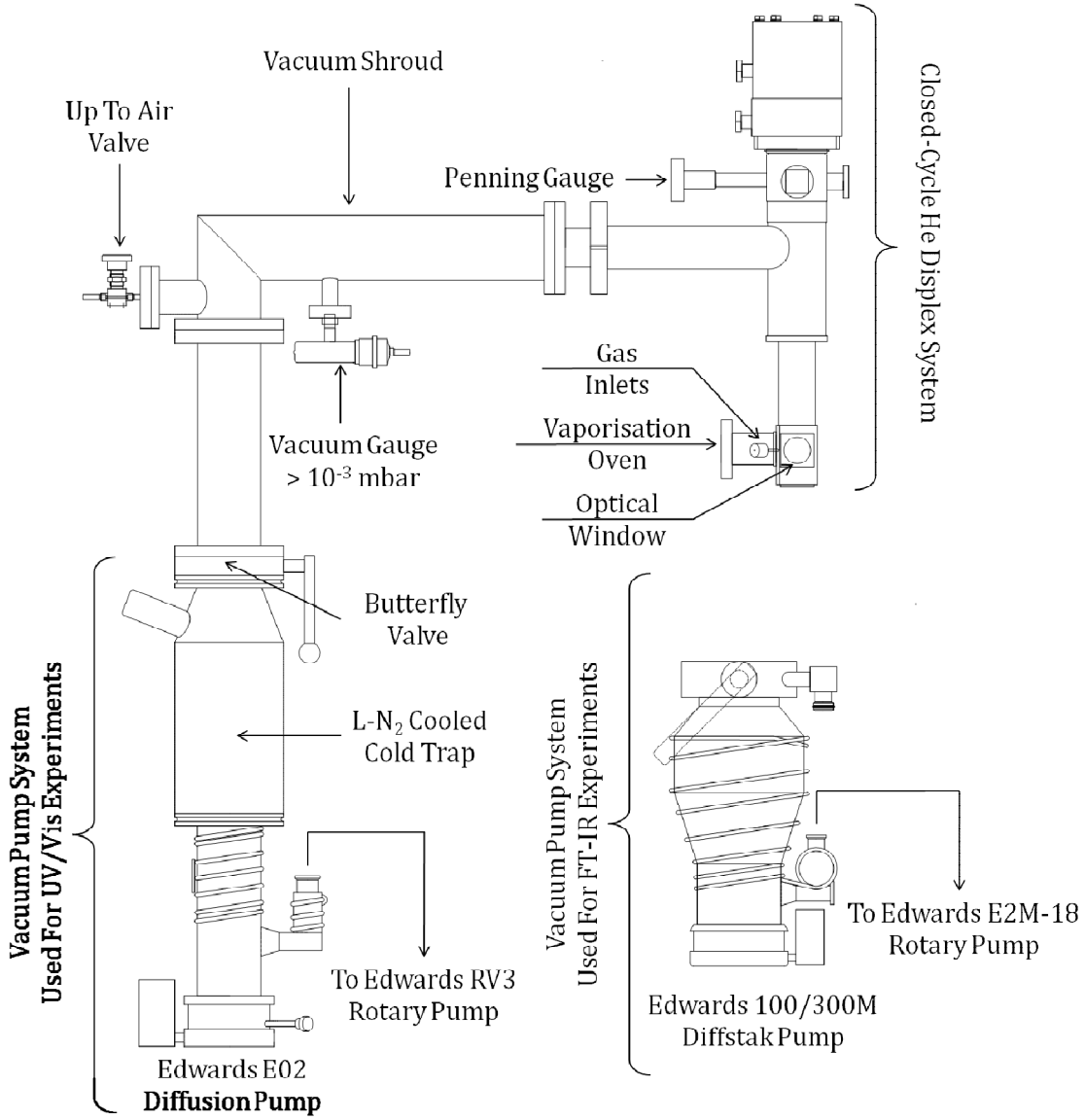

Figure II.1: Diagram of matrix-isolation apparatus showing the pump systems used for both the UV-Vis and FTIR experiments

Figure II.2 shows the APD Cryogenics closed-cycle helium displex system used to achieve temperatures of approximately 12 K at the sample window. The system operates by pumping high-pressure helium at 270 psi from an APD Cryogenics HC-2 compressor[4] via gas lines into an APD Cryogenics DE-202 two-stage refrigeration unit[5]. Heat is removed by the Gifford-McMahon refrigeration cycle by expansion of the compressed helium within the two stages. The gas is recycled by returning the warm helium to the displex compressor. The initial stage reaches ~77 K while the

lower second stage typically reached temperatures of 12 K. A nickel plated copper holder for a ¾" sample window was mounted to the end of the second refrigeration stage. The temperature of the window was controlled and monitored by a Scientific Instruments 9600-1 heater and silicon diode[6] attached to the copper holder. The sample window was placed within the copper holder with an indium seal to obtain good thermal contact[1].

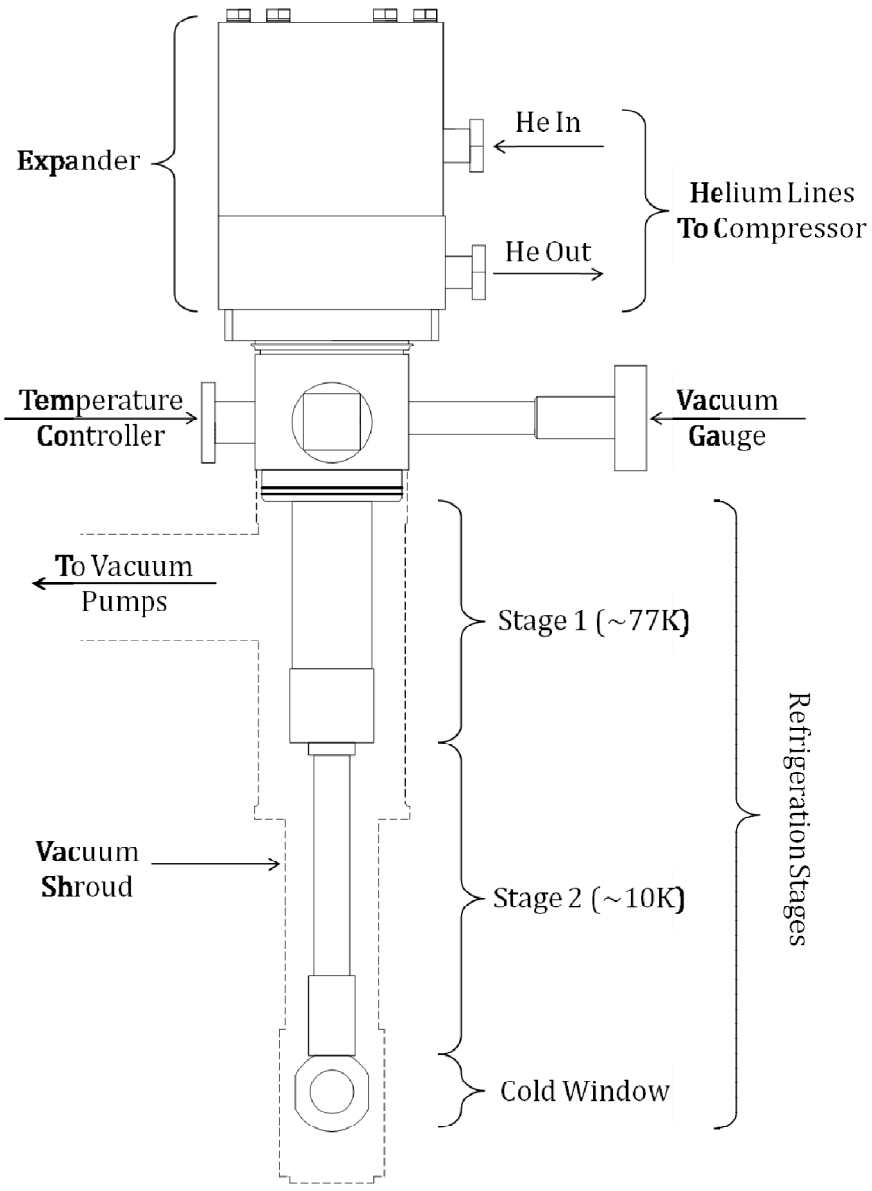

Figure II.2: APD Cryogenics closed-cycle helium displex system. Sample temperatures of ~12K were achieved using the two stage refrigeration system shown.

Three 1½" x 4 mm external windows were attached via a Viton® O-ring seal to the vacuum manifold to allow spectroscopic analysis of the sample on the cold window. Materials with suitable transmission ranges were selected for the cold and external windows. For the UV-Vis experiments, calcium fluoride (CaF_2)

windows with a transmission range from approximately 129 nm to 1176 nm (77,519 to 850 cm^{-1}) were used. For the FTIR experiments, potassium bromide (KBr) with an approximate transmission range 230 nm to 40 μm (43,500 to 250 cm^{-1}) was used. CaF_2 is only sparingly soluble in water (0.0017 g/100g) and may be regarded as insoluble. KBr is a hygroscopic soft salt with a high water solubility (53.4 g/100g @ 20 °C) and must be kept under dry conditions and cleaned carefully with non-polar solvents[1].

II.3 Gas Handling System (GHS)

The gases used in both the UV-Vis and FTIR experiments were handled using two distinct yet similarly designed gas handling systems (GHS) shown in Figure II.3. A vacuum of $\sim 10^{-8}$ mbar was maintained in the UV-Vis GHS using a Pfeiffer Balzers TPU-180H turbo-molecular pump[7] backed by an integral bellows pump[8]. The pumping system was attached to the GHS via an AEI MV38 all-metal angle valve. The gas pressures within the GHS were monitored using two Tylan General Capacitance Diaphragm Gauges; a model CDLD-11 with a pressure range of 0-10 torr and a model CDLD-31 with a pressure range of 0-1000 torr[9]. The pumping system for the FTIR experiment consisted of the same pump set-up used in the FTIR MI apparatus *i.e.* an Edwards 100/300M *Diffstak* oil diffusion pump backed with an Edwards E2M-18 rotary pump. The pumps were attached to the GHS with an MKS ¾" angle valve (AV-075M) and gas pressures were monitored using two MKS Type 626 *Baratron*® gauges with pressure ranges of 0-10 and 0-1000 torr[10].

The Baratron type gauges allow gas flows to be monitored during deposition and gas mixtures to be produced either directly using the lower pressure gauge or by serial dilution. In both experimental set-ups, the matrix gas flows during deposition were regulated using a Granville-Phillips type 203 variable leak valve[11]. The Granville-Phillips variable leak valve allowed the isolation of the GHS from the vacuum manifold of the MI apparatus and was attached to the Pc vaporisation oven via a length of ¼" VRC tubing (see Section II.4.I).

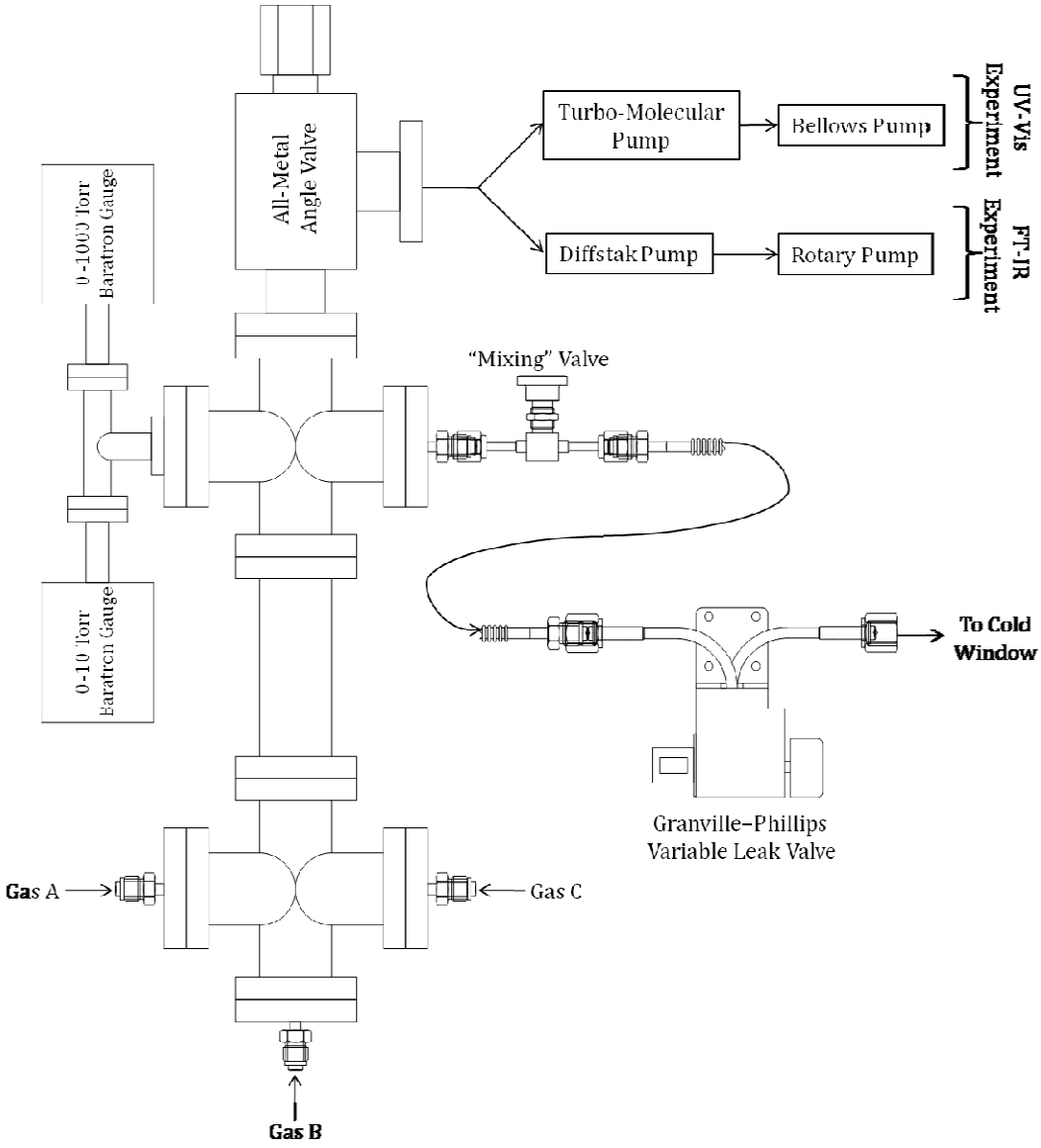

Figure II.3: Schematic of Gas Handling System used to prepare gases for deposition.

II.4 Sample Preparation

Matrix-isolated samples were prepared by co-condensing the guest species simultaneously with a bulk host gas onto a cryogenically cooled window. Rare-gases (Ar, Kr and Xe) and a molecular gas (N_2) were used as hosts. The gases were prepared using the gas handling system described above. The temperature at which the samples were deposited depended on the melting points, M_p, of the host gases (listed in Table II.4) with maximum deposition temperatures ~1/4 of the M_p of the host gas[2]. In order to produce a sufficiently isolated matrix sample, the guest species must be fully vaporised.

Table II.1: Host gas purities, suppliers and melting points.

Host Gas	Chemical Purity	Supplier	M_p (K)[12]	Refractive Index[13,14]
Rare Gases				
Argon (Ar)	99.998%	BOC UK	83.8	1.29, 1.32
Krypton (Kr)	99.995%	Linde Gas UK	115.79	1.28, 1.428
Xenon (Xe)	99.999%	Linde Gas UK	161.4	1.49
Molecular Gas				
Nitrogen (N_2)	99.999%	Linde Gas UK	63.15	1.22

The sample thickness was measured by monitoring the scattering of a monochromatic light during deposition. A 657 nm laser diode was directed at the sample window and the angle of incidence between the laser and monochromator was measured. The monochromator was set at 657 nm and the variation of the reflected laser intensity was recorded during deposition. The sample thickness d was determined using the equation:

$$d = \frac{m\lambda}{2n\,cos\theta} \qquad \text{(II.1)}$$

where m is the number of interference fringes recorded during deposition, λ is the wavelength of the incident light in metres (6.57×10^{-7} m), n is the refractive index of the solid (see Table II.1) and θ is the angle of incidence (15°). For example, an argon sample deposited with a gas flow rate of 2 torr/min was monitored for 80 seconds resulting in 11 interference fringes. The thickness determined using equation II.1 was 3.66×10^{-6} m or a rate of 2.74×10^{-3} mm/min. Assuming the same deposition rate throughout the experiment, a 220 torr sample would be ~0.3 mm.

II.4.I Phthalocyanine Vapour Generation

Zinc phthalocyanine (ZnPc) and free-base phthalocyanine (H_2Pc) were purchased from Sigma Aldrich and Fluka respectively and were used without further purification. Matrix samples were prepared by heating the phthalocyanines to around 350 °C and using the flowing host gas to entrain the XPc vapour for deposition on a cryogenically cooled window. The oven design used (shown in Figure II.4.II) consisted of a crucible made from solid stainless steel cylinder into which a hollow screw, containing either ZnPc or H_2Pc, was fitted. The top of this screw was positioned to

emerge at right angles to a 2 mm opening passing the length of the cylinder. The crucible was connected by a Swagelok compression seal to a ¼" gas inlet line. Resistive heating of the cylinder was used to achieve vaporisation and the temperature was monitored using a thermocouple device. The entire crucible assembly was surrounded in a stainless steel heat shield. In order to direct the XPc/gas mixture more efficiently to the window, a stainless steel nozzle was attached to the outlet of the crucible nearest the window. To achieve isolation of the XPc as a monomer, large gas flows (40 mmol/hr) were required.

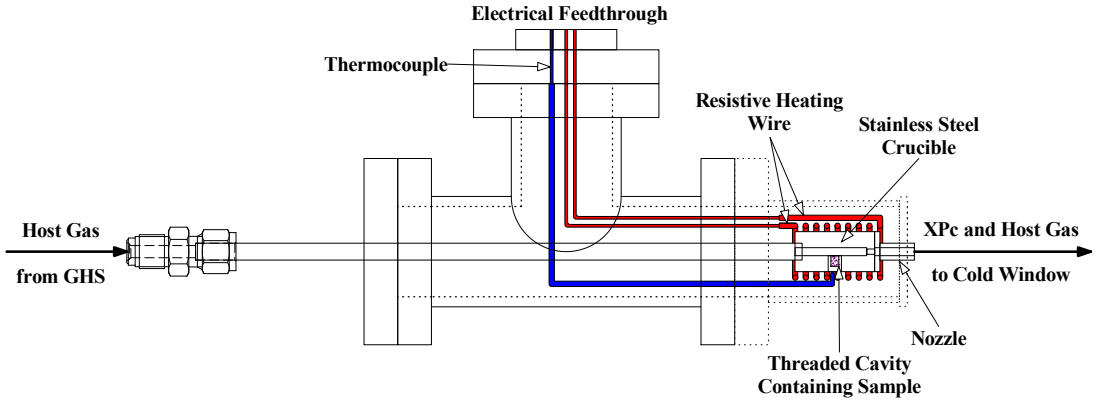

Figure II.4: Oven design used in the vaporisation of phthalocyanines. The oven was attached directly to the vacuum manifold via an o-ring compression seal near the cryogenic window.

The samples were deposited onto the sample window at 20-25 K for Ar and N_2 matrices. Slightly higher temperatures of 25-27 K were used for the heavy rare gas matrices Kr and Xe, in order to avoid the formation of highly scattering samples. All spectra were recorded at 13 K. Longer deposition times of up to 1 hour were required to achieve acceptable IR absorption strengths and were at least twice as long as for the samples used in visible spectroscopic studies. Concentrations of XPc in the host matrix were controlled by adjusting the oven temperature and gas flow.

II.4.II Deuterated Free-Base Phthalocyanine Preparation

Deuterated free-base phthalocyanine (D_2Pc) was prepared using a procedure similar to that described by Fitch *et al.*[15] where the two inner hydrogen atoms were exchanged with a deuterated acid. In the following procedures, one D_2Pc sample was prepared using deuterated trichloroacetic acid (TCA-d_1) and another sample with deuterated trifluoroacetic acid (TFA-d_1).

TCA-d_1 was prepared by adding 12 ml of D_2O (Apollo Scientific, 99.9% D-atom purity) to 48.6 g trichloroacetic acid (Sigma Aldrich). The solution was heated to

approximately 70 °C and the water was removed by vacuum distillation. The process was repeated 5 times to maximise deuteration. Deuterated phthalocyanine was then prepared by adding 0.5 g of normal free-base phthalocyanine to the deuterated TCA prepared above. This mixture was equilibrated under Ar at 80 °C with continuous stirring for 3 h. The D_2Pc was precipitated by addition of 30 ml of D_2O. The precipitate was filtered, washed 5 times with hot D_2O and dried in an oven at 110 °C. A second sample of D_2Pc was prepared using 99.5% D trifluoroacetic acid-d_1 purchased from Sigma Aldrich. Under Ar, 0.5 g of normal free-base phthalocyanine was added to 25 g of TFA-d_1 and was refluxed for 3 h. As with the preparation using TCA-d_1, the D_2Pc was precipitated with 30 ml D_2O, filtered, washed with hot D_2O and dried in an oven at 110 °C. In both syntheses, mixtures of H_2Pc, HDPc and D_2Pc resulted. Proton NMR analysis of the starting and deuterated phthalocyanine samples was attempted to determine the ratio of deuterated and non-deuterated products but was unsuccessful. Though easily dissolved in acidic solvents, phthalocyanine was found to be insoluble or very sparingly soluble in aprotic solvents.

II.5 Luminescence Measurements

In the analysis of the matrix isolated XPc samples, two classes of visible luminescence spectroscopy were employed: steady-state spectroscopy using continuous lamp excitation and time-resolved spectroscopy using pulsed laser excitation. The following section will describe the optical set-up, detectors and excitation sources used for both classes of visible spectroscopy.

II.5.I Steady-State Spectroscopy

The spectrometer set-up used for the recording of steady-state luminescence spectra is shown in Figure II.5. Continuous lamp excitation was performed using a tungsten (W) lamp (30 W, GE DZA) with a wide spectral range from the visible to the near infrared (NIR) or a deuterium (D_2) lamp (Hamamatsu L6310[16] with a Cathodeon C713 power supply[17]) with a spectral range of 180-500 nm. These light sources were passed through an Acton Research Corporation (ARC) SpectraPro-300i monochromator[18] with a focal length of 300 mm and were used for recording absorption and excitation spectra. This excitation monochromator was installed with two diffraction gratings- a high resolution 1200 grooves/mm grating blazed at 300 nm and a lower resolution 300 grooves/mm grating also blazed at 300 nm. The ARC SpectraPro-300i monochromator when fitted with the 1200 grooves/mm

grating resulted in a resolution of 0.1 nm at 435.8 nm. Light exiting the monochromator was focused onto the CaF_2 sample window through the external windows made of the same material using a 1" focusing lens.

For the recording of absorption spectra, the monochromatic light transmitted through the sample was focused onto a Photo-Multiplier Tube (PMT) using a 1" collecting lens. Two absorption PMTs were used in this work, either a 'blue' sensitive Hamamatsu IP28 (185-650 nm) or a 'red' sensitive Hamamatsu R928 (185-900 nm)[19]. The absorption spectra, A, may be determined by the Beer-Lambert law, using the equation,

$$A = -\log_{10}(I/I_0) \quad \text{(II.2)}$$

where I_0 is the intensity of the light entering the sample from the monochromator and I is the intensity of the light transmitted through the sample. As the spectrometer described above is a single beam experiment, an absorption spectrum of XPc/Gas sample was calculated using I equal to a transmitted XPc/Gas spectrum and I_0 equal to a separately recorded transmitted spectrum of a solid pure gas sample of the same thickness.

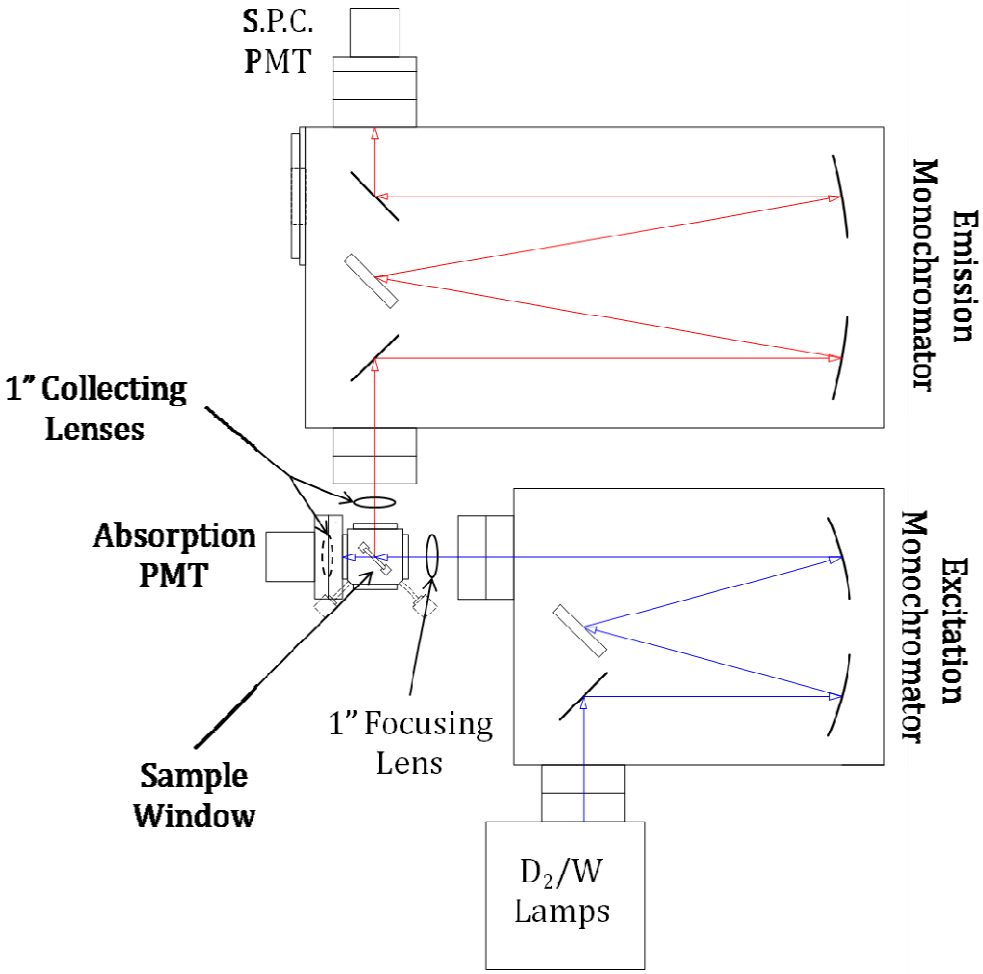

Figure II.5: Luminescence spectrometer set up used for steady-state spectroscopy.

Emission was monitored perpendicular to the excitation axis by focusing light emitted at 90° to the excitation source using a 1" collecting lens into an ARC SpectraPro-500i monochromator with a focal length of 500 mm[20]. This monochromator was installed with 3 diffraction gratings- a 1200 grooves/mm grating blazed at 300nm, a 600 grooves/mm grating blazed at 600nm and a 150 grooves/mm grating blazed at 300nm. The ARC SpectraPro-500i 'emission' monochromator, when fitted with the 1200 grooves/mm grating, had a resolution of 0.05 nm at 435.8 nm. This represents a factor of 2 improvement in resolution compared with shorter focal length excitation spectrometer. Steady-state emission was recorded using a Hamamatsu R928-P PMT[21,22] cooled to -20 °C in a Products for Research Photocool S600 cooled-housing[23]. This sensitive PMT has a spectral range of 185-900 nm with a peak max at 400 nm. The ARC NCL control unit and SpectraSense software package were used to control both spectrometers and the data acquisition from the PMTs.

II.5.II Time-Resolved Spectroscopy

Time-resolved emission and excitation spectra were recorded using the experimental set-up shown in Figure II.6. A Quantel YG 980E-10 Nd:YAG laser operating at 10 Hz was used as a pulsed excitation source[24]. This laser consists of a Neodymium (Nd) doped Yttrium Aluminium Garnet (YAG) crystal as a gain medium excited by flash-lamps within a resonator cavity. The nanosecond pulsed output of the laser was controlled using a Q-switch with the optimum laser output achieved with a flash-lamp/Q-switch delay of 242 s. The fundamental output of the Nd:YAG is 1064 nm with 2nd, 3rd and 4th harmonic wavelengths of 532, 355 and 266 nm generated using suitable optics.

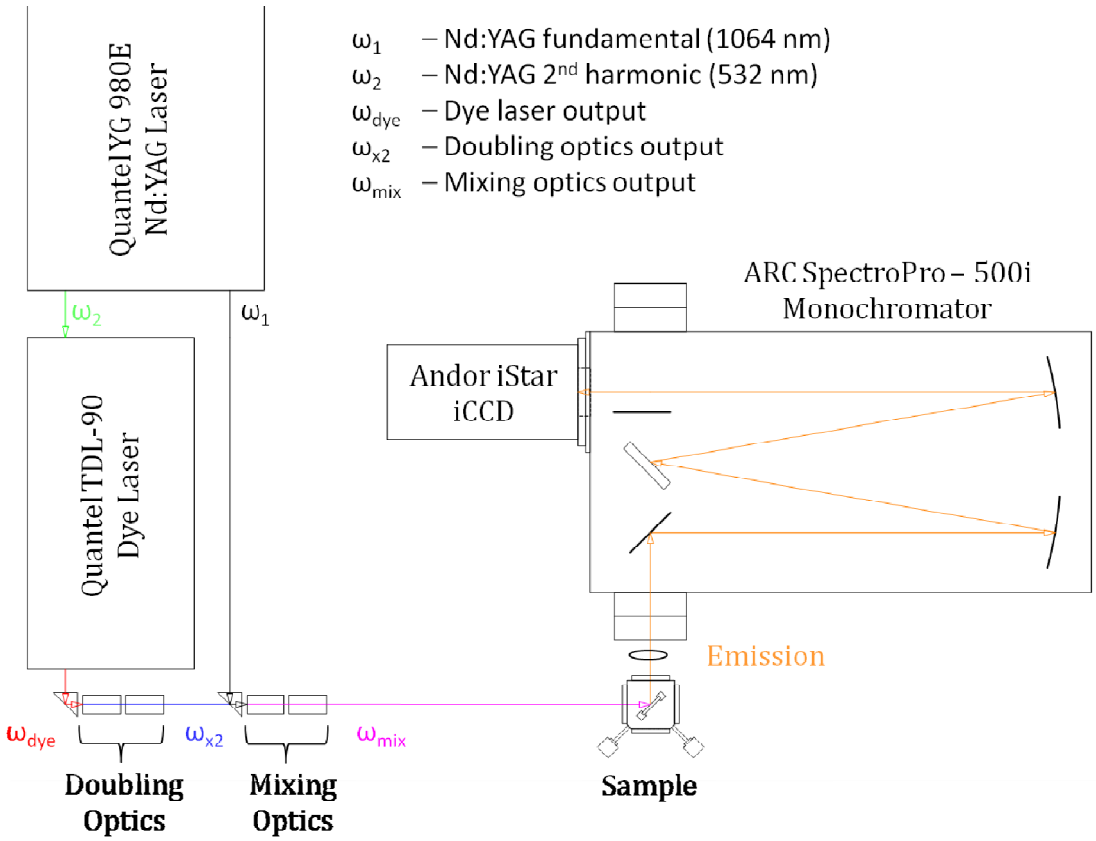

Figure II.6: Schematic showing the experimental set-up used for recording time-resolved spectra using the Andor iStar iCCD with laser excitation.

In order to produce tuneable visible laser excitation, a Quantel TDL-90 dye laser[25] pumped by the 2nd harmonic of the Nd:YAG was used. In the TDL-90 dye laser excitation of the dye was carried out through three stages, oscillator, pre-amplifier and amplifier stages, with increasing laser intensity with each stage. Output from each of these stages may be selected depending on the laser power required. As the laser dyes used have broad emission bands, the dye laser may be tuned using a diffraction grating to select a particular wavelength within the dye

laser emission range. Rhodamine 610, DCM and LDS 698 laser dyes[26] were used for the visible excitation of the phthalocyanines (see Table II.2). Direct laser output from the TDL-90 was used for visible excitation but frequency doubling and mixing optics (with a Pellin-Broca prism for wavelength separation) could be used to achieve UV excitation.

Table II.2: Characteristics of the laser dye materials used for XPc excitation. All dyes were dissolved in ethanol and excited by the 532 nm 2nd harmonic output of the Nd:YAG laser.

Dye Material	Manufacturer	Absorption Max. (nm)	Fluorescence Max (nm)	Dye Laser Range (nm)
Rhodamine 610	Exciton	554	592	579-606
DCM	Exciton	472	639	615-660
LDS 698	Exciton	476	690	665-730

The ARC SpectraPro-500i monochromator used for the monitoring of steady-state emission described above, was also used to monitor time-resolved emission. Emission was collected at 90° to the pulsed laser excitation beam with a 1" lens and focused into the monochromator (see Figure II.6). Instead of directing radiation towards the emission PMT, a swing mirror was removed from the optical path, allowing the dispersed light from the diffraction grating to fall onto an Andor Technologies iStar iCCD (Intensified Charged Coupled Device) camera[27]. The iStar iCCD (Model DH 720-25F-03) comprises of a two-dimensional array of 256 rows x 1024 columns (262,144 pixels or 0.25 megapixels) photo-sensors on a silicon based semiconductor chip. The effective area of each pixel was 26 m^2 with an active area of the CCD of 25 mm x 6.7 mm consisting of 960 x 256 pixels. In order to reduce thermal noise, the iCCD was maintained at -15 °C by an integral fan cooling system. The operation of the iStar iCCD was controlled via a PC equipped with a CCI-101 control card and the Andor Solis software. This software was also used to control the ARC SpectraPro-500i monochromator via a RS232 cable.

The iCCD is a multichannel detector which was placed in the focal plane of the dispersed light from the monochromator without an exit slit. Each column of pixels simultaneously detects a different wavelength of the diffracted light, allowing it to act as a multiplexing detector. The spectral resolution of the iCCD is determined by the resolution of the dispersing element (diffraction grating) and limited by the number and size of pixels available to process the radiation. The dispersal range and resolution obtained using the Andor iStar iCCD mounted to the SpectraPro-

500i monochromator with the three different diffraction gratings are shown in Table II.3. The iCCD camera was mounted on the SpectraPro-500i and positioned so that the dispersed light and focal plane of the camera were aligned.

Table II.3: Maximum resolution achievable employing the Andor iStar iCCD camera for each of the diffraction grating mounted in the ARC SpectraPro-500i monochromator.

Diffraction Grating - ARC SpectraPro-500i	Dispersal Range (nm)	Resolution (nm)
1200 g/mm; Blz: 300 nm	40	0.04
600 g/mm; Blz: 600 nm	80	0.08
150 g/mm; Blz: 300 nm	320	0.32

The wavelengths detected by a CCD are dispersed nonlinearly across the pixels of the detector array, making spectral calibration more difficult[28]. A calibration curve must be used to present the array detector data collected on a wavelength scale. The Solis software was used to calibrate data collected by the iStar iCCD using pre-installed calibration curves for the model of monochromator and diffraction grating. Alignment of the iCCD camera was performed in the UV spectral region using the Hg $^1S_0$—$^3P_1$ emission line at 253.6521 nm, generated using a low pressure mercury arc pen lamp[29] and in the visible region using the Na $^2S_{1/2}$—$^2P_{3/2}$ and $^2S_{1/2}$—$^2P_{1/2}$ emission lines at 588.995 and 589.5924 nm[30] respectively, generated using a sodium hollow cathode lamp[31]. Initially the monochromator was centred on one of the spectral lines (e.g. 253.6521 nm using the Hg pen lamp) and the pixels off-set so that the central wavelength displayed coincided with the spectral line. The camera was rotated so that each of the pixels along a column of the CCD detected the same wavelength and the lines observed were as narrow as the resolution of the grating and monochromator allowed. The centre of the monochromator was then changed so that the emission lines were still seen in the display window but were now detected at higher or lower pixel numbers. The distance of the iCCD camera from the monochromator was then adjusted until the pixels detecting the emission lines coincided with the values displayed using the calibration curve. CCD data may also be calibrated using customised quadratic curves.

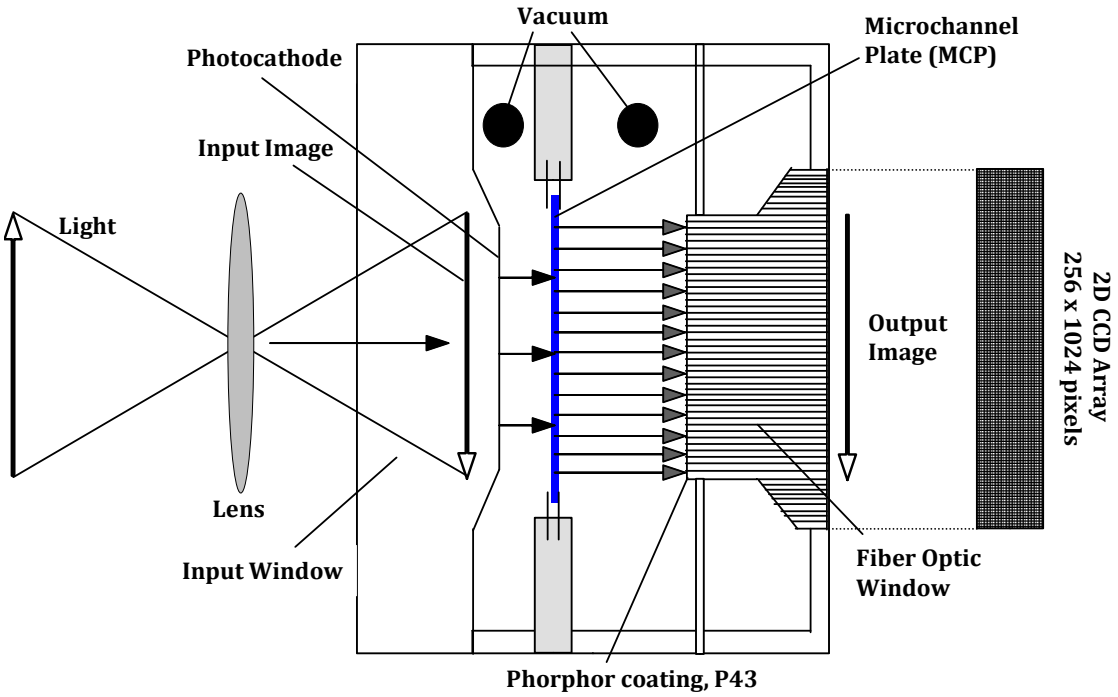

Figure II.7: Schematic of the Andor iStar iCCD image intensifier.

A schematic of the image intensifier used to amplify the signal detected by the CCD is shown in Figure II.7. A photon entering the iCCD via a quartz window hits a photocathode, producing an electron. This electron is drawn towards a micro-channel plate (MCP) by an electrical field. The initial electron emitted by the photocathode starts a cascade of electrons down the honeycomb channels of the MCP, producing secondary electrons. This results in a $\sim 10^4$ amplification of the initial electron produced by the incident photon. The shower of electrons from the MCP is accelerated by a potential difference and focused towards a phosphor coating (P42) on the fibre-optic exit window of the intensifier. This phosphor coating emits photons which strike the photo-sensors on the CCD producing a change in charge which is proportional to the intensity. The final spectrum is generated by a process of "vertical binning" where the charge from each column of pixels is added vertically together by a series of horizontal transparent electrodes and is removed by efficient charge transport (or charge coupling) process across the rows of the CCD[32]. The signal from these electrodes is transferred to an on-chip amplifier and then to an analogue/digital (A/D) converter on the CCI-010 control card.

Time-resolved and time-gated emission spectra were obtained using the iCCD by synchronisation with the laser pulse and control of the temporal gate width of the camera. Synchronisation of the iCCD with the laser was accomplished by

triggering the camera using the TTL output from the Q-switch pre-pulse of the YG 980 Nd:YAG laser. Time-gating was achieved using an integrated digital delay generator (DDG) on the iStar iCCD. The timing when the photocathode is to be switched on or off was controlled by the DDG and set using the Solis software. By varying the delay between the TTL pulse and activation of the photocathode and/or varying the time duration (gate width) when the photocathode is switched on, time-gated emission spectra may be recorded using the iCCD. Time-resolved emission spectra were obtained by recording a series of time-gated spectra, setting a suitably short gate width and stepping in time by the same gate width. Emission lifetimes were determined by analysis of the time-resolved emission. The temporal profile of an emission feature was found by taking a 'kinetic slice' through a time-resolved spectrum, extracting a plot of the emission intensities at a particular wavelength against time. The decay times were then obtained by fitting single or multiple exponential functions, modelling the rise and decay function of the temporal profile. The fits were convoluted with the temporal profile of the excitation source (i.e. the pulsed laser) to extract the excited state decay times.

II.6 Fourier Transform Infrared (FT-IR) Measurement

Fourier transform infrared (FTIR) absorption spectra were recorded using a Bruker Optics IFS 66/S FTIR spectrometer[33]. A schematic of the spectrometer is shown in Figure II.8. The light source for mid-IR (MIR) absorption spectroscopy consisted of a silicon carbide Globar® with an optional tungsten lamp for near-IR (NIR) spectroscopy. The amount of light entering the spectrometer was regulated with a rotating diaphragm aperture wheel with opening sizes from 0.25 to 12 mm. The IR beam was focused into a Michelson interferometer onto a beamsplitter. A Ge/KBr beamsplitter with a range of 7,800 – 370 cm^{-1} was primarily used for MIR experiments but could be exchanged for beamsplitters made of other materials[34] e.g. a Si/CaF_2 with a spectral range of 15,000 – 1,200 cm^{-1}. After impinging on the beamsplitter, the half of the light is transmitted to the moving mirror while half is reflected to the stationary mirror. After reflecting off the mirrors and impinging again on the beamsplitter, the light leaves the interferometer and is directed towards the sample compartment and detectors.

The quality of the spectra recorded by a FTIR spectrometer depends on the type of bearing on which the moving mirror moves. In the IFS 66/S, the moving mirror

moves on a cylindrical air bearing. The use of an air bearing over mechanical bearings results in little or no friction between the mirror and mirror path and minimal velocity errors during scans. Higher optical throughput may also be achieved due to the larger mirrors that can be mounted on an air bearing as opposed to a mechanical bearing. The air bearing in the IFS 66/S required a constant flow of dry air which was supplied by a Peak Scientific Instruments PG28L air drier. This air supply was also used to purge the optical path and sample compartment with dry air to reduce the carbon dioxide and water peaks seen in the IR spectra recorded and to protect the water sensitive KBr optics.

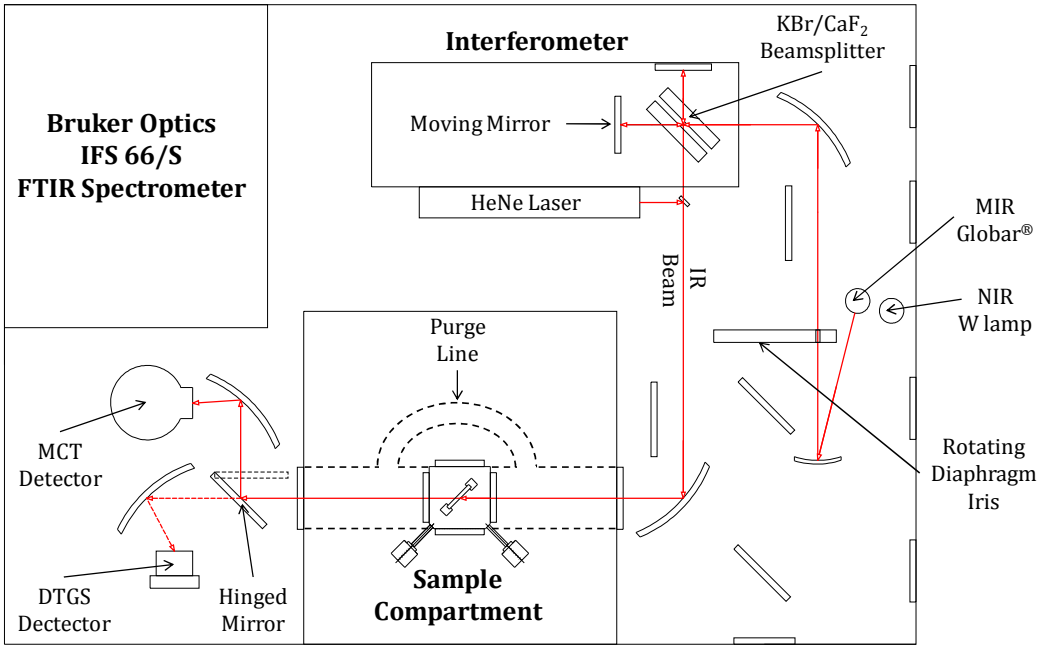

Figure II.8: Schematic of Bruker Optics IFS 66/S FTIR Spectrometer.

Movement of the mirror and calibration of the spectrometer were controlled by a 632.8 nm Helium-Neon (HeNe) laser beam which was reflected by a small beamsplitter into the interferometer, below the axis of the IR beam. Some of the HeNe laser was split into three separate beams and was transmitted parallel to the IR beam towards the detectors to act as a positioning guide for the sample. The matrix-isolation apparatus was placed in the sample compartment and the sample window positioned at the focal point of the three laser beams so that the IR beam would pass through the cryogenic sample. The bulky MI apparatus made closing the sample compartment cover impossible and broke the dry air purge of the spectrometer. A purge line made of large rubber tubing was constructed, connecting the spectrometer to the MI apparatus, ensuring a dry air purge along

the IR beam path and protecting the external KBr optical windows of the MI apparatus.

Two MIR detectors were installed within the spectrometer[35] - a room temperature Bruker Optics DLaTGS or DTGS (Deuterated L-alanine doped Triglycine Sulphate, L-alanine dropped in DTGS acronym) detector and a liquid nitrogen cooled Kolmar Technologies MCT [Mercury Cadmium Tellurium] detector. The properties of the detectors available in this work for operation with the IFS 66/S are tabulated in Table II.4. Both detectors were used together during experiments and were selected using a hinged mirror. The DLaTGS detector has a spectral range down to 250 cm^{-1} but was limited to 370 cm^{-1} by the Ge/KBr beamsplitter. The MCT detector though with a smaller spectral range than the DLaTGS detector, was almost 100 times more sensitive. The MCT was used for recording weak absorption bands and for highly scattering samples with low IR throughput. The MCT was also supplied with a fast-preamplifier allowing it to be used in nanosecond resolution step-scan experiments. Two NIR detectors were also available - a room temperature Indium Gallium Arsenide (InGaAs) diode detector and a more sensitive liquid nitrogen cooled Indium Antimony (InSb) detector which, like the MCT detector, was supplied with a fast-preamplifier.

Table II.4: MIR and NIR detectors installed in Bruker IFS 66/S FTIR Spectrometer.

Detector	Manufacturer	Part/Model No.	Range (cm^{-1})	Sensitivity/Noise
DLaTGS	Bruker Optics	ID 301/8	12,000-250	$D^* > 4 \times 10^8$ cm $Hz^{½}$ W^{-1}
MCT	Kolmar Technologies	ID 317x8F 100-1-B-7/190	10,000-850	$D^* > 3 \times 10^{10}$ cm $Hz^{½}$ W^{-1}
InGaAs Diode	Bruker Optics	D 424	12,800-5,800	NEP < 2×10^{-14} W $Hz^{-½}$
InSb	InfraRed Associates	D413	12,800-1,850	$D^* > 1.5 \times 10^{11}$ cm $Hz^{½}$ W^{-1}

II.6.I The Michelson Interferometer and Fourier Transforms

At the heart of a FTIR spectrometer is an interferometer. A simplified diagram of an infrared Michelson interferometer is shown Figure II.9. In the diagram, light from a broad band IR light source is collimated onto a beamsplitter. 50% of the light is transmitted to a moving mirror while 50% is reflected to a stationary

mirror. The light is reflected back off the two mirrors towards the beamsplitter where the light is either reflected or transmitted. After leaving the beamsplitter, the two light beams recombine and are focused onto a detector. In a conventional steady-state scan, the moving mirror moves continuously along one axis increasing and decreasing the path length which the light has to travel while the IR detector records the intensity of the recombined light coming from the interferometer[28,36-38].

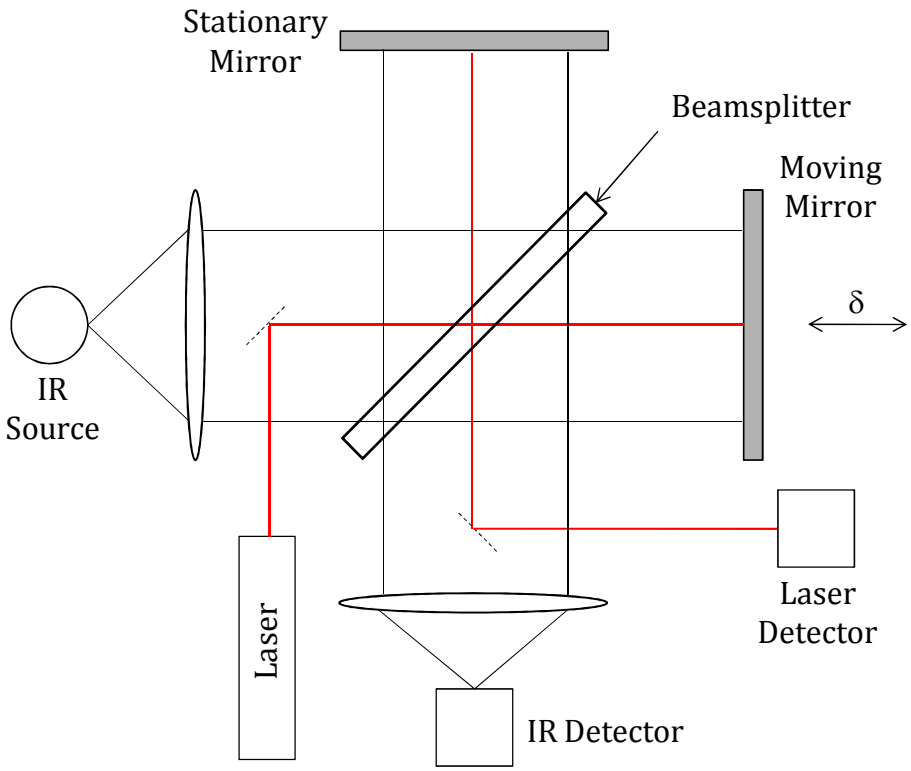

Figure II.9: Schematic of a general Michelson interferometer.

During a scan, a signal is recorded at different positions of the moving mirror relative to the stationary mirror. The difference in path length between the stationary and moving mirrors is known as the Optical Path Difference (OPD) or optical retardation, δ[37]. The plot of the intensity as a function of the moving mirror position is know as an interferogram, I(δ). When the beams recombine, the wavelengths of the light can either interfere constructively or destructively. For a broadband light source, when the difference in pathlengths between the mirrors is zero (sometimes called the Zero Path Difference, ZPD) all wavelengths will interfere constructively and a large intensity will be recorded. At larger optical path differences, wavelengths will interfere both constructively and destructively resulting in a lower intensity recorded. A typical interferogram of a broadband source is presented in the left-hand panel of Figure II.10 showing the characteristic

'centre-burst' shape with large intensity interference at the centre of the interferogram and lower intensity at the wings.

In order to measure an accurate moving mirror position when a signal is recorded, a monochromatic laser beam is sent along the same optical path as the IR beam into the interferometer. Like the IR source, the laser is split by the beamsplitter with half the laser beam going to the stationary mirror and half to the moving mirror. The laser beams are reflected back to the beamsplitter, recombined and sent to a separate laser detector. As the laser is monochromatic, in an ideal interferometer, a perfect sine-squared pattern interferogram would be generated as shown in the lower plot of Figure II.10. In an actual interferometer, the fringes of the laser interferogram are used to calibrate the position of the moving mirror and to indicate when the detector should record a signal, as shown by the vertical dashed lines in Figure II.10.

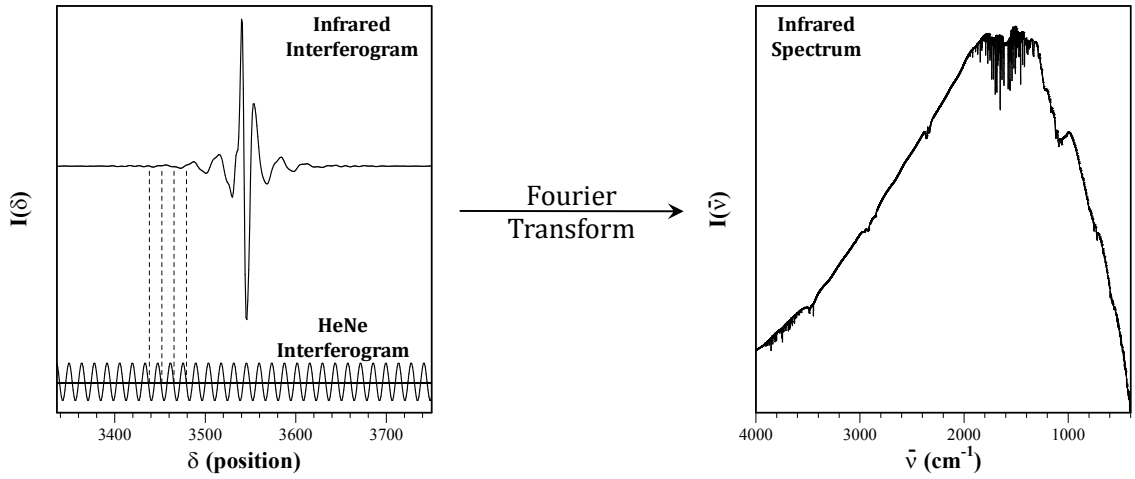

Figure II.10: Schematic of the FTIR recording process. The left-hand panel shows an IR interferogram recorded using a Michelson interferometer. The fringes of the HeNe interferogram shown in the lower plot are used to calibrate the position of the moving mirror during a scan. Using a CPU, a Fourier Transform is applied to the calibrated IR interferogram resulting in an IR spectrum shown in the right-hand panel.

All spectral information is contained within an interferogram but cannot be seen directly without the use of a Fourier transform. A mathematical transform to convert an interferogram, $I(\delta)$, into a wavenumber spectrum, $I(\bar{\nu})$, may be expressed by the integral

$$I(\bar{\nu}) = \int_{-\infty}^{+\infty} I(\delta) cos\,(2\pi\bar{\nu}\delta) d\delta \qquad \text{(II.3)}$$

where $\bar{\nu}$ is the frequency in wavenumbers and δ is the optical retardation of the moving mirror[28,36,37]. The transform can be understood by considering how two sine waves of the same frequency interfere constructively or destructive. The intensity of the combined waves is dependent on the difference in phase between the waves which in turn is determined by the difference in path lengths the two waves travelled (i.e. $\delta = \alpha_1 - \alpha_2$ where α_1 and α_2 are the phase angles of the two waves). A derivation of this Fourier transform for a broad spectral distribution is given in ref. 28.

Actual experimental interferograms are not recorded continuously but are digitised into a finite number of points. It is therefore not practical to apply Equation II.3. To transform a digitised experimental interferogram of *N* points, a discrete Fourier transform (DFT)[36] is applied and may be given by

$$S(k\Delta\bar{\nu}) = \sum_{n=0}^{N-1} I(n\Delta\delta) exp\left(\frac{2\pi i.n.k}{N}\right) \qquad \text{(II.4)}$$

where *k* and *n* are the spectral and interferogram points and the spectral resolution $\Delta\bar{\nu} = 1/N\Delta\delta$. To solve this equation, Fast Fourier Transform (FFT) algorithms have been developed, the most commonly used being the Cooley-Tuckey FFT[39]. A problem with applying the discrete Fourier transform to a digitised interferogram is the "picket fence" effect where an interferogram contains frequencies that do not correspond to the frequency sample points $k\Delta\bar{\nu}$ of the discrete Fourier transform. The resulting spectrum will be periodically missing frequencies and the spectrum will appear to be viewed from behind a picket fence. To overcome this effect a technique called zero filling may be used where zeros are added to the end of the interferogram, increasing the number of points per wavenumber in the final spectrum. This interpolation of the spectrum does not introduce errors as the overall instrumental line shape is not changed. Extensive zero filling is essential for gas phase and matrix-isolated IR spectra where narrow absorption lines may be missing or reduced in intensity.

In order to obtain a complete spectrum from an interferogram, the optical retardation sampled must range from $-\infty$ to $+\infty$. This range is of course experimentally impossible and real interferograms are recorded within a finite range ($-\delta$ to $+\delta$) and are a truncation of the infinite interferogram. Mathematically, a finite interferogram may be considered as a convolution of the infinite

interferogram by applying a function with values of 1 from -δ to + δ and 0 outside these limits. This simple function is called a Boxcar function and the process of truncation, apodization (from the Greek *αποδ* meaning 'footless' or 'feet removed')[37,38,40]. Applying a Fourier transform to a Boxcar apodized interferogram (*i.e.* a raw experimental interferogram) results in the broadening spectral lines and the production of oscillating side-lobes to spectral lines also called 'leakage' or 'ringing' (see first panel in Figure II.11).

A solution to the problem of leakage is to use an apodization function that gradually brings the ends of the interferogram to zero[41]. Some of these functions are shown in the inset plots of Figure II.11. The simple triangular function applies linear functions from zero to one between the ends of the interferogram and the centre. The trapezoidal or four-point function is a boxcar function between two breakpoints equidistant from the centre with linear functions to the ends of the interferogram. The Happ-Genzel or Hamming function consists of a cosine wave function on a boxcar function where the parameters have been optimised to suppress the side-lobe fringes. The three- and four-term Blackmann-Harris functions are similar to the Happ-Genzel function with multiple parameters that reduce the interferogram smoothly to zero at the ends of the interferogram. As shown in Figure II.11, all apodization functions produce spectra with lower side-lobe intensity relative to the simple Boxcar function. In particular the n-Term Blackmann-Harris functions are very effective at reducing ringing, but the resulting spectral lines are broadened and reduce the resolution of the spectra[40,41].

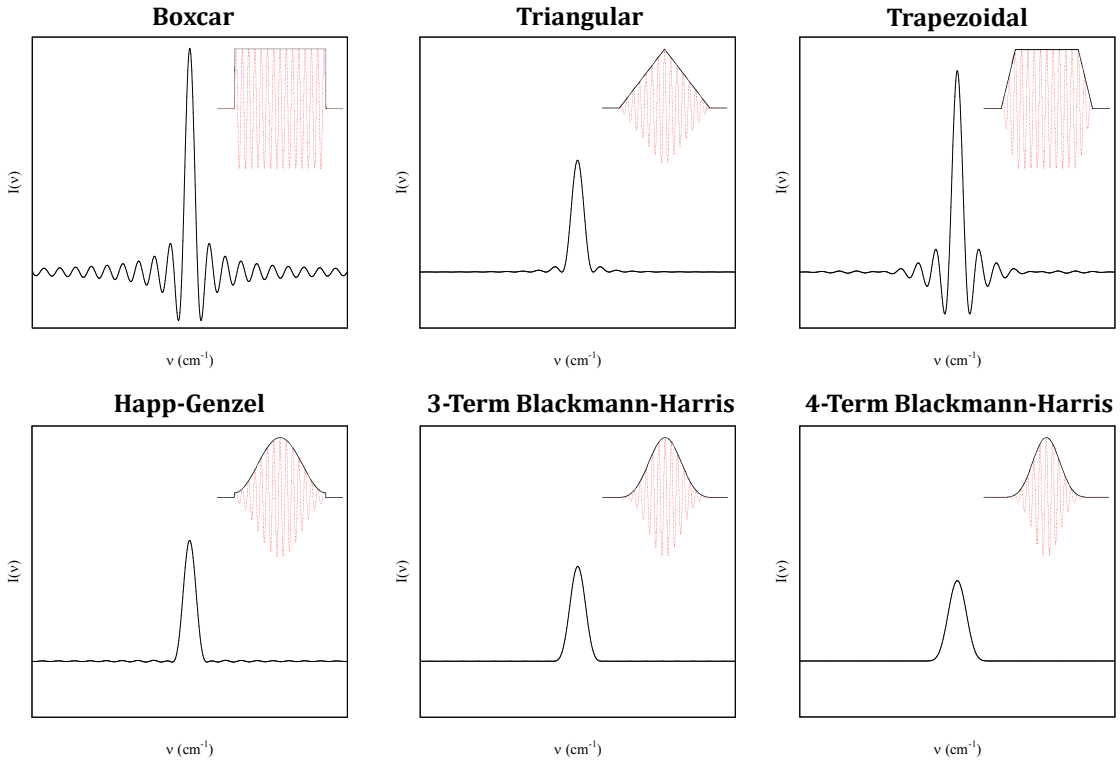

Figure II.11: The effect of various apodization functions on the DFT transformed interferogram of a monochromatic light source. Shown inset are the shapes of the apodization functions and their effect on a finite interferogram of a monochromatic light source (red-dotted trace).

Generally interferograms recorded are not perfectly symmetric and require phase correction. The asymmetry of an interferogram about the zero path difference originates from phase delays due to the optics, detector or electronics, sampling positions not coinciding with the ZPD and longer sampling of one side of the interferogram than the other. Phase correction attempts to remove sine components, introduced by asymmetry into the interferogram, in order to compute the correct spectral intensities. The most commonly used phase correction method is the Mertz algorithm[42]. This method first calculates a low resolution phase spectrum by performing a Fourier transform on a small amount of data centred on the ZPD. This low resolution phase spectrum is sufficient as the phase varies slowly as a function of the frequency. After the Fourier transform has been applied to the full interferogram, the low resolution phase spectrum calculated previously is used to correct the entire spectrum by interpolation.

Another potential source of unwanted artifacts that may be produced when applying a discrete FT to a finite interferogram is due to aliasing[40]. When a discrete Fourier transform like equation II.4 is applied to an interferogram of N points sampled at optical path differences Δx, a spectrum of N points is produced with a wavenumber resolution of $\Delta\nu$. The resulting spectrum not only produces the actual

spectrum looked for in first N/2 points but also produces a mirror image of this spectrum over the second N/2 points. This 'folding' or 'aliasing' of the spectrum occurs about the Nyqvist wavenumber, ν_f, given by,

$$\nu_f = (N/2)\Delta\nu = 1/2\Delta x \quad \text{(II.5)}$$

with replication of the spectrum and its mirror image occurring over all integer multiples of N. If the range of the spectrum is greater than Nyqvist value (i.e. when the maximum wavenumber $\nu_{max} > \nu_f$), alias overlapping can occur with the intensities of the signals greater than ν_f appearing in the opposite, low wavenumber end of the spectrum. The sampling positions determined by a HeNe laser with a wavelength of $\lambda = 1/15{,}798.002$ cm^{-1} occur at the zero crossing points $\lambda/2$ leading to a minimum sampling spacing $\Delta x_{min} = 1/31{,}596.004$. Inserting this Δx_{min} value into equation II.5 results in $\nu_f = 15{,}798.002$ cm^{-1} which is the maximum bandwidth that can be measured without overlapping occurring. The bandwidths observed in mid-IR absorption are much smaller than this value and it is often useful to use an m-fold integer multiple of Δx, reducing the size of the interferogram (e.g. 2 x Δx_{min} = 15,798.002 cm — ν_f = 7899.001 cm^{-1}). In FT emission experiments, the higher frequency excitation light may enter the interferometer along with the emission radiation and if ν_f is small, will form folding artifacts in the resultant spectrum. To reduce these artifacts, filters may be placed in the emission beam path, blocking unwanted frequencies and allowing a smaller interferogram to be recorded.

II.6.II Advantages and Disadvantages of FT Spectrometry

As an interferogram records all frequencies simultaneously, measurements can be made faster than monochromator scans. The ability to record interferograms more quickly mean that multiple interferometer scans may be recorded in the same time it takes to record one monochromator scan. These interferograms may be co-added together to improve signal to noise levels. This is called the Fellgett Advantage or multiplexing advantage[43,44]. One disadvantage of multiplexing is that if noise appears in one part of the source spectrum it will spread throughout the whole spectrum when the Fourier transform is applied. In a monochromator recorded spectrum the noise will only appear in the part of the spectrum where the noise occurred.

In monochromators, optical throughput is limited by the narrow slits required for high resolution scans. In an interferometer, the resolution is not dependent on the slit size and a larger amount of light is allowed to pass through the spectrometer's aperture. This improvement in optical throughput is known as the Jacquinot Advantage[43,45]. The resolution of an interferometer is dependent on the maximum optical path difference between the moving and stationary mirrors. So, the longer the path difference is the higher the resolution of the resultant spectrum will be. There is, however, a limitation on the aperture size for higher resolution spectra. The light beams within the interferometer need to be collimated along the entire path length the light travels. It can be difficult to maintain a wide beam parallel along longer path lengths so narrower beams may be needed for higher resolution spectra.

The use of a laser to control and calibrate the mirror position means that the spectrometer should never need to be user calibrated. This internal calibration is called the Connes Advantage[28,38]. The use of a 15,798.002 cm^{-1} HeNe laser provides up to 0.01 cm^{-1} calibration accuracy[46]. It should also be noted that FTIR spectrometers are mechanically very simple with the mirror being the only continuously moving part. Inconsistent moving mirror speeds that may develop over time will not adversely effect the interferograms as positioning is calibrated by the HeNe laser. Unlike dispersive spectrometers using CCD cameras consisting of a 2-d array of photo-sensitive detectors, FTIR spectrometers generally include only a single detecting element. These single element detectors are much easier to saturate than the detector arrays in CCDs leading to errors across the resulting spectrum after a Fourier transform has been applied. Careful control of the IR radiation intensity reaching the detector (by varying the aperture size used) must therefore be taken to prevent saturation.

II.7 References

(1) Dunkin, I. R. *Matrix-Isolation: A Practical Approach*; Oxford University Press: Oxford, 1998.
(2) Cradock, S.; Hinchcliffe, A. J. *Matrix Isolation*; Cambridge University Press: Cambridge, 1975.
(3) Granville-Phillips, *275 Wide-Range Convectron Vacuum Gauges*, 1990.
(4) APD Cryogenics Inc., *Helium Compressor HC-2D Technical Manual*, Jan 1992, (256685A)
(5) APD Cryogenics Inc., *DE-202 Expander Technical Manual*, May 1989 (257519A)
(6) Scientific Instruments Inc., *Instruction Manual, Series 9600 microprocessor – based digital temperature indicators/controllers manual #A090-145*, March 6th, 1990.
(7) Balzers, *Operating Instructions, Turbo-molecular pump, TPU 180H*, Ed. 3
(8) Balzers, *Operating Instructions, Diaphragm Vacuum Pumps, MD-4T*, Ed. 1.
(9) Tylan General, *Technical Sheets, Capacitance Diaphragm Gauges CDL Series*.
(10) MKS Instruments, Inc., *MKS Baratron® Type 622B/623B/626B Absolute Pressure Transducers Manual*
(11) Granville-Phillips, *203 Variable Leak Valve, Technical Manual*, 1993.
(12) *CRC Handbook of Chemistry and Physics*; 76 ed.; Lide, D. R., Ed.; CRC Press: Boca Raton, FL, 1995.
(13) The refractive indices of Ar, Kr and Xe are 1.29, 1.28 and 1.49 recorded at 60 K and 488 nm from H. J. Jodl, *Solid-state Aspects of Matrices in The Chemistry and Physics of Matrix-Isolated Species*, North-Holland, 1989.
(14) The refractive index for solid Ar at 233 nm is 1.32 at 6 K and for solid Kr at 2241 nm 1.428 at 12 K. (P. Gurtler, unpublished results)
(15) Fitch, P. S. H.; Haynam, C. A.; Levy, D. H. *Journal of Chemical Physics* **1980**, *73*, 1064.
(16) Hamamatsu, *L2D2 Series Deuterium Lamps, Specifications*, Aug. 1998, p. 4.
(17) Cathodeon, *Deuterium Lamp Power Supply C713, Operation Notes, Specifications*.
(18) Acton Research Corporation, *Operating Instructions SpectraPro – 300i, SP – 300i Manual*, Rev. 997.1
(19) Hamamatsu Data Sheet title '*Side-On Photomultiplier Tubes*'
(20) Acton Research Corporation, *SpectraPro – 500i, 500i Manual V1097.1.*
(21) Hamamatsu Data Sheet title '*Photomultiplier Tubes R928, R955*'
(22) Hamamatsu Photonics, *Photonmultiplier Tubes: Basics and Applications*, 3rd Ed., 2007
(23) Products for Research, Inc., *Photocool Series Power Supply, Instruction Manual*, (Model PC177CE009 for R928).
(24) *Instruction Manual QUANTEL YG 980 Q-switched Nd:YAG laser*, Doc. 980, Version `#1, anglaise PM/DT (12.05.97).
(25) *Quantel – TDL 90, Instruction Manual* – Issue 1.
(26) Synonyms and chemical formulae of the laser dyes used- Rhodamine 610 (or Rhodamine B): N-[9-(2-carboxyphenyl)-6-(diethylamino)-3H-xanthen-3-ylidine]-N-ethyl-ethanaminium chloride, ($C_{28}H_{31}N_2O_3.Cl$), DCM: [2-[4-[4-(dimethylamino)phenyl]-1,3-butadienyl]-1-ethylpyridinium monoperchlorate ($C_{19}H_{17}N_3O.ClO_4$) and LDS 698: [2-[4-[4-(dimethylamino)phenyl]-1,3-butadienyl]-1-ethylpyridinium monoperchlorate ($C_{19}H_{23}.ClO_4$)
(27) Andor Technology, *A User's Guide to the Andor iStar*, Version 3B

(28) Diem, M. *Introduction to modern vibrational spectroscopy*; Wiley-Interscience: New York, 1993.
(29) ARC Mercury Pen-Ray Light Source (Model MS-416)
(30) Ralchenko,Yu., Kramida, A.E., Reader, J., Saloman, E.B., Sansonetti,J.E., Curry, J.J., Kelleher, D.E., Fuhr, J.R., Podobedova, L., Wiese, W.L., Olsen, K. (2008). *NIST Atomic Spectra Database* (version 3.1.5), [Online]. available: http://physics.nist.gov/asd3 [2010, September 1]. National Institute of Standards and Technology, Gaithersburg, MD.
(31) Cathodeon Ltd. Sodium Hollow Cathode Lamp (Type 3UNX/Na)
(32) Janesick, J. R. *Scientific charge-coupled devices*; SPIE Press: Bellingham WA, 2001.
(33) Bruker Optik GmbH, *IFS 66/S User's Manual*, 2000
(34) Bruker Optics, *Product Note M26-02/08 Beamsplitters*, 2008
(35) Bruker Optics, *Product Note M25-01/04, Detectors for Bruker FT-IR and FT-NIR Spectrometers*, 2004.
(36) Gronholz, J.; Herres, W. *Comp. Appl. Lab* **1984**, *4*, 216.
(37) Perkins, W. D. *Journal of Chemical Education* **1986**, *63*, A5.
(38) Griffiths, P. R.; de Haseth, J. A. *Fourier Transform Infrared Spectroscopy*, 2nd ed.; Wiley-Interscience: New York, 2007.
(39) Cooley, J. W.; Tukey, J. W. *Math Comput* **1965**, *19*, 297.
(40) Gronholz, J.; Herres, W. *Instruments and Computers* **1985**, *4*, 10.
(41) Harris, F. J. *P Ieee* **1978**, *66*, 51.
(42) Mertz, L. *Infrared Phys* **1967**, *7*, 17.
(43) Perkins, W. D. *Journal of Chemical Education* **1987**, *64*, A269.
(44) Fellgett, P. *J Phys-Paris* **1958**, *19*, 187.
(45) Jacquinot, P. 17e Congres du GAMS, 1954, Paris.
(46) Bertie, J. E. *Pure Applied Chemistry* **1998**, *70*, 2039.

Chapter III: Theoretical Background and Methods

III.1 Introduction

In order to interpret the spectroscopic results of the relatively complicated phthalocyanine molecules, a theoretical study using quantum mechanics (QM) was carried out. The ground state properties, including geometries, vibrational frequencies, infra-red absorption and Raman scattering intensities, were calculated using Density Functional Theory (DFT) while the electronic excitations and oscillator strengths were calculated using Time-Dependent Density Functional Theory (TDDFT). All QM calculations were implemented using the Gaussian 03 package[1] running on a Linux workstation with two AMD "Barcelona" 64-bit quad-core processors running at 2.0 GHz and with 16GB RAM.

The problems and approximations made in solving the electronic Schrödinger equation using *ab initio* methods will be introduced in Part III.2 while Part III.3 will outline ground state DFT using the Kohn-Sham method. Part III.4 describes the vibrational problem, how the harmonic vibrational energies and intensities are calculated and the problems found when anharmonicity is neglected. Part III.5 will introduce TDDFT and describe how it was used to predict electronic excitation energies and oscillator strengths. Finally, Part III.6 will introduce how point group theory and molecular symmetry is used to simplify calculations and interpret spectroscopic results and Part III.7 will outline the calculation procedure used to determine the molecular properties of a polyatomic molecule.

III.2 The Electronic Problem

III.2.I Background

III.2.I.a The Schrödinger Equation

The quantum mechanical behaviour of molecules may be described using the Schrödinger equation[2], a partial differential wave equation that describes the wavefunction of a physical system. The non-relativistic time-independent Schrödinger equation is expressed as:

$$\hat{H}\Psi_{tot}(r,R) = E\Psi_{tot}(r,R) \quad \text{(III.1)}$$

where $\hat{H}$ is the time-independent Hamiltonian and $\Psi_{tot}(r, R)$ is the time-independent wavefunction, r and R are the coordinates of the electrons and nuclei and E is the energy of the system.

III.2.I.b The Molecular Hamiltonian

The Hamiltonian $\hat{H}$ of a system of N nuclei and n electrons is comprised of the following terms:

$$\hat{H} = \hat{T}_N + \hat{T}_e + \hat{V}_{Ne} + \hat{V}_{NN} + \hat{V}_{ee} \quad \text{(III.2)}$$

$\hat{T}_N$ is the operator associated with the kinetic energy of the N nuclei and $\hat{T}_e$ the kinetic energy operator of the electrons. $\hat{V}_{ee}$, $\hat{V}_{NN}$ and $\hat{V}_{Ne}$ are the Coulombic potentials between the electrons (ee), nuclei (NN) and between the electrons and nuclei (Ne). If $\hat{H}$ is expressed in atomic units the following expression is obtained:

$$\hat{H} = -\sum_{A=1}^{N}\frac{\nabla_A^2}{2M_A} - \sum_{i=1}^{n}\frac{\nabla_i^2}{2} - \sum_{A=1}^{N}\sum_{i=1}^{n}\frac{Z_A}{r_{Ai}} + \sum_{A=1}^{N}\sum_{B>A}^{n}\frac{Z_A Z_B}{r_{AB}} + \sum_{i=1}^{n}\sum_{j>i}^{n}\frac{1}{r_{ij}} \quad \text{(III.3)}$$

where the indices A and B are associated with the nuclei and the indices i and j are associated with the electrons. Z_A and M_A are the charge and mass of a nucleus in atomic units. In the atomic units system, the mass of an electron and $\hbar$ are equal to unity and $\frac{e^2}{4\pi\varepsilon_0} = 1$. ∇_A^2 and ∇_i^2 are Laplacian operators, where ∇^2 ("del-squared") of a particle p is:

$$\nabla_p^2 = \nabla_p \cdot \nabla_p = \frac{\partial^2}{\partial x_p^2} + \frac{\partial^2}{\partial y_p^2} + \frac{\partial^2}{\partial z_p^2} \quad \text{(III.4)}$$

III.2.I.c The Born-Oppenheimer Approximation

The Schrödinger equation for a polyatomic molecule (consisting of N nuclei and n electrons) cannot be solved exactly. A simplification is possible if one considers that the mass of the nuclei are much greater than the electrons and thus the movement of the nuclei is much slower compared to the electrons. This is called the Born-Oppenheimer approximation[3]. The movement of the electrons is therefore considered to adapt instantaneously to the movement of the nuclei. The wave-function describing the particles $\Psi_{tot}(r, R)$ can be then expressed in the form of a product of wavefunctions characterising the nuclei and the electrons separately:

$$\Psi_{tot}(r,R) = \Psi_{el}(r,R)\Psi_N(R) \quad \text{(III.5)}$$

The coordinates of the nuclei (R) become parameters in the Schrödinger equation and are no longer variables. The nuclei are now considered fixed and the solutions of $\Psi_{el}(r,R)$ depend on the positions of the nuclei but not on their speed.

$$\hat{H}_{tot}\Psi_{tot}(r,R) = E_{tot}\Psi_{tot}(r,R) \quad \text{(III.6)}$$

The electronic energy is found by solving the following equation:

$$\hat{H}_{el}\Psi_{\mathrm{el}}(\mathrm{r},\mathrm{R}) = \mathrm{E}_{\mathrm{el}}(\mathrm{R})\Psi_{\mathrm{el}}(\mathrm{r},\mathrm{R}) \quad \text{(III.7)}$$

where the electronic Hamiltonian $\hat{H}_{el}$ is the electronic Hamiltonian associated with a fixed nuclear geometry and is given as:

$$\hat{H}_{el} = -\sum_{i=1}^{n}\frac{\nabla_i^2}{2} - \sum_{A=1}^{N}\sum_{i=1}^{n}\frac{Z_A}{r_{Ai}} + \sum_{i=1}^{n}\sum_{j>i}^{n}\frac{1}{r_{ij}} \quad \text{(III.8)}$$

The total energy of the system with fixed nuclei is given as:

$$E_{el}^{tot}(E) = E_{el}(R) + \sum_{A=1}^{N}\sum_{B>A}^{n}\frac{Z_A Z_B}{r_{AB}} \quad \text{(III.9)}$$

To find $\Psi_{tot}(r,R)$ it is necessary to solve the following equation:

$$(\hat{T}_N + E_{el}^{tot}(R))\Psi_{el}(r,R)\Psi_N(R) = E_{tot}\Psi_{el}(r,R)\Psi_N(R)$$

with the nuclear kinetic energy $\hat{T}_N$:

$$\hat{T}_N = -\sum_{A=1}^{N}\frac{\nabla_A^2}{2M_A} \quad \text{(III.10)}$$

The Born-Oppenheimer approximation may be inappropriate in cases near degenerate electronic levels where conical intersections occur (for example the Jahn-Teller and Renner-Teller effects), when there are rapid collisions or in cases of strong vibrational excitations. In the absence of these situations, the approximation is completely satisfactory.

III.2.I.d The Independent Particle Approximation and the Slater Determinant

The electronic problem of polyatomic molecules is a problem of n>2 bodies which one cannot solve analytically. One way to circumvent this problem is to express the electronic wave function $\Psi_{el}(r,R)$ as a product of mono-electronic functions Ψ_n:

$$\Psi_{el}(r,R) = \psi_1.\psi_2.\psi_3 \ldots \psi_n = \Psi(1,2,\ldots) \quad \text{(III.11)}$$

The principle of indiscerniblity postulates that particles of the same type are indistinguishable from each other. In other words, the probability density $|\Psi(1,2,\ldots)|^2$ does not depend on the permutation of 2 particles:

$$|\Psi(1,2,\ldots)|^2 = |\Psi(2,1,\ldots)|^2 \quad \text{(III.12)}$$

As a consequence, the function used to describe the exchange between the two particles can be either symmetric (e.g. $\Psi(1,2,\ldots) = \Psi(2,1,\ldots)$) or anti-symmetric (e.g. $\Psi(1,2,\ldots) = -\Psi(2,1,\ldots)$).

There only exist 2 linear combinations which satisfy the principle of indiscerniblity:

$$\Psi_S = \Psi(1,2,3,\ldots) + \Psi(2,1,3,\ldots) + \Psi(3,2,1,\ldots) \quad \text{(III.13)}$$

$$\Psi_A = \Psi(1,2,3,\ldots) - \Psi(2,1,3,\ldots) - \Psi(3,2,1,\ldots) + \Psi(2,3,1,\ldots) \quad \text{(III.14)}$$

The expression Ψ_S allows two particles to be in the same quantum state. It states that every state of a particle may be populated for an unspecified number of particles. These particles have a null or integral spin and are called Bosons, i.e. they obey Bose-Einstein statistics. In contrast, the expression Ψ_A does not permit 2 particles to have the same quantum state. It results in every state a particle may have being populated by only one particle. These particles are called Fermions, i.e. they obey Fermi-Dirac statistics, and have half-integer spin quantum numbers.

Electrons being Fermions (particles with a half spin) must satisfy the Pauli principle, which is to say that the wave function of a poly-electronic system must be anti-symmetric by describing the permutation of the spatial coordinates and the spin of two unspecified electrons.

The Slater determinant of order N is defined as a determinant of order N formed by N distinct spinorbitals (χ_i is composed of a spatial function (ψ_i) and of a spin function (α ($\sigma_i = +1/2$) or $\beta(\sigma_i = -1/2)$).

$$\Psi_{el}(r,R) = \frac{1}{\sqrt{N!}} \begin{vmatrix} \chi_1(1) & \chi_2(1) & \cdots & \chi_n(1) \\ \chi_1(2) & \chi_2(2) & \cdots & \chi_n(2) \\ \vdots & \vdots & \ddots & \vdots \\ \chi_1(n) & \chi_2(n) & \cdots & \chi_n(n) \end{vmatrix} = \Psi \quad \text{(III.15)}$$

where $\chi_j(i)$ is the spin-orbital *j* which contains the electron *i*. The factor $\frac{1}{\sqrt{N!}}$ is a normalisation factor valid if the spin-orbitals are themselves normalised. With the permutation of the spatial coordinates and of the spin of two electrons correspond

to the permutation of the two corresponding lines of the determinant. The Slater determinants satisfy the anti-symmetric principle, in effect a determinant changes the sign when it permutates any two lines. This property is also valid for a linear combination of determinants.

III.2.II The Hartree-Fock Method

III.2.II.a The Hartree-Fock Approximation

It has been seen that the simplest antisymmetric wave function which may be used to describe the fundamental state of a system of *n* electrons is the Slater determinant: Ψ_0. The variational principle establishes that for a set of spin orbits, the Slater determinant that gives the lowest average energy E_{el} is closest to the energy of the exact solution of electronic Schrödinger equation:

$$E_{el} = \langle \Psi_0 | \hat{H}_{el} | \Psi_0 \rangle = \sum_{i=1}^{n} \langle \chi_i(i) | \hat{h} | \chi_i(i) \rangle + \frac{1}{2} \sum_{i=1}^{n} \sum_{j=1}^{n} \langle \chi_i(i) | \hat{J}_j(i) - \hat{K}_j(i) | \chi_i(i) \rangle \quad \text{(III.16)}$$

where $\hat{J}$ is the Coulombic operator and $\hat{K}$ the exchange operator:

$$\hat{J}_j(i)\chi_i(i) = \langle \chi_j(j) | \hat{h}_{ij} | \chi_j(j) \rangle \chi_i(i) \quad \text{(III.17)}$$

$$\hat{K}_j(i)\chi_i(i) = \langle \chi_j(j) | \hat{h}_{ij} | \chi_j(i) \rangle \chi_j(i) \quad \text{(III.18)}$$

The Coulombic operator has an analogy in classical mechanics: one may interpret it as the Coulombic repulsion undergone by one electron moving in the field of a second electron. The exchange operator is a purely quantum term, without an analogy in classical mechanics. It describes the spin correlation, resulting from taking into account the antisymmetry.

While minimising E_{el}, the Hartree-Fock equation can be derived:

$$\hat{F} | \chi_i(i) \rangle = \varepsilon_i | \chi_i(i) \rangle \quad \text{(III.19)}$$

where the Fock operator ($\hat{F}$) is the monoelectronic operator according to:

$$\hat{F} = \hat{h} + \hat{v}^{HF} = \hat{h} + \sum_{j}^{n} [\hat{J}_j(i) - \hat{K}_j(i)] \quad \text{(III.20)}$$

Equation (III.20) must be solved iteratively, with the operators $\hat{J}_j(i)$and $\hat{K}_j(i)$ depending on the orbital $\chi_i(i)$ that one seeks to obtain. At every stage a new $\chi_i(i)$ is obtained, which allows a new Fock operator to be obtained for the following stage, and thus continues until convergence. This is the Self Consistent Field (SCF)

principle. The eigenfunctions obtained, the orbitals $\chi_i(i)$, are said to be canonical orbitals. Each one of these orbitals is a molecular orbital with an eigenvalue associated with the orbital energy ε_i. The electronic energy E_{el} is then expressed as:

$$E_{el} = \sum_{i=1}^{n} \varepsilon_i - \frac{1}{2}\sum_{i=1}^{n}\sum_{j=1}^{n}(J_{ij} - K_{ij}) \quad \text{(III.21)}$$

III.2.II.b Restricted (R) and Unrestricted (U) Wavefunctions

Every spinorbital χ_i is composed of a spatial function (ψ_i) and of a spin function α $(\sigma_i = +1/2)$ or $\beta(\sigma_i = -1/2)$. The Fock operators for the electrons α and β may be written as:

$$\hat{F}^{\alpha} = \hat{h} + \sum_{j=1}^{n_\alpha}(\hat{J}_j^{\alpha} - \hat{K}_j^{\alpha}) + \sum_{j=1}^{n_\beta}\hat{J}_j^{\beta} \quad \text{(III.22)}$$

$$\hat{F}^{\beta} = \hat{h} + \sum_{j=1}^{n_\beta}\left(\hat{J}_j^{\beta} - \hat{K}_j^{\beta}\right) + \sum_{j=1}^{n_\alpha}\hat{J}_j^{\alpha} \quad \text{(III.23)}$$

In practice, the Hartree-Fock equations cannot be solved except for atoms or for linear systems, where the radial and angular parts of the orbitals can be separated without approximation. In other cases the method most usually used to express the molecular orbitals in atomic basis-sets is LCAO-MO (Linear Combination of Atomic Orbitals-Molecular Orbitals):

$$\chi_i = \sum_a C_{a,i}\eta_a \quad \text{(III.24)}$$

In the case where a system is said to be closed-shell (RHF, Restrict Hartree-Fock), there are as many electrons with spin α as electrons with spin β (Figure III.1). The orbitals occupied with these electrons can be considered to have the same spatial wave functions ($\psi_i^{\alpha} = \psi_i^{\beta}$) and one can write the RHF Fock operator with complete shells as:

$$\hat{F}^{RHF} = \hat{h} + \sum_{j=1}^{n/2}(2\hat{J}_j - \hat{K}_j) \quad \text{(III.25)}$$

In using the LCAO-MO method, the Hartree-Fock equations lead to the Roothaan equations:

$$\sum_{v=1}^{n/2} F_{j,v} C_{v,i} = \varepsilon_i \sum_{v=1}^{n/2} S_{j,v} C_{v,i} \tag{III.26}$$

where $S_{j,v} = \langle \eta_j | \eta_v \rangle$ is the overlap integral between two atomic orbitals. The coefficients are themselves also optimised at the same time as the SCF procedure, like the Fock operator and the energy.

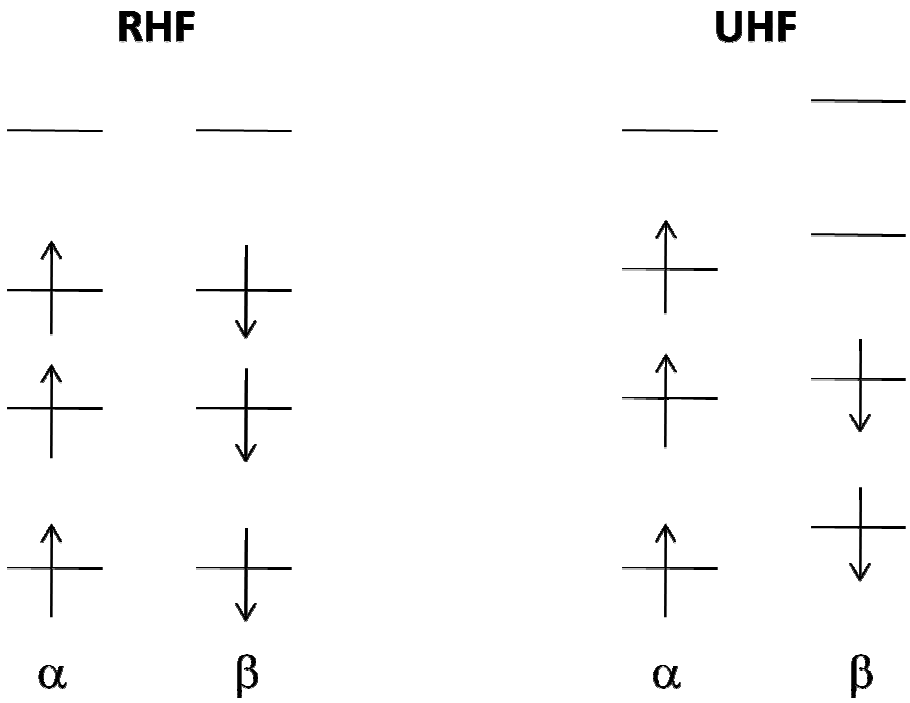

Figure III.1: Restricted (RHF) and Unrestricted (UHF) wave function occupancy.

In the case of systems with open-shells (radicals, certain excited states of molecules with closed-shells) there are more electrons of spin α than electrons of spin β (Figure III.1). In this case the spatial wave functions are different $\left(\psi_i^\alpha \neq \psi_i^\beta\right)$ and one may not use the Roothaan formalism. In its place the equations of Pople and Nesbet may be used:

$$\sum_{v=1}^{n_\alpha} F_{j,v}^\alpha C_{v,i}^\alpha = \varepsilon_i^\alpha \sum_{v=1}^{n_\alpha} S_{j,v} C_{v,i}^\alpha \tag{III.27}$$

$$\sum_{v=1}^{n_\beta} F_{j,v}^\beta C_{v,i}^\beta = \varepsilon_i^\beta \sum_{v=1}^{n_{\alpha\beta}} S_{j,v} C_{v,i}^\beta \tag{III.28}$$

These equations are solved in an iterative manner like that for Roothaan. It is important to note that these two equations must be solved at the same time because $F_{j,v}^\alpha$ and $F_{j,v}^\beta$ are dependent at the same time on $C_{v,i}^\alpha$ and $C_{v,i}^\beta$.

This method is also called UHF (Unrestricted Hartree-Fock). It allows a very good description of the dissociation of molecules, which is not possible with RHF. One major disadvantage is that it does not allow for pure spin states. For example, a doublet state may be contaminated by quartet, sextet etc. states. It is very important to compare the value of $\langle S^2 \rangle$ calculated with that obtained for the pure state in order to validate the UHF calculation.

III.2.II.c Basis Sets

In order to calculate the wavefunctions of a system, a mathematical formula (basis function) or set of formulae (basis set) is needed to best represent the initial atomic orbitals. One approach is to use Slater Type Orbitals (STO) which have the general form,

$$\eta^{STO} = Nr^{n-1}exp[-\zeta r]Y_{l,m}(\theta, \phi) \quad \text{(III.29)}$$

where N is a normalisation factor, r is the distance from the nucleus, n is the principal quantum number and $Y_{l,m}$ represents the angular parts of the function in terms of spherical harmonics. ζ (Zeta) represents the orbital exponent, which determines how compact or diffuse the function will be. STOs produce functions which make good approximations of exact functions (Figure III.2). Unfortunately, because the solutions of their integrals need to be solved numerically rather than analytically, STOs can be computationally difficult.

An alternative approach is to use Gaussian Type Orbitals (GTO) whose integrals, unlike STOs, may be solved analytically and are typically expressed in Cartesian coordinates x, y and z as,

$$\eta^{GTO} = Nx^l y^m z^n exp[-\alpha r^2]. \quad \text{(III.30)}$$

Like STOs, N is a normalisation factor with α the orbital exponent. The exponents l, m and n are used to control the angular momentum or shape of the orbitals using the relationship $L = l + m + n$, where $L = 0$ gives s-functions, $L = 1$ gives p-functions, $L = 2$ gives d-functions, etc. Single, primitive GTOs do not describe the exact function of an electron accurately but may be improved by using linear combinations of GTOs to produce a Contracted Gaussian Function (CGF)-

$$\eta_n^{CGF} = \sum_i^n x_i \, \eta_i^{GTO}. \quad \text{(III.31)}$$

The term x_i is a contraction coefficient used to adjust the contribution of a primitive GTO, η_i^{GTO}, to produce a CGF closer to the exact function (Figure III.2).

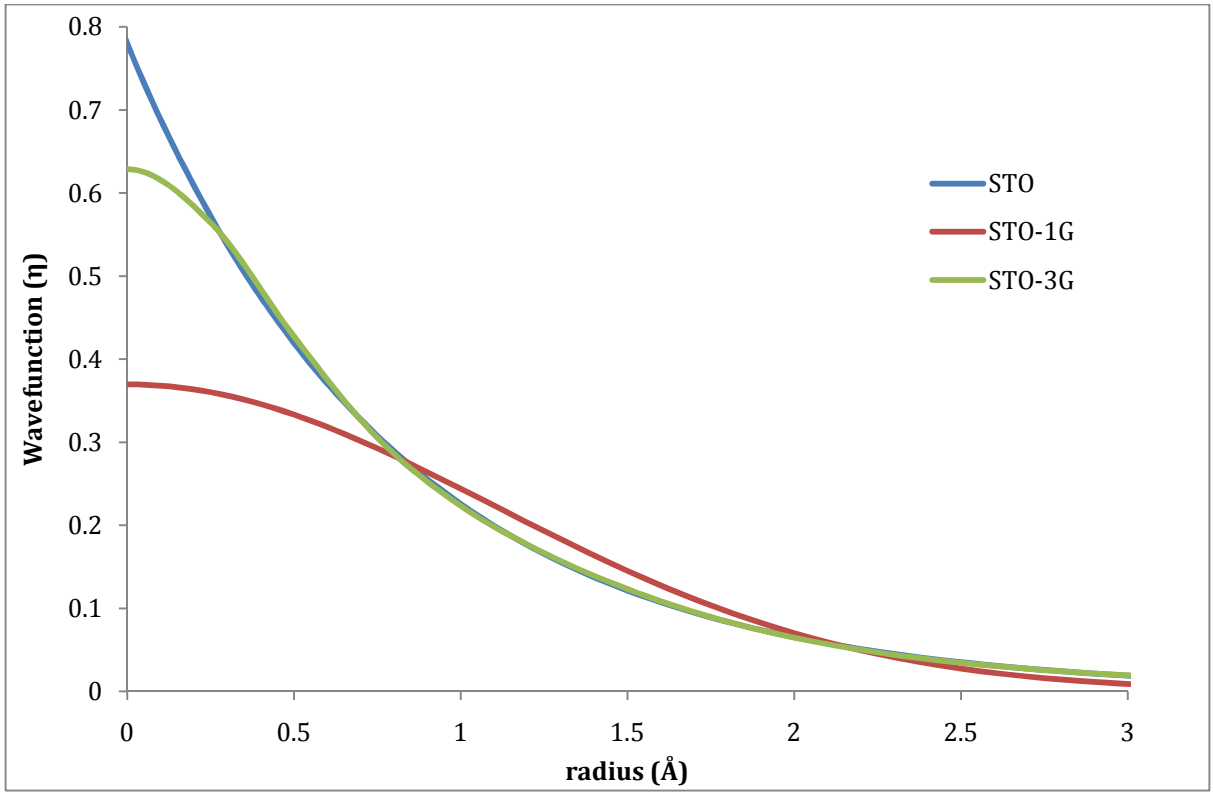

Figure III.2: One-dimensional plots of the hydrogen 1s orbital using a Slater Type Orbital (STO), a single primitive Gaussian Type Orbital (STO-1G) and a three Gaussian Contracted Gaussian Function (STO-3G).

The basis sets so far described are called minimal basis sets and do not make a distinction between core and valence electrons. Split-valence basis sets do make a distinction by performing a quick calculation on the core orbitals and a more rigorous calculation on the more important valence orbitals. The valence orbital calculations are usually performed using multiple zeta values to improve the accuracy of the calculation. The basis set can further be improved by adding diffuse functions, which allow for electron density further away from the nucleus, and polarized functions, which allow for orbitals with higher angular momentum than in the ground state.

For example, the *6-311+G(d,p)* basis set[4] is a split-valence basis set where the core orbitals are calculated using one contracted Gaussian function with six primitive GTOs (*6*-). The valence orbitals are more rigorously treated with a triple-zeta calculation (*311*) made using one set of three GTOs and two sets of single

GTOs. Diffuse functions have also been added (*+*) and there is d polarization of the p-orbitals and p polarisation of the s-orbitals (*(d,p)*).

III.3 Density Functional Theory

The Hartree-Fock method unfortunately does not adequately account for the interaction (or correlation) between the motions of electrons in a system. One method that does account for electron correlation is density functional theory (DFT). Unlike other post-Hartree-Fock electron correlation methods, which are wavefunction based, DFT uses the electronic density: the probability of an electron occupying a volume element at point r. The electron density function $\rho(r)$ is:

$$\rho(r) = N \int |\Psi|^2 \, dr_1 \cdots dr_n \tag{III.32}$$

Contrary to the wavefunction Ψ, the density $\rho(r)$ can be observed experimentally, for example, by x-ray diffraction[5]. The molecular properties of a system can be shown to be calculated from $\rho(r)$ (see Part III.3.I). The total electronic density only depends on three spatial variables (x, y, z):

$$\rho(r) = \rho(x, y, z) \tag{III.33}$$

III.3.I Kohn-Sham DFT

Density functional theory (DFT) is based on the Hohenberg-Kohn theorems[6]. The first of these theorems proves that the ground state properties of a poly-electron system are uniquely determined by the electron density. The second theorem proves that the exact minimum energy of the fundamental state is a functional of the exact electronic density.

$$E = E[\rho] = E[\rho(r)] \tag{III.34}$$

This allows us to say that for a value of (x, y, z), there exists one and only one value for the energy E. Thus E and the other molecular properties are defined in a unique way by the electronic density. Unfortunately, the theorems do not provide what form the $E[\rho]$ functional should have to produce a minimum energy.

The equation which allows us to find the electronic density is the Kohn-Sham equation[7]. It states that the energy of the fundamental state of a system of N electrons is given by:

$$E_{DFT}[\rho] = T[\rho] + V_{Ne}[\rho] + J_{ee}[\rho] + E_{xc}[\rho] \tag{III.35}$$

where $T[\rho]$ is the kinetic energy of the electrons, $V_{Ne}[\rho]$ is the nucleus-electron attraction and $J_{ee}[\rho]$ is the purely Coulombic repulsion between the electrons. $E_{xc}[\rho]$ is the exchange-correlation (XC) energy functional which takes into account all the non-classical interactions between the electrons. The difficulty of the DFT method is to find the expression for $E_{xc}[\rho]$.

The Kohn-Sham mono-electronic orbitals $\left(\phi_i^{KS}(r_1)\right)$ are solutions of the Kohn-Sham equation:

$$h_i^{KS}\phi_i^{KS}(r_1) = \varepsilon_i^{KS}\phi_i^{KS}(r_1) \tag{III.36}$$

By inserting the expressions for the energy terms, equation III.36 may be expressed as:

$$\left\{-\frac{1}{2}\nabla_1^2 - \sum_a\left(\frac{Z_a}{r_{1a}}\right) + \int\frac{\rho(r_2)dr_2}{r_{12}} + V_{xc}[\rho(r_1)]\right\}\phi_i^{KS}(r_1) = \varepsilon_i^{KS}\phi_i^{KS}(r_1) \tag{III.37}$$

where the exchange-correlation potential, $V_{xc}[\rho] = \frac{\delta(E_{xc}[\rho])}{\delta\rho}$. On condition of knowing $E_{xc}[\rho]$, the Kohn-Sham equations can be solved in a similar manner to Hartree-Fock. Since the potential which acts on electron 1 depends on the position of all the other electrons, the equation must be solved in an iterative way.

III.3.II Exchange-Correlation Functionals

To perform the DFT calculations, it is necessary to know the exchange-correlation energy, $E_{xc}[\rho]$. This energy may be divided into a sum of the exchange energy and the correlation energy functionals:

$$E_{xc}[\rho] = E_x[\rho] + E_c[\rho] \tag{III.38}$$

Many different functionals have been developed to determine the exchange and correlation energies. Most of these can be placed into the following categories-

- LDA (Local Density Approximation): functionals depending on $\rho(r)$ only where ε_{xc} is the exchange-correlation energy of a uniform electron gas

$$E_{xc}^{LDA}[\rho] = \int\rho(r)\varepsilon_{xc}\big(\rho(r)\big)d^3r \tag{III.39}$$

- GGA (Generalized Gradient Approximation): functionals depending on $\rho(r)$ and on its gradient $\nabla\rho(r)$

$$E_{xc}^{GGA}[\rho(r)] = \int f(\rho(r), \nabla\rho(r))d^3r \quad \text{(III.40)}$$

- Meta-GGA: functionals depending on $\rho(r)$, $\nabla\rho(r)$ and the Laplacian of the density $\nabla^2\rho(r)$

$$E_{xc}^{m-GGA}[\rho(r)] = \int f\big(\rho(r), \nabla\rho(r), \nabla^2\rho(r)\big)d^3r \quad \text{(III.41)}$$

- Hybrid DFT: functionals containing the exact Hartree-Fock (HF) exchange in the exchange functional

$$E_{xc}^{hybrid} = E_x^{HF} + E_c^{DFT} \quad \text{(III.42)}$$

Even though, "purely" *ab initio* functionals do exist (e.g. LDA), most functionals contain empirical parameters. These experimentally derived empirical parameters usually appear in the integrand f in GGA methods and in the ratio of HF to DFT energies in hybrid functionals. For this reason DFT is sometimes not considered an *ab initio* method.

The big advantage of the DFT method in comparison with *ab initio* methods is that it demands much less calculation time. DFT gives more accurate results than Hartree-Fock, due to electron correlation being included, but the computational costs are very similar. In general, DFT results are only less accurate than those determined higher order Moller-Plesset (e.g. MP4) and coupled clusters methods. Due to the electron density being dependent on only 3 dimensions, DFT computational time scale as N^3, where N is the number of basis functions, but post-Hartree-Fock scales as N^4 or higher. The smaller calculation time necessary for DFT calculations allows it to be used for very large sized systems, like biological systems, where a treatment of systems with tens or hundreds of atoms with correlated *ab initio* methods would be impossible. As the search to find more accurate exchange-correlation energy functionals whose results approach those of experiment is still an ongoing topic of research, the number of functionals available continues to increase.

III.3.III The B3LYP Functional

B3LYP is a hybrid functional and is one of the most commonly used DFT functionals by chemists. B3LYP has its origins in an older functional developed by Becke[8]. The B3PW91 exchange-correlation energy functional he proposed may be written as,

$$E_{xc}^{B3PW91} = (1 - a_0)E_x^{LDA} + a_0E_x^{HF} + a_x\Delta E_x^{B88} + E_c^{LDA} + a_c\Delta E_c^{PW91}. \quad \text{(III.43)}$$

This functional is a hybrid of the exact Hartree-Fock exchange energy, E_x^{HF}, and local-density approximation exchange and correlation energies, E_x^{LDA} and E_c^{LDA}. Also included in the functional are Becke's gradient corrected exchange functional[9], ΔE_x^{B88}, and the Perdew-Wang gradient corrected correlation functional[10], ΔE_c^{PW91}. The values of the semi-empirical coefficients, $a_0 = 0.2$, $a_x = 0.72$ and $a_c = 0.81$, were determined from experimental data.

The B3LYP functional itself, was first fully described by Stephens *et al*[11,12]. The exchange-correlation energy functional they gave was:

$$E_{xc}^{B3LYP} = (1 - a_0)E_x^{LDA} + a_0E_x^{HF} + a_x\Delta E_x^{B88} + a_cE_c^{LYP} + (1 - a_c)E_c^{VWN}. \quad \text{(III.44)}$$

In this functional, the PW91 correlation functional used in B3PW91 has been replaced with a gradient corrected correlation functional, E_c^{LYP}, by Lee, Yang and Parr (LYP) [13]. Since E_c^{LYP} is not easily separable, a local correlation energy functional, E_c^{VWN}, by Vosko, Wilk and Nusair (VWN)[14] has been used to determine the ratio of local and gradient corrected correlation functionals using the a_c coefficient. The same values as used in the B3PW91 functional for the a_0, a_x and a_c coefficients were used in the B3LYP functional.

III.4 The Vibrational Problem

Once the electronic Schrödinger equation is solved, as solution must be found for the vibrational problem, that is to say the movement of the nuclei. In the Born-Oppenheimer approximation, the total molecular wavefunction was separated into the electronic wavefunction and the nuclear wavefunction. The Schrodinger equation for the movement of the nuclei may then be written as:

$$\hat{H}_N\Psi_N(R) = E_N\Psi_N(R) \quad \text{(III.45)}$$

where the nuclear Hamiltonian ($\hat{H}_N$) is written as the sum of the kinetic energy of the nuclei, $\hat{T}_N$, and of the electronic potential, $\hat{V}_e$:

$$\left[\hat{T}_N + \hat{V}_e\right](R) = E_N\Psi_N(R) \quad \text{(III.46)}$$

For N atoms, this equation has 3N degrees of freedom.

III.4.I Separation of Movement

If the system studied is defined in the mobile reference frame having for the origin the centre of mass (G) of the molecule, 3 of the 3N coordinates describe the

translation of the molecule. Since these 3 coordinates are not coupled with the 3N-3 coordinates, they can be separated out without any approximations.

$$\hat{H}_N = \hat{H}_{trans} + \hat{H}_{rovib} \quad \text{(III.47)}$$

$$\Psi_N(R) = \Psi_N = \Psi_{trans}\Psi_{rovib} \quad \text{(III.48)}$$

If the molecule is considered to be a rigid rotor, then the approximation can be made that there is no coupling between the rotations and vibrations. The rotational and vibrational coupled terms in equations III.42 and III.43, can be written:

$$\hat{H}_{rovib} = \hat{H}_{rot} + \hat{H}_{vib} \quad \text{(III.49)}$$

$$\Psi_{rovib} = \Psi_{rot}(\theta, \varphi, \chi)\Psi_{vib}(x_i, y_i, z_i) \quad \text{(III.50)}$$

where (θ, φ, χ) are the Euler angles which describe the rotation of the molecule within the mobile reference and (x_i, y_i, z_i) are the Cartesian coordinates of the atoms defined in relation to G. The separation of the rotation and the vibration reduces the number of degrees of freedom for vibration to 3N-6 (except for a linear molecule where the number of degrees of freedom is equal to 3N-5).

The rotational energy for a given vibrational level may be calculated by solving the rotational eigenvalue equation:

$$\hat{H}_{rot}\Psi_{rot} = E_{rot}\Psi_{rot} \quad \text{(III.51)}$$

with

$$\hat{H}_{rot} = \frac{\hat{J}_a^2}{2I_a} + \frac{\hat{J}_b^2}{2I_b} + \frac{\hat{J}_c^2}{2I_c} \quad \text{(III.52)}$$

where a, b and c are the axes of inertia of the molecule, $\hat{J}_x$ $(x = a, b, c)$ are the projections of the total angular moment on the principal axes and I_x is the principal moment of inertia associated with these axes and defined by:

$$I_x = \sum_i^N m_i (d_i^x)^2 \quad \text{(III.53)}$$

where m_i is the mass of atom i and d_i^x is its distance in relation to the axis of inertia x.

III.4.II Normal Coordinates

To solve the vibrational equation according to:

$$\hat{H}_{vib}\Psi_{vib} = \left[\hat{T} + \hat{V}\right]\Psi_{vib} = E_{vib}\Psi_{vib}, \quad \text{(III.54)}$$

it is important to make a good choice of coordinates.

Using the Cartesian coordinates (x_i, y_i, z_i) and the equilibrium coordinates $(x_i^{eq},\ y_i^{eq},\ z_i^{eq})$ of every atom, the mass weighted displacement Cartesian coordinates (q_i) may be written, for example:

$q_1 = \sqrt{m_1}\left(x_1 - x_1^{eq}\right),\ q_2 = \sqrt{m_1}\left(y_1 - y_1^{eq}\right),\ q_2 = \sqrt{m_1}\left(z_1 - z_1^{eq}\right),\ q_4 = \sqrt{m_2}\left(x_2 - x_2^{eq}\right), etc.$

The normal coordinates, Q_k, can then be written as linear combinations of the balanced weighted Cartesian coordinates:

$$Q_k = \sum_{i=1}^{3N} c_{ik} q_i \tag{III.55}$$

In this system of normal coordinates, the vibrations are independent from each other and Q_k is orthogonal. The kinetic energy is written now as:

$$\hat{T} = \frac{1}{2}\sum_{k=1}^{3N} Q_k^2 \tag{III.56}$$

and the vibrational Hamiltonian in the system of normal coordinates as:

$$-\frac{\hbar^2}{2\mu_i}\sum_{i=1}^{3N}\frac{\partial^2}{\partial Q_i^2}\Psi_{vib} + \hat{V}\Psi_{vib} = E_{vib}\Psi_{vib} \tag{III.57}$$

III.4.III Harmonic Vibrational Approach

The potential energy arises from the electronic calculation and depends on Q_k. If the movement of the nuclei is taken to be a weak oscillation around the equilibrium position, the potential $\hat{V}$ can be developed into a Taylor series:

$$\hat{V} = V_{eq} + \sum_i \left(\frac{\partial V}{\partial Q_i}\right)_{eq} Q_i + \frac{1}{2}\sum_{i,j}\left(\frac{\partial^2 V}{\partial Q_i \partial Q_j}\right)_{eq} Q_i Q_j + \frac{1}{6}\sum_{i,j,k}\left(\frac{\partial^3 V}{\partial Q_i \partial Q_j \partial Q_k}\right)_{eq} Q_i Q_j Q_k + \cdots \tag{III.58}$$

$$\hat{V} = V_{eq} + \sum_i f_i Q_i + \frac{1}{2}\sum_{i,j} f_{ij} Q_i Q_j + \frac{1}{6}\sum_{i,j,k} f_{ijk} Q_i Q_j Q_k + \cdots \tag{III.59}$$

A null potential at the equilibrium, $V_{eq} = 0$, can be taken as a reference. The equilibrium state is a minimum, therefore the first order derivatives of the potential with respect to the coordinates Q_k are null:

$$\left(\frac{\partial V}{\partial Q_i}\right)_{eq} = f_i = 0 \tag{III.60}$$

The first non null term of the Taylor development is then the second order term. If the amplitude of the vibration is weak, the higher order terms can be neglected (that is to say: $f_{ijk} = 0$, etc.). The nuclear vibrations are treated as harmonic vibrations and since the coordinates Q_k are orthogonal to each other, the harmonic vibrational Hamiltonian can be written as:

$$-\frac{\hbar^2}{2\mu_i}\sum_{i=1}^{3N}\frac{\partial^2}{\partial Q_i^2}\Psi_{vib}^{har} + \frac{1}{2}\sum_{i}^{3N} f_{ii}Q_i^2\Psi_{vib}^{har} = \mathrm{E}_{vib}^{har}\Psi_{vib}^{har} \tag{III.61}$$

This is then the equation of a one dimensional harmonic quantum oscillator, the solutions of which are well known. It is written as a function of a quantum number v and of a characteristic harmonic frequency $\omega = \frac{1}{2\pi}\sqrt{\frac{k}{\mu}}$, and where the wavefunction depends on Hermite polynomials $H_v(z)$:

$$\Psi_{vib}^{i}(z) \propto H_v(z)e^{-\frac{1}{2}z^2} \propto \left[(-1)^v e^{z^2}\frac{\partial^v}{\partial z^v}e^{-z^2}\right]e^{-\frac{1}{2}z^2} \tag{III.62}$$

with

$$z = \left(\frac{k\mu}{\hbar^2}\right)^{\frac{1}{4}}(r - r_{eq}) \tag{III.63}$$

The vibrational energy of a normal mode i (non-degenerate) is written then as:

$$E_{vib}^{i} = \left(v + \frac{1}{2}\right)\hbar\omega_i \tag{III.64}$$

The quantum number v can take the values 0, 1, 2 etc. with a selection rule of $\Delta v = \pm 1$ between vibrational levels.

It is important to note that the solution of equation **Error! Reference source not found.** gives 3N wave functions and 3N harmonic frequencies ω, whereas it is known that there exists only 3N-6 vibrations of a non-linear system (3N-5 for a linear system). The 6 supplementary vibrations (or 5 for a linear system) correspond to the 3 translational movements and to the 3 rotational movements (or 2 rotational movements in linear systems). If the potential has been calculated correctly and if the system is at a stationary point of the potential energy surface, the frequencies for these 6/5 degrees of freedom should be equal to zero.

The vibrational wavefunction is written thus as a product of the eigenfunctions of the harmonic oscillators and the vibrational energy as the sum of the associated

energies of each one of the normal vibration modes, with each function depending on a quantum number v_i and of a characteristic vibration frequency ω_i:

$$E_{vib}^{har} = E_{vib}^{1} + E_{vib}^{2} + \cdots + E_{vib}^{3N-6} = \sum_{i=1}^{3N-6} \left(v_i + \frac{1}{2}\right) \hbar\omega_i \quad \text{(III.65)}$$

$$\Psi_{vib}^{har} = \Psi_{vib}^{1}(Q_1)\Psi_{vib}^{2}(Q_2) \cdots \Psi_{vib}^{3N-6}(Q_{3N-6}) \quad \text{(III.66)}$$

III.4.IV Anharmonicity and Scaling Factors

III.4.IV.a The Anharmonic Oscillator

Vibrational frequencies calculated using the harmonic oscillator model are consistently found to be higher than experimentally recorded values. The reasons for these errors are partly due to the approximations made in the level of calculation (including electron correlation and incomplete basis sets). Even for methods that use an extensive basis set and treat electron correlation (e.g. DFT, Configuration Interaction, Møller–Plesset perturbation theory etc.), errors between experimental and calculated vibrational frequencies still exist due to the neglect of anharmonicity in the calculation.

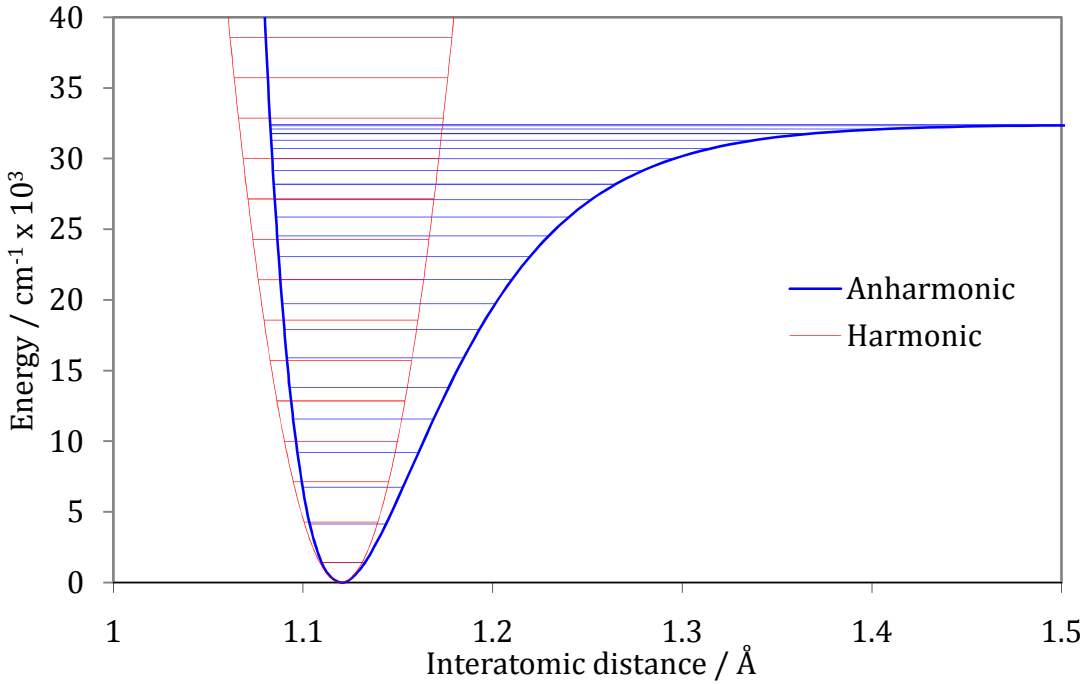

Figure III.3: Plots illustrating the effect of anharmonicity on the energy of a vibrational mode. The harmonic oscillator potential energy has been modelled using Hooke's law ($\boldsymbol{V_{har} = \frac{1}{2}kq^2}$) and the anharmonic oscillator using the Morse potential ($\boldsymbol{V_{anhar} = D_e(1 - e^{-\beta q})^2}$). The energy levels have been described using $\boldsymbol{E_{har} = \bar{\omega}\left(v + \frac{1}{2}\right)}$ and $\boldsymbol{E_{anhar} = \bar{\omega}_e\left(v + \frac{1}{2}\right) - \bar{\omega}_e x_e\left(v + \frac{1}{2}\right)^2}$.

The harmonic oscillator method approximates the movement of nuclei during a vibration as a simple oscillation around an equilibrium distance with equal restoring forces upon compression and stretching but in reality their vibrations have an anharmonic motion where the restoring forces are different for compression and stretching and whose potential is better described using the Morse potential (see Figure III.3). The quantum mechanical energy levels of an anharmonic oscillator, similar to the harmonic energy levels given in equation III.64, may be written as:

$$E = \bar{\omega}_e\left(v+\frac{1}{2}\right) - \bar{\omega}_e x_e\left(v+\frac{1}{2}\right)^2 + \bar{\omega}_e y_e\left(v+\frac{1}{2}\right)^3 + \cdots \qquad \text{(III.67)}$$

where $\bar{\omega}_e$ is the fundamental frequency equal to the harmonic frequency and $\bar{\omega}_e x_e$, $\bar{\omega}_e y_e$,... etc. are the anharmonic constants. As $\bar{\omega}_e x_e \gg \bar{\omega}_e y_e$, usually only the first anharmonic term is considered and the higher order terms are ignored. Selection rules between vibrational states are also different from the harmonic approximation with $\Delta v = \pm 1, \pm 2, \pm 3, \ldots etc$. Calculations of anharmonic frequencies, though accurate, are computationally expensive due to the need to calculate extensive potential energy surfaces.

III.4.IV.b Overtone and Combination Bands

The selection rules for an harmonic oscillator allow for transitions with $\Delta v = \pm 1$. An anharmonic oscillator has looser selection rules with $\Delta v = \pm 1, \pm 2, \pm 3, \ldots$, allowing transitions between multiple energy levels and coupling between modes with excitation by one photon. Overtones occur when transitions between states have $\Delta v \geq 2$ and for a fundamental mode ν_i are designated $2\nu_i$, $3\nu_i$, $4\nu_i$ etc. They are much weaker than the fundamental mode and decrease in intensity with each successive overtone. Overtones are at a lower frequency than the simple multiple of the harmonic frequency due to the decrease in spacing between anharmonic energy levels. Combination and difference bands can arise from the coupling between different fundamental modes and their overtones- $n\nu_i \pm m\nu_j$. Like overtones, most combination and difference bands are much weaker than the fundamental modes and are at a lower frequency than the sum or difference of the harmonic frequencies. Whether or not a combination or overtone is spectroscopically allowed is dependent on the combined symmetry of the modes[15,16] and may permit the frequency of an otherwise symmetry forbidden mode to be determined from its symmetry allowed combinations.

Although most combinations and overtones are very weak, some transitions may gain intensity via Fermi resonance. When a weak combination or overtone is degenerate (or nearly degenerate) with an intense fundamental mode of the same symmetry, the weaker band can "borrow" intensity from the stronger band. The frequencies of the bands will also separate, with one band shifting to a slightly higher frequency and the other to a slightly lower frequency. One of the reasons proposed for Fermi resonance occuring is due to the fact that higher degeneracy than allowed for the symmetry of a system is forbidden and must be avoided by separating and mixing the two states[15]. When Fermi resonance occurs it may be difficult assign the individual modes due to the shift in frequency and change in intensity.

III.4.IV.c Anharmonic Scaling Corrections

In order to compare calculated harmonic to experimental vibrational frequencies scaling factors may be applied. These scaling factors have usually been determined by comparing a large set of theoretical frequencies, ω_i^{theor}, to experimental frequencies, ν_i^{exp}. Using the least-squares technique, the scaling factor λ is determined from-

$$\lambda = \sum_i \omega_i^{theor} \nu_i^{exp} \Big/ \sum_i \left(\omega_i^{theor}\right)^2 \tag{III.68}$$

and the root-mean square error for n vibrational frequencies from-

$$rms = \sqrt{\sum\nolimits_1^n \left(\omega_i^{theor} - \nu_i^{exp}\right)^2 / n} \tag{III.69}$$

A number of scaling factors have been presented in the literature for different sets of molecules, theoretical levels and applications. The simplest way to scale harmonic frequencies is to apply one single scaling factor to the whole set of vibrational modes[17-19]. Unfortunately this technique does not reproduce experimental results accurately as the amount of anharmonicity exhibited by modes is not uniform. For example, high frequency stretches are generally more anharmonic than low frequency bends. Recognising these differences, different scaling factors have been developed for frequency ranges[20] e.g. low frequency regions (e.g. < 1800cm^{-1}) and high frequency regions (e.g. > 1800cm^{-1}). A more accurate procedure is to apply suitable scaling factors to the individual normal coordinates that make up a normal mode. For example, a mode involving a C-C

stretch coupled to a C-H bend would have distinct scaling factors applied to the force constants for the C-C stretch and C-H bend normal coordinates. Examples of this technique include Pulay's Scaled Quantum Mechanical force fields technique (SQM)[21-23] and the newer Effective Scaling Frequency Factor technique (ESFF)[24,25].

Unfortunately, no tabulated scaling factors for the B3LYP/6-311++G(2d,2p) calculation level used in this study could be found in the literature. Scaling factors for this level of calculation were found by comparing FTIR and Raman experimental results with the DFT harmonic frequencies. For all frequencies below 2000cm^{-1}, a simple scaling factor of 0.98 was used. For the more anharmonic C-H and N-H stretches, scaling factors of 0.96 and 0.93 were used respectively. These factors are similar to some of those reported in the literature. Spanget-Larsen[26] used a uniform scaling factor of 0.98 to compare B3LYP/6-311++G(d,p) frequencies to matrix-isolated FTIR results. In a study of the polycyclic aromatic compounds naphthalene, azulene, phenanthrene and anthracene, Martin et al[27] found scaling factors of 0.96 for C-H stretches, 0.983 for in-plane bends and 0.97 for lower frequency vibrations when comparing B3LYP/cc-pVDZ[28] calculated frequencies and 0.965 for C-H stretches and 0.975 for all lower frequency vibrations when comparing B3LYP/cc-pVTZ[28].

III.4.V Infrared Absorption Intensity

The infrared intensity of an infrared mode i is determined from the integrated absorption coefficient[29] and using the harmonic oscillator approximation, may be given by[30]

$$I_i^{IR} = \frac{N\pi d_i}{3c^2}\left|\frac{d\mu}{dQ_i}\right|^2 \qquad \text{(III.70)}$$

where N is the total number of molecules per unit volume expressed as Avogadro's number (mol^{-1}) , d_i is the degeneracy of normal mode i and c is the speed of light. The absolute infrared intensity, $|d\mu/dQ_i|^2$, is the square of the derivative of the electric dipole moment μ with respect to the mass weighted normal coordinates Q_i. The absolute infrared intensity is the only molecular parameter used in determining the IR intensity and may be given in the non-SI units of $\left(\mathrm{D/Å}\right)^2\mathrm{amu}^{-1}$. However, it is usually converted to the SI derived units for absorption intensity of km mol^{-1} (where $1\ \left(\mathrm{D/Å}\right)^2\mathrm{amu}^{-1} = 42.2561\ \mathrm{km\ mol}^{-1}$), which are commonly used when comparing experimental results[31,32].

III.4.VI Raman Scattering Intensity

The Raman scattering activity S_i and depolarization ratio ρ_i of Stokes Raman modes[31,33-35], collected at right angles to the incident plane polarized light, can be computed using the expressions:

$$S_i^{\perp} = g_i[45(\alpha_i')^2 - 7(\beta_i')^2] \tag{III.71}$$

and

$$\rho_i = \frac{3(\beta_i')^2}{45(\alpha_i')^2 + 4(\beta_i')^2} \tag{III.72}$$

where g_i is the degeneracy of the normal mode. $(\alpha_i')^2$ and $(\beta_i')^2$ are the squares of the derivatives of the trace and of the anisotropy of the polarizability tensor-

$$(\alpha_i')^2 = \frac{1}{9}\left(\sum_n \frac{\partial \alpha_{nn}}{\partial Q_i}\right)^2, \qquad n = x, y, z \tag{III.73}$$

$$(\beta_i')^2 = \frac{1}{2}\left\{\sum_{nm}\left(\frac{\partial \alpha_{nn}}{\partial Q_i} - \frac{\partial \alpha_{mm}}{\partial Q_i}\right)^2 + 6\sum_{nm}\left(\frac{\partial \alpha_{nm}}{\partial Q_i}\right)^2\right\} \; n, m = x, y, z \;\; n \neq m \tag{III.74}$$

The $\partial \alpha_{nm}/\partial Q_i$ terms are the derivatives of the polarizability tensor with respect to normal-mode coordinate Q_i.

An alternative expression is used for determining Raman scattering intensities recorded at 0° or 180° to the incident light where the 7 is replaced with a 4,

$$S_i^{\parallel} = g_i[45(\alpha_i')^2 - 4(\beta_i')^2] \tag{III.75}$$

The absolute differential Raman scattering cross section[33,35], which corresponds to the absolute Raman intensity of a normal mode i, is given by,

$$\frac{\partial \sigma_i}{\partial \Omega} = \frac{(2\pi)^4}{45}(\nu_0 - \nu_i)^4 \frac{h}{8\pi^2 c \nu_i B_i} S_i \tag{III.76}$$

where ν_0 and ν_i are the frequencies of the incident light and normal mode i and h, k and c are Planck and Boltzmann constants and the speed of light. B_i is the Boltzmann distribution of the normal modes and is dependent on temperature T:

$$B_i = 1 - exp\left(-\frac{h\nu_i c}{kT}\right) \tag{III.77}$$

B_i may be ignored for experiments at low temperatures or for modes with higher frequencies as this factor approaches 1.

To simulate an experimental Raman spectrum, the intensities of the different modes may be calculated using the formula given by Michalski and Wysokinski[35],

$$I_i^{Ram} = \frac{C(\nu_0 - \nu_i)^4 \cdot S_i}{\nu_i B_i} \tag{III.78}$$

where the *C* term is a constant made up of a geometry factor and the physical constants *h*, *k* and *c*.

III.4.VII Zero-Point Energy (ZPE)

The particular case where all ν_i values are null, the energy that remains is the energy of the fundamental vibrational state, more usually called the zero-point energy (ZPE), which corresponds to the sum of the ZPEs of all the vibration modes:

$$ZPE = \sum_{i=1}^{3N-6} \frac{1}{2}\hbar\omega_i \tag{III.79}$$

The total energy of the studied system in its fundamental state is written then as the sum of the electronic energy and the ZPE:

$$E_{tot} = ZPE + E_{el} \tag{III.80}$$

III.5 Time-Dependent Density Functional Theory

Time-Dependent Density Functional Theory (TDDFT) has foundations in the Runge-Gross theorem[36], which is a time-dependent extension of the Hohenberg-Kohn theorems (see Part III.3). In this theorem it is proven that there exists a unique one-to-one correspondence between the time-dependent external potential and the time-dependent electron density for a fixed initial state. In order to simplify the calculations, a scheme is chosen which uses a system that is non-interacting to form the density of the interacting system. The time-dependent Kohn-Sham (TDKS) equations[37], analogous to those in static DFT, may be described by the Schrödinger equation:

$$\left(-\frac{1}{2}\nabla^2 + \nu_{KS}[\rho](r,t)\right)\phi_i(r,t) = i\frac{\partial}{\partial t}\phi_i(r,t) \tag{III.81}$$

When $\phi_i(r,t)$ orbitals satisfy the TDKS equations, the time-dependent density is determined by

$$\rho(r,t) = \sum_i^N |\phi_i(r,t)|^2 \tag{III.82}$$

Again, analogous to time-independent DFT, the potential $\nu_{KS}[\rho](r,t)$ is given by,

$$v_{KS}[\rho](r,t) = v_{ext}(r,t) + \int dr' \frac{\rho(r',t)}{|r-r'|} + v_{XC}(r,t) \quad \text{(III.83)}$$

which includes the time-dependent external potential, $v_{ext}(r,t)$, the Coulombic electron repulsive potential and the time-dependent exchange-correlation potential, $v_{XC}(r,t)$. This exchange-correlation potential is the functional derivative of the exchange-correlation action, A_{XC} over both space and time,

$$v_{XC}[\rho](r,t) = \frac{\delta A_{XC}[\rho]}{\delta\rho(r,t)} \approx \frac{\delta E_{XC}[\rho_t]}{\delta\rho_t(r)} = v_{XC}[\rho_t](r) \quad \text{(III.84)}$$

However, the adiabatic approximation[37,38] may be used to approximate A_{XC} by the time-independent exchange-correlation functional, E_{XC}, which is a function of the density at a fixed time t.

If the external perturbation is assumed to be weak, that is the external field does not destroy the ground state electronic structure completely, linear response theory[39] may be used to calculate the spectral values of the excitations[38,40-42]. The advantage of applying this theory is that the changes in the system will only depend on the ground state of the system. The dynamic polarizability, $\bar{\alpha}(\omega)$, describes the response of a dipole moment to an electric field and may expressed by the sum-over-states (SOS) relationship[42],

$$\bar{\alpha}(\omega) = \sum_I \frac{f_I}{\omega_I^2 - \omega^2} \quad \text{(III.85)}$$

The poles of this expression determine the excitation energies, ω_I, while the oscillator strengths are determined by the residues, f_I. Following this, the values of the transition energies, Ω_n, are obtained from solving the eigenvalue problem,

$$\left[\omega_{ij\sigma}^2 \delta_{ik}\delta_{jl}\delta_{\sigma\tau} + 2\sqrt{f_{ij\sigma}\omega_{ij\sigma}}\mathrm{K}_{ij\sigma,kl\tau}\sqrt{f_{kl\tau}\omega_{kl\tau}}\right]F_n = \Omega_n^2 F_n \quad \text{(III.86)}$$

where the coupling matrix, $\mathrm{K}_{ij\sigma,kl\tau}$, is given by,

$$\mathrm{K}_{ij\sigma,kl\tau} = \iint \phi_{i\sigma}^*(r)\phi_{j\sigma}(r)\left(\frac{1}{|r-r'|} + \frac{\partial v_\sigma^{XC}(r)}{\partial\rho_\tau(r')}\right) \times \phi_{k\tau}(r')\phi_{l\tau}^*(r')drdr' \quad \text{(III.87)}$$

The indices i, j, σ and k, l, τ in the above expressions correspond to the occupied states, unoccupied states and the spin of the initial and perturbed states. $\phi(r)$ are the Kohn-Sham orbitals, $f_{ij\sigma}$ are the differences in occupation between the states and $v_\sigma^{XC}(r)$ is the exchange-correlation functional. The oscillator strengths are obtained from the eigenvectors, F_n.

III.6 Molecular Symmetry and Point Group Theory

Knowing the symmetry of a molecule can help simplify quantum mechanical problems and offer insights into the physical properties of a molecule. Molecules may have several symmetry operations, e.g. rotations, reflections, improper rotations or inversion operations, performed about geometric, symmetry elements, e.g. a rotation axis, an improper rotation axis, a reflection plane or a point of inversion, that leave the molecule indistinguishable before and after the operation. Molecules also have an identity operation which does not move any of the atoms and can be thought of as a rotation of the molecule by 360°. Group theory offers a general, mathematical treatment of molecular symmetry. A point group is a set of symmetry operations which form the group elements of a mathematical group. A point group, G, must satisfy 4 requirements:

- A group must have closure: $AB = X \; where \; A, B, X \in G$
- A group must contain the identity element E: $EX = XE = X \; where \; E, X \in G$
- Associative law of combination must apply for all combinations of elements: $A(BC) = (AB)C = X \; where \; A, B, C, X \in G$
- Every element of G has a reciprocal: $AA^{-1} = E \; where \; A, A^{-1}, E \in G$

A character table for a group may be produced which show the irreducible representations consisting of the simplest set of characters that satisfy the requirements of the group. A molecule can be assigned to a particular point group by identifying all the symmetry operations of a molecule.

Relationships between irreducible representations are defined by the Great Orthogonality Theorem[43] or GOT:

$$\sum_R \Gamma_i(R)_{mn}\Gamma_j(R)_{m'n'} = \frac{h}{d_i}\delta_{ij}\delta_{mm'}\delta_{nn'} \qquad \text{(III.88)}$$

where $\Gamma_i(R)_{mn}$ is the matrix element of the operation R in the i^{th} representation, d_i is the dimension of i and h is the order of the group. δ_{ij}, $\delta_{mm'}$ and $\delta_{nn'}$ are Kronecker delta functions defined such that $\delta_{\alpha\beta} = 0$ if $\alpha \neq \beta$ and $\delta_{\alpha\beta} = 1$ if $\alpha = \beta$. Some of the relationships derived from the GOT include:

- The number of irreducible representations of a group is equal to the number of symmetry classes.
- The character for the identity operation E in the i^{th} irreducible representation is equal to the dimension of the representation, $\chi_i(R) = d_i$.

- The sum of the squares of the characters of the characters in any irreducible representation equals the order of the group, h, $\sum_R[\chi_i(R)]^2 = h$, or where g_c is the order of the class c: $\sum_{R_c} g_c[\chi_i(R_c)]^2 = h$.
- Any two different irreducible representations, χ_i and χ_i, are orthogonal to each other: $\sum_{R_c} g_c[\chi_i(R_c)]\left[\chi_j(R_c)\right] = 0$.

One of the most important derivations from the GOT is an equation which allows one to reduce a representation into its constituent irreducible representations:

$$n_i = \frac{1}{h}\sum_c g_c\chi_i(R_c)\chi_r(R_c) \tag{III.89}$$

In this equation, n_i is the number of times the irreducible representation χ_i occurs in the reducible representation χ_r. Therefore, a reducible representation may be reduced into a sum of irreducible representations: $\chi_r = \sum n_i\chi_i$.

The following sections will describe how molecular symmetry and group theory may be applied in quantum mechanics and in the determination of the physical properties of molecules. In particular, in determining the molecular orbitals, vibrational normal modes and IR, Raman and electronic transition selection rules of the highly symmetric molecules H_2Pc and ZnPc.

III.6.I Point Groups of ZnPc and H_2Pc

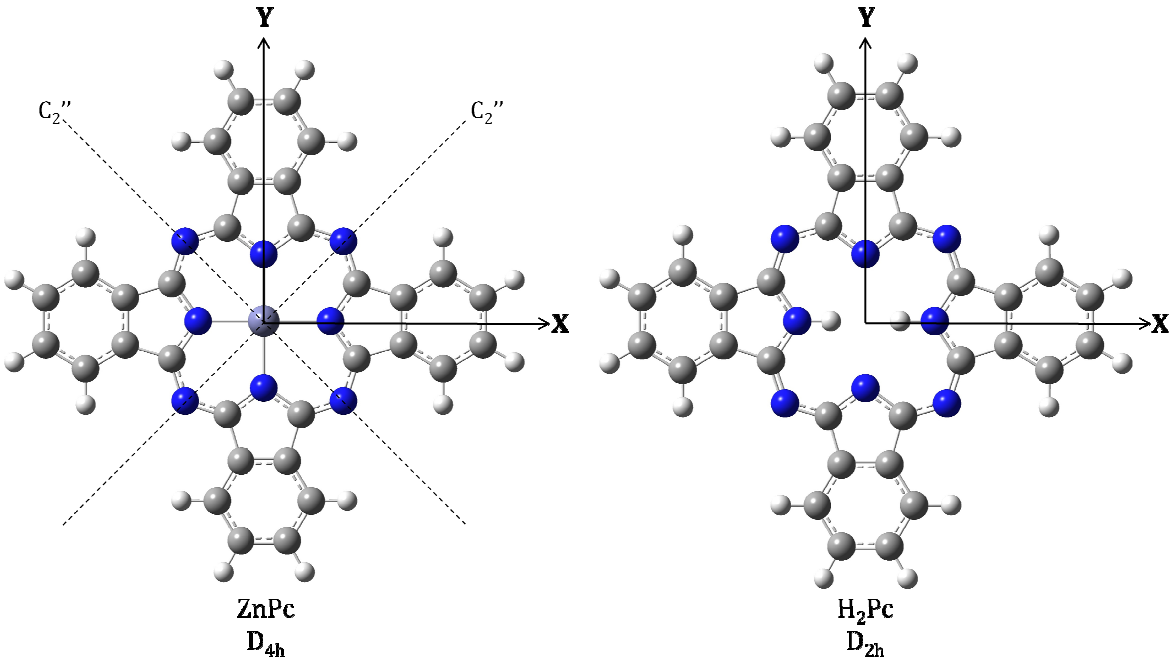

Figure III.4: ZnPc and H_2Pc molecular structures depicting the x and y Cartesian axes. The molecules have been orientated on the xy plane, perpendicular to the z axis. The C_2'' rotation axes of ZnPc are also shown.

Figure III.4 shows the molecular structures of the large planar zinc phthalocyanine (ZnPc) and free-base phthalocyanine (H_2Pc) molecules. The highest order rotational axis of ZnPc is identified as the C_4 axis passing through the central Zn atom at right angles to the plane of the molecule and following convention, is assigned as the principal axis and placed along the *z* Cartesian axis with the rest of the atoms on the *xy* plane as shown in Figure III.4. About this axis two C_4 operations are identified, C_4 and C_4^3, and one C_2 rotation collinear to the C_4 axis. Four other C_2 rotations are identified: two C_2' rotations about the *x* and *y* axes and two C_2'' rotations about axes at 45° to the *x* and *y* axes. An inversion operation *i* exists though the origin as well as two improper S_4 rotation operations involving C_4 and C_4^3 rotations around the principal axis followed by a reflection through the *xy* plane. There are three classes of reflection operations: one horizontal σ_h reflection through the *xy* plane, two vertical σ_v reflections through the *xz* and *yz* planes and two dihedral σ_d reflections though the planes containing the *z* and C_2'' axes. Including the identity operation E, the point group which contains these 10 symmetry operation is identified as the D_{4h} point group, whose character table is shown in Table III.1.

Table III.1: Character table of D_{4h} point group.

D_{4h}	E	$2C_4$	C_2	$2C'_2$	$2C''_2$	i	$2S_4$	σ_h	$2\sigma_v$	$2\sigma_d$	Linear	Quadratic
A_{1g}	1	1	1	1	1	1	1	1	1	1		x^2+y^2, z^2
A_{2g}	1	1	1	-1	-1	1	1	1	-1	-1	R_z	
B_{1g}	1	-1	1	1	-1	1	-1	1	1	-1		x^2-y^2
B_{2g}	1	-1	1	-1	1	1	-1	1	-1	1		xy
E_g	2	0	-2	0	0	2	0	-2	0	0	(R_x, R_y)	(xz, yz)
A_{1u}	1	1	1	1	1	-1	-1	-1	-1	-1		
A_{2u}	1	1	1	-1	-1	-1	-1	-1	1	1	z	
B_{1u}	1	-1	1	1	-1	-1	1	-1	-1	1		
B_{2u}	1	-1	1	-1	1	-1	1	-1	1	-1		
E_u	2	0	-2	0	0	-2	0	2	0	0	(x,y)	

Looking at H_2Pc, three C_2 rotation operations can identified, two about axes in the plane of the molecule and one perpendicular to them. Usually when two or more highest order rotational axes exist, the axis passing through the most number of geometric points (atoms) is chosen to be the principal z axis. In H_2Pc this would be the axis containing the central N-H bonds with the y axis at right angles in the plane of the molecule and the x axis coming out of the plane. However, in order to ease the comparison with ZnPc, the z and x axes of H_2Pc have been switched as shown in Figure III.4. Three reflection operations exist, one through the xy plane, one through the xz plane and one through the yz plane. Like ZnPc, an inversion operation is found through the origin. Again including the identity operation, the D_{2h} point group is identified as the group containing the previously described 8 symmetry operation classes whose character table is shown in Table III.2

Table III.2: Character table of D_{2h} point group.

D_{2h}	E	$C_2(z)$	$C_2(y)$	$C_2(x)$	i	$\sigma(xy)$	$\sigma(xz)$	$\sigma(yz)$	Linear	Quadratic
A_g	1	1	1	1	1	1	1	1		x^2, y^2, z^2
B_{1g}	1	1	-1	-1	1	1	-1	-1	R_z	xy
B_{2g}	1	-1	1	-1	1	-1	1	-1	R_y	xz
B_{3g}	1	-1	-1	1	1	-1	-1	1	R_x	yz
A_u	1	1	1	1	-1	-1	-1	-1		
B_{1u}	1	1	-1	-1	-1	-1	1	1	z	
B_{2u}	1	-1	1	-1	-1	1	-1	1	y	
B_{3u}	1	-1	-1	1	-1	1	1	-1	x	

Restricting a molecule to a particular symmetry can reduce CPU time and memory requirements during a geometry optimisation calculation. Restrictions on the symmetry of the molecule means that displacements of atoms and groups made during an optimisation are limited to those that do not break the symmetry of the molecule and must be applied across the symmetry elements. The more symmetry elements a molecule has, the more restrictions are placed on these displacements. The symmetry of a molecule may have to be changed to a lower symmetry if the geometry of a molecule does not converge to a local energy minimum or if the minimum found is not the global minimum of a ground state, optimised geometry (e.g. saddle points, transition states).

III.6.II Molecular Orbitals and Symmetry Adapted Linear Combinations

Group theory can be useful in simplifying *ab initio* calculations and saving on computational time. One of the most important uses of symmetry and group theory is in the constructing of molecular orbitals and calculating their energy. All molecular orbitals must form the basis for some irreducible representation of the point group of the molecule[43]. Consequently, as MOs are usually constructed of linear combinations of atomic orbitals, the linear combinations used must also form the basis of an irreducible representation.

For an integral to be non zero ($\int f(x)\,dx \neq 0$), the integrand must transform as the totally symmetric representation A ($\Gamma(f(x)) = A$). For example, if the overlap integral, S_{mn}, between two orbitals, ϕ_m and ϕ_n is to be non-zero (indicating an bonding or anti-bonding interaction between the orbitals), the direct product of the representations of the orbitals must be equal to the totally symmetric representation:

$$\int \phi_m{}^* \phi_n \, d\tau \neq 0 \iff \Gamma(\phi_m) \times \Gamma(\phi_n) = A \tag{III.90}$$

$$\int \phi_m{}^* \phi_n \, d\tau = 0 \iff \Gamma(\phi_m) \times \Gamma(\phi_n) \neq A \tag{III.91}$$

When the product of the irreducible representations of two functions results in the totally symmetric representation (or for the case of degenerate representations, results in a sum containing the totally symmetric representation), then the functions must have the same irreducible representation.

Other integrals like the Fock integrals, where the Fock operator is totally symmetric, may be treated in the same way to determine if the integral is zero or non-zero. Using LCAOs of suitable symmetry and analyzing how their representations multiply can lead to savings in calculation time. Many integrals need not be fully calculated due to their symmetry and some matrices (e.g. the Fock matrix) are automatically block diagonalized due to only those elements of the matrix having the same symmetry being non-zero.

In order for LCAOs to conform to the symmetry requirements of the point group of a molecule, symmetry adapted linear combinations or SALCs must be formed from the basis functions that define the atomic orbitals. For simple systems, SALCs may be deduced by inspecting the atomic orbitals of the molecules but for larger systems a more systematic and rigorously defined method is required. Use of a projection operator is one such method.

A projection operator used in finding the symmetry adapted linear combinations may be written as:

$$S_i \propto P_i \phi_n = \frac{d_i}{h} \sum_R \chi_i^R R_j \phi_n \tag{III.92}$$

The operator P_i for a particular irreducible representation i is applied to a basis function ϕ_n which projects out a linear combination of basis functions S_i. The operator works by applying each of the symmetry operations R_j to ϕ_n and multiplying by the corresponding character χ_i^R of the irreducible representation i. The factor $\frac{d_i}{h}$, made of the dimension of i, d_i, and the order of the group h, is often ignored as the resulting MOs need to be normalised and this factor would be included then. Problems with this form of the projection operator may arise when applied to degenerate irreducible representations. An initial SALC S_i^1 will be formed from ϕ_1 but to find the other partners to S_i^1 ($S_i^1, S_i^2, \ldots S_i^{d_i}$) either P_i should be applied to a different basis function, e.g. ϕ_2, or a suitable symmetry operation may be applied to S_i^1 to find new SALCs, S_i^X. This new SALC may not necessarily be the partner of S_i^1 but may a positive or negative of S_i^1 or linear combination of S_i^1 and one or more partners we are looking for. If S_i^X is a linear combination of S_i^1 and/or the SALCs of the degenerate representation i we are looking for, it will not be orthogonal to S_i^1 or any previously determined SALC. The linear combinations

can then be found by finding small integer values or a, b, c, … to solve the simple relationship $S_i^X = aS_i^1 + bS_i^2 + cS_i^3 + \cdots$.

III.6.III Normal Modes

A molecule containing N atoms has a finite number of fundamental vibrational motions called normal modes. If each atom is considered to have three degrees of freedom, then the number of normal modes a nonlinear molecule of N atoms may have is 3N, where 3 of these modes are translational, 3 are rational and the remainder 3N-6 modes are vibrational. Linear molecules have only 2 rotational modes and hence have 3N-5 vibrational modes. Each normal mode is described by a normal coordinate and by applying the symmetry operations for the point group of the molecule, will form the basis for an irreducible representation[16,43].

In order to find the number of vibrational modes of each symmetry a molecule has, the representation of the total modes, Γ_{3N}, must be determined. A simple way of doing this is to apply each of the symmetry operations of the group to the molecule and count the number of atoms unmoved during each operation to find the representation of unmoved atoms, $\Gamma_{unmoved}$, and multiply by the representation of degrees of freedom i.e. the sum of the x, y and z irreducible representations, Γ_{xyz}. To find the representation for the vibrational modes (Γ_{Vib}), the representations for the 3 translational (Γ_{Trans}) and 3 rotational (Γ_{Rot}) may be subtracted from Γ_{3N}. ZnPc and H_2Pc with 57 and 58 atoms, have a total of 171 and 174 normal modes respectively. The results for the calculation of the different representations for ZnPc and H_2Pc are shown in Table III.3 and Table III.4.

Table III.3: Calculation of the representations of the vibrational modes of ZnPc.

	ZnPc									
D_{4h}	E	$2C_4$	C_2	$2C'_2$	$2C''_2$	i	$2S_4$	σ_h	$2\sigma_v$	$2\sigma_d$
$\Gamma_{unmoved}$	57	1	1	3	3	1	1	57	3	3
$\otimes\Gamma_{xyz}$	3	1	-1	-1	-1	-3	-1	1	1	1
Γ_{3N}	171	1	-1	-3	-3	-3	-1	57	3	3
$-\Gamma_{Trans}$	3	1	-1	-1	-1	-3	-1	1	1	1
$-\Gamma_{Rot}$	3	1	-1	-1	-1	3	1	-1	-1	-1
Γ_{Vib}	165	-1	1	-1	-1	-3	-1	57	3	3

Table III.4: Calculation of the representations of the vibrational modes of H_2Pc.

	H_2Pc							
D_{2h}	E	$C_2(z)$	$C_2(y)$	$C_2(x)$	i	$\sigma(xy)$	$\sigma(xz)$	$\sigma(yz)$
$\Gamma_{unmoved}$	58	0	2	4	0	58	4	2
$\otimes\Gamma_{xyz}$	3	-1	-1	-1	-3	1	1	1
Γ_{3N}	174	0	-2	-4	0	58	4	2
$-\Gamma_{Trans}$	3	-1	-1	-1	-3	1	1	1
$-\Gamma_{Rot}$	3	-1	-1	-1	3	-1	-1	-1
Γ_{Vib}	168	2	0	-2	0	58	4	2

Once Γ_{Vib} has been determined, the number of modes of each symmetry may be found by decomposing Γ_{Vib} into its irreducible representations. By applying the reduction formula to Γ_{Vib}, ZnPc is found to have 14 A_{1g}, 13 A_{2g}, 14 B_{1g}, 13 E_g, 6 A_{1u}, 8 A_{2u}, 7 B_{1u}, 7 B_{2u} and 28 E_u vibrational modes while H_2Pc has 29 A_g, 28 B_{1g}, 14 B_{2g}, 13 B_{3g}, 13 A_u, 15 B_{1u}, 28 B_{2u} and 28 B_{3u} vibrational modes.

A normal coordinate Q_k, as expressed in section III.4.II, may be described as a linear combination of mass weighted Cartesian coordinates q_i. For smaller molecules, the symmetry of the normal modes may be seen by inspection but for larger, more complicated molecules this would be very difficult. To find a set of normal coordinates that form the basis for an irreducible representation, sometimes called symmetry coordinates[29], a projection operator similar to that used to form Symmetry Adapted Linear Combinations of atomic orbitals may be used:

$$Q_i \propto P_i q_i = \frac{d_i}{h}\sum_R \chi_i^R R_j q_i \qquad \text{(III.93)}$$

This projection operator works in a similar way to the projection operator for SALC-AOs. The operator P_i for a particular irreducible representation i is applied to a weighted Cartesian coordinated q_i which projects out a linear combination of coordinates forming a symmetry adapted normal coordinate, Q_i.

III.6.IV Infra-red Selection Rules

As seen in section III.4.IV, the infrared intensity is dependent on the change in electric dipole moment μ with respect to the normal coordinate Q_i. In order for a transition to be allowed, the transition moment integral, $\boldsymbol{\mu}_{Q_i}$, that connects the

ground state vibrational wave function ψ''_{Q_i} to the excited state vibrational wave function ψ'_{Q_i} via the electric dipole operator $\hat{\mu}$ must be non-zero:

$$\boldsymbol{\mu}_{Q_i} = \int \psi'_{Q_i} \hat{\mu} \, \psi''_{Q_i} d\tau \neq 0 \tag{III.94}$$

As $\hat{\mu}$ consists of x, y and z components, equation III.90 may be rewritten as:

$$\boldsymbol{\mu}_{Q_i} = \int \psi'_{Q_i} \hat{\mu}_x \, \psi''_{Q_i} d\tau + \int \psi'_{Q_i} \hat{\mu}_y \, \psi''_{Q_i} d\tau + \int \psi'_{Q_i} \hat{\mu}_y \, \psi''_{Q_i} d\tau \neq 0 \tag{III.95}$$

Therefore, for a transition to be allowed, one or more of the three components of $\boldsymbol{\mu}_{Q_i}$ must be non-zero. Considering symmetry arguments, for an integral to be non-zero the direct product of the representations of the wave functions and dipole operators must contain the totally symmetric representation, for D_{4h} and D_{2h}, A_{1g} and A_g respectively:

$$\Gamma(\psi'_{Q_i}) \times \Gamma(\hat{\mu}_x) \times \Gamma(\psi''_{Q_i}) \supseteq A_{1g/g} \tag{III.96}$$

and/or

$$\Gamma(\psi'_{Q_i}) \times \Gamma(\hat{\mu}_y) \times \Gamma(\psi''_{Q_i}) \supseteq A_{1g/g} \tag{III.97}$$

and/or

$$\Gamma(\psi'_{Q_i}) \times \Gamma(\hat{\mu}_z) \times \Gamma(\psi''_{Q_i}) \supseteq A_{1g/g} \tag{III.98}$$

The Boolean operator $\supseteq$ meaning contains or is equal to is used to account for degenerate vibrational states, like those found in the D_{4h} molecule ZnPc. These equations may be simplified by considering transitions from the ground vibrational level only which has an irreducible representation equal to $A_{1g/g}$. As the product of $A_{1g/g}$ and any other representation leaves that representation unchanged, only the symmetries of $\hat{\mu}_x$ and ψ'_{Q_i}need to be considered.

$$\Gamma(\psi'_{Q_i}) \times \Gamma(\hat{\mu}_x) \supseteq A_{1g/g} \tag{III.99}$$

and/or

$$\Gamma(\psi'_{Q_i}) \times \Gamma(\hat{\mu}_y) \supseteq A_{1g/g} \tag{III.100}$$

and/or

$$\Gamma(\psi'_{Q_i}) \times \Gamma(\hat{\mu}_z) \supseteq A_{1g/g} \tag{III.101}$$

The dipole operator $\hat{\mu}$ is a vector quantity in some direction respective to the molecule. Generally, each of its components has an irreducible representation equal to the corresponding x, y and z irreducible representations: $\Gamma(\hat{\mu}_x) = \Gamma(x)$, $\Gamma(\hat{\mu}_y) = \Gamma(y)$ and $\Gamma(\hat{\mu}_z) = \Gamma(z)$.

When the product of two irreducible representations results in the totally symmetric representation, the two irreducible representations must have been identical. If the product of two degenerate representations, results in a sum containing the totally symmetric representation, these irreducible representations again must have been identical. This leads to the conclusion that for a normal mode Q_i to be IR active, its irreducible representation $\Gamma(\psi'_{Q_i})$ must be equal to one or more of the x, y and z irreducible representations:

$$\Gamma(\psi'_{Q_i}) = \Gamma(x) \tag{III.102}$$

and/or

$$\Gamma(\psi'_{Q_i}) = \Gamma(y) \tag{III.103}$$

and/or

$$\Gamma(\psi'_{Q_i}) = \Gamma(z) \tag{III.104}$$

By applying these selection rules to ZnPc and H_2Pc, ZnPc has a total of 36 IR active modes (8 A_{2u} and 28 E_u) and H_2Pc has a total of 71 IR active modes (15 B_{1u}, 28 B_{2u} and 28 B_{3u}).

III.6.V Raman Selection Rules

From section III.4.VI, the Raman scattering intensity is dependent on the change in polarizability α with respect to the normal coordinate Q_i. The magnitude of the scattering intensity is dependent on the strength of the external electric field, E. Similar to infra-red transitions, a transition moment integral P_{Q_i} describing a Raman transition between ψ''_{Q_i} and ψ'_{Q_i} may be written; and, as the external electric field is independent of the molecule, E may be removed from the integral. Again, for a Raman transition to be allowed the integral must be non-zero:

$$P_{Q_i} = \int \psi'_{Q_i} \alpha E \, \psi''_{Q_i} d\tau \propto \int \psi'_{Q_i} \alpha \, \psi''_{Q_i} d\tau \neq 0 \tag{III.105}$$

The polarizability α is a tensor comprising of a 3 x 3 matrix:

$$\alpha = \begin{bmatrix} \alpha_{xx} & \alpha_{xy} & \alpha_{xz} \\ \alpha_{xy} & \alpha_{yy} & \alpha_{yz} \\ \alpha_{xz} & \alpha_{yz} & \alpha_{zz} \end{bmatrix} \tag{III.106}$$

Equation III.105 may now be rewritten as a sum of the integrals containing the 9 components of α:

$$P_{Q_i} \propto \sum_{m,n} \int \psi'_{Q_i} \alpha_{mn} \, \psi''_{Q_i} d\tau \neq 0 \,, \tag{III.107}$$

where $m, n = x, y \; or \; z$. If any of the integrals of the nine integrals of P_{Q_i} is non-zero, then the normal mode Q_i will be Raman active.

The symmetry considerations with regard to Raman activity run similar to those for IR active modes. For P_{Q_i} to be non-zero, the direct product of the representations of the wave functions and polarizability tensor components must contain the totally symmetric representation:

$$\Gamma(\psi'_{Q_i}) \times \Gamma(\alpha_{mn}) \times \Gamma(\psi''_{Q_i}) \supseteq A_{1g/g}, \tag{III.108}$$

where $m, n = x, y \; or \; z$. Simplifications may be made when evaluating the Raman activity of a mode by considering transitions from the ground state only, where $\Gamma(\psi''_{Q_i}) = A_{1g/g}$:

$$\Gamma(\psi'_{Q_i}) \times \Gamma(\alpha_{mn}) \supseteq A_{1g/g} \tag{III.109}$$

A further simplification may be made as the tensor α is symmetric, only the 6 unique components of α (α_{xx}, α_{yy}, α_{zz}, α_{xy}, α_{xz} and α_{yz}) need to be taken into account. As stated previously, the sum of two identical irreducible representations results in the totally symmetric representation. This means that if the representation of a normal mode Q_i equals the representation of a polarizability tensor component, then Q_i is Raman active:

$$\Gamma(\psi'_{Q_i}) = \Gamma(\alpha_{mn}) \tag{III.110}$$

The symmetries of α_{mn} are equal to the symmetries of the binary products of x, y and z usually shown by the quadratic terms in the last column of the character tables.

If these Raman selection rules are applied, ZnPc is found to have 14 A_{1g}, 14 B_{1g}, 14 B_{2g} and 13 E_g Raman active modes and H_2Pc to have 29 A_g, 28 B_{1g}, 14 B_{2g} and 13 B_{3g} Raman active modes. Any remaining modes that are neither IR nor Raman active are considered to be inactive or optically silent. ZnPc has 13 A_{2g}, 6 A_{1u}, 7 B_{1u} and 7 B_{2u} inactive modes while H_2Pc has 13 A_u inactive modes.

III.6.VI Vibronic Selection Rules

Electronic states of polyatomic molecules are dependent not just on the electronic wavefunctions ψ_e but also on the vibrational wavefunctions ψ_v of the vibrational states within the electronic states. The coupling between electronic and vibrational states is called vibronic coupling. The probability of a transition

between two vibronic states induced by an oscillating electric field is proportional to the square of the transition moment integral:

$$_{e,n} = \int \psi'_e \psi'_v \psi'_s \, (\hat{\mu}_e + \hat{\mu}_n) \psi''_e \psi''_v \psi''_s \, d\tau \qquad \text{(III.111)}$$

ψ''_e, ψ''_v and ψ''_s are the wavefunctions of initial ground electronic, vibrational and spin states and ψ'_e, ψ'_v and ψ'_s are the wavefunctions of the final excited electronic, vibrational and spin states. $\hat{\mu}_e$ and $\hat{\mu}_n$ are the electric and nuclear dipole moment operators connecting the states.

Ignoring the weak nuclear dipole moment contributions[44] and dividing the electronic transition moment integral into its different components, $_e$ may be written as:

$$_e = \int \psi'_v \psi''_v \, d\tau \int \psi'_e \, \hat{\mu}_e \psi''_e \, d\tau \int \psi'_s \psi''_s \, d\tau \qquad \text{(III.112)}$$

These three integrals describe the three selection rules for electronic transitions and for a transition to be fully allowed all three integrals must be non-zero. The first integral is the Franck-Condon factor which describes the overlap between the vibrational states in the ground and excited electronic states. It is the quantum mechanical description of the Franck-Condon principle. The second integral describes the Orbital Selection rules and is sometimes called LaPorte's rule. For molecule with a centre of symmetry, a transition is fully allowed if there is a change in inversion symmetry i.e. $u \rightarrow g$ and $g \rightarrow u$ are allowed while $u \nrightarrow u$ and $g \nrightarrow g$ are not allowed. The third integral is the Spin Selection rule. For a transition to be spin allowed there must be no change in spin during transition i.e. only singlet to singlet, triplet to triplet etc. transitions are fully allowed.

Considering only spin allowed transitions, equation III.107 may be written as:

$$_{el} = \int \psi'_e \, \psi'_v \hat{\mu}_e \psi''_e \psi''_v \, d\tau \qquad \text{(III.113)}$$

Applying symmetry arguments to this integral, to be non-zero the direct product of the symmetry representations must equal or contain the totally symmetric irreducible representation $A_{1g/g}$:

$$\Gamma(\psi'_e) \times \Gamma(\psi'_v) \times \Gamma(\hat{\mu}_e) \times \Gamma(\psi''_e) \times \Gamma(\psi''_v) \supseteq A_{1g/g} \qquad \text{(III.114)}$$

Closed shell molecules with filled orbitals fulfilling the Pauli exclusion principle have ground electronic wavefunctions transforming as the totally symmetric

irreducible representation of the corresponding group. Similar to infra-red transitions, the direct product may be simplified by considering transitions from the ground vibrational level only which has an irreducible representation equal to $A_{1g/g}$.

$$\Gamma(\psi_e') \times \Gamma(\psi_v') \times \Gamma(\hat{\mu}_e) \supseteq A_{1g/g} \quad \text{(III.115)}$$

Again similarly to IR transitions, the electric dipole operator $\hat{\mu}_e$ consists of x, y and z components which transform as the x, y and z irreducible representations. If the symmetry and geometry of the excited electronic state is known, the vibronic structure of the UV-Vis absorption or excitation spectra may be predicted.

Group theory may be applied to luminescent processes, relaxation from an excited state to the ground state resulting in the emission of a photon. A direct product describing the selection rules for fluorescence (luminescent transitions involving no change in spin) similar to the one for absorption may be written, with the initial and final states reversed:

$$\Gamma(\psi_e'') \times \Gamma(\psi_v'') \times \Gamma(\hat{\mu}_e) \times \Gamma(\psi_e') \times \Gamma(\psi_v') \supseteq A_{1g/g} \quad \text{(III.116)}$$

If transitions from the lowest vibrational state in the excited state, $\Gamma(\psi_v') = A_{1g/g}$, to the ground electronic state, $\Gamma(\psi_e'')$, again assuming a closed shell electronic ground state with an $A_{1g/g}$ representation, equation III.112 may be simplified to:

$$\Gamma(\psi_v'') \times \Gamma(\hat{\mu}_e) \times \Gamma(\psi_e') \supseteq A_{1g/g} \quad \text{(III.117)}$$

The same selection rules may be used for phosphorescence where there is a change in spin during the transition.

The visible fluorescence for ZnPc involves a transition from the lowest vibrational state of a degenerate excited electronic state with E_u symmetry to the ground vibronic states. Inserting $\Gamma(\psi_e') = E_u$ and the irreducible representations for the x, y and z dipole operators, the following results are found:

$$\Gamma(\psi_v'') \times A_{2u} \times E_u = \Gamma(\psi_v'') \times E_g \supseteq A_{1g} \quad \text{(III.118)}$$

$$\Gamma(\psi_v'') \times E_u \times E_u = \Gamma(\psi_v'') \times \left(A_{1g} + A_{2g} + B_{1g} + B_{2g}\right) \supseteq A_{1g} \quad \text{(III.119)}$$

The fluorescence of ZnPc is predicted to relax to vibrational states with A_{1g}, A_{2g}, B_{1g}, B_{2g} and E_g symmetry. These states include the Raman active modes, A_{1g}, B_{1g}, B_{2g} and E_g, and the inactive A_{2g} modes.

Visible absorption in H_2Pc occurs between the ground state to two non-degenerate states with B_{1u} and B_{2u} symmetry, or B_{3u} and B_{2u} states when the axes have been re-orientated to match those of ZnPc. In solids and liquids, fluorescence is only seen from the lower energy B_{3u} state. Considering emission from this state only and the x, y and z irreducible representations, the following direct products are found:

$$\Gamma(\psi_v'') \times B_{1u} \times B_{3u} = \Gamma(\psi_v'') \times B_{2g} \supseteq A_g \quad \text{(III.120)}$$

$$\Gamma(\psi_v'') \times B_{2u} \times B_{3u} = \Gamma(\psi_v'') \times B_{1g} \supseteq A_g \quad \text{(III.121)}$$

$$\Gamma(\psi_v'') \times B_{3u} \times B_{3u} = \Gamma(\psi_v'') \times A_g \supseteq A_g \quad \text{(III.122)}$$

The fluorescence from the B_{3u} electronic state of H_2Pc is predicted to relax to vibronic states with A_g, B_{1g} and B_{2g} symmetry. Like ZnPc, these modes are similar to the Raman active modes A_g, B_{1g}, B_{2g} and B_{3g} except B_{3g} modes are predicted to be vibronically forbidden. By applying symmetric arguments to transitions from the B_{2u} excited electronic state, relaxation to the A_g, B_{1g} and B_{3g} vibronic states are predicted to be allowed for gas phase H_2Pc.

III.7 Calculation Procedure

The following section will describe the procedure used to determine the various molecular properties calculated in this work. An outline of how the quantum mechanical software package Gaussian 03 implements the theoretical principles described in this chapter will be given. The order in which the calculations were conducted was as follows:

- The geometries of the molecules were optimised
- The force constant matrix and vibrational frequencies were determined
- The infrared absorption and Raman scattering intensities were calculated
- The vibrational frequencies, IR and Raman intensities of the isotopic analogues of the molecules were determined
- The energy and oscillator strengths of the electronic transitions were determined using TD-DFT

III.7.I Geometry Optimisation

As molecules vibrate about their equilibrium structure, the first step in calculating the properties of a real molecule is to find equilibrium structure of the molecule we are interested in. Geometry optimisation attempts to find an equilibrium structure

by locating a minimum on the potential energy surface (PES) of the molecules atomic coordinates. A minimum is found by calculating the first derivative of the energy with respect to the atomic coordinates, also known as the gradient. When the gradient is equal to zero a stationary point is found where the forces are also equal to zero. A stationary point may not necessarily be the minimum we are looking for but may be a saddle point on the PES. During an optimisation procedure, the energy and gradient are calculated at each point and are used to determine how far and in what direction to move the atoms in order to find a minimum. An approximate value of the second derivatives of the energy is also computed creating a force constant or Hessian matrix. This Hessian matrix determines the curvature of the PES at a point and is used to help determine the next step to be taken.

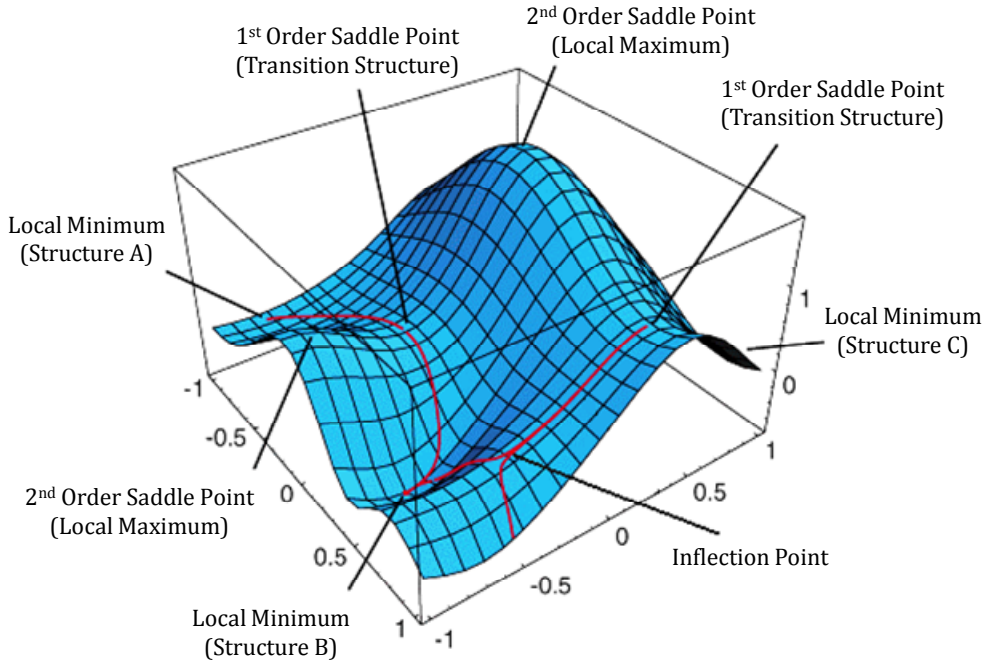

Figure III.5: Potential Energy Surface (PES) showing stationary points and reaction coordinates between three molecular structures. Image © H. Bernhard Schlegel, Wayne State University.

When an energy minimised structure is found the optimisation is said to have converged. The optimisation algorithm and convergence procedure used by Gaussian 03 is the Berny algorithm and is based on an algorithm developed by H. Bernhard 'Berny' Schlegel[45]. The four convergence criteria used in the Berny algorithm are that the maximum force and root-mean-square of the forces must be close to zero and that the maximum displacement and root-mean-square of the displacements for the next step must be small. The cut off threshold points for these criteria are set by the user for each optimisation. Tight convergence criteria

were used throughout this work with the max and RMS energy thresholds of 1.5 x 10^{-5} and 1.0 x 10^{-5} au respectively while the max and RMS displacement thresholds were of 6.0 x 10^{-5} and 4.0 x 10^{-5} au respectively. More relaxed convergence criteria (i.e. larger energy and displacement criteria) may be needed for molecules with shallow minimum potential energy wells.

III.7.II Vibrational Frequencies

Once a converged geometry is found, the vibrational frequencies may be determined using the GF method of E. B. Wilson[29] and implemented in Gaussian 03 using the method described by Ochterski in a white paper released by Gaussian Inc.[46]. The first calculation made in determining the vibrational frequencies is to calculate the full Hessian matrix of the second derivatives, H_{cart}, with respect to the atomic Cartesian coordinates, x. As this is second order term of the Taylor series described in Section III.4.III, the energy and first order terms (determined in during geometry optimisation) must both be equal to zero. It is for this reason that frequency calculations are only meaningful if they are calculated using a geometry optimised to a stationary point and that they are calculated at the same level of theory used in the geometry optimisation procedure. Once the second derivatives with respect to Cartesian coordinates are found, this Hessian is mass weighted, transforming it into a matrix, H_{MWC}, of the second derivatives with respect to mass weighted coordinates or normal modes, q.

$$H_{cart} = \left(\frac{\partial^2 V}{\partial x_i \, \partial x_j}\right)_0 \Rightarrow H_{MWC} = \frac{H_{cart}}{\sqrt{m_i m_j}} = \left(\frac{\partial^2 V}{\partial q_i \, \partial q_j}\right)_0 \qquad \text{(III.123)}$$

In order to remove the lower energy translational and rotational frequencies, the principal axis of inertia is found and a 3 x 3 moment of inertia tensor is determined. This tensor is used to generate a transformation matrix, D, which transforms the mass weighted Hessian into internal coordinates, H_{int}, removing the translational and rotational modes. This Hessian is diagonalised yielding the eigenvalues corresponding to the frequencies and the eigenvectors corresponding to the normal modes. Transforming H_{int} using the eigenvector matrix L yields the diagonal matrix Λ of the eigenvalues. The individual eigenvalues λ are equal to $4\pi^2\nu^2$ and each of the vibrational frequencies i are calculated in cm^{-1} using the equation:

$$\tilde{\nu}_i = \sqrt{\frac{\lambda_i}{4\pi^2 c^2}} \qquad \text{(III.124)}$$

The reduced mass, force constants and normalised Cartesian displacements of each normal mode are also calculated. As the calculation of H_{cart} matrix is the most time consuming procedure in the calculation of the molecular vibration frequencies, the values of this matrix are stored in a 'checkpoint' file. With the H_{cart} stored, frequencies of other isotope analogues may be quickly and easily calculated without having to calculate the force constant matrix again.

Some of the eigenvalues calculated may be negative and after determining their frequency in cm^{-1} using the absolute value of λ, Gaussian flags these as negative frequencies. These negative or imaginary frequencies show that the starting geometry was not optimised to a local minimum but was instead optimised to a saddle point on the PES. One imaginary frequency indicates a first order saddle point was found and that the geometry was optimised to a transition state (which may have been the goal of the calculation). More than one imaginary frequency indicates higher order saddle points and the geometry may have to be re-optimised along the direction of the Cartesian displacement of the imaginary normal mode with the highest absolute frequency.

III.7.III IR and Raman Intensities

In order to calculate the IR and Raman intensities described in sections III.4.V and III.4.VI, the dipole moment and polarizability derivatives must be calculated. To determine these derivatives, the potential energy gradients, g, in the presence of an electric field, F, are calculated[47]. The first derivatives of g are equivalent to the derivatives of the dipole moment, , with respect to the molecular Cartesian coordinates, x, while the second derivatives are equivalent to the derivatives of the polarizability, α.

$$\frac{\partial}{\partial x_i} = -\frac{\partial}{\partial x_i}\frac{\partial E}{\partial F} = -\frac{\partial}{\partial F}\frac{\partial E}{\partial x} = -\frac{\partial g_i}{\partial F} \qquad \text{(III.125)}$$

$$\frac{\partial \alpha}{\partial x_i} = -\frac{\partial}{\partial x_i}\frac{\partial}{\partial F} = -\frac{\partial}{\partial F}\frac{\partial}{\partial x_i} = -\frac{\partial^2 g_i}{\partial F^2} \qquad \text{(III.126)}$$

As the polarizability derivatives involve the calculation of the second derivatives of the gradients, Raman intensities are computationally more demanding than IR intensities which involve first derivatives. To transform the dipole moment and polarizability derivatives with respect to Cartesian coordinate into derivatives with respect to the normal modes, the following expressions are used[48],

$$\frac{d}{dQ_k} = \sum_i \frac{\partial x_i}{\partial Q_k}\frac{\partial}{\partial x_i} \equiv \sum_i M_{ik}L_{ik}\frac{\partial \alpha}{\partial x_i} \quad \text{(III.127)}$$

$$\frac{d\alpha}{dQ_k} = \sum_i \frac{\partial x_i}{\partial Q_k}\frac{\partial \alpha}{\partial x_i} \equiv \sum_i M_{ik}L_{ik}\frac{\partial \alpha}{\partial x_i} \quad \text{(III.128)}$$

where $\partial x_i/\partial Q_k$ are the mass weighted Cartesian displacements determined during the frequency calculations and are equivalent to the eigenvector matrix L.

III.7.IV Electronic Excitation Energies

Using the expressions developed from linear response time-dependent DFT, the excitation energies and oscillator strengths of molecules can in principle be calculated exactly. In practice, the accuracy of these calculations depends on the quality of the exchange-correlation functional and the basis sets used to describe the KS orbitals. Linear response TDDFT is unsuitable for the treatment of certain excitations including those involving strong external potentials (large perturbation of the ground state electronic structure), charge transfer transitions (system cannot be assumed to be non-interacting) and Rydberg states (ground state exchange-correlation functionals do not predict the properties of asymptotes correctly).

TD-DFT is implemented in Gaussian 03 using the Casida formalism[49]. In practice, the DFT functional and basis set are selected as well as the number of excited states and whether singlet and/or triplet states are desired. The ground state geometry of the molecular system of interest, usually one that has been optimised previously using DFT or another *ab initio* method, is also inputted or read from a checkpoint file. Previous TD-DFT calculations using the same basis set may be used as a starting point for further calculations (e.g. more excited states, different exchange-correlation functionals, etc.). Once the excited state has converged, Gaussian outputs, among other results, the excitation energies, oscillator strengths (f), transition dipole moments and symmetry assignments of the excited states. The coefficients of singly excited orbital configurations contributing to the excited state wavefunctions are also given, analogous to those found using *ab initio* CI methods. Due to the change in spin during a triplet transition, the orbital coefficients are normalised to 1 while the singlet orbital coefficients are usually normalised to 0.5. As the state symmetries are not calculated directly, the direct product of the symmetry of the singly excited orbital configurations is used to assign the states.

III.8 References

(1) Gaussian 03, Revision E.01, M. J. Frisch, G. W. Trucks, H. B. Schlegel, G. E. Scuseria, M. A. Robb, J. R. Cheeseman, J. A. Montgomery, Jr., T. Vreven, K. N. Kudin, J. C. Burant, J. M. Millam, S. S. Iyengar, J. Tomasi, V. Barone, B. Mennucci, M. Cossi, G. Scalmani, N. Rega, G. A. Petersson, H. Nakatsuji, M. Hada, M. Ehara, K. Toyota, R. Fukuda, J. Hasegawa, M. Ishida, T. Nakajima, Y. Honda, O. Kitao, H. Nakai, M. Klene, X. Li, J. E. Knox, H. P. Hratchian, J. B. Cross, V. Bakken, C. Adamo, J. Jaramillo, R. Gomperts, R. E. Stratmann, O. Yazyev, A. J. Austin, R. Cammi, C. Pomelli, J. W. Ochterski, P. Y. Ayala, K. Morokuma, G. A. Voth, P. Salvador, J. J. Dannenberg, V. G. Zakrzewski, S. Dapprich, A. D. Daniels, M. C. Strain, O. Farkas, D. K. Malick, A. D. Rabuck, K. Raghavachari, J. B. Foresman, J. V. Ortiz, Q. Cui, A. G. Baboul, S. Clifford, J. Cioslowski, B. B. Stefanov, G. Liu, A. Liashenko, P. Piskorz, I. Komaromi, R. L. Martin, D. J. Fox, T. Keith, M. A. Al-Laham, C. Y. Peng, A. Nanayakkara, M. Challacombe, P. M. W. Gill, B. Johnson, W. Chen, M. W. Wong, C. Gonzalez, and J. A. Pople, Gaussian, Inc., Wallingford CT, 2004.

(2) Schrödinger, E. *Annalen der Physik* **1926**, 384, 361.

(3) Born, M.; Oppenheimer, R. *Annalen der Physik* **1927**, 389, 457.

(4) Frisch, J. M.; John, A. P.; Binkley, J. S. *The Journal of Chemical Physics* **1984**, 80, 3265.

(5) Eberhard, B. *Journal of Physics: Condensed Matter* **2001**, 13, 7477.

(6) Hohenberg, P.; Kohn, W. *Physical Review B* **1964**, 136, B864.

(7) Kohn, W.; Sham, L. J. *Physical Review* **1965**, 140, 1133.

(8) Becke, A. D. *The Journal of Chemical Physics* **1993**, 98, 5648.

(9) Becke, A. D. *Physical Review A* **1988**, 38, 3098.

(10) Perdew, J. P. In *Electronic Structure of Solids*; Ziesche, P., Eschrig, H., Eds.; Akademie Verlag: Berlin, **1991**.

(11) Stephens, P. J.; Devlin, F. J.; Chabalowski, C. F.; Frisch, M. J. *Journal of Physical Chemistry* **1994**, 98, 11623.

(12) Stephens, P. J.; Devlin, F. J.; Ashvar, C. S.; Chabalowski, C. F.; Frisch, M. J. *Faraday Discussions* **1994**, 103.

(13) Lee, C. T.; Yang, W. T.; Parr, R. G. *Physical Review B* **1988**, 37, 785.

(14) Vosko, S. H.; Wilk, L.; Nusair, N. *Canadian Journal of Physics* **1980**, 58, 1200.

(15) Carter, R. L. Molecular *Symmetry and Group Theory*; John Wiley & Sons, Inc.: New York, **1998**.

(16) Harris, D. C.; Bertolucci, M. D. *Symmetry and spectroscopy: an introduction to vibrational and electronic spectroscopy*; Dover Publications, Inc.: New York, 1989.

(17) Wong, M. W. *Chemical Physics Letters* **1996**, 256, 391.

(18) Scott, A. P.; Radom, L. *The Journal of Physical Chemistry* **1996**, 100, 16502.

(19) Merrick, J. P.; Moran, D.; Radom, L. *The Journal of Physical Chemistry A* **2007**, 111, 11683.

(20) Halls, M. D.; Velkovski, J.; Schlegel, H. B. *Theoretical Chemistry Accounts* **2001**, 105, 413.

(21) Baker, J.; Jarzecki, A. A.; Pulay, P. *The Journal of Physical Chemistry A* **1998**, 102, 1412.

(22) Pulay, P.; Fogarasi, G.; Pongor, G.; Boggs, J. E.; Vargha, A. *Journal of the American Chemical Society* **1983**, 105, 7037.

(23) Rauhut, G.; Pulay, P. *The Journal of Physical Chemistry* **1995**, 99, 3093.

(24) Borowski, P.; Drzewiecka, A.; Fernández-Gómez, M.; Fernández-Liencres, M. P.; Ruiz, T. P. *Chemical Physics Letters* **2008**, 465, 290.

(25) Borowski, P.; Fernández-Gómez, M.; Fernández-Liencres, M.-P.; Ruiz, T. P. *Chemical Physics Letters* **2007**, 446, 191.
(26) Spanget-Larsen, J. *Chemical Physics* **1999**, 240, 51.
(27) Martin, J. M. L.; El-Yazal, J.; Francois, J.-P. *The Journal of Physical Chemistry* **1996**, 100, 15358.
(28) Dunning, T. H. *Journal of Chemical Physics* **1989**, 90, 1007.
(29) Wilson Jr., E. B.; Decius, J. C.; Cross, P. C. *Molecular Vibrations*; McGraw-Hill: New York, **1955**.
(30) Sosa, C.; Schlegel, H. B. *Journal of Chemical Physics* **1987**, 86, 6937.
(31) Porezag, D.; Pederson, M. R. *Physical Review B* **1996**, 54, 7830.
(32) Swanton, D. J.; Bacskay, G. B.; Hush, N. S. *Journal of Chemical Physics* **1986**, 84, 5715.
(33) Polavarapu, P. L. *Journal of Physical Chemistry* **1990**, 94, 8106.
(34) Long, D. A. *The Raman Effect : a unified treatment of the theory of Raman scattering by molecules*; John Wiley & Sons Ltd: Chichester, **2002**.
(35) Michalska, D.; Wysokinski, R. *Chemical Physics Letters* **2005**, 403, 211.
(36) Runge, E.; Gross, E. K. U. *Physical Review Letters* **1984**, 52, 997.
(37) Gross, E. K. U.; Kohn, W. Time-Dependent Density-Functional Theory. In *Advances in Quantum Chemistry*; Per-Olov, L., Ed.; Academic Press, **1990**; Vol. Volume 21; pp 255.
(38) Casida, M. E. Time-Dependent Density Functional Response Theory of Molecular Systems: Theory, Computational Methods, and Functionals. In *Recent Development and Applications of Modern Density Functional Theory*; Seminario, J. M., Ed.; Elsevier: Amsterdam, 1996; pp 391.
(39) Gross, E. K. U.; Kohn, W. *Physical Review Letters* **1985**, 55, 2850.
(40) Petersilka, M.; Gossmann, U. J.; Gross, E. K. U. *Physical Review Letters* **1996**, 76, 1212.
(41) Bauernschmitt, R.; Ahlrichs, R. *Chemical Physics Letters* **1996**, 256, 454.
(42) Casida, M. E.; Jamorski, C.; Casida, K. C.; Salahub, D. R. *The Journal of Chemical Physics* **1998**, 108, 4439.
(43) Eyring, H.; Walter, J.; Kimball, G. E. *Quantum Chemistry*; John Wiley And Sons Inc.: New York and London, **1944**.
(44) The transition moment integral including electronic and nuclear contributions may be written as:

$$_{\mathrm{e,n}} = \int \psi'_e\, \psi'_v \psi'_s (\hat{\mu}_e + \hat{\mu}_n) \psi''_e \psi''_v \psi''_s \, d\tau$$

This integral may be separated into both electronic and nuclear dipole parts and further divided into the integrals of electronic, vibrational and spin wavefunctions, ψ_e, ψ_v and ψ_s.

$$_{\mathrm{e,n}} = \int \psi'_e\, \psi'_v \psi'_s \hat{\mu}_e \psi''_e \psi''_v \psi''_s \, d\tau + \int \psi'_e\, \psi'_v \psi'_s \hat{\mu}_n \psi''_e \psi''_v \psi''_s \, d\tau$$

$$_{\mathrm{e,n}} = \int \psi'_v \psi''_v \, d\tau \int \psi'_e\, \hat{\mu}_e \psi''_e \, d\tau \int \psi'_s \psi''_s \, d\tau + \int \psi'_e\, \psi''_e \, d\tau \int \psi'_v \hat{\mu}_n \psi''_v \, d\tau \int \psi'_s \psi''_s \, d\tau$$

As different electronic wavefunctions are orthogonal, $\int \psi'_e\, \psi''_e \, d\tau = 0$, the nuclear dipole equals zero. $\int \psi'_v \psi''_v \, d\tau$ does not necessarily equal zero because ψ'_v and ψ''_v are coupled to different electronic states and may or may not be orthogonal.
(45) Schlegel, H. B. *Journal of Computational Chemistry* **1982**, 3, 214.
(46) Ochterski, J. W. *Vibrational Analysis in Gaussian*; Gaussian Inc: Pittsburg, PA, **1999**.
(47) Komornicki, A.; Mciver, J. W. *Journal of Chemical Physics* **1979**, 70, 2014.

(48) Hess, B. A.; Schaad, L. J.; Carsky, P.; Zahradnik, R. *Chemical Reviews* **1986**, 86, 709.
(49) Casida, M. E. Time-dependent density-functional response theory for molecules. In *Recent Advances in Density Functional Methods, Part I*; Chong, D. P., Ed.; World Scientific: Singapore, **1995**; Vol. 1; pp 155.

Chapter IV: Infra-red and Raman Spectroscopy of Free-Base and Zinc Phthalocyanines

IV.1 Introduction

This chapter will present the results from a study of the vibrational spectroscopy of free-base and zinc phthalocyanine. The matrix infra-red absorption spectra of H_2Pc and its isotopomers D_2Pc and HDPc isolated in inert gas solids were recorded along with the spectra of the metallo-phthalcyanine, ZnPc, for comparison. The Raman spectra of H_2Pc, D_2Pc and ZnPc in KBr disks were also recorded. DFT calculations using the B3LYP/6-311++G(2d,2p) method were performed in order to assign the vibrational modes observed in both the matrix-isolated infra-red absorption and KBr Raman spectra.

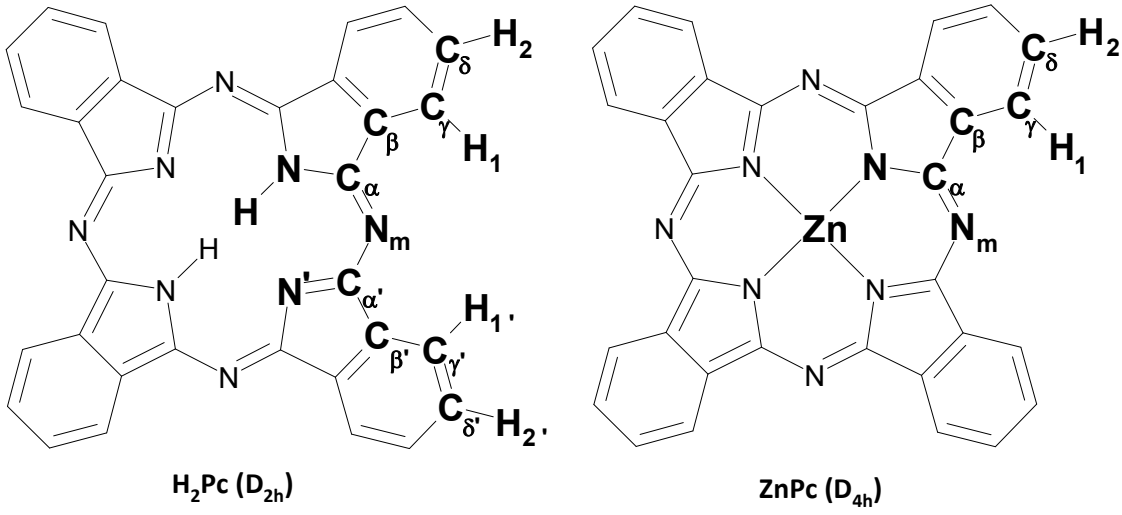

Figure IV.1: The structures of free-base and zinc phthalocyanine determined by large basis [311++G(2d,2p)] set DFT geometry optimisation using the B3LYP functional. Both structures were found to be planar yielding molecular structures with D_{2h} and D_{4h} symmetries for H_2Pc and ZnPc respectively. The atom labelling used in these calculations is indicated and the values determined are provided in Table IV.5.

The experimental results for matrix IR and KBr Raman spectra recorded for ZnPc, H_2Pc and of the effects of deuteration are presented in Parts IV.2.I, IV.2.II and IV.2.III. Part IV.3 gives an overview of the DFT data including the optimised geometries and the vibrational modes calculated for ZnPc and H_2Pc. A discussion of

both the experimental and computational data obtained for ZnPc, H_2Pc and its isotopomers D_2Pc and HDPc is given in Part IV.4. This discussion is divided into three parts dealing with (IV.4.I) IR spectra, (IV.4.II) Raman spectra and (IV.4.III) isotopic shifts. The final part summarises the main conclusions made.

IV.2 Experimental Results

IV.2.I ZnPc

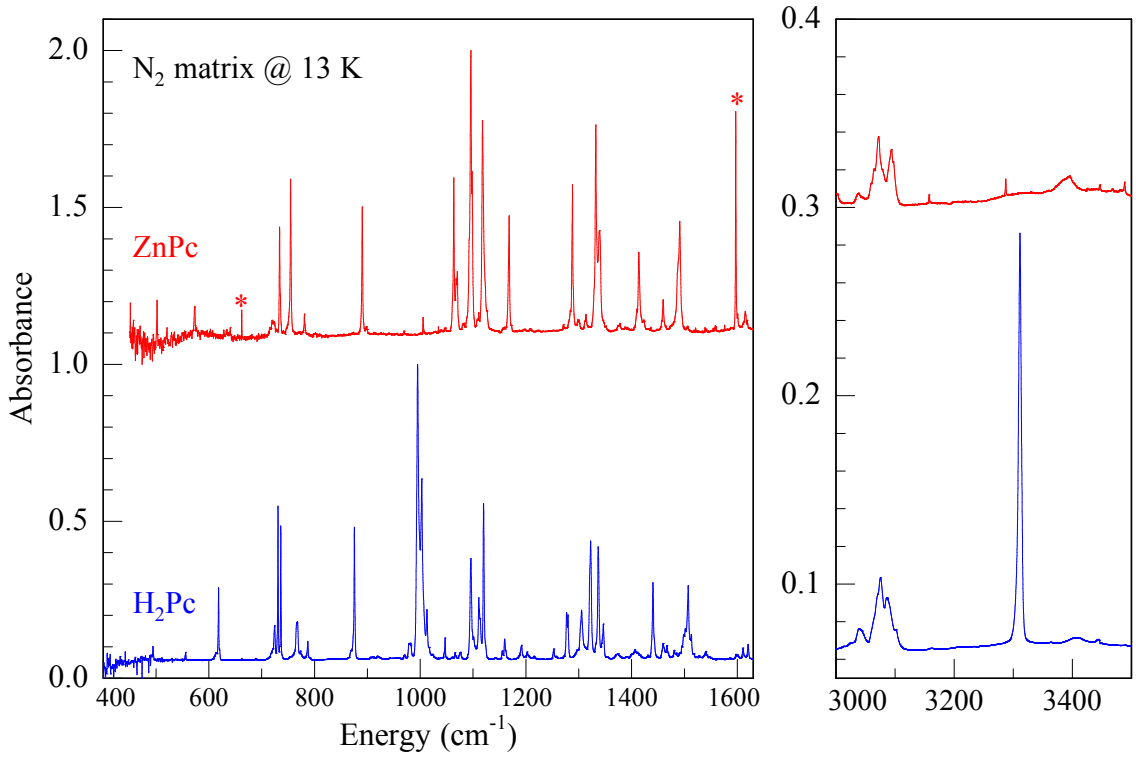

Figure IV.2: Infrared spectra of ZnPc and H_2Pc molecules isolated in a N_2 matrix at 13 K in the two spectral regions with the strongest absorptions. The asterisks (*) denote small amounts of the matrix-isolated impurities carbon dioxide and water.

An infrared absorption spectrum recorded for ZnPc isolated in a N_2 matrix is shown in the upper panel of Figure IV.2. The most intense infrared active bands of this molecule are situated between 400 and 1650 cm^{-1}. Other less intense bands, arising from C-H stretching modes are located, as shown in the panel on the right, around 3100 cm^{-1}. Weak bands observed between 1650 and 3000 cm^{-1}, are expected to be combination modes and were not investigated. The most intense vibrational bands of ZnPc in the mid-IR are situated at 1095.9, 1117.8 and 1332.2 cm^{-1} in N_2 matrices. Weaker bands in the C-H stretching mode region are, as shown in the right hand panel, situated at 3038.3, 3072.3 and 3093.5 cm^{-1}. The spectra of ZnPc in other matrices (Ar, Kr and Xe) are similar to the spectrum

shown for N_2 in Figure IV.2, but the bands shift slightly to lower energies as exemplified by the absorption spectra in Figure IV.3.

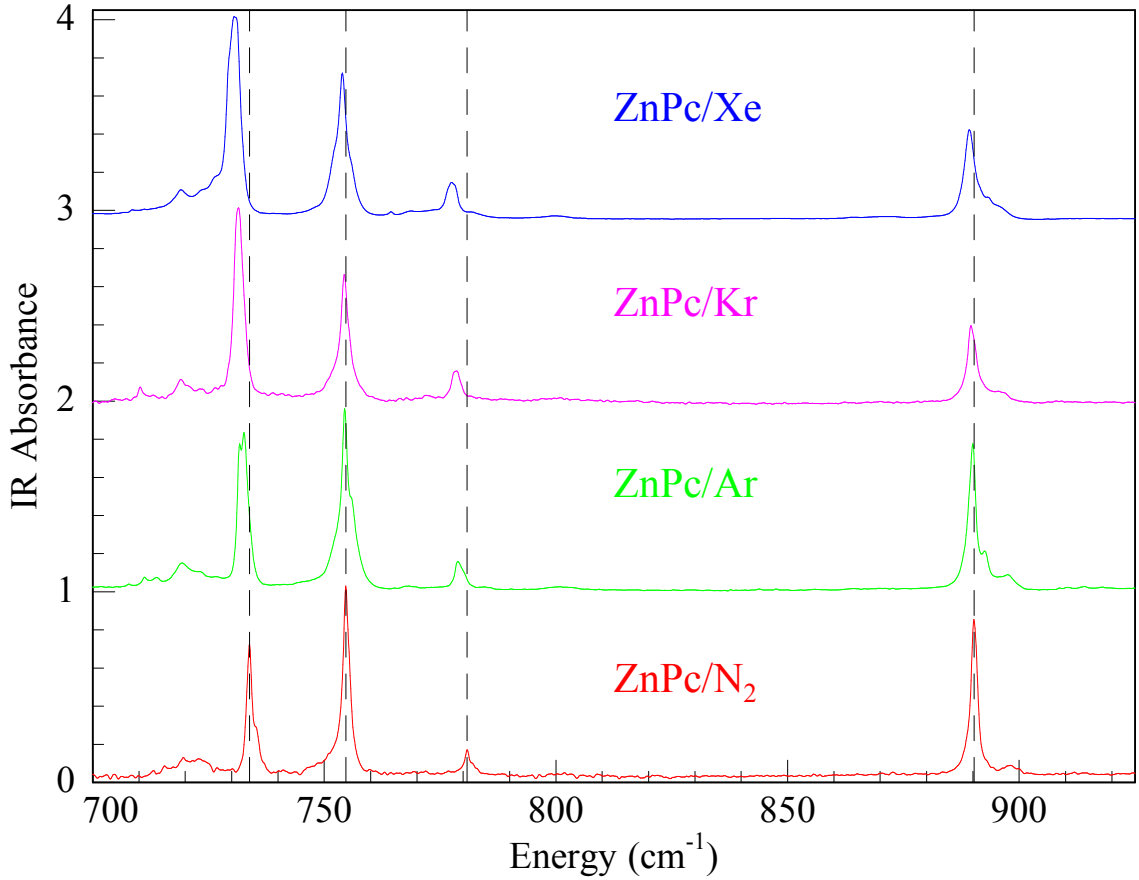

Figure IV.3: FT-IR absorption spectra of ZnPc in N_2, Ar, Kr and Xe solids in the 700 – 925 cm^{-1} spectral region. The vertical dash lines indicate the absorption bands in N_2 and help illustrate the shift to lower energies in the other matrices.

The observed vibrational bands are in good agreement with the KBr disc IR spectrum published by Tackley *et al.*[1] although the bands in cryogenic matrices are better resolved and shifted to the blue. The frequencies of the observed fundamental modes in all matrices studied are given in Table IV.1 along with KBr data recorded in the present work. Very small shifts of vibrational frequencies are noticeable from one host gas to another. In cryogenic matrices, all the bands are quite narrow, except in the CH stretch region. The structure in this region could be due to site effects, since the C-H bonds of the aryl group are located on the outer part of the molecule. As a result, these stretching modes are most sensitive to the trapping environment as revealed by a pronounced KBr – matrix shift in Table IV.1.

Table IV.1: Infra-red frequencies (in cm^{-1}) observed for ZnPc trapped in different solids. The symmetries provided were obtained from DFT calculations. The corresponding theoretical frequencies have been scaled by a factor of 0.98 below 2000 cm^{-1}, while a value of 0.96 has been used for the C-H modes in the vicinity of 3000 cm^{-1}. The symmetry labels given for the molecular vibrations of ZnPc utilise the D_{4h} group. The experimental values shown in bold are the most intense bands. The values indicated by an asterisk are possible combination bands, while those indicated "sh" are unresolved shoulders on more intense bands.

KBr	Ar	Kr	Xe	N_2	DFT (scaled)	DFT (unscaled)	Sym
435	-	-	430.0	-	437.3	446.2	A_{2u}
499	502.2	-	501.2	502.0	501.4	511.4	E_u
571	573.4	573.8	572.0	573.4	574.1	585.8	E_u
635	637.3	-	640.4	640.7	639.8	652.8	E_u
727	**732.7**	**731.5**	**730.8**	**733.9**	734.0	749.0	A_{2u}
752	**754.4**	**754.4**	**754.0**	**754.7**	752.6	768.0	E_u
782	778.8	778.2	777.7	780.8	781.1	797.0	A_{2u}
887	**890.1**	**889.6**	**889.4**	**890.2**	887.9	906.0	E_u
1004	1004.7	1004.5	1003.7	1005.5	1009.4	1030.0	E_u
1060	**1063.1** 1069.3	**1062.4** 1068.4	**1061.4** 1068.6	**1063.6** 1070.2	1062.8	1084.5	E_u
1088	**1094.8**	**1094.5**	**1093.6**	**1095.9**	1089.0	1111.1	E_u
1116	**1117.4**	**1116.8**	**1114.5**	**1117.8**	1115.5	1138.2	E_u
1164	**1167.7**	**1167.3**	**1165.7**	**1168.2**	1166.2	1190.0	E_u
1**285**	**1287.1** 1296.0	**1287.1** 1295.0	**1285.8** 1292.1	**1288.1** 1297.8	1294.0	1320.4	E_u
-	1310.7	1307.8	1306.6	1313.5	1316.9	1343.8	E_u
1331	**1331.8** 1338.0	**1331.5** 1337.6	**1331.8** 1336.8	**1332.2** 1339.4	1332.4	1359.6	E_u
1409	1412.2	1411.7	1410.5	1413.5	1407.9	1436.6	E_u
1454	1459.3	1458.1	1458.4	1459.7	1461.2	1491.0	E_u
1482	**1491.0**	**1490.4**	**1488.9**	**1491.0**	1481.4	1511.6	E_u
1607	-	-	1613.9	1615.1	1608.5	1641.3	E_u
3020*	3035.1*	3034.8*	3031.1*	3038.3*	-	-	
-	3061.5sh	3059.1sh	3054.0sh	3064.0sh	3061.3	3174.0	E_u
3045	3069.2	3067.6	3061.1	3072.3	3074.4	3187.6	E_u
-	3093.0	3092.1	3086.7	3093.5	3091.0	3204.8	E_u

Raman spectra of ZnPc were recorded only in KBr pellets at room temperature. The 100 -1700 cm^{-1} range is shown in the upper panel of Figure IV.4. The most intense bands are situated at 676.5, 1338.3 and 1506.8 cm^{-1}. As expected, the results we obtained with 532 nm excitation, compare well with the spectrum recorded by Tackley[2] who employed an excitation wavelength of 514 nm. Beyond 1700 cm^{-1}, the Raman spectrum exhibits several bands, consisting mostly of overtones or combinations bands, so that the C-H stretching modes are difficult to identify clearly. On the other hand, our results reveal only four very low frequency (below 400 cm^{-1}) modes. The frequencies of the recorded Raman bands are collected in Table IV.2.

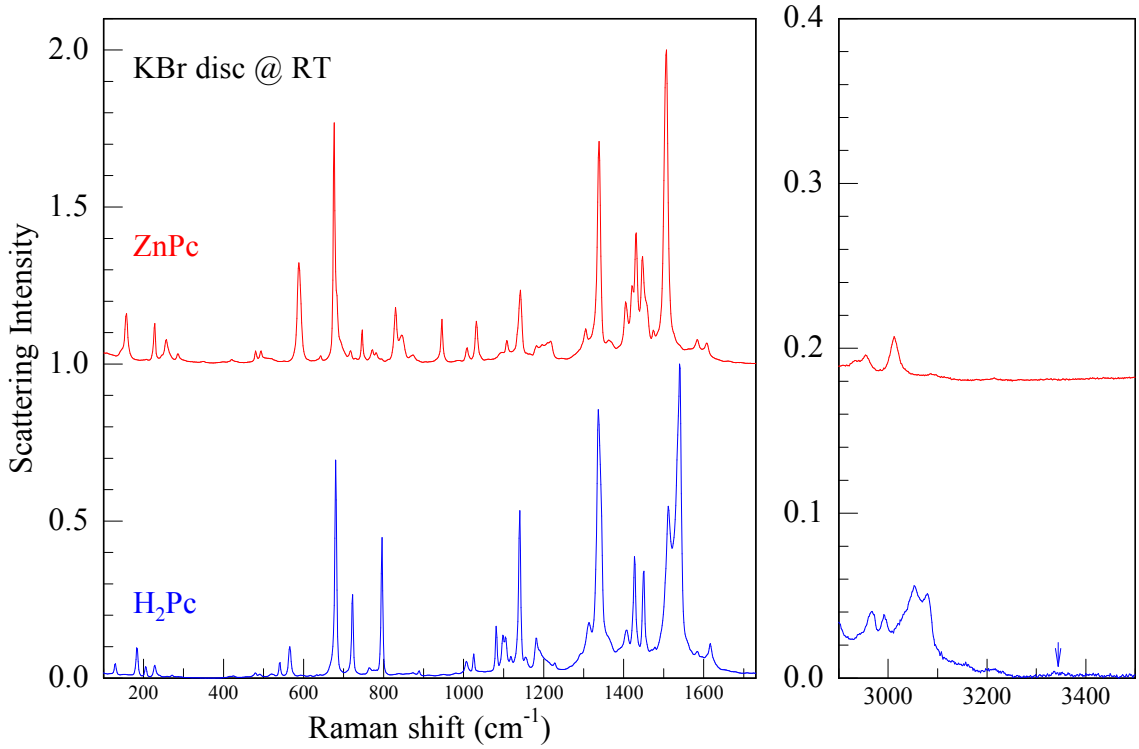

Figure IV.4 Raman spectra of ZnPc and H_2Pc in KBr pellets recorded at room temperature with 532 nm excitation. Conspicuous in the high frequency spectral region is the absence of a strong symmetric N-H stretch which is quite pronounced in the corresponding IR spectrum of H_2Pc. Its possible location, obtained with DFT prediction, is indicated by the arrow.

Table IV.2: Vibrational frequencies (in cm^{-1}) measured in KBr pellets for the Raman active modes of D_2Pc, H_2Pc and ZnPc. The DFT results are shown scaled by a factor of 0.98 and unscaled. The strongest observed bands are shown in bold.

D_2Pc	H_2Pc				ZnPc			
Obs.	Obs.	Calc.scaled	Calc. unscaled	Sym	Obs.	Calc. Scaled	Calc. unscaled	Sym.
128.7 (w)	129.9 (w)	130.2 (.002)	132.9	A_g	157.4 (m)	154.5 (.001)	157.6	B_{1g}
183.7 (m)	182.9 (m)	177.6 (.002)	181.2	B_{1g}	228.3 (m)	227.2 (.002)	231.8	B_{2g}
206.0 (w)	204.7 (w)	207.7 (.000)	211.9	B_{1g}				
228.3 (w)	228.3 (w)	225.4 (.004)	229.7	A_g	257.2 (w)	253.2 (.003)	258.4	A_{1g}
-	-				286.0 (w)	282.6 (.000)	288.4	E_g
479.4 (w)	479.9 (w)	477.9 (.007)	487.6	B_{1g}	479.9 (w)	479.9 (.006)	489.7	B2g
					494.0 (w)	498.5 (.000)	508.7	E_g
540.4 (w)	541.3 (w)	540.3 (.002)	551.3	A_g				
565.6 (m)	565.7 (m)	566.0 (.002)	577.5	A_g	**588**.3 (s)	588.1 (.006)	600.1	A_{1g}
					642.0 (w)	645.9 (.000)	659.1	E_g
680.0 (s)	**679.9** (s)	676.6 (.020)	690.4	A_g	**676.5** (vs)	676.1 (.016)	689.9	A_{1g}
					717.2.(w)	724.3 (.000)	739.1	E_g
720.2(m)	722.8 (m)	728.6 (.060)	743.5	A_g	746.8 (w)	749.5 (.050)	764.8	B_{1g}
764.7 (vw)	764.7 (vw)	763.7 (.001)	779.3	A_g	772.3 (vw)	772.3 (.020)	788.7	B_{1g}
					782.0 (vw)	792.8 (.000)	809	E_g
794.5 (s)	**796.1** (s)	794.5 (.009)	810.7	A_g	830.0 (m)	834.5 (.008)	851.6	A_{1g}
					845.0 (w)			
					873.0 (w)	879.8 (.000)	897.8	E_g
888.1 (w)	888.9 (w)	889.3 (.000)	907.4	B_{1g}				
1006.9 (w)	1007.3 (w)	1008.4 (.012)	1029.0	A_g	1008.9(w)	1009.8 (.026)	1030.4	A_{1g}
986.1(w) 1026.3 (w)	1026.3 (w)	1028.7 (.012)	1049.7	B_{1g}	1032.0 (m)	1035.5 (.006)	1056.6	B_{2g}
1044.1(m) 1082.7 (m)	1081.4 (m)	1084.8 (.002)	1107.0	B_{1g}	945.8(m)	944.3 (.002)	963.6	B_{2g}
1097.6 (m)	1099.1 (m)	1099 (.000)	1121.7	B_{1g}				
1105.0 (m)	1104.4 (m)	1109.9 (.020)	1132.5	B_{1g}	1107.6 (w)	1109.3 (.019)	1131.9	B_{2g}
1116 9(vw)	1117.4 (w)	1116.0 (.050)	1138.3	A_g				
1139.2 (s)	**1140.3** (s)	1140.7 (.130)	1164.0	A_g	1141.9(m)	1141.0 (.144)	1164.3	B_{1g}
1155.6 (w)	1154.9(vw)	1161.3 (.180)	1185.2	A_g				
1183.8 (vw)	1180.9 (w)	1179.9 (.060)	1211.4	A_g	1182.5 (w)	1178.1 (.066)	1202.1	B_{1g}
					1197.1(w)			
1217.9 (w)	1227.8 (w)	1233.5 (.140)	1258.7	B_{1g}	1210.0 (w)	1207.4 (.037)	1232.0	B_{2g}
					1218.1(w)			
1313.1(w)	1312.8 (w)	1312.5 (.009)	1339.3	B_{1g}	1304.9 (w)	1304.8 (.023)	1331.4	B_{2g}
1335.4(vs)	**1336.7** (vs)	1333.7 (.134)	1360.9	A_g	**1338.3** (vs)	1336.5 (.107)	1363.8	A_{1g}
1344.3(vs)		1345.8 (.146)	1373.3	A_g		1341.5 (.088)	1368.9	B_{1g}
1402.2 (m)	1406.5 (w)	1393.9 (.025)	1422.4	A_g	1404.9 (m)	1393.0 (.030)	1421.4	A_{1g}
1427.5 (s)	1426.9 (m)	1430.8 (.053) 1431.6 (.148)	1459.0 1460.9	B_{1g}	1431.7 (m)	1427.9 (.024)	1457.0	B_{2g}
1449.8 (m)	1450.5 (m)	1452.0 (.094)	1481.6	A_g	1447.4 (m)	1449.1 (.101)	1478.7	B_{1g}
-	-	-	-	-	1474.0 (w)	1479.4 (.011)	1509.6	B_{2g}
1518.1 (s)	**1511.5 (s)**	1510.3 (.088)	1541.1	A_g		-	-	-
1540.4(vs)	**1539.5** (vs)	1551.2 (1.00)	1582.9	A_g	**1506.8** (vs)	1526.0 (1.000)	1557.2	B_{1g}
1583.5 (w)	1584.4 (w)	1579.1 (.006)	1611.4	A_g	1584.4 (w)	1582.4 (.004)	1614.7	B_{1g}
1616.2 (w)	1616.8 (w)	1613.9 (.004)	1646.8	B_{1g}	1607.6 (w)	1609.6 (.002)	1642.5	B_{2g}

IV.2.II H_2Pc

The IR spectrum of H_2Pc in N_2 is shown in the lower panel of Figure IV.2. The main difference with the spectrum of ZnPc is the appearance of two new intense bands - a triplet centred around 1000 cm^{-1} and a sharp singlet band at 3311.5 cm^{-1}. These bands have been attributed in the infra-red spectra of KBr discs[3] to the N-H deformation and N-H stretching modes respectively. The latter assignment is entirely appropriate, the former will be examined in detail later in this chapter. Spectra recorded in other matrices (Ar, Kr and Xe) are similar to the one shown in Figure IV.2 for N_2 but are also shifted to lower energies (Figure IV.5). As in ZnPc, all the bands are narrow, except those corresponding to CH stretching modes between 3000 and 3100 cm^{-1}. The frequencies of the observed modes of H_2Pc in all matrices studied are collected in Table IV.3. Spectral shifts from one matrix host to another are very small, but as previously found with ZnPc, the shifts are larger between KBr and the inert gas hosts. The IR signatures of ZnPc and H_2Pc can be compared in Figure IV.2, illustrating the differences between the entries in Table IV.1 and Table IV.3 for these molecules.

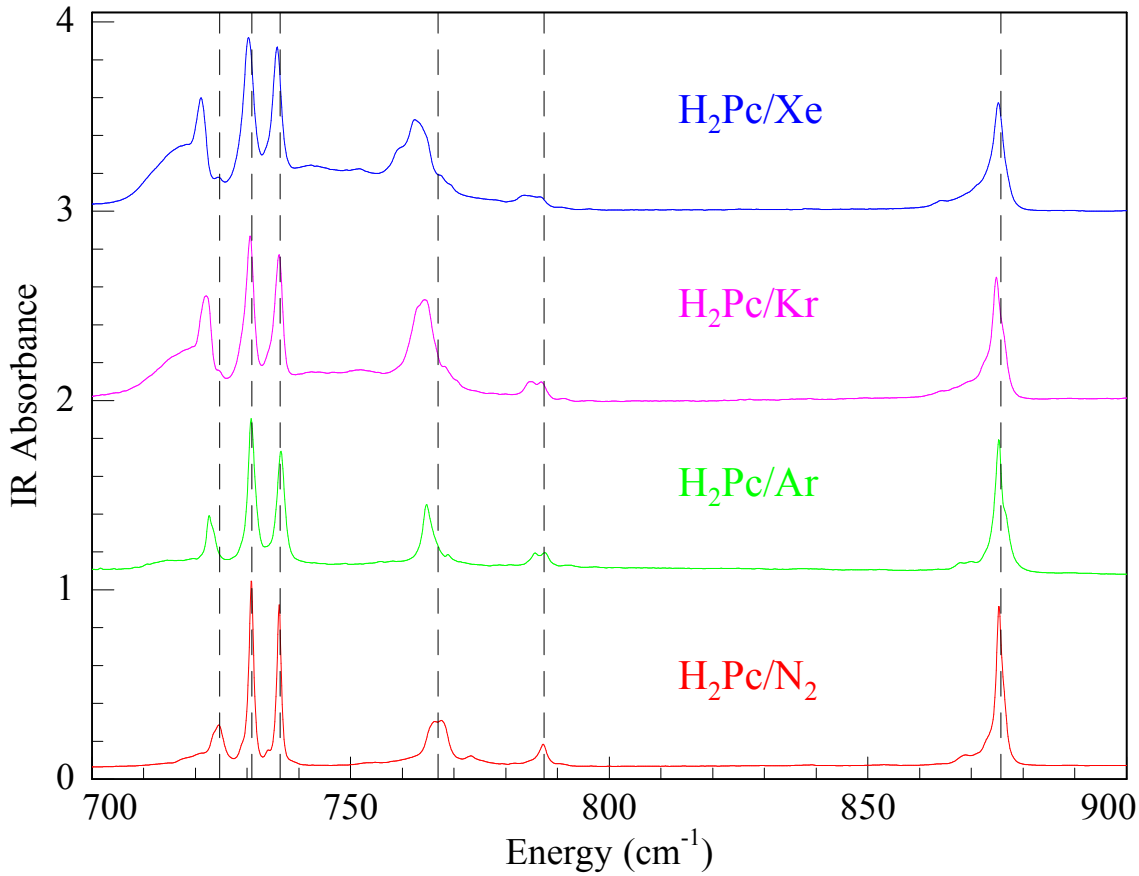

Figure IV.5: FT-IR absorption spectra of H_2Pc in N_2, Ar, Kr and Xe solids in the 700 – 900 cm^{-1} spectral region. The vertical dash lines indicate the absorption bands in N_2. The presence of broad absorption bands due to aggregates can be clearly seen in Kr and Xe matrices underneath the narrower, more intense isolated bands.

Table IV.3: Infra-red frequencies (in cm^{-1}) observed for H_2Pc trapped in different solids. The DFT results shown have been scaled with the same factors as used in Table IV.1. The symmetry labels given for the vibrations utilise the D_{2h} point group, with the z-axis perpendicular to the molecular plane. Some of the weakest unassigned bands may arise from site splitting or Pc aggregates.

KBr	Ar	Kr	Xe	N_2	DFT (Scaled)	DFT (Unscaled)	Sym
493	494.3	494.6	493.4	494.4	492.5	502.6	B_{3u}
556	556.6	555.8	556.0	556.2	556.0	567.4	B_{3u}
618	**618.2**	**617.9**	**617.5**	**618.4**	619.6	632.3	B_{3u}
	722.7	722.0	721.2	724.7	725.7	740.5	B_{1u}
730	**731.0**	**730.6**	**730.5**	**730.9**	731.5	746.5	B_{3u}
735	**736.6**	**736.3**	**735.9**	**736.4**	735.8	750.8	B_{2u}
765	764.8	764.6	762.6	766.9	762.8	778.4	B_{1u}
-	785.6	784.7	783.6	787.4	783.1	799.1	B_{3u}
874	**875.4**	**874.8**	**875.3**	**875.7**	874.0	891.8	B_{3u}
-	980.9	980.4	976.0	980.8	-	-	
1007	**991.5**	**995.7**	**994.6**	**995.0**	1016.5	1037.2	B_{3u}
-	997.6	1001	1001.0	1003.0	-	-	
	1011.3	1011.1	1010.4	1012.7	-	-	
1045	1044.6	1045.4	1045.7	1047.1	1047.0	1068.4	B_{2u}
	1065.4	1064.8	1064.5	1065.9	1064.3	1086.9	B_{3u}
	1075.7	1072.9	1070.2	1074.9	-	-	
1094	**1096.1**	**1095.0**	**1094.2**	**1096.0**	1086.9	1109.0	B_{2u}
1110	**1110.7**	**1110.5**	**1101.3**	**1112.4**	1109.3	1131.9	B_{3u}
1118	**1120.0**	**1119.2**	**1118.6**	**1120.6**	1116.8	1139.6	B_{2u}
	-	1154.8	1152.5	1155.3	1157.8	1181.4	B_{2u}
1160	1158.9	1158.1	1157.6	1159.7	1162.4	1186.1	B_{3u}
1189	1191.1	1190.5	1188.7	1192.2	1190.3	1214.6	B_{2u}
-	1201.8	1200.0	1197.9	1202.5	-	-	
	1251.6	1252.0	1251.5	1252.7	1260.7	1286.4	B_{2u}
1277	**1276.2**	**1277.9**	**1277.3**	**1277.3**	1286.3	1312.6	B_{3u}
	1279.0	-	-	**1280.2**			
1303	1302.2	1301.2	1300.0	1305.3	1307.4	1334.1	B_{2u}
	1309.0	1307.5	1307.4	-			
1321	**1322.2**	**1322.2**	**1321.5**	**1323.2**	1313.1	1339.9	B_{2u}
1335	**1336.6**	**1336.1**	**1336.5**	**1336.4**	1331.6	1358.8	B_{3u}
1343^{sh}	1346.5	1345.9	1345.5	1346.7	1343.1	1370.6	B_{2u}
1438	**1440.8**	**1439.9**	**1438.9**	**1441.1**	1444.0	1473.5	B_{2u}
1459	1459.5	1459.5	1460.0	1459.4	-	-	
-	1466.5	1464.9	1461.9	1466.8	1460.8	1490.7	B_{3u}
-	1496.3	-	-	1494.9			
-	1498.8	1498.4	1497.6	1498.4	1499.4	1530.0	B_{2u}
	1501.2	-	-	1501.6	-	-	
1503	**1506.1**	**1505.2**	**1504.3**	**1507.3**	1500.9	1531.5	B_{3u}
-	1513.1	1512.0	-	1513.1			
	-	1538.7	1537.9	1540.8	1536.5	1567.9	B_{2u}
1609	1607.8	1610.3	1608.8	1610.7	1606.3	1639.1	B_{3u}
	1623.5	1620.1	1618.7	1621.1	1613.8	1646.8	B_{2u}
3049*	3039.6*	3035.2*	3034.6*	3041.0*	-	-	
-	3063.4^{sh}	3057.9^{sh}	-	-	3058.6	3172.8	B_{3u}
					3063.8	3176.6	B_{2u}
3075	3072.8	3070.4	3066.0	3075.6	3073.4	3186.5	B_{2u}
					3076.8	3190.1	B_{3u}
-	3086.1	3082.3	3079.5	3087.2	3089.9	3203.6	B_{2u}
					3093.0	3207.8	B_{3u}
3289	**3310.0**	**3308.1**	**3309.2**	**3311.5**	3307.3	3556.3	B_{3u}

The infrared absorption spectrum of H_2Pc in KBr discs has been published previously by Shurvell and Pinzuti[4]. As found in ZnPc, the H_2Pc bands in KBr are red-shifted and broadened compared to the matrix bands because of the interaction between dopant molecules in KBr. This effect is clearly evident in Figure IV.6 which presents a comparison of the spectra recorded in solid Ar and in KBr. However, in contrast to the ZnPc system, several significant differences exist between the KBr and matrix spectra of H_2Pc. The most significant differences are evident in the 740 and 1000 cm^{-1} regions, which have been the subject of much debate and confusion. Several bands present in KBr (685, 712.1 and 716.5 cm^{-1}) are absent in the matrix spectra. The fact that they are absent or observed with a drastic reduction in intensity (compared to the bands around 730 and 736 cm^{-1}) in the matrix spectra indicates that these bands are due to H_2Pc aggregates. The strongest band in KBr at 1006.5 cm^{-1} is much narrower and located at a lower frequency (995 cm^{-1}) in the N_2 matrix. All other modes in inert host matrices are observed at higher energy than in KBr. As a result of the comparison shown in Figure IV.6, it can be concluded that the most intense band in the KBr IR spectrum arises predominantly from phthalocyanine aggregates.

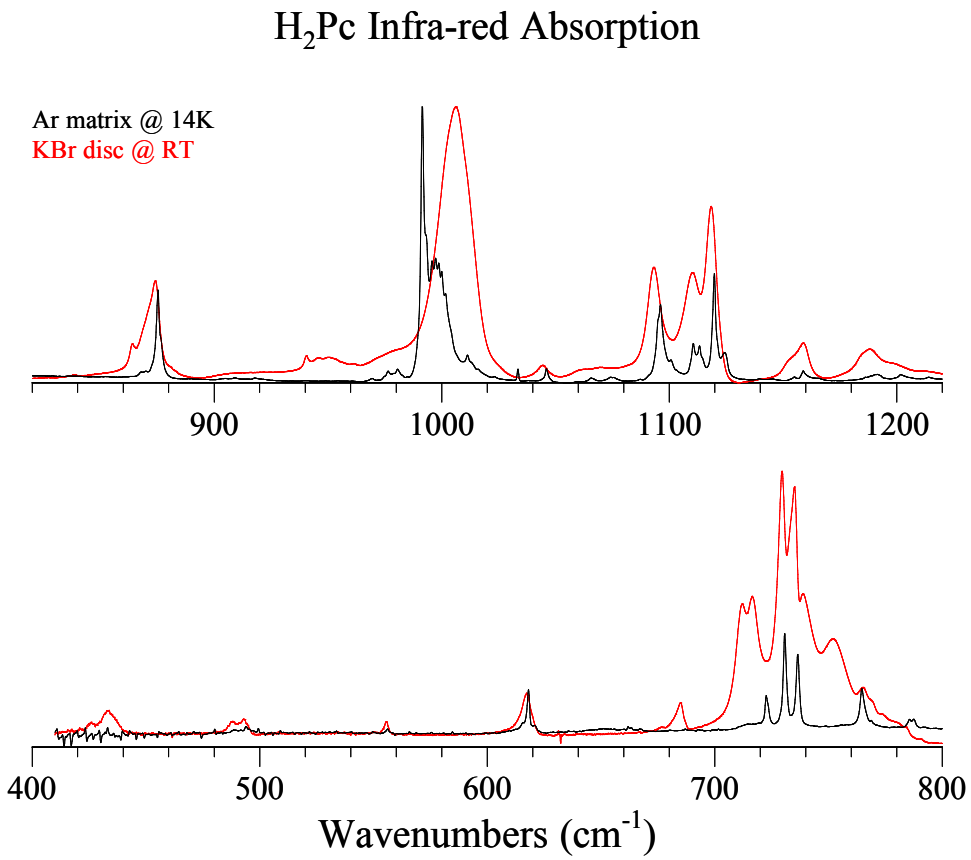

Figure IV.6: A comparison of the IR spectra recorded for H_2Pc trapped in an Ar matrix at 14 K and in a KBr pellet at room temperature. Major differences in the spectra are evident in the 740 and 1000 cm^{-1} regions, both of which have, been attributed to the N-H bending modes in the literature.

The Raman spectrum of H_2Pc in KBr discs, recorded under the same conditions as ZnPc in KBr is shown in the lower panel of Figure IV.4 while the corresponding vibrational frequencies are reported in Table IV.2. The similarities between H_2Pc and ZnPc Raman spectra are striking, and much more extensive than between the corresponding IR spectra shown in Figure IV.2. This behaviour would immediately suggest that the N-H modes of free-base phthalocyanine are only weakly Raman active.

IV.2.III Deuteration effects

Two syntheses of D_2Pc were used in matrix-IR experiments yielding mixtures of H_2Pc, HDPc and D_2Pc with, as shown by the lower traces in Figure IV.7, slightly different compositions for two spectra recorded in Ar. The plot on the right shows the N-H stretching region. The less intense band at 3310.0 cm^{-1} is the antisymmetric stretching of H_2Pc, which was already observed in pure H_2Pc samples and is shown for comparison by the black trace in Figure IV.7 (bottom). The more intense band is the N-H stretching of HDPc at 3337.1 cm^{-1}. The left panel in Figure IV.7 shows the region of the N-D stretching. The highest energy feature at 2538.6 cm^{-1} is a combination band already present in the spectrum of pure H_2Pc shown by the black trace. The absorption at 2480.5 cm^{-1} is more intense in mixture 1 and since this sample contains most D_2Pc, this band is assigned to the N-D antisymmetric stretching mode of the fully deuterated molecule.

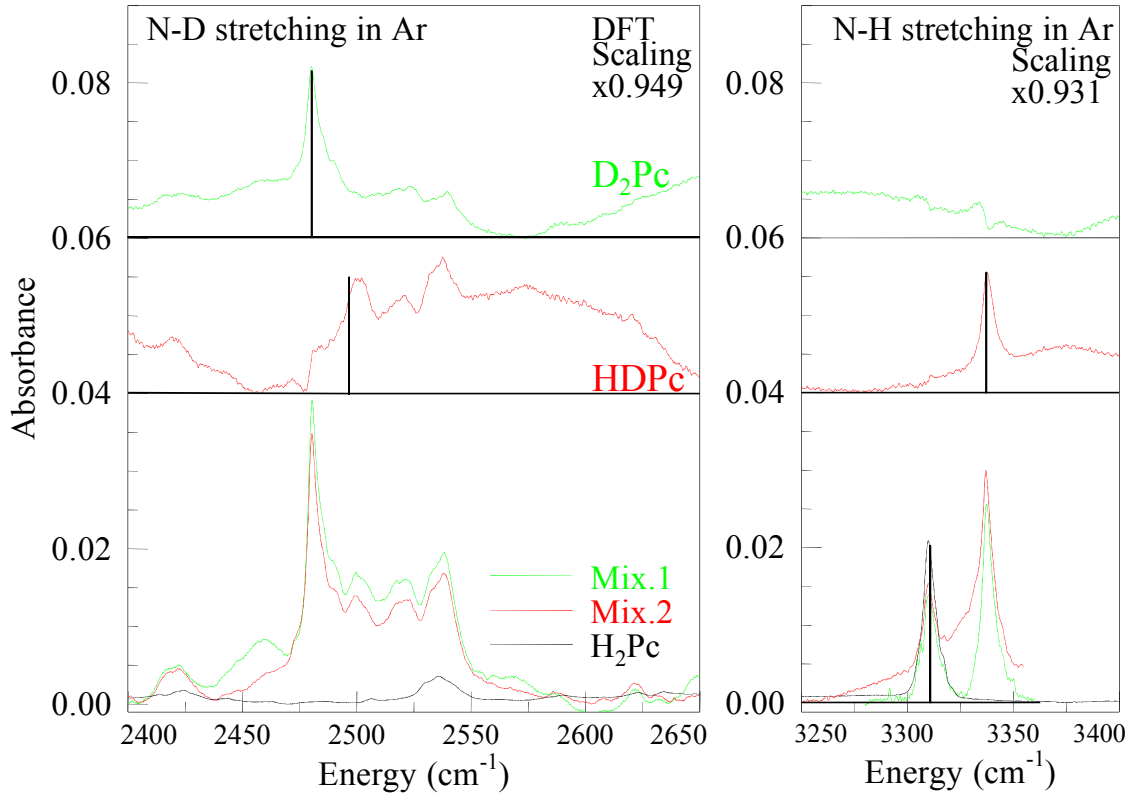

Figure IV.7: Raw spectra of the two mixtures of H_2Pc, HDPc and D_2Pc in solid Ar obtained by synthesis 1 and 2. Spectrum of 2 has been divided by a factor of 1.45 in order to make the intensities of the bands of H_2Pc and D_2Pc coincide. The absorption of a sample containing only H_2Pc is shown to allow identification of a combination mode at 2538 cm^{-1}. The upper section shows the difference spectra in the region of the N-D and N-H stretching modes of H_2Pc, HDPc and D_2Pc in an Ar matrix. The broad underlying curvature present in the two difference spectra is a result of working with two samples having slightly different thicknesses. DFT predictions are shown by the stick spectra scaled by the indicated factors.

This assignment is fully supported by data extracted from the difference spectra. Difference spectra containing only HDPc or D_2Pc were obtained with the following procedure. First: the spectrum of pure H_2Pc is multiplied by a coefficient and subtracted from those of mixtures 1 and 2, so in the difference spectra the intensity of the pure N-H stretching mode in H_2Pc (in argon the band at 3310 cm^{-1}) is equal to 0. Two spectra, containing only HDPc and D_2Pc: mixture 1' and 2', are thereby obtained. Second: the spectrum of 1' is multiplied by a coefficient and subtracted from spectrum 2' so the intensity of the N-D stretching mode band of D_2Pc (at 2480.5 cm^{-1} in Ar) is equal to 0. This difference spectrum is now that of pure HDPc. Third: the spectrum of 2' is multiplied by a coefficient and subtracted from spectrum 1', so the intensity of the band of HDPc at 3337.1 cm^{-1} in Ar (N-H stretching mode) is equal to 0. This difference spectrum shows only D_2Pc bands.

The difference spectra generated for HDPc and D_2Pc isolated in an Ar matrix are presented in the upper panels of Figure IV.7 in the N-D (left panel) and N-H

stretching regions. Two unaccounted bands are located at 2499.0 and 2523.3 cm^{-1} in the raw spectra of the both mixtures but with the help of difference spectra, the former can be assigned to the N-D stretching in HDPc. In conclusion, the N-H and N-D stretching modes of HDPc are at 3337.1 and 2499.0 cm^{-1} respectively.

The overlap between the bands of the three isotopomers in the 400 to 1600 cm^{-1} region does not allow us to use the raw mixture spectra to identify the lower frequency modes for each species. This problem can be resolved if "difference" spectra are used instead. The signal-to-noise ratio in the difference spectra is lower than in the original mixture spectra and as a result, this method can only be used to analyse the most intense IR bands.

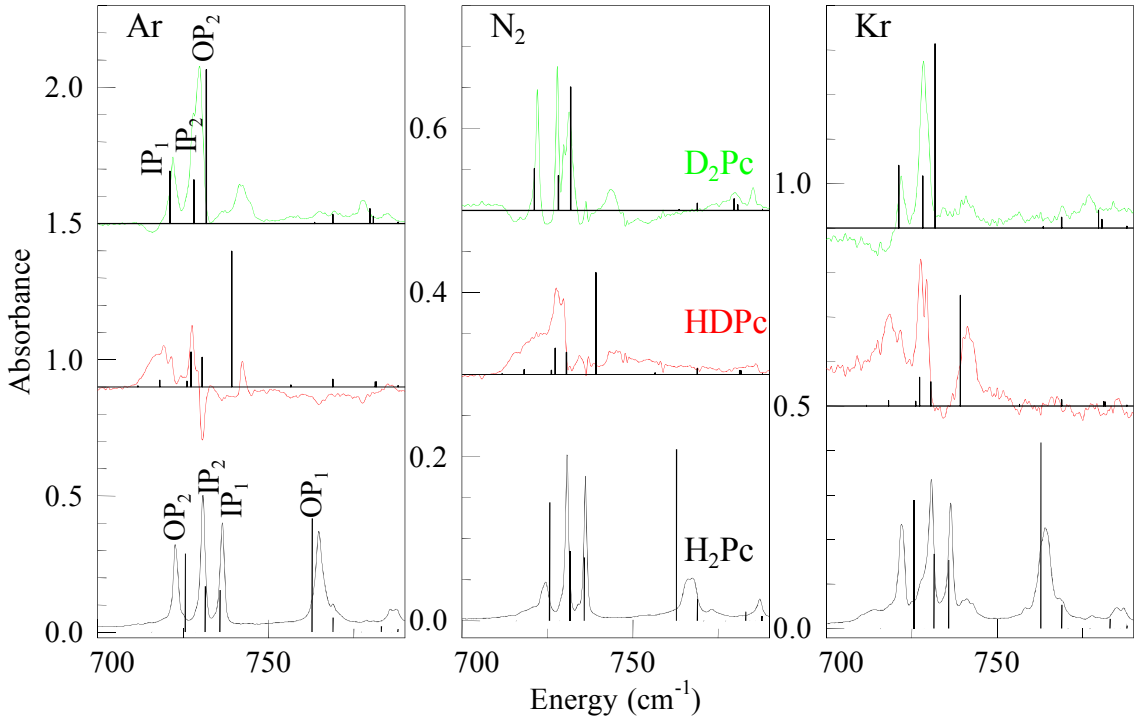

Figure IV.8: Infra-red spectra in the region of 700-800 cm^{-1} of H_2Pc, HDPc and D_2Pc trapped in different solids (Ar, N_2 and Kr). The results of the DFT calculations on these three isotopomers are shown by the stick spectra. For comparison purposes the DFT results have been scaled by 0.98. The labels OP and IP indicate out-of-plane and in-plane bending modes respectively. Particularly noteworthy is the mode labelled OP_2 whose frequency increases from the light (H_2Pc) to the heavy (D_2Pc) isotopomer.

Figure IV.8 and Figure IV.9 show the difference spectra extracted for HDPc and D_2Pc in the 700-800, the 900-1150 and the 1150-1300 cm^{-1} regions together with the pure H_2Pc spectrum. Other than the N-H(D) stretching regions, these are the spectral ranges where the largest shifts were observed between the spectra of the three isotopomers. All the other bands are only slightly shifted (<2 cm^{-1}) upon H/D substitution. As shown in the left panel of Figure IV.8, the band of H_2Pc at 764.8 cm^{-1} in Ar appears to shift to 742.5 cm^{-1} in HDPc. No new bands are observed for

D_2Pc in the lower energy part of the spectrum shown. On the other hand, the strong 728 cm^{-1} band of D_2Pc exhibits a structure, the resolution of which depends strongly on the matrix host, as shown in Figure IV.8. The spectra recorded in N_2 matrices (centre panel) are the best resolved and reveal the presence of two bands for D_2Pc at 728.0 and 731.4 cm^{-1} instead of the one broad, but intense band in Ar and Kr. Assuming a pair of lines is also present in the Ar and Kr data - a reasonable assumption given their widths and indications of unresolved structure on both - then in N_2 the three bands of H_2Pc at 724.7, 730.9 and 736.4 cm^{-1}, are located at 722.1, 728.0 and 731.4 cm^{-1} in D_2Pc. This proposal will be examined further in conjunction with the discussion of the DFT predictions of isotopic shifts.

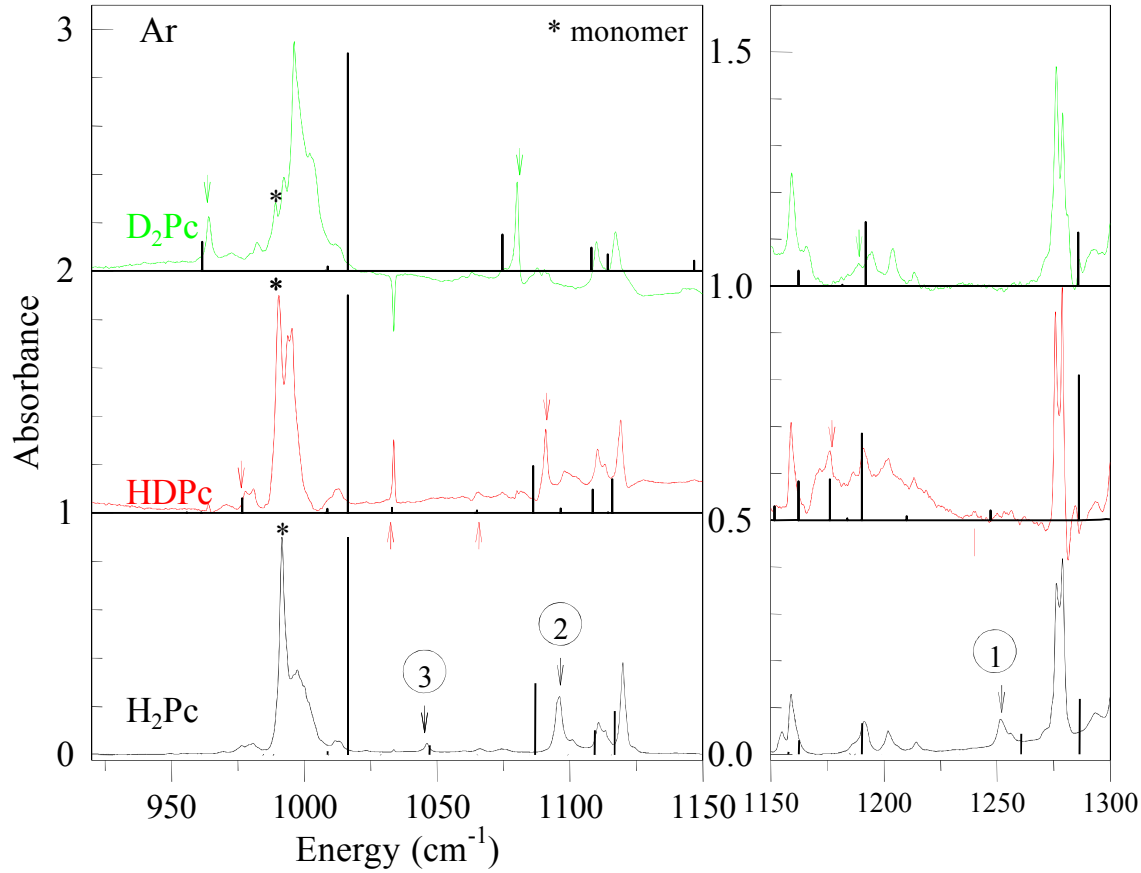

Figure IV.9: Difference spectra of H_2Pc, HDPc and D_2Pc in an Ar matrix in the 900-1150 and 1150-1300 cm^{-1} regions. The asterisks (*) indicate the absorptions of fully isolated monomer molecules. As in the previous figure, scaled (x0.98) DFT results are shown by the stick spectra for comparison purposes. The modes exhibiting a significant dependence on isotopic substitution are numbered and discussed in detail in the text.

The left panel of Figure IV.9 shows the spectral range from 900 to 1150 cm^{-1} in solid Ar in which it is immediately evident that this region is dominated by the strong 1000 cm^{-1} band. However, a pronounced shift is not exhibited upon isotopic substitution by the most intense band located at 991.5 cm^{-1}. Concentration studies reveal that the 1000 cm^{-1} band changes extensively on the

high energy side indicating that the blue region is where aggregates of the Pcs absorb. Thus in the D_2Pc spectrum presented on the top in Figure IV.9, the most intense feature is shifted towards the blue but this effect is arising as a result of an increased amount of aggregates and is not an isotope effect. As indicated by the asterisks in Figure IV.9, the location of the monomer band is only very slightly isotope dependent. The observed positions for the monomer bands of H_2Pc, HDPc and D_2Pc in solid Ar are 991.5, 990.4 and 989.3 cm^{-1} respectively.

In contrast to the dominant band, several of the weaker bands in this region do show pronounced H/D isotope dependence. Thus in D_2Pc a strong band is observed at 964.1 cm^{-1} (indicated by the green arrow on the extreme left in Figure IV.9) which is not present in the two lighter isotopomers. HDPc does exhibit a new band at 977.8 cm^{-1} (red downward arrow) but due to its proximity to the dominant band at 990 cm^{-1}, the significance of this band cannot be estimated from experimental data alone. Another difficulty in the present attributions is the large intensity variations amongst the lines of the different isotopomers. The right panel in Figure IV.9 presents the isotope dependence observed in the 1150-1300 cm^{-1} region. The most pronounced effect exhibited here is the removal of the moderately intense band of H_2Pc at 1252 cm^{-1}. No new, well-defined feature is evident in D_2Pc; the occurrence of new bands is obscured by residual in the difference spectra of the strong band of H_2Pc at the same location.

The frequencies of the vibrational modes most shifted upon deuteration in solid Ar are reported in Table IV.4. No significant differences in the frequency shifts are detected in other matrices. In order to further investigate the observed isotope shifts and thereby obtain mode assignments of the IR absorption bands, theoretical predictions are required. More detailed comments on these experimental results will be presented in the discussion.

Table IV.4: Comparison of the experimental IR frequencies (cm^{-1}) recorded for free base phthalocyanine in an Ar matrix and DFT computed frequencies for the modes exhibiting the largest shifts upon H/D isotopic substitution. A scaling factor of 0.98 has been used for all modes less than 2000 cm^{-1}. Larger scaling factors, as indicated have been used for the higher frequency N-H stretching modes reflecting the larger anharmonicities of these modes. Experimental values shown in parenthesis are either very weak or only partially resolved.

Exp.		**Ar**			**DFT**	**6-311 ++G(2d,2p)**				**Mode assignment**
H_2Pc	HDPc	D_2Pc	Shift	Shift[a]	H_2Pc	HDPc	D_2Pc	Shift	Shift[a]	
	719.3	729.9	-10.6	-7.1		718.2 (14)	731.8 (249)	-13.6	-6.1	C-H N-D OPB (doming)
722.8	?		?		725.7 (127)	711.8 (2)		13.9		C-H N-H OPB (doming)
	?	555	?	209.8		516.3 (4)	555.0 (18)	-38.7	207.8	N-D C-H OPB
764.8	742.5		22.3		762.8 (184)	739.3 (275)		23.5		N-H C-H OPB
	727.6	722.1	5.5	14.5		727.4 (71)	721.2 (85)	6.2	14.6	N-D IPB, isoindole deformation
736.5	?		?		735.8 (68)	756.6 (4)		-20.8		N-H IPB, isoindole deformation
	977.8	964.1	13.7	82.1		976.6 (45)	961.5 (89)	15.1	85.5	N-D IPB, pyrrole rocking
1046.2	1033.6		12.6		1047.0 (29)	1033.0 (15)		14		N-H IPB, pyrrole rocking
	(1065.6)	1080.2	-14.6	15.9		1065.0 (8)	1074.6 (112)	-9.6	12.2	N-D C-H IPB isoindole stretching,
1096.1	1090.9		5.2		1086.8 (217)	1086.2 (143)		0.6		N-H C-H IPB isoindole stretching
	(1176.1)	(1188.9)	18.5	62.7		1176.2 (14)	1192.0 (60)	-15.8	68.7	C-H N-D IPB, C-C stretching pyrrole
1251.4	(1240.4)		11.2		1260.7 (19)	1247.2 (3)		13.5		C-H N-H IPB, C-C stretching pyrrole
	2501.4	2480.5	20.9	829.5		2496.7 (59)	2480.3 (113)	16.4	830.5	N-D stretching (x 0.949)
3310.0	3337.1		-27.1		3310.8 (134)	3337.3 (64)		-26.5		N-H stretching (x 0.931)

[a] Shift H_2Pc - D_2Pc

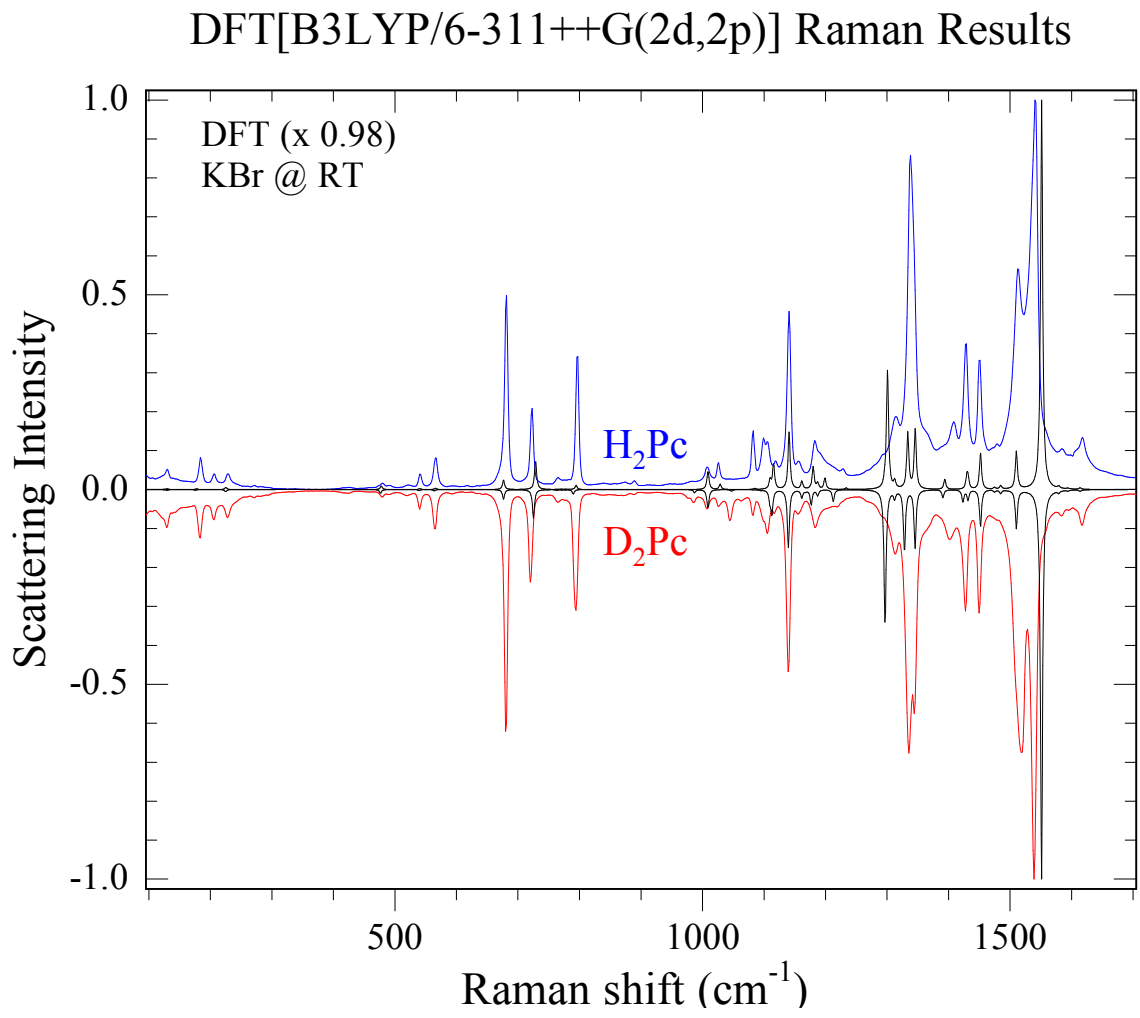

Figure IV.10: A comparison of the Raman spectra recorded for H_2Pc and D_2Pc. The experimental data were recorded at room temperature in a KBr pellet with 532 nm excitation. The DFT predicted spectra (shown by the black traces) were obtained by convoluting the calculated lines with a 3 cm^{-1} Lorentzian lineshape function. The bands exhibiting the largest isotopic shifts are discussed in the text.

Raman data for the deuterated species have been recorded in KBr pellets, with a D_2Pc sample slightly contaminated by a small amount of hydrogenated isotopomers. The corresponding spectrum is presented in Figure IV.10 and compared with that of H_2Pc in KBr recorded under identical experimental conditions. The observed bands are reported in Table IV.2. The D_2Pc and H_2Pc Raman spectra are very similar, behaviour in agreement with the previous observation concerning the similarities between H_2Pc and ZnPc Raman spectra due to the weak Raman active modes involving NH motion. The main differences involve the appearance of new weak bands at 986.1 cm^{-1}, 1044.1 cm^{-1} and 1064.9 cm^{-1}, slight shifts of the 1227.8 cm^{-1} and 1408.2 cm^{-1} bands of H_2Pc to 1219.5 cm^{-1} and 1402.7 cm^{-1} for D_2Pc respectively, and a structure in the strongest band around 1340 cm^{-1}. The band around 1400 cm^{-1} seems to shift with the sample preparation and is assigned to clusters or complexes. As in the case of IR data, the

isotope shifts in the Raman data will be discussed in the light of theoretical predictions obtained using DFT calculations.

IV.3 DFT calculations data

Density Functional Theory was used to generate force fields from the optimised molecular geometries of ZnPc and H_2Pc. Computed vibrational frequencies of ZnPc and the isotopomers H_2Pc, HDPc and D_2Pc were then analysed and compared with the recorded IR and Raman spectra to examine in particular, the N-H vibrational modes.

IV.3.I Optimised Geometries

The geometries of ZnPc and H_2Pc were optimised in D_{4h} and D_{2h} symmetries respectively and the fact that no negative frequencies were observed, indicates that planar structures are predicted for the phthalocyanines with the B3LYP functional and 6-311++G(2d,2p) basis set used. This result is in contrast to previous DFT calculations[1] for ZnPc, in which a "domed" C_{4v} structure was found employing a smaller 6-31G(d,p) basis set. Full geometric details of the optimised structures of ZnPc and H_2Pc resulting from use of the B3LYP functional are presented as Table IV.5. The atom labelling systems used for ZnPc and H_2Pc are those provided in Figure IV.1. It is noteworthy that at this level of theory, the bond lengths in particular match the crystal data[5] better and are shorter than the previous highest level [6-311+G(d)] DFT calculation of ZnPc by Nguyen and Pachter[6]. A smaller improvement has been obtained for H_2Pc compared with the results of the recent higher level calculation by Strenalyuk *et al.*[7] utilising the same hybrid functional (B3LYP) and the 6-311++G(d,p) basis set. The total energies calculated for ZnPc and H_2Pc were, with ZPE correction, -3446.5966 and -1668.3496 hartrees respectively.

Table IV.5: Bond lengths and angles determined for H_2Pc and ZnPc from DFT calculations. The atom labelling system used is provided in Figure IV.1

	H_2Pc		ZnPc	
Lengths (Å)	**Exp[8]**	**B3LYP**	**Exp[5]**	**B3LYP**
N-H(Zn)	0.923	1.009	1.980	1.998
N-C_α	1.377	1.375	1.369	1.369
C_α-N_m	1.326	1.313	1.331	1.327
C_α- C_β	1.453	1.450	1.455	1.459
C_β- C_β	1.398	1.409	1.400	1.407
C_β- C_γ	1.388	1.394	1.393	1.391
C_γ- C_δ	1.380	1.386	1.391	1.390
C_δ- C_δ	1.398	1.406	1.396	1.403
C_γ- H_1	0.950	1.080	NA	1.080
C_δ- H_2	0.950	1.081	NA	1.081
N'-C_α'	1.369	1.362		
C_α'- N_m	1.327	1.332		
C_α'- C_β'	1.460	1.465		
C_β'- C_β'	1.395	1.400		
C_β'- C_γ'	1.391	1.389		
C_γ'- C_δ'	1.387	1.392		
C_δ'- C_δ'	1.393	1.401		
C_γ'- H_1'	0.950	1.081		
C_δ'- H_2'	0.951	1.081		
Angles (deg)				
H(Zn)-N-C_α	128.5	123.736	125.4	125.057
N-C_α- N_m	129.1	128.100	127.8	127.456
C_α-N-C_α	109.8	112.527	109.1	109.887
N-C_α-C_β	108.1	106.135	108.8	108.452
C_α-C_β-C_β	107.4	107.601	106.6	106.605
C_β-C_β-C_γ	120.7	120.960	121.3	121.021
C_β-C_γ-C_δ	117.7	117.829	117.3	117.836
C_γ-C_δ-C_δ	121.6	121.211	121.5	121.144
C_β-C_γ-H_1	121.2	120.586	NA	120.709
C_γ-C_δ-H_2	119.2	119.622	NA	119.638
N'-C_α'- N_m	128.4	121.688		
C_α'-N'-C_α'	108.0	107.226		
N'-C_α'-C_β'	109.5	110.697		
C_α'-C_β'-C_β'	106.8	105.690		
C_β'-C_β'-C_γ'	121.8	121.223		
C_β'-C_γ'-C_δ'	117.0	117.670		
C_γ'-C_δ'-C_δ'	121.3	121.107		
C_β'-C_γ'-H_1'	121.5	120.925		
C_γ'-C_δ'-H_2'	119.3	119.636		

IV.3.II Vibrational modes

ZnPc with 57 atoms has 165 fundamental vibrational modes, which can be categorised as $A_{1u}(6)$, $A_{2u}(8)$, $B_{1u}(7)$, $B_{2u}(7)$ $E_u(28)$, $A_{1g}(14)$, $A_{2g}(13)$, $B_{1g}(14)$, $B_{2g}(14)$ and $E_g(13)$ in D_{4h} symmetry. H_2Pc, with one additional atom, has 168 fundamental vibrational modes and with its reduced D_{2h} symmetry, yields $A_u(13)$, $B_{1u}(15)$, $B_{2u}(28)$ $B_{3u}(28)$, $A_g(29)$, $B_{1g}(28)$, $B_{2g}(14)$ and $B_{3g}(13)$ modes. Due to their very close geometries, strong similarities[9] exist between the vibrational modes of ZnPc and H_2Pc. From group theory correlations, the $A_{1u,g}$ [$A_{2u,g}$] and $B_{1u,g}$ [$B_{2u,g}$] modes of D_{4h} symmetry are merged in the $A_{u,g}$ [$B_{1u,g}$] modes of D_{2h} symmetry respectively, and the degenerate $E_{u,g}$ modes of D_{4h} symmetry are split in $B_{2u,g}$ and $B_{3u,g}$ modes in D_{2h} symmetry. In this perspective, the additional modes of H_2Pc compared to ZnPc, are three *gerade* modes with A_g, B_{1g} and B_{2g} symmetries. In ZnPc, only 36 *u* modes are infrared-active [A_{2u} and E_u modes] while 55 *g* modes [A_{1g}, B_{1g}, B_{2g} and E_g modes] are Raman-active. The corresponding numbers in the free-base are thus 71 infrared active *u* modes [$B_{1u}(15)$, $B_{2u}(28)$ and $B_{3u}(28)$], and 84 Raman active *g* modes [$A_g(29)$, $B_{1g}(28)$, $B_{2g}(14)$ and $B_{3g}(13)$].

Harmonic frequencies have been calculated for the normal modes of ZnPc, H_2Pc and its isotopomers HDPc and D_2Pc. All the vibrational modes obtained for ZnPc, H_2Pc and D_2Pc are reported in Table IV.A.1 (infrared-active modes) and Table IV.A.2 (Raman-active modes) in the Appendices. The 13 non-reported modes (with no optical activity) are found to be identical in H_2Pc and D_2Pc with only very small shifts in frequencies between the free-base isotopologues and zinc phthalocyanine. An effort was made in these tables to arrange the corresponding modes of the three species along the same lines. This mode association has been achieved with the assistance of the animated pictures generated by Gaussian 03 for the normal modes. All *u* modes have *g* counterparts in the same range of frequencies; they correspond to the same bond motions but with different symmetries. For instance DFT results indicate the intense IR modes in the 1100 to 1200 cm^{-1} range arise from the IP bending modes of the aryl ring-C-H bonds. This finding is supported by the pronounced isotope shifts observed by Gladkov *et al.*[10] in the Raman spectra of ZnPc-d_{16} in KBr pellets.

The correspondence between the vibrational modes of zinc and free-base phthalocyanine is very clear in most cases, especially for the B_{3u}, A_g, B_{2g} and B_{3g} symmetry modes of the free-base. The three additional *gerade* modes are found

logically to be strongly influenced by NH(D) motions. With the assistance of animated pictures it is obvious that fifty-fifty mixtures of ZnPc A_{1g} and B_{1g} C-H stretching modes are correlated to H_2Pc A_g C-H stretching modes. Correlations are much less evident in the case of In-Plane Bending modes (ZnPc E_u, A_{2g} and B_{2g} modes) between 1000 and 1500 cm^{-1} when the N-H(D) In-Plane bending motion of the free-base perturbs the rings motions (see Part IV.4.III of the Discussion). The frequency ratios (ν_H/ν_D) calculated for the vibrational modes of H_2Pc and D_2Pc highlight the influence of N-H motion on the modes. Table IV.6 presents a summary of the computed frequency modes involving a ν_H/ν_D ratio significantly different from unity.

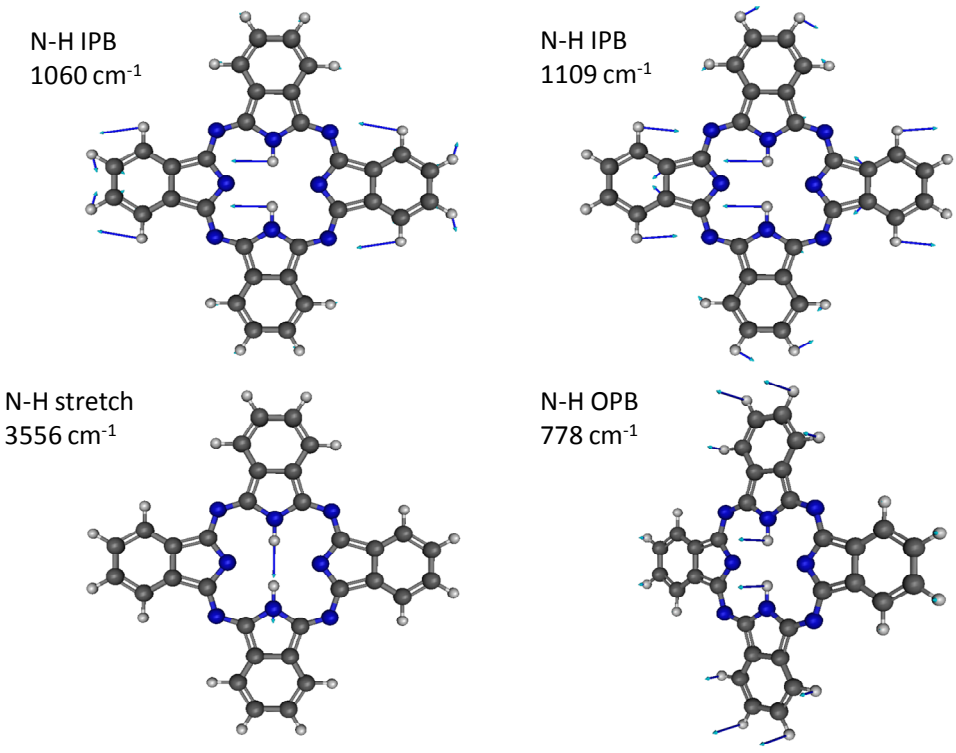

Figure IV.11: Vector displacement representations of the N-H vibrations of H_2Pc calculated with the DFT method for the most intense IR absorptions. The diagrams depict the extent of the coupling between the N-H in-plane bends (IPB) and out-of-plane bends (OPB) with the bending of the C-H bonds on the aryl groups. In contrast, the N-H stretch can be considered a pure, isolated motion. The numbers listed are the unscaled DFT calculated values.

Table IV.6: The vibrational modes of H_2Pc exhibiting the largest isotopic shifts upon H-D substitution according to DFT calculations. For comparison, the vibrational frequencies of ZnPc are also provided as are the predicted intensities in parenthesis. The values given in italics are ambiguous correlations between H_2Pc and ZnPc. The frequencies (ν) are given in cm^{-1} while the intensities (int) are given in units of km mol^{-1}.

IR modes

ZnPc ν (int)	H_2Pc ν (int)	D_2Pc ν (int)	ν_H/ν_D
Out-of-plane bending			
A_{2u}	B_{1u}		
250 (0)	217 (7)	214 (8)	1.0143
749 (247)	740 (127)	747	0.9916
123 (11)	**778 (184)**	**566 (18)**	**1.3744**
797 (31)	804 (5)	796 (24)	1.0105
In-plane bending			
E_u	B_{2u}		
511 (8)	499 (2)	489 (1)	1.0197
768 (61)	751 (68)	736 (85)	1.0202
906 (56)	**855 (0)**	**779 (2)**	**1.0969**
1111 (174)	**1068 (29)**	**981 (89)**	**1.0889**
1084 (154)	1109 (217)	1096 (112)	1.0114
1190 (30)	1181 (2)	1170	1.0096
250 (5)	**1286 (19)**	**1216 (60)**	**1.0576**
1360 (234)	1568 (8)	1546 (2)	1.0142
In-plane stretching			
E_u	B_{3u}		
250 (5)	**3556 (134)**	**2614 (113)**	**1.3606**

Raman modes

ZnPc ν (int)	H_2Pc ν (int)	D_2Pc ν (int)	ν_H/ν_D
E_g	B_{2g}		
235 (2)	220 (3)	214 (3)	1.0276
509 (0)	506 (0)	511 (0)	0.9891
	680 (0)	**495 (0)**	**1.3738**
A_{2g}+ B_{2g}	B_{1g}		
589 (0)	580 (2)	563 (2)	1.0305
629 (0)	612 (1)	600 (0)	1.0212
864 (0)	***841 (1)***	***880 (0)***	***0.9563***
	907 (1)	***763 (5)***	***1.1900***
1057 (116)	**1050 (228)**	**1007 (134)**	**1.0422**
964 (42)	**1107 (43)**	**1068 (65)**	**1.0360**
1157 (0)	*1224 (520)*	*1191 (59)*	*1.0270*
1232 (741)	*1259 (73)*	*1237 (536)*	*1.0173*
1485 (0)	1566 (3)	1550 (14)	1.0105
A_{1g}+ B_{1g}	A_g		
--	**3612 (13)**	**2649 (36)**	**1.3634**

The assignment of N-H(D) stretching modes is straightforward in both B_{3u} and A_g symmetry groups, with only one mode yielding a large ν_H/ν_D ratio of 1.36, close to $\sqrt{2}$. Theoretical values are 3556 [2613] and 3612 [2649] cm^{-1} for N-H[D] *u* and *g* stretching modes respectively. The former values (scaled by 0.96) are in excellent agreement with the previously described IR experimental values. The symmetric Out-of Plane Bending (OPB) NH(D) modes (B_{1u} and B_{2g}) also show a similarly high isotopic ratio (1.37) providing a clear assignment 778 [566] and 680 [495] cm^{-1} for the N-H[D] *u* and *g* OPB modes respectively. Conversely, only ratios close to one are obtained in the case of the In-Plane Bending (IPB) NH[D] modes (B_{2u} and B_{1g} symmetry). Thus it would appear there is no normal mode corresponding to a pure IPB motion of the NH groups alone. As mentioned in the previous work of Zhang *et al.*[11], this motion is strongly coupled with the ring breathing modes. Figure IV.11 illustrates the extent of the coupling between IP bending of the aryl C-H bonds and the N-H bending motions. At least eight IPB modes of each symmetry are affected by deuteration. This is especially true with the *gerade* modes for which correlations between H_2Pc and D_2Pc (and ZnPc) modes are difficult to establish. From animated pictures, the IPB modes involving the largest NH bending motion (H_2Pc) are computed at 1286 cm^{-1} (B_{2u}) and 1107/907 cm^{-1} (B_{1g}), and those involving largest ND bending (D_2Pc) at 981 cm^{-1} (B_{2u}) and 763 cm^{-1} (B_{1g}). These frequencies are located in a dense part of the vibrational manifold of free-base phthalocyanine.

IV.4 Discussion

IV.4.I IR absorption

The computed IR absorption spectrum of ZnPc is compared with frequencies scaled by a factor of 0.98 in the upper panel of Figure IV.12 with that recorded in a N_2 matrix where the close agreement that exists, both in terms of the band positions and the band intensities, is quite evident. Very significant improvement was obtained by increasing the basis set from 6-31G(d,p) to 6-311++G(2d,2p) – an indication of the importance of having diffuse and polarisation functions present. This basis set yields much better agreement in the region up to 1000 cm^{-1} than that which Tackley *et al.*[1] achieved with the 6-31G(d,p) basis comparing with data recorded for ZnPc in KBr discs. Calculated (scaled) frequencies are compared to experimental results in Table IV.1. In the 400-1650 cm^{-1} spectral range, all the

lines with a calculated intensity larger than 3 km/mol are observed and assigned. The symmetries of the modes listed in the last column were assigned through DFT calculations. Only two of the bands (reported for KBr pellets at 727.9 and 781.3 cm^{-1}) correspond to out-of-plane modes.

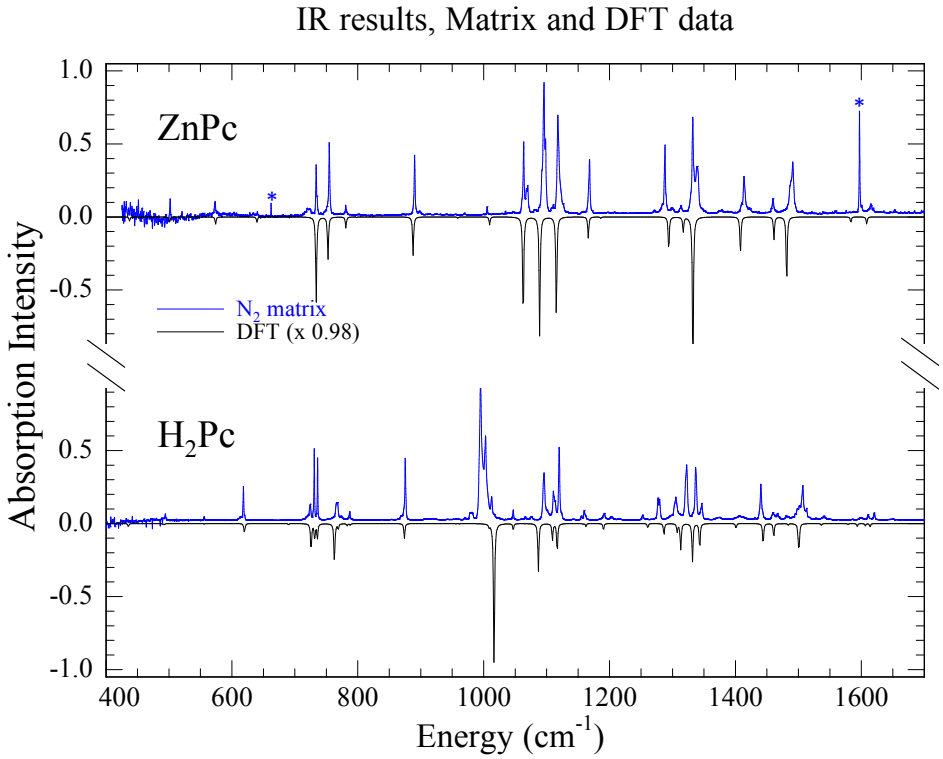

Figure IV.12: A comparison of the observed and calculated infrared absorption spectra for ZnPc (upper panel) and H_2Pc (lower panel). The experimental data were recorded at 14 K in a nitrogen matrix while the predicted values were obtained with a DFT calculation using the B3LYP functional and a 6-311++G(2d,2p) basis set.

Two of the three C-H stretching modes have much larger computed intensities than the other. According to this remark, the clearly observed doublet located at 3072.3 and 3093.5 cm^{-1} in N_2 should be assigned to these two modes. The additional structures in the spectra shown in the upper panel of Figure IV.2, are probably due to site effects in the matrix. A third weaker but clearly identifiable band at 3038.3 cm^{-1} is attributed to a strong combination band. The third (weakest) C-H stretching mode which has not been resolved in the matrix spectra, is probably a shoulder on the red wing of the 3072.3 cm^{-1} band .

In the lower panel of Figure IV.12 the matrix and computed IR spectra of H_2Pc are compared. As found for ZnPc, excellent agreement exists below 1000 cm^{-1} but is not quite as good in the region above this. From a combination of the increased number of optically active modes in H_2Pc and the removal of the degeneracy of the

E modes of ZnPc, free-base phthalocyanine is expected to exhibit a significantly richer vibrational spectroscopy than its metal-counterparts, and indeed, the IR H_2Pc spectrum presents many more resolved lines than ZnPc. However, due to their similar geometries, a close correspondence exists between the modes of both molecules as illustrated in Figure IV.12, except around 1000 cm^{-1}.

While the ZnPc spectrum is dominated by three nearly equivalent strong bands between 1000 and 1200 cm^{-1} (1063.6, 1096.0 and 1117.8 cm^{-1} in N_2) there is one intense feature slightly below 1000 cm^{-1} in the free-base spectrum. The strongest band in the calculated free-base spectrum is located at 1016 cm^{-1} (scaled) and from its dominant intensity, this mode must correspond to the most intense band observed at 995.0 (991.5) cm^{-1} in N_2 (Ar) spectra. The additional structure on the blue side of the recorded band is attributed to the presence of small amounts of aggregates.

Correlations deduced from DFT calculations (Table IV.A.1 of the appendix to this chapter) indicate that the 1117.8 cm^{-1} band of ZnPc in N_2 (E_u symmetry) splits into the 1112.4 and 1120.6 cm^{-1} bands of H_2Pc in N_2 (B_{3u} and B_{2u} symmetry, respectively) with moderate intensities (vector diagrams for the modes calculated at 1138.3, 1131.9 and 1139.3 cm^{-1} are shown in Figure IV.13). In contrast, the 1063.6 cm^{-1} band of ZnPc in N_2 (calculated at 1084.5 cm^{-1}) corresponds only to one band located at 1096.0 cm^{-1} in N_2 (B_{2u} symmetry) while in the case of the free base, the corresponding B_{3u} mode shows almost no IR intensity. Conversely, the most intense free-base B_{3u} mode located at 995.0 cm^{-1} in N_2, is correlated with the third component in the ZnPc/N_2 spectrum at 1096 cm^{-1}. The B_{2u} counterpart mode of the free base, located at 1047.1 cm^{-1} in N_2, is a weak line disappearing upon deuteration. Of the IPB modes, this motion involves the most pronounced N-H bending – it occurs in combination with in-plane stretching of the C_α-N-C_α bonds in the two pyrrole rings that contain N-H bonds (calculated at 1068 cm^{-1} in Table IV.6).

DFT results reveal that the corresponding B_{3u} component to this mode (995 cm^{-1} in N_2, calculated at 1037.2 cm^{-1}) does not involve N-H motion, but is an in-plane stretch of the C_α-N-C_α bonds in the two pyrrole rings (see Figure IV.13) that do not contain N-H bonds. This mode of the monomer is, as shown by the asterisks in Figure IV.9, only marginally shifted in HDPc and D_2Pc, entirely consistent with DFT findings. A similar finding was made by Zhang *et al.*[11], based on a comparison

between predicted MgPc and H_2Pc spectra. The large shift of this strong mode involving no N-H motion from H_2Pc to ZnPc explains the long-standing conflicting behaviour that an apparently new mode of H_2Pc (which is not present in ZnPc with a similar frequency or intensity) shows no dependence on isotope substitution. The present DFT calculations, including the results obtained for the metallo-phthalocyanine ZnPc, strongly confirm the mode assignments and fully explain the unexpected isotope behaviour.

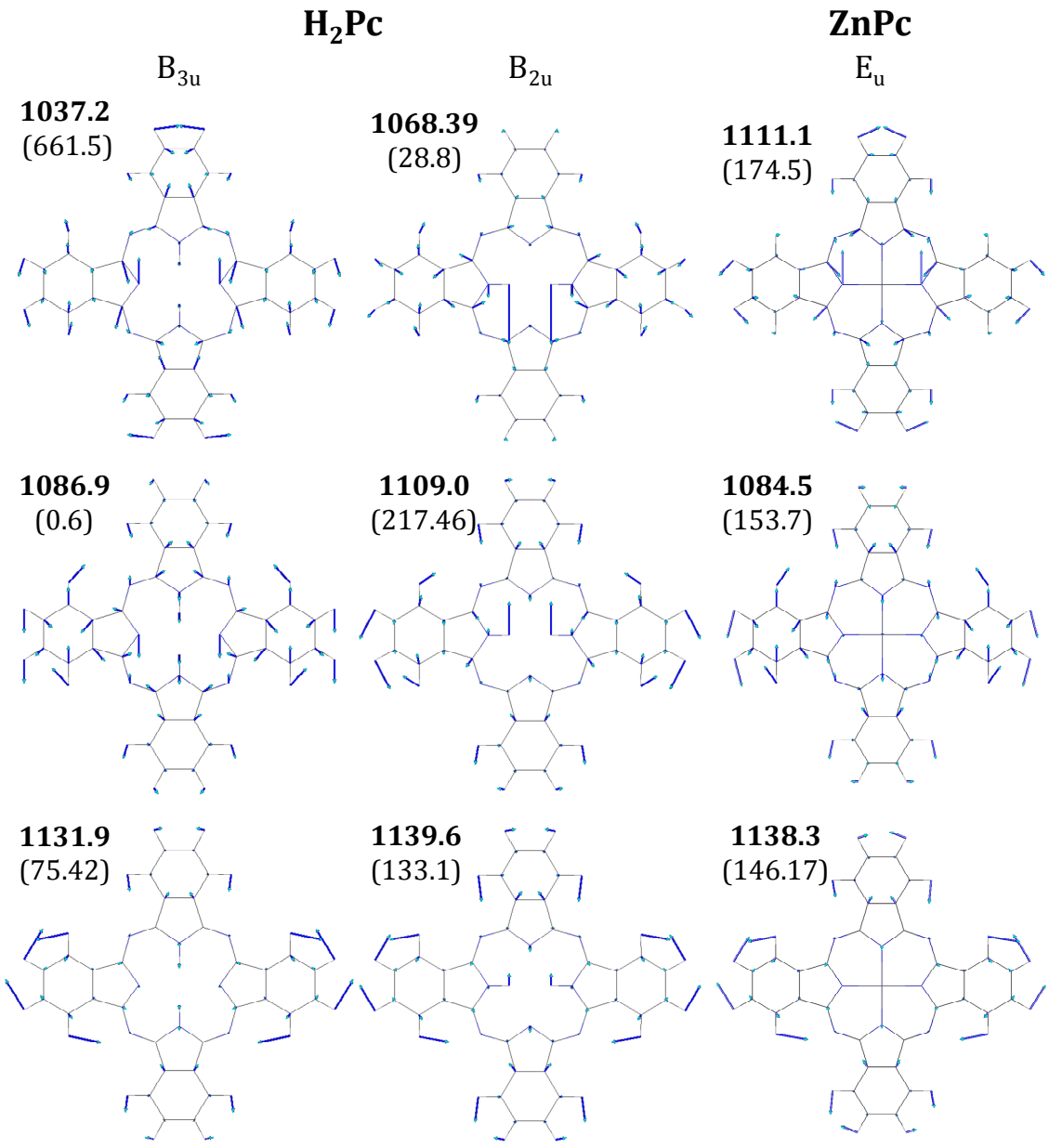

Figure IV.13: Displacement vector diagrams calculated by DFT of H_2Pc and ZnPc. The H_2Pc modes shown are of B_{3u} and B_{2u} symmetry and have been compared to their ZnPc equivalents of E_u symmetry. The numbers in bold are the un-scaled, calculated vibrational frequencies (in cm^{-1}) and the values in parenthesis are the calculated intensities (in km/mol). The H_2Pc B_{3u} modes have been rotated by 90° to emphasise the correlation with the B_{2u} modes of H_2Pc and E_u modes of ZnPc.

In the C-H stretching region, the recorded IR spectra of the free-base and ZnPc are very similar. DFT calculations for H_2Pc predict a splitting of the three bands occurring for ZnPc. However, this splitting, arising from the reduced symmetry in the free-base, is not evident in the recorded matrix spectra. Details of NH deuteration effects on the IR spectra will be discussed in Part IV.4.III.

IV.4.II Raman Scattering

The computed Raman spectra of ZnPc and H_2Pc are compared with those recorded at room temperature in KBr discs in Figure IV.14, while all the computed peak positions are collected in Table IV.2. It is evident from these comparisons that very good positional agreement exists in the case of both molecules. A noteworthy distinction between absorption and scattering spectroscopies of the phthalocyanines is that both in-plane and out-of-plane motions are IR-active while only the in-plane vibrations are observed in Raman spectra. The out-of-plane E_g modes of ZnPc, while allowed by group theory, are predicted to be much too weak to be experimentally observed. In the computed Raman spectrum, the in-plane A_{1g} and B_{1g} modes carry most of the intensity with the B_{2g} modes much weaker. Similarly, for H_2Pc only two in-plane [A_g, B_{1g},] mode symmetries are found to exhibit significant Raman activities. As a result of this intensity behaviour, it is found that only a limited number of modes dominate the recorded Raman spectra of both molecules. The Raman modes fall mainly into two categories, those involving motion of the central ring and those of the aryl and pyrrole parts of the isoindole groups.

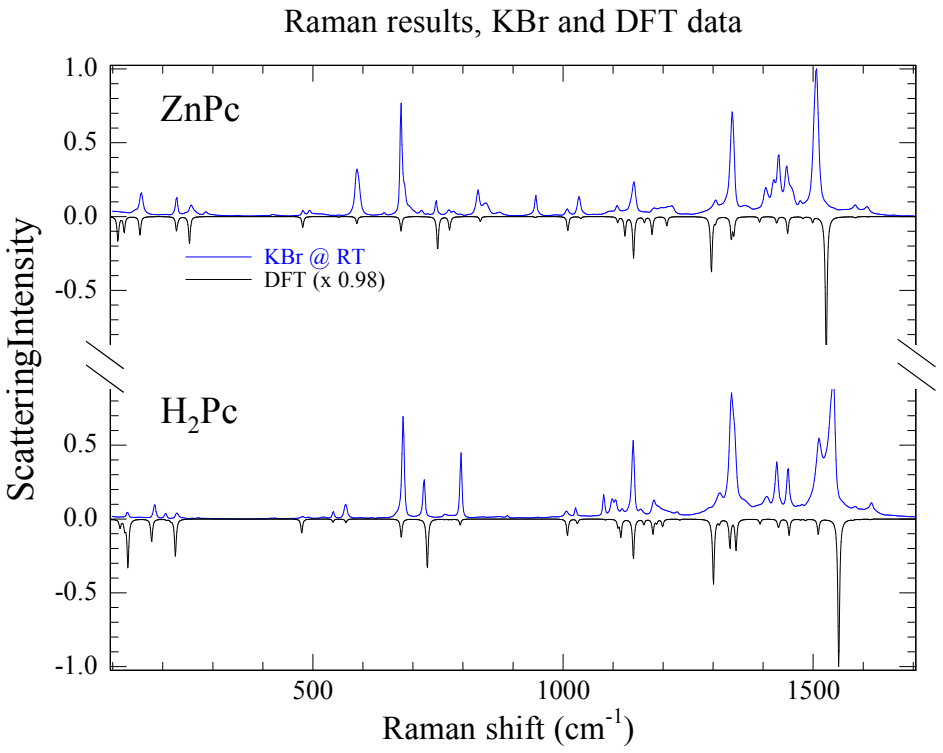

Figure IV.14: A comparison of the observed and calculated Raman spectra for ZnPc (upper panel) and H_2Pc (lower panel). The experimental data were recorded at room temperature in a KBr pellet with 532 nm excitation. The predicted spectra were obtained by transforming the computed Raman activities to Raman intensities with the method outlined in the text.

DFT predictions for the Raman intensity seem to be much less accurate than frequency predictions. For example, assignment of the ZnPc (H_2Pc) strong Raman band at 1338.3 (1336.7) cm^{-1} is not straightforward. From DFT calculations, the most intense band in this range is predicted at 1296.5 (1300.5) cm^{-1}, whereas, from frequency positions, the experimental band could be assigned to either 1336.7 (1333.8) or 1341.6 (1345.5) cm^{-1} predicted bands, or the sum of both. From the structure observed in the case of D_2Pc in KBr, the last assignment is preferred as it is consistent with the observation, depicted in Figure IV.10, that the predicted spectral shift between these two modes is larger for D_2Pc than for H_2Pc. A possible reason for the intensity discrepancies between predicted and observed Raman spectra probably arises from small contributions from resonance effects. This was examined in the earlier work by Tackley *et al.*[2] who chose a range of laser excitation wavelengths from 457 to 1064 nm to record Raman spectra of ZnPc.

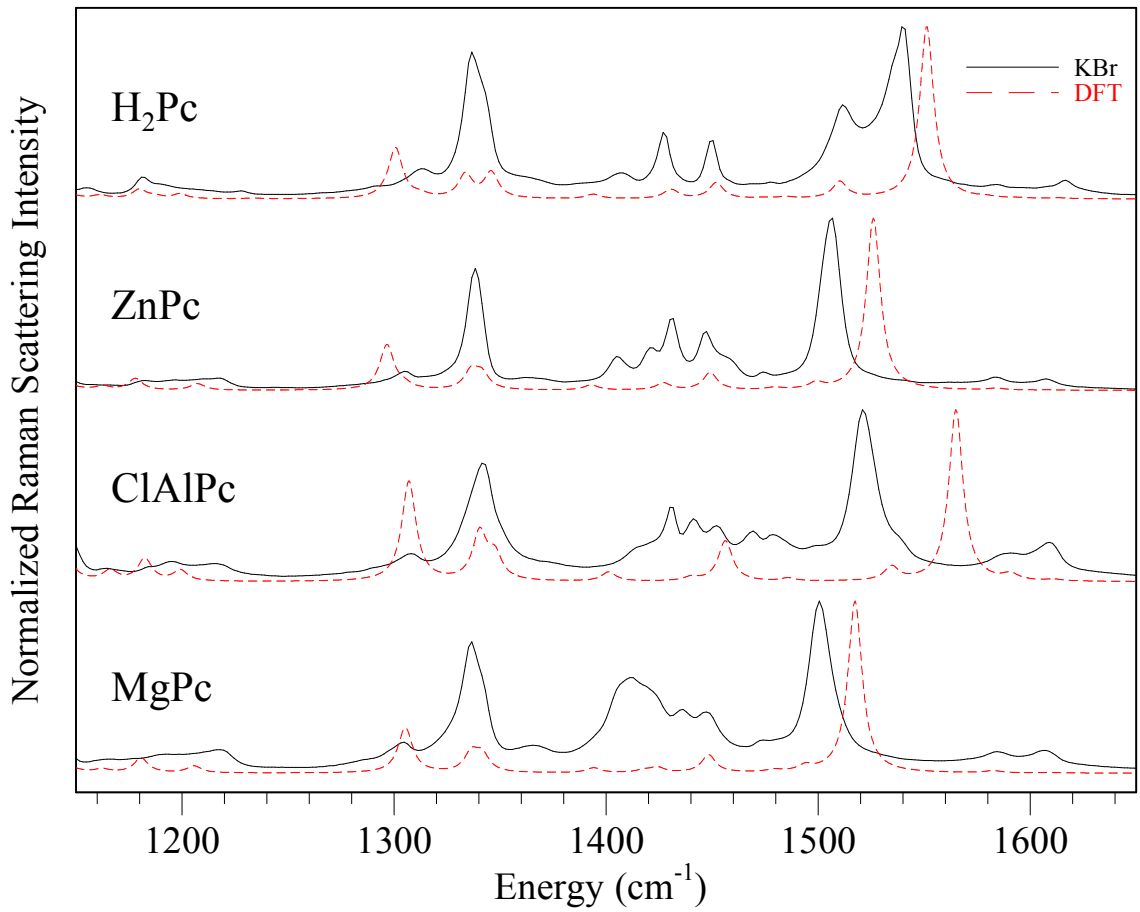

Figure IV.15: Comparison of the experimental Raman spectra in KBr (solid traces) and DFT predicted spectra (dashed traces) of H_2Pc, ZnPc, ClAlPc and MgPc. The DFT results have been fitted using a Lorentzian fitting function with a width of 8 cm^{-1} to simulate the broadening and merging of Raman bands seen in KBr samples.

The main discrepancy between the experimental frequencies and their DFT predicted values concerns the positions of the two most intense Raman bands located at 1539.5 cm^{-1} (H_2Pc) and 1506.8 cm^{-1} (ZnPc). For ZnPc the strongest band is predicted 19 cm^{-1} higher than the observed band while in H_2Pc it is 12 cm^{-1} higher. The attribution in Table IV.2 of the strongest predicted Raman line in ZnPc and H_2Pc spectra is unavoidable due to the dominance of this band in both theory and experiment. Previous calculations by Liu *et al.*[12] for ZnPc and Strenalyuk *et al.*[7] for H_2Pc found even larger discrepancies for these modes. As shown in Figure IV.15, this small lack of agreement between theory and experiment on the most intense Raman mode has been found in the high level calculations of all the Pcs (H_2Pc, ZnPc, MgPc and ClAlPc) for which we have Raman data (see Appendix IV.B for DFT results for magnesium phthalocyanine and chloro-aluminium phthalocyanine). We have nevertheless observed that increasing the size of the basis set leads to improved agreement for these B_{1g}/A_g modes for both ZnPc and H_2Pc. On the other hand, the existence of well-resolved bands at 3080 and 3012 cm^{-1} in the Raman spectra of H_2Pc and ZnPc respectively can be readily attributed

to first overtones of the strongest fundamental modes at 1539.5 and 1506.8 cm^{-1} (see Figure IV.17). As the difference between the observed overtones and the values predicted by simply doubling the fundamental frequencies are so small (c. 1 cm^{-1}) it can be concluded that the anharmonicities of these modes are small. This is an important result as it indicates the frequencies of the true (unperturbed) fundamentals have been identified in the experimental spectra.

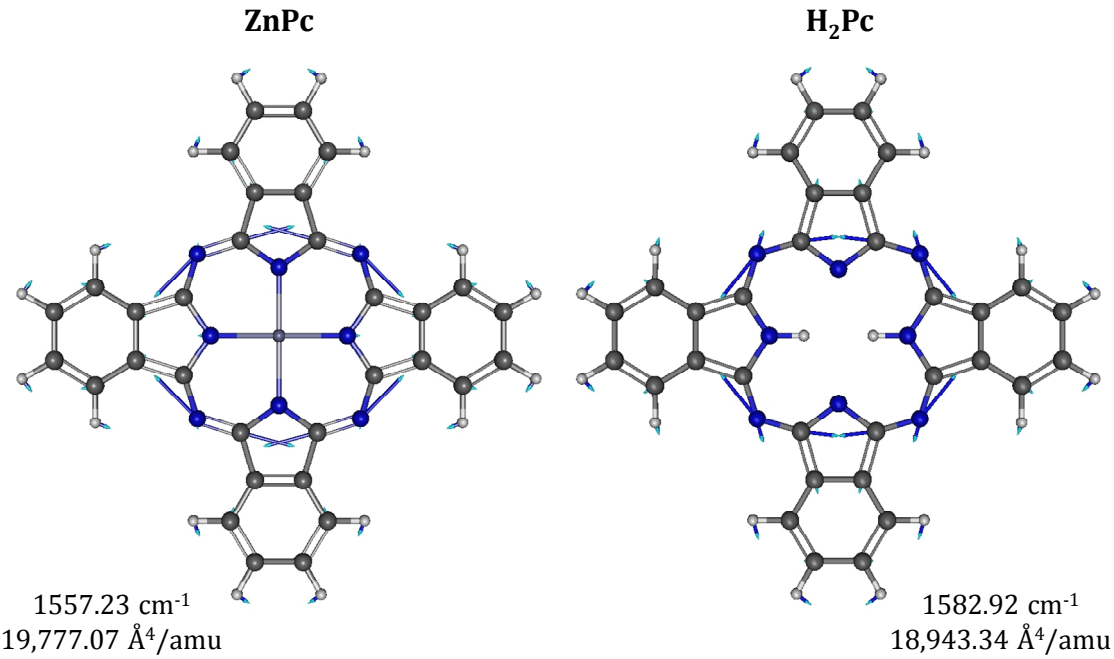

Figure IV.16: Vector displacement representations of the most intense Raman active vibrational modes of ZnPc and H_2Pc calculated using the B3LYP/6-311++G(2d,2p) method.

The most intense 1506.8 and 1539.5 cm^{-1} Raman modes of ZnPc and H_2Pc respectively are of considerable significance since their frequencies shift with the metal centre and as a result, they have been proposed[2] as spectroscopic markers of the ring size in the Pcs. They are also of particular interest, because these are the modes which exhibit amplified emission with pulsed laser excitation[13]. DFT calculations reveal that this mode involves the same motion in both ZnPc and H_2Pc corresponding to the antisymmetric stretch of the four bridging C_α-N_m-C_α bonds and symmetric stretching of the C_α-N-C_α bonds in the four pyrrole groups (see Figure IV.16). From these descriptions, it is clear that this normal mode involves stretching of all 16 C-N bonds in the central ring of the tetrapyrrole. The experimental results of H_2Pc and ZnPc in different low-temperature solids exhibiting amplified emission and a discussion of the properties associated with this unusual phenomenon will be given in Chapter VI.

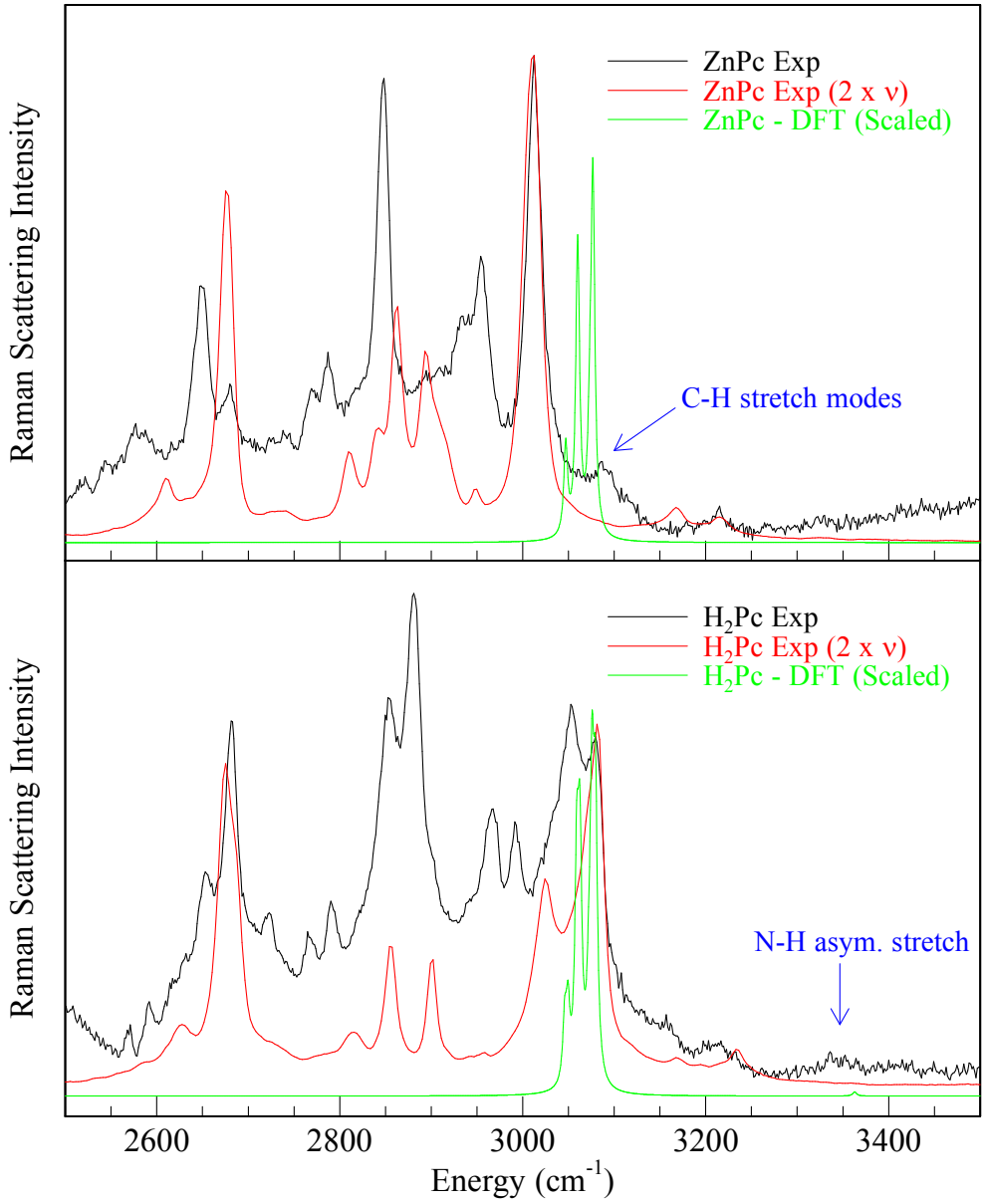

Figure IV.17: Raman spectra of the high frequency stretching regions for ZnPc (upper panel) and H_2Pc (lower panel). To identify any overtones in this region, the frequencies of the intense fundamentals at lower frequencies have been doubled and their intensities reduced. The calculated Raman spectra have been overlapped with suitable scaling for the C-H and N-H stretching modes (0.96 and 0.931 respectively). The frequencies assigned to the C-H stretching modes of ZnPc and N-H asymmetric stretching modes of H_2Pc have been marked with labels and blue arrows.

The first overtones of the strong fundamentals in the 1300 to 1550 cm^{-1} range make it difficult to locate the positions of the weak symmetric fundamental C-H stretching modes of both ZnPc and H_2Pc in the experimental spectra (see Figure IV.17). Symmetric and antisymmetric C-H stretching modes are predicted with very similar frequencies. By eliminating easily identifiable overtone and combination bands and with the help of DFT calculations, the strongest Raman active C-H mode of ZnPc can be identified at 3086.9 cm^{-1}. The corresponding band of H_2Pc has not been identified as it is overlapped by a stronger (factor of 20) overtone band at 3080 cm^{-1} as shown in the lower panel of Figure IV.17.

IV.4.III Isotope Shifts

Table IV.6 summarizes the vibrational modes influenced by N-H deuteration as predicted by DFT calculations. One can notice that theoretically none of these modes exhibit strong Raman activity. In particular, no N-H out-of-plane modes are predicted to be observable in the Raman spectrum. Fortuitously, the new IR experimental data give much more information on these modes. In the D_{2h} point group, only the B_{1u}, B_{2u} and B_{3u} symmetry modes are infrared active. These are the symmetries of the out-of plane N-H bend (NH-OPB), the in-plane N-H bend (NH-IPB) and the antisymmetric N-H stretch modes respectively. DFT values reported in Table IV.6 indicate that these three kinds of modes (in *u* and *g* symmetries) should appear in three distinct spectral ranges 500-800 cm^{-1}, 800-1300 cm^{-1} and around 2500 (D)/3500 (H) cm^{-1} respectively. Table IV.4 summarizes the IR experimental isotopic shifts compared with DFT calculations, allowing a more complete description of these modes.

IV.4.III.a N-H Stretching Modes

The antisymmetric N-H stretching mode has been identified at 3290 cm^{-1} in KBr pellets[3] and at 3273 cm^{-1} in Nujol[3]. This assignment has been supported by the observation of the N-D antisymmetric stretching at 2458 cm^{-1}. Our matrix results also confirm this assignment with the N-H stretching mode of H_2Pc observed in Ar (see Figure IV.2) at 3310 cm^{-1} while the N-D stretching mode of D_2Pc is at 2480.5 cm^{-1}. For a molecule such as HDPc with C_{2v} symmetry, the N-H and N-D bonds are inequivalent and both stretches are expected. Accordingly, the N-H stretch mode of HDPc is observed at 3337.1 cm^{-1} while the N-D stretch is at 2499.0 cm^{-1}. It is clear in Table IV.4 that the experimental and calculated shifts for the N-H stretching modes in H_2Pc and HDPc are in very good agreement. The same can be said for the shift of the N-D stretching modes in HDPc and D_2Pc.

As previously mentioned, the symmetric N-H stretching vibration of H_2Pc (the highest frequency fundamental mode) is predicted to be only very weakly Raman active but the present KBr spectra do show a weak band at 3343 cm^{-1} which could be identified as this stretching mode. A slightly more pronounced band is observed in the Raman spectrum of D_2Pc at 2504.7 cm^{-1} which can be assigned to the symmetric N-D stretching mode. This is in agreement with DFT results but the

location of this N-D mode is in a spectral region where stronger combination and overtone bands render its identification difficult.

IV.4.III.b In-Plane Bending (NH-IPB) modes

Because of its absence in KBr IR spectra of metal-phthalocyanines, Shurvel *et al.*[4] assigned the most intense band of H_2Pc at 1006 cm^{-1} to an N-H deformation. However, assignment of the experimentally observed band at 1006 cm^{-1} to the N-H bending mode appears now to be incorrect for the reasons presented previously in Part IV.4.I. Consistent with experiments, DFT calculations show the corresponding unscaled band (with B_{3u} symmetry) at 1037.22 cm^{-1} in H_2Pc and at 1037.12 cm^{-1} (unscaled) in D_2Pc.

As mentioned in Part IV.4.I, DFT calculations reveal that the corresponding B_{2u} mode occurs at a higher frequency but with greatly reduced intensity. In H_2Pc it is predicted at 1068.4 cm^{-1} (unscaled) and weaker by a factor of more than 20 relative to the most intense mode in the IR spectrum. The corresponding mode in D_2Pc is located at 981.15 cm^{-1} (unscaled) but stronger by a factor of 4 than its H_2Pc counterpart. The locations of these modes in Ar are indicated in Figure IV.9 by the arrows while the stick spectra present the scaled (x0.98) DFT-predictions. This band was found to exhibit the largest shift upon deuteration among the observed IPB modes. The agreement, evident in Figure IV.9 between experiment and theory for the isotope dependence of this mode is excellent. The N-D IPB mode of HDPc is located at 977.8 cm^{-1}, consistent with scaled DFT predictions but the N-H IPB mode of HDPc (predicted at 1033 cm^{-1} with a very low intensity) is masked by an artefact of the difference method used in generating the spectrum shown, its position is indicated by the upward red arrow in Figure IV.9.

In a molecule as large as phthalocyanine, it is important to remember that the vibrational modes are strongly coupled and only the N-H (and N-D) stretching vibrations can be considered to be a pure motion. This coupling is the primary reason why so many different assignments of NH-OPB and NH-IPB modes have been made because attributing them to the experimentally observed modes is not direct. It is especially severe in the case in N-H IPB modes. An indication of the strongly coupled nature of the N-H-bending modes is depicted in the vector diagrams presented in Figure IV.11. As a result, none of the mode correlations yield a ν_H/ν_D ratio larger than about 1.1. This is borne out by the small shifts observed in the 1000-1300 cm^{-1} matrix IR spectra of D_2Pc (Figure IV.9). The

highest frequency N-H IP bending mode that has been found in DFT calculations of H_2Pc is at 1567.89 cm^{-1} which shifts only to 1545.9 cm^{-1} in D_2Pc. The vibrational frequencies calculated by Zhang *et al.*[11] with the smaller 6-31G* basis set are lower — at 1533 cm^{-1} for H_2Pc, shifted to 1514 cm^{-1} in D_2Pc — but consistent with our findings. The reason for the small ν_H/ν_D ratio of 1.014 for this mode becomes evident from the vector displacement diagram where it is clear that this mode is primarily stretching of the bridging C_α-N_m-C_α bonds – a motion which secondarily induces NH-IP bending. Dispersion of the NH-IP bending mode amongst this and other stretching vibrations reduces the ν_H/ν_D ratio and makes this mode very difficult to identify in isotope substitution work. Moreover, the mode at 855 [779] cm^{-1} which corresponds to the most pronounced deuteration effect in the *ungerade* NH IPB modes, is also predicted to have a vanishingly small IR activity.

Five of the N-H IPB modes reported in Table IV.6 are observed in IR matrix spectra of H_2Pc, but only the four located at 1251.6, 1096.1, 1044.6 and 736.6 cm^{-1} in Ar are, with the help of DFT calculations (see Table IV.4), intense enough to be followed upon deuteration. The first of these is numbered (1) and marked by an arrow in the right panel of Figure IV.9. The assignments for the bands in the HDPc spectrum are only tentative as the predicted IR intensities are very weak for this mode. The second mode, involving a small isotopic shift from 1096.1 for H_2Pc to 1080.2 cm^{-1} for D_2Pc in Ar, is the most intense and is clearly observed as indicated by number 2 in the left panel of Figure IV.9. In the HDPc case only the NH component at 1090.9 cm^{-1} in Ar is intense. The third one was discussed above and is marked by arrows in Figure IV.9. The last one present at 736.6 cm^{-1} is included in the spectral range corresponding to NH OPB modes and is shown as IP_1 in Figure IV.8. Following DFT predictions, this mode appears at 722.1 cm^{-1} for D_2Pc and at 727.6 cm^{-1} for HDPc in Ar.

Four of the symmetric N-H IPB modes are observed with weak intensities in Raman spectra. Their frequencies are given in Table IV.2 at 1025.5, 1081.4, 1190, 1227.8 cm^{-1} while their unscaled DFT values are listed in Table IV.6 as 1050, 1107, 1223 and 1259 cm^{-1}. According to DFT calculations, two of the new bands observed for D_2Pc at 986 and 1044 cm^{-1} are the deuterated counterparts of the two first bands. The third band at 1190 cm^{-1} does not appear in the D_2Pc spectrum, and the fourth band is slightly shifted to 1219.5 cm^{-1} in the deuterated sample, in very good agreement with theoretical predictions. These observations reinforce the

assignment of these bands to *gerade* NH IPB modes. As most of the modes involving Raman activity are present in fluorescence spectra, these results can also be related to the emission work of Shkirman *et al.*[14]. They show that deuteration of H_2Pc had only a weak effect on the fluorescence, consistent with the findings of the present Raman spectra and DFT computations. Shkirman *et al.* noted the disappearance of a mode at 1357 cm^{-1} together with the appearance of a mode at 990 cm^{-1} upon H/D substitution. The assignment of the first mode to H_2Pc is doubtful, because it is absent in our experiments and calculations, but the mode at 990 cm^{-1} is in a perfect agreement with the Raman active ND IPB modes measured at 986.1 cm^{-1} (1007 cm^{-1} in Table IV.6).

IV.4.III.c Out-of-Plane Bending (NH-OPB) modes

The antisymmetric NH-OPB mode has previously been assigned to several bands in the 710-760 cm^{-1} range. According to Shurvell *et al.*[4] it is the band at 716 cm^{-1}, while Sammes[3] identified it as the band at 735 cm^{-1}, which shifts to 549 cm^{-1} in D_2Pc. However, as shown in Figure IV.6 this spectral region is extremely complex in KBr spectra due to the presence of multiple bands, most of which are cluster related. In our matrix spectra, only a single H_2Pc band clearly disappears upon deuteration in this region. As shown in Figure IV.8 this is the 764.8 cm^{-1} band of H_2Pc in Ar labelled OP_1. In contrast to the IP bending modes, DFT calculations predict a clear correlation for the OP bending modes between the high frequency modes in H_2Pc and the low frequency modes in D_2Pc. Thus for one specific IR mode of H_2Pc at 778.36 cm^{-1} a shift to 566.3 cm^{-1} (unscaled values) is expected as indicated in Table IV.6. For this reason we assign the band around 765 cm^{-1} as the main NH-OPB mode of H_2Pc. The band shifts to 742.5 cm^{-1} in HDPc in agreement with the DFT calculations showing an unscaled frequency of 754.4 cm^{-1} for the only HDPc OP mode with a large IR intensity in this region. The calculated frequency for the ND-OPB mode in D_2Pc (566.3 cm^{-1}) is in good agreement with earlier predictions of Zhang *et al.*[11]. Unfortunately, this D_2Pc mode is so weak that it is not easily detected. However, a very weak band has been observed in an Ar matrix at 555 cm^{-1}. On the other hand, a weak new band at 777.8 cm^{-1} appears in D_2Pc spectrum, it corresponds to the unobserved band calculated at 804 cm^{-1} (788 cm^{-1} scaled) for H_2Pc.

Figure IV.8 shows a triplet centred at 730 cm^{-1} in the H_2Pc spectrum, becoming very complex in HDPc and congested in D_2Pc spectra. The most intense component at 731 cm^{-1} in Ar (labelled IP_2 in Figure IV.8) is assigned to a B_{3u} mode and is nearly unshifted upon deuteration. It constitutes one part of the broader structured feature in HDPc and D_2Pc. The component of highest energy is the NH IPB mode discussed in the previous part (IP_1), shifted from 736.5 to 727.6 to 722.1 cm^{-1} from H_2Pc to HDPc to D_2Pc in Ar, and constitutes the lowest IP bending mode of the D_2Pc spectrum. The last component (OP_2 at 722.8 cm^{-1} in Figure IV.8) at the lowest frequency in H_2Pc spectrum is another NH OPB mode. As reported in Table IV.6 it is affected by deuteration but in an unexpected way. It is predicted at 732 cm^{-1} (scaled) in D_2Pc, i.e. at the same frequency as the B_{3u} mode, explaining the experimental broadening (or structure in N_2) of this band. A comparison of scaled (x0.98) DFT frequencies is presented in Figure IV.8 with the recorded spectra showing very close agreement.

A surprising finding of the present and Zhang's earlier[11] DFT calculations is that this last N-D OP bending mode of D_2Pc is predicted at a higher frequency than the corresponding mode of H_2Pc. Such behaviour is predicted for a few other modes, as revealed in Table IV.6. An analysis of this unexpected behaviour follows directly.

IV.4.III.d Inverse isotope substitution effects

In order to correlate the complex frequency shifts of H_2Pc and D_2Pc, the DFT computed frequencies were generated by increasing the masses of the two central hydrogens from 1 to 2 amu in increments of 0.05 amu. The results of this calculation are shown in Figure IV.18 for B_{1u} symmetry between 550 and 850 cm^{-1}. The correlations were made by visually inspecting the vector displacement diagrams, four of which are presented in the figure.

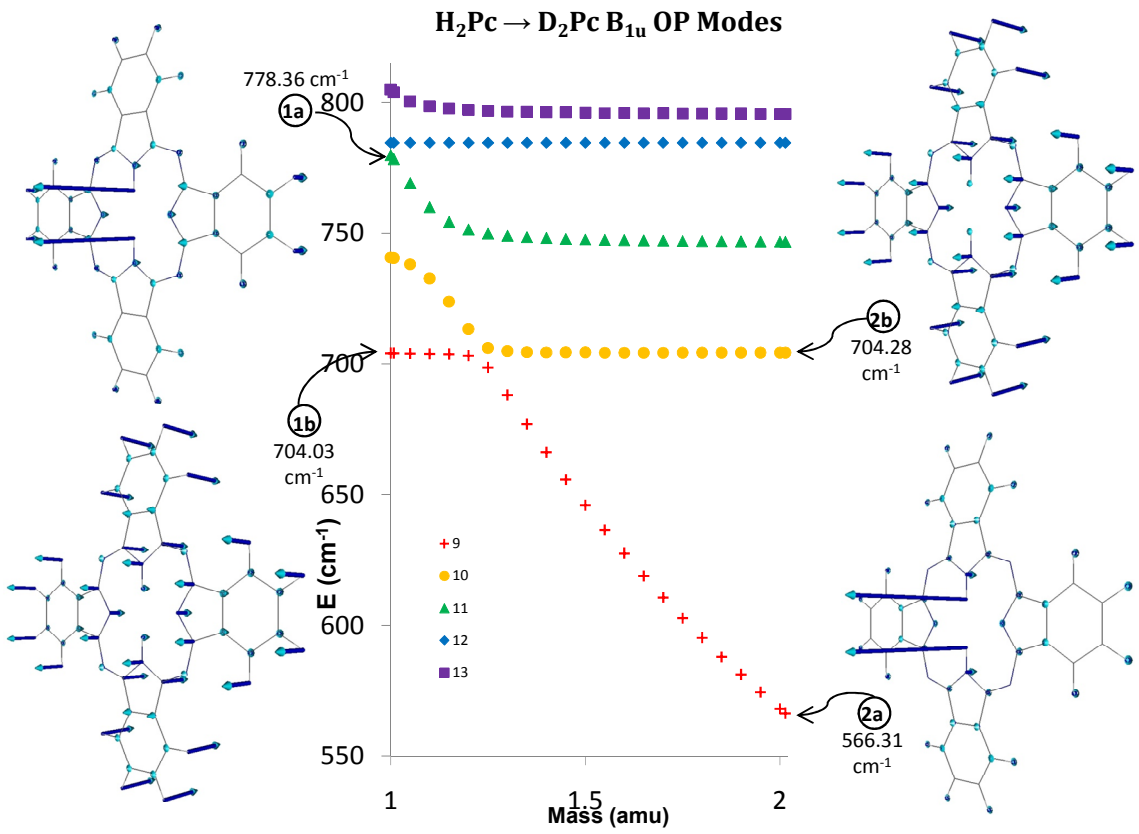

Figure IV.18: DFT predictions of the isotope dependence of the IR-active OPB B_{1u} modes in H_2Pc and D_2Pc calculated at 0.05 amu increments. The vector displacements, two of which are shown on either side of the plot, were used in establishing the correlations.

From the vector diagrams shown in Figure IV.18, it is evident that the purest N-H OPB modes in H_2Pc is located at 778.36 cm^{-1} (unscaled) which shifts down to 566.31 cm^{-1} in D_2Pc. This correlation results in the expected (within the accuracy of the DFT calculation) ν_H/ν_D ratio of 1.374 for H/D isotope substitution in a "pure" N-H mode. The large frequency shift of the pure NH-OPB mode results in it crossing several other out-of-plane bending modes. These crossings are more or less avoided depending on the coupling between modes. In Figure IV.18, it is clear that there is almost no avoided crossing with the mode at 704 cm^{-1} which as shown, involves no NH bending. In contrast, there is a strong avoided crossing with the mode at 740 (747) cm^{-1} in H_2Pc (D_2Pc). These values when scaled by 0.98 (725.6 and 731.8 cm^{-1}) correspond to the resolved bands at 724.7 and 730.9 cm^{-1} in N_2, shown in the middle panel of Figure IV.8. A consequence of this avoided crossing is that the 740 cm^{-1} H_2Pc mode exhibits the unusual behaviour of having an increased frequency (747 cm^{-1}) in the heavier isotopomer.

Even though this is only a small upward shift (ν_H/ν_D = 0.992) it greatly complicates the recorded spectra as it occurs in the region where two strong in-

plane modes of H_2Pc (D_2Pc) are located at 730.9 (728.0) and 736.4 (722.1) cm^{-1} in N_2. Contrary to expectation, the mode-crossing results in the lowest frequency mode (OP_2 at 724.5 cm^{-1}) of the 730 cm^{-1} H_2Pc triplet, shifting up to the highest frequency mode of the D_2Pc triplet (at 731.4 cm^{-1}). These calculations show clearly that the band at 729.9 cm^{-1} in D_2Pc is an NH-OPB mode but distinct from the two strong bands in HDPc and H_2Pc at 742.5 and 767.9 cm^{-1} (values in Ar) respectively.

The last important avoided crossing evident in Figure IV.18 is located near the mass 1 (H_2Pc). In fact, while the 566 cm^{-1} mode of D_2Pc involves almost pure ND motion, the 778 cm^{-1} mode of H_2Pc also exhibits CH bending motions. Similar curvature is present for the weak IR active mode of H_2Pc at 804 cm^{-1}. The vector diagram of Figure IV.11 highlights the similarities between the motions in these two modes in H_2Pc, however the curvature of the higher energy mode in Figure IV.18 occurs only in the vicinity of mass 1.

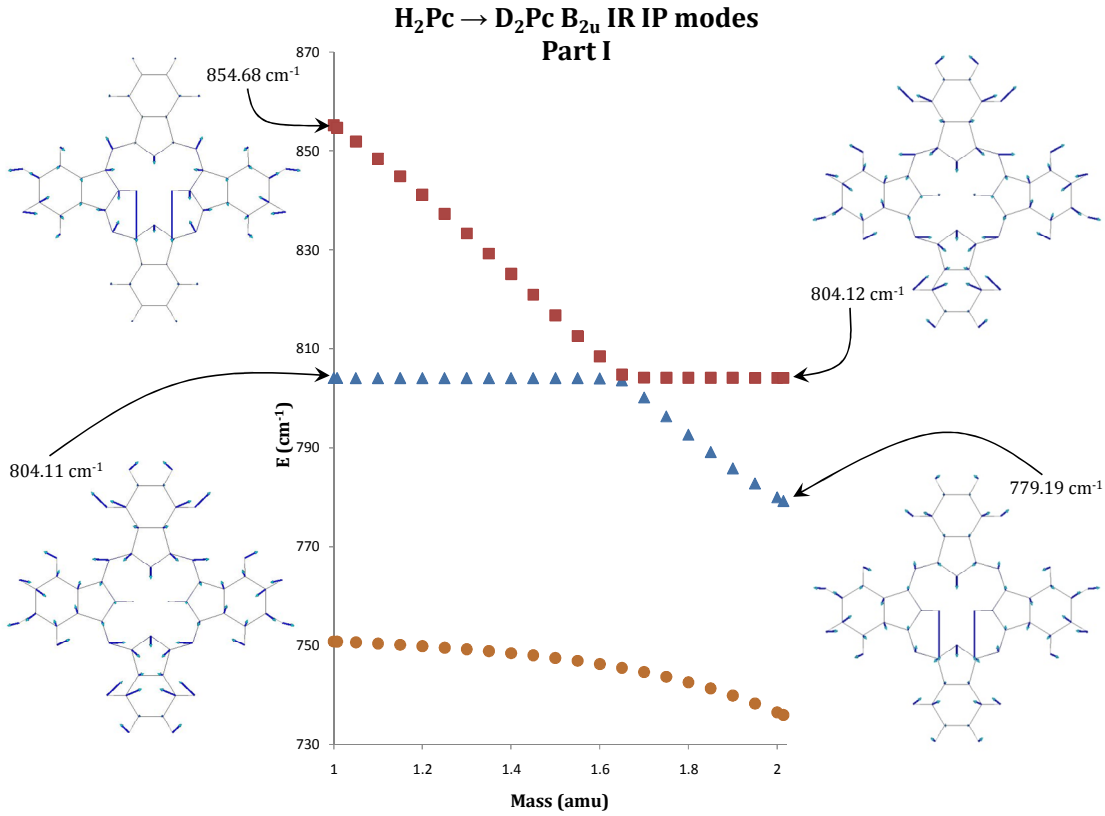

Figure IV.19: DFT predictions of the isotope dependence of the lower frequency IR-active IPB B_{2u} modes in H_2Pc and D_2Pc calculated at 0.05 amu increments. One avoided crossing is seen in this plot while another at higher frequencies is shown in Figure IV.20. The vector displacement diagrams for the modes involved are also shown.

Such correlation curves have been calculated for all the symmetry groups. Two strong avoided crossing events were apparent for the IR active B_{2u} modes involving In-Plane Bends (IPB). The lower frequncy modes are shown in Figure IV.19. The H_2Pc mode at 854.68 cm^{-1}, predominately involving a N-H bending

motion with a small amount of coupling to the benzene and central rings, was correlated to a similar mode at 779.19 cm^{-1} in D_2Pc while the mode at 804.11 cm^{-1} in H_2Pc was correlated with the 804.12 cm^{-1} in D_2Pc. The modes at ~804.1 cm^{-1} involve an asymmetric 'breathing' motion of the isoindole rings not containing the N-H bonds with distortion of the other two isoindole rings. Though the increase in energy of 0.01 cm^{-1} in the 804.1 cm^{-1} modes is small and may be ascribed to calculation error, close inspection of the region were the curves appear to cross reveals an avoided crossing. The energy values calculated at NH hydrogen masses of 1.6, 1.65 and 1.7 amu for the mode originating at 854.68 cm^{-1} (represented in Figure IV.19 square symbols) were 808.44, 804.75 and 804.19 cm^{-1}, while those values for the mode originating at 804.11 cm^{-1} (represented by triangle symbols) were 804.04, 803.63 and 800.18 cm^{-1} indicating no crossing of the two curves.

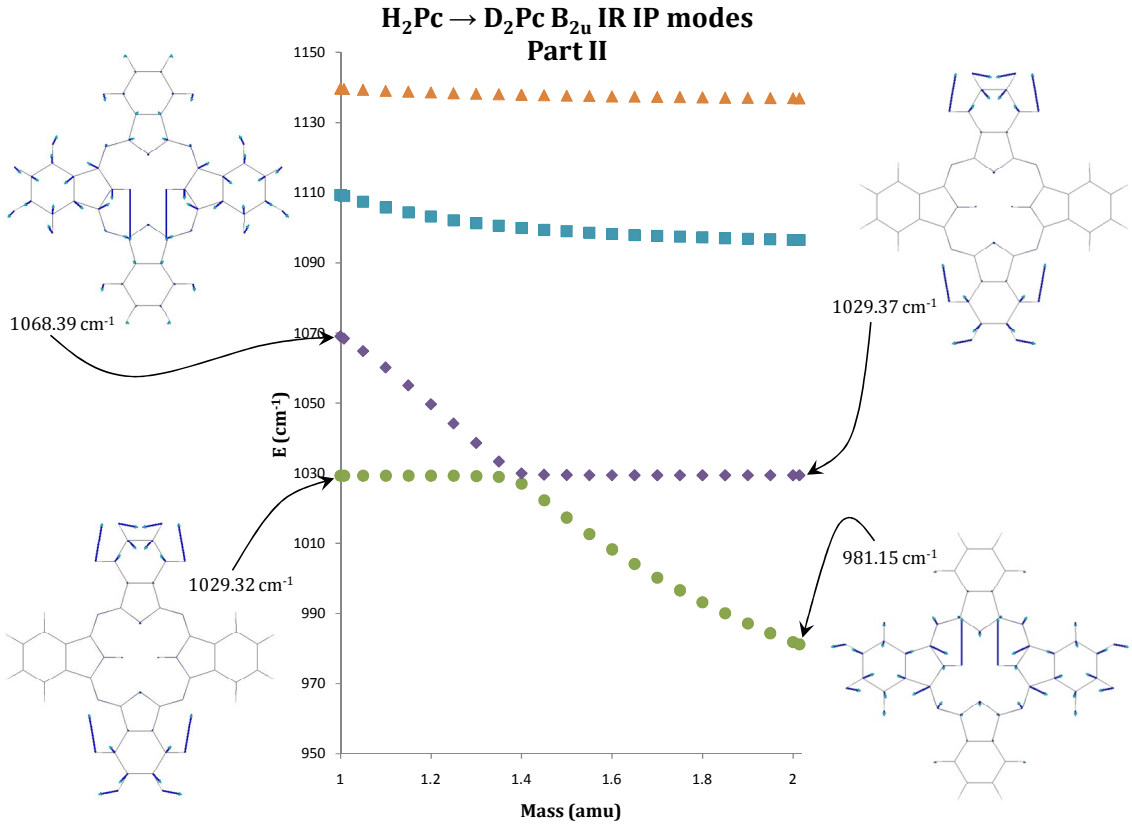

Figure IV.20: DFT predictions of the isotope dependence of the higher frequency IR-active IPB B_{2u} modes in H_2Pc and D_2Pc calculated at 0.05 amu increments. One avoided crossing event is seen in this plot while another at lower frequencies is shown in Figure IV.19. The vector displacement diagrams for the modes involved are also shown.

The other avoided crossing seen for B_{2u} symmetry modes in a higher frequency region shown in Figure IV.20 involve an N-H bending mode coupled to a rocking motion of the attached pyrrole ring distorting the benzene ring, seen in H_2Pc at 1068.39 cm^{-1} and correlated to the D_2Pc mode at 981.15 cm^{-1}. The curve

connecting these modes appear to cross the curve connecting the asymmetric benzene 'breathing' modes seen in H_2Pc at 1029.32 cm^{-1} and at 1029.37 cm^{-1} in D_2Pc. Again inspecting the apparent crossing region, the energy values for the H masses 1.35, 1.40 and 1.45 amu for the curve originating at 1029.32 cm^{-1} (green circle symbols) were found to be 1029.00, 1027.00 and 1022.22 cm^{-1} and those for the curve originating at 1068.39 cm^{-1} (purple diamond symbols), 1033.31, 1029.94 and 1029.54 cm^{-1}. The origin of the mode at 1029.37 cm^{-1} from the mode at 1068.39 cm^{-1} can be confirmed by observing that the relative direction of the benzene 'breathing' motions to the weakly coupled N-H motions in D_2Pc is the same as the relative direction the weakly coupled benzene 'breathing' motions to the strong N-H motions in the H_2Pc mode.

The results for the correlation curves for the Raman active modes are shown in Figure IV.21 within the spectral region of the NH OP and IP bending modes (B_{2g} and B_{1g} symmetry). Like the IR active modes discussed above, few crossings occur between masses 1 and 2 for OPB modes while the diagrams are more complex for IPB modes, involving both large avoided crossings and the traversal of weakly coupling modes. In all cases where a ν_H/ν_D ratio of less than 1 occurs, it is evident from the mode correlation diagrams that it results from avoided crossings. Moreover, the vector displacement diagrams reveal that in these cases, the direction of the N-H bending motion changes between the light and the heavy isotopomers.

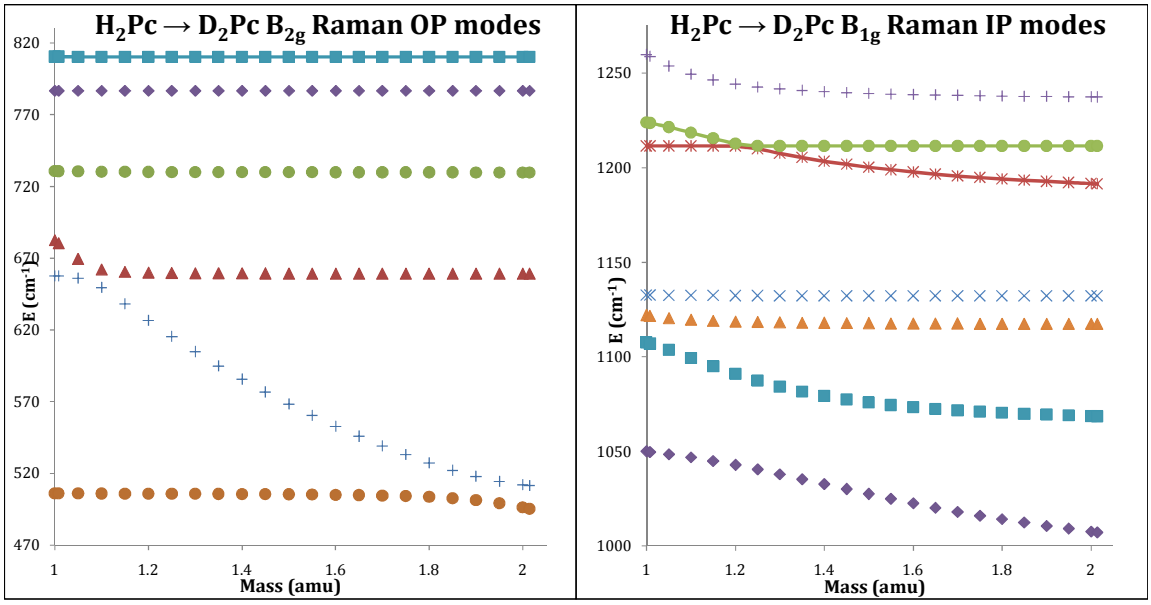

Figure IV.21: DFT predictions of the isotope dependence of the Raman active OPB B_{2g} (left panel) and IPB B_{1g} (right panel) modes in H_2Pc and D_2Pc calculated at 0.05 amu increments.

Initial attempts to correlate the B_{1g} modes of the free-base phthalocyanine isotopomers and the A_{2g} and B_{2g} modes of zinc phthalocyanine were found to be difficult. In particular, the B_{1g} modes of H_2Pc calculated at 841.82 and 907.44 cm^{-1} with those belonging to D_2Pc calculated at 762.54 and 880.30 cm^{-1} and one of these free-base modes with the optically inactive A_{2g} mode of ZnPc at 864.41 cm^{-1}. Comparisons of the very similar vector diagrams for these vibrations in Figure IV.22 found that the best matches for the 864.41 cm^{-1} mode of ZnPc were the 841.82 cm^{-1} mode of H_2Pc and 880.30 cm^{-1} mode of D_2Pc. The remaining H_2Pc vibration at 907.44 cm^{-1} was correlated with the D_2Pc vibration at 762.54 cm^{-1} with a ν_H/ν_D ratio of 1.19. The ν_H/ν_D ratio for the former pair of vibrations was, however, exceptional low at 0.9563. From the results of the calculation of the isotope dependence of the B_{1g} vibrational energies shown in the right-hand panel of Figure IV.21, a clear correlation between the 841.82 and 762.54 cm^{-1} modes and 907.44 and 880.30 cm^{-1} of H_2Pc and D_2Pc was seen, reversing the previous assignments and giving more orthodox ν_H/ν_D ratios of 1.1040 and 1.0308 respectively. The 864.41 cm^{-1} mode of ZnPc has been tentatively assigned to the 907.44 and 880.30 cm^{-1} modes of H_2Pc and D_2Pc due to their lower ν_H/ν_D ratio and that the additional H_2/D_2Pc B_{1g} symmetry mode was expected to contain a significant contribution from the N-H IP bending motion.

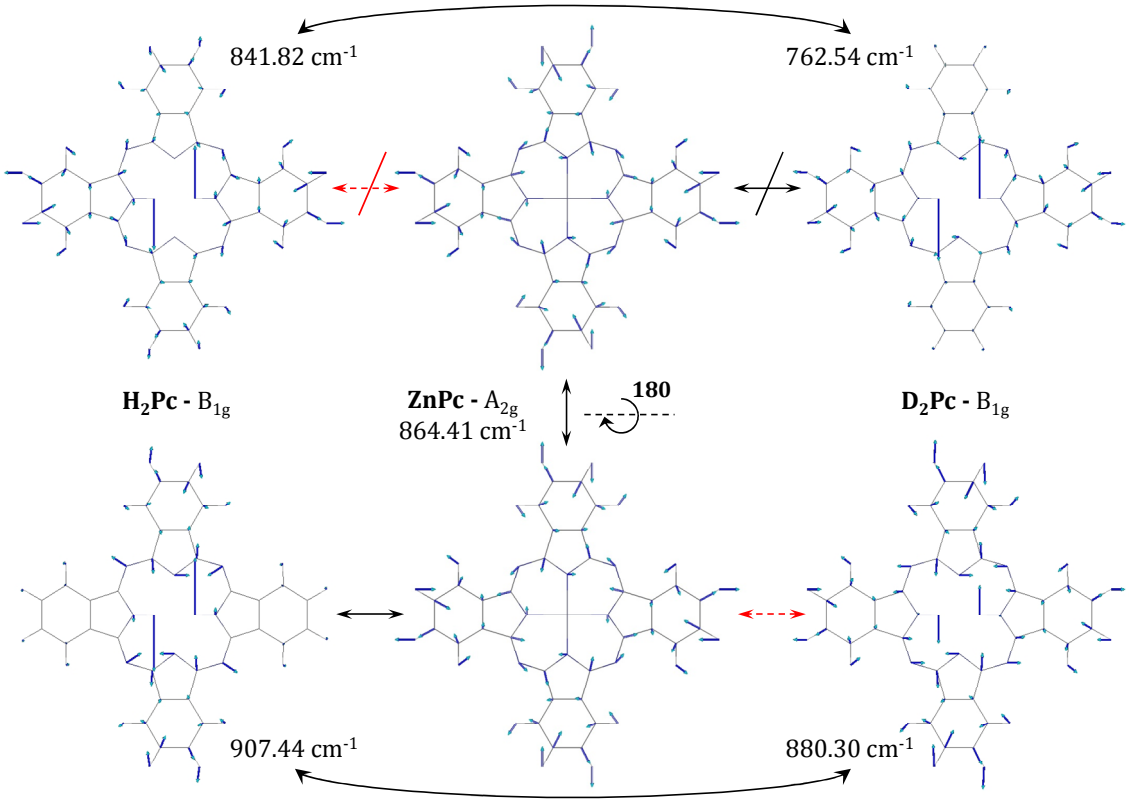

Figure IV.22: Correlation of B_{2g} symmetry modes of H_2Pc and D_2Pc and A_{2g} mode of ZnPc. The curved arrows indicate the corresponding H_2Pc and D_2Pc modes matched by comparing the diagrams shown and using the mass correlation plot in Figure IV.21. The ZnPc diagram may be rotated by 180° around the N-Zn-N bonds for comparison with the H_2/D_2Pc modes. The dashed arrows represent the initial correlations made between the H_2/D_2Pc and ZnPc modes using the vector diagrams only.

IV.5 Summary and conclusions

The use of the low temperature, matrix-isolation technique provides narrow IR lines and spectra that are largely free of aggregate species compared with conventional sampling methods. It allows new assignments of the N-H In Plane Bending (NH-IPB) and N-H Out-of-Plane Bending (OPB) IR modes of free-base phthalocyanine. The assignments were confirmed by isotopic substitution with deuterium for the two central N-H bonds and by DFT calculations. The calculated frequencies are in very good agreement with the experimental values.

DFT calculations are an indispensible tool for band assignments and essential for predictions of non-observed vibrational modes. They are conducted on the three isotopomers of the free-base (H_2Pc, HDP, and D_2Pc) together with a metallo-phthalocyanine (ZnPc). An overview of the vibrations of these molecules is necessary to achieve global assignments and establish correlations between the modes of the four molecules. All the computational data, combined with IR and

Raman experimental results, give a comprehensive overview of the vibrational behaviour of phthalocyanines, with a specific emphasis on the NH motion of the free-base Pc.

The NH stretching modes are confirmed to be well isolated from other motions of the Pc skeleton. Thus the H_2Pc (D_2Pc) NH(D) antisymmetric stretch is located around 3310 (2480) cm^{-1} in rare gas matrices (a slightly higher value than in KBr) while the NH(D) stretch of HDPc is at 3337 (2500) cm^{-1} in the same solids. The H_2Pc (D_2Pc) symmetric stretch is predicted 52 (34) cm^{-1} above its antisymmetric counterpart, corresponding to very weak bands of Raman spectra in KBr located at 3363 cm^{-1} (2504.7 cm^{-1}).

Two of the OP bending modes are found to be specifically assigned to NH bends, around 700 cm^{-1} for NH and around 500 cm^{-1} for ND. Only one of these two is IR active in H_2Pc and D_2Pc. They are observed around 765 cm^{-1} and 555 cm^{-1} respectively in rare gas matrices. The corresponding NH band of HDPc is experimentally identified at 742 cm^{-1}, whereas theoretical results clearly show a less isolated NH bending motion in this isotopomer. In partial agreement with Zhang's results[11], we find other OPB modes affected upon H/D substitution.

Calculations established that previous assignments of the IR NH-IPB in H_2Pc and D_2Pc in KBr or Nujol were not correct. The present work leads only partly to the same conclusions as Zhang's calculations. The NH-IP bending modes are spread out over eight modes, four of which have been clearly identified in the matrix IR spectra. The others are predicted to be too weak to be observed. The IPB most affected modes by NH(D) motion are located between 750 and 1250 cm^{-1} for both IR and Raman modes. The largest observed ν_H/ν_D ratio for this kind of mode is 1.083 for the band at 1045 cm^{-1} in the IR spectrum of H_2Pc in rare gas matrices. The small ratio arises as a result of the coupling of the mode with other modes and its ensuing dilution over these modes.

Several N-H bending modes exhibit the peculiar behaviour of $\nu_H < \nu_D$ in H/D substitution work, one of them, an OPB mode, is observed in the 730 cm^{-1} region. This behaviour can be traced back to the avoided-crossing of these modes by the "pure" NH bending mode. This effect has been examined in a theoretical study involving a continuous change of the isotopic mass from H_2Pc to D_2Pc. A consequence of this frequency increase in the heavier isotopomer is that the direction of the N-D OP bend is reversed from the N-H OP bending.

The spectral window between the C-H stretching and the N-H stretching modes (3100 - 3300 cm^{-1}) was carefully examined in the low temperature matrix-IR spectra for evidence of the *cis* isomer of H_2Pc, predicted by DFT calculations from the work of Strenalyuk *et al.*[7] to absorb in this region. One unaccounted for band is located at 3104 cm^{-1} in Ar and using the scaling factor of 0.93 we found appropriate for the N-H stretch, it is close to the predicted value of 3094 cm^{-1} (unscaled 3323 cm^{-1}). However, as this band is only a partially resolved feature on the shoulder of the strongest C-H stretching mode of the dominant *trans* form, the existence of the unstable *cis* isomer cannot be identified in the present study. To examine this possibility adequately, one would propose working with H_2Pc-d_{16} but in addition, a means of increasing the content of the *cis* form must be utilised. A possible approach for enhanced isolation of the *cis* form involves electronic promotion of the interconversion of the two *trans* forms of H_2Pc.

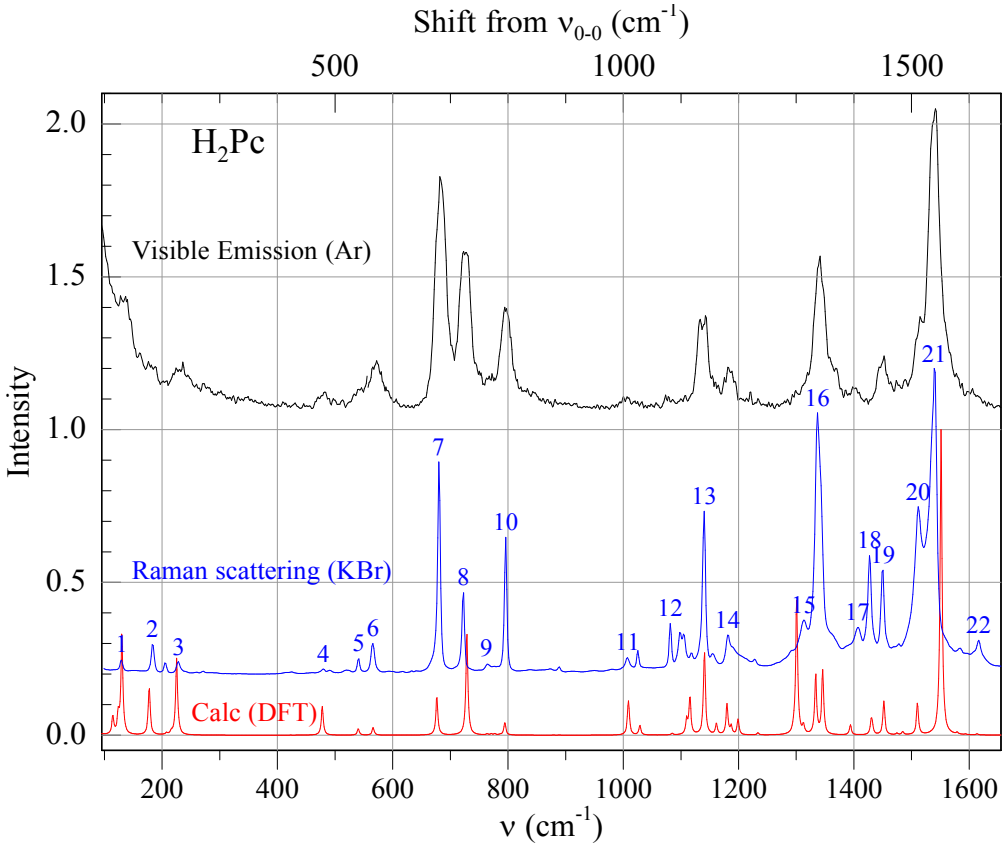

Figure IV.23: A comparison of the experimentally recorded Raman spectrum and the visible fluorescence spectrum of H_2Pc in an Ar matrix. The correspondence between the two spectra is striking especially with regard to the line positions. DFT prediction of the ground state vibrations clearly allows assignment of the emission bands.

The Raman spectra of H_2Pc in KBr reveal, as presented in Figure IV.23 a striking resemblance to the fluorescence recorded for the same molecules isolated in rare gas and nitrogen matrices (see Chapter VI). The very evident similarities

between the recorded Raman scattering and the matrix fluorescence spectra indicates the close correspondence between the vibrational levels accessed in these transitions. This behaviour can be understood when it is noted that the observed Raman modes all involve in-plane vibrations and it is known[15] that the fluorescence lines involve *gerade*, and in-plane vibrational modes of the ground state, more precisely A_{1g}, A_{2g}, B_{1g} and B_{2g} modes for ZnPc and A_g and B_{1g} modes for H_2Pc. Since the selection rules for Raman scattering and $S_1 - S_0$ vibronic intensity distributions are very similar, the present Raman analysis will be very useful for band assignments of the emission spectra.

The ground state vibrational analysis conducted in this study is an essential precursor to understanding the transitions to and from the first excited electronic states. The Raman active N-H in-plane band observed at 1025.5 cm^{-1} is identified as the most likely mode capable of coupling the v=0 level of the S_2 (Q_Y) electronic state and vibrationally excited levels of the S_1 (Q_X) states of H_2Pc. Moreover, its shift to 986.1 cm^{-1} for D_2Pc is fully consistent with Bondybey's results[16] on fluorescence excitation of the H_2Pc and D_2Pc in solid Ar

IV.6 References

(1) Tackley, D. R.; Dent, G.; Smith, W. E. *Physical Chemistry Chemical Physics* **2000**, *2*, 3949.

(2) Tackley, D. R.; Dent, G.; Smith, W. E. *Physical Chemistry Chemical Physics* **2001**, *3*, 1419.

(3) Sammes, M. P. *Journal of the Chemical Society-Perkin Transactions 2* **1972**, 160.

(4) Shurvell, H. F.; Pinzuti, L. *Canadian Journal of Chemistry* **1966**, *44*, 125.

(5) Scheidt, W. R.; Dow, W. *Journal of the American Chemical Society* **1977**, *99*, 1101.

(6) Nguyen, K. A.; Pachter, R. *Journal of Chemical Physics* **2001**, *114*.

(7) Strenalyuk, T.; Samdal, S.; Volden, H. V. *Journal of Physical Chemistry A* **2008**, *112*, 4853.

(8) Matsumoto, S.; Matsuhama, K.; Mizuguchi, J. *Acta Crystallographica Section C-Crystal Structure Communications* **1999**, *55*, 131.

(9) The D_{2h} symmetry labels of the normal modes of H_2Pc produced by the Gaussian 03 package has, by convention, the z-axis aligned along the N-H bonds in the molecular plane. In contrast the z-axis is perpendicular to the plane of the molecule for the D_{4h} symmetry of ZnPc. For ease of comparison of the vibrational modes of these two molecules it is advantageous to re-orient the z-axis of H_2Pc perpendicular to the molecule plane. This has the effect of interchanging the 1 and 3 subscript labels of the Mulliken symbols.

(10) Gladkov, L. L.; Konstantinova, V. K.; Ksenofontova, N. M.; Sokolov, N. A.; Solov'ev, K. N.; Shkirman, S. F. *Journal of Applied Spectroscopy* **2002**, *69*, 47.

(11) Zhang, X.; Zhang, Y.; Jiang, J. *Vibrational Spectroscopy* **2003**, *33*, 153.

(12) Liu, Z.; Zhang, X.; Zhang, Y.; Jiang, J. *Spectrochimica Acta Part A: Molecular and Biomolecular Spectroscopy* **2007**, *67*, 1232.

(13) Dozova, N.; Murray, C.; McCaffrey, J. G.; Shafizadeh, N.; Crepin, C. *Physical Chemistry Chemical Physics* **2008**, *10*, 2167.

(14) Shkirman, S. F.; Sokolov, N. A.; Konstantinova, V. K.; Solov'ev, K. N. *Journal of Applied Spectroscopy* **2001**, *68*, 410.

(15) Huang, T. H.; Rieckhoff, K. E.; Voigt, E. M. *Journal of Chemical Physics* **1982**, *77*, 3424.

(16) Bondybey, V. E.; English, J. H. *Journal of the American Chemical Society* **1979**, *101*, 3446.

Appendix IV.A: DFT vibrational frequencies of H_2Pc, D_2Pc and ZnPc

IV.A.1 Introduction

In this appendix the vibrational frequencies and infra-red absorption and Raman scattering intensities of H_2Pc, D_2Pc and ZnPc calculated using the DFT B3LYP functional and 6-311++G(2d,2p) basis set. By convention the D_{2h} symmetry labels of the normal modes of H_2Pc produced by the Gaussian-03 computational software package has the z-axis aligned with the N-H bonds in the molecular plane. In contrast it has the z-axis perpendicular to the plane of the molecule for the D_{4h} symmetry of ZnPc. For ease of comparison of the vibrational modes of these two molecules it is advantageous to re-orient the z-axis of H_2Pc perpendicular to the molecule plane. This has the effect of interchanging the 1 and 3 subscript labels of the Mulliken symmetry symbols. The symmetry labels listed for D_2Pc are also valid for H_2Pc.

IV.A.2 IR and Raman DFT vibrational frequencies

Table IV.A.1 contains the infra-red vibrational frequencies and intensities. The IR active B_{2u} and B_{3u} symmetry modes of H_2Pc/D_2Pc correlate to the degenerate E_u modes of ZnPc. The IR active B_{1u} modes of H_2Pc/D_2Pc however correlated with the IR active ZnPc A_{2u} modes and optically silent B_{2u} modes. Table IV.A.2 contains the Raman active vibrational frequencies and intensities. The A_g modes of H_2Pc/D_2Pc correlate with the A_{1g} and B_{1g} modes of ZnPc. The B_{3g} and B_{2g} symmetry modes H_2Pc/D_2Pc correlate with the degenerate E_g modes of ZnPc. The Raman active B_{1g} modes of H_2Pc/D_2Pc correlate with the Raman active B_{2g} and optically silent A_{2g} modes of ZnPc.

Table IV.A.1: DFT B3LYP / 6-311++G(2d,2p) computed infra-red frequencies (ν, cm^{-1}) and intensities (km/mole) for H_2Pc, D_2Pc and ZnPc.

	H_2Pc		**D_2Pc**			**ZnPc**			**ν_H / ν_D**
	ν_H	Int	ν_D	Int	Sym	ν_{Zn}	Int	Sym	**Ratio**
1	122.96	4.73	122.90	4.73	B_{3u}	120.61	3.60	E_u	1.0005
2	283.07	8.16	282.74	8.09	B_{3u}	306.37	2.51	E_u	1.0012
3	502.57	6.18	502.48	6.30	B_{3u}	511.37	7.87	E_u	1.0002
4	567.38	2.59	564.42	1.59	B_{3u}	585.85	10.37	E_u	1.0052
5	632.31	38.21	630.00	41.13	B_{3u}	652.85	7.78	E_u	1.0037
6	746.46	74.09	743.13	70.60	B_{3u}	768.00	61.07	E_u	1.0045
7	799.06	9.49	796.68	11.85	B_{3u}	814.13	0.81	E_u	1.0030
8	891.84	69.19	889.97	67.59	B_{3u}	906.01	55.53	E_u	1.0021
9	1028.73	1.99	1028.57	1.17	B_{3u}	1030.03	11.40	E_u	1.0002
10	1037.22	661.50	1037.12	660.35	B_{3u}	1111.13	174.45	E_u	1.0001
11	1086.86	0.64	1085.32	0.94	B_{3u}	1084.48	153.67	E_u	1.0014
12	1131.89	75.42	1130.74	71.07	B_{3u}	1138.25	146.17	E_u	1.0010
13	1186.12	13.25	1185.99	14.29	B_{3u}	1190.02	30.39	E_u	1.0001
14	1209.22	0.53	1205.74	1.17	B_{3u}	1210.25	2.10	E_u	1.0029
15	1312.67	52.22	1312.06	50.11	B_{3u}	1320.40	49.72	E_u	1.0005
16	1338.84	11.65	1330.91	0.00	B_{3u}	1343.80	21.81	E_u	1.0060
17	1358.84	176.97	1355.29	186.12	B_{3u}	1359.59	233.93	E_u	1.0026
18	1429.46	22.07	1427.69	16.16	B_{3u}	1436.61	56.00	E_u	1.0012
19	1490.66	61.09	1490.66	60.72	B_{3u}	1491.01	32.70	E_u	1.0000
20	1504.98	0.51	1504.97	0.43	B_{3u}	1509.13	0.14	E_u	1.0000
21	1531.54	119.23	1531.48	121.27	B_{3u}	1511.62	97.41	E_u	1.0000
22	1610.84	4.40	1610.83	4.49	B_{3u}	1615.53	8.41	E_u	1.0000
23	1639.07	10.05	1639.07	10.13	B_{3u}	1641.29	10.73	E_u	1.0000
24	3172.80	5.45	3172.80	5.45	B_{3u}	3173.97	5.98	E_u	1.0000
25	3190.06	27.20	3190.06	27.29	B_{3u}	3187.58	30.09	E_u	1.0000
26	3200.16	12.59	3200.16	12.63	B_{3u}	3201.49	9.71	E_u	1.0000
27	3207.80	37.96	3207.81	37.34	B_{3u}	3204.81	46.69	E_u	1.0000
28	3556.22	133.75	2613.61	112.94	B_{3u}	250.27	5.38	E_u	1.3607
1	121.79	3.64	121.49	3.60	B_{2u}	120.61	3.60	E_u	1.0025
2	275.06	0.11	272.15	0.05	B_{2u}	306.37	2.51	E_u	1.0107
3	499.06	2.13	489.42	0.71	B_{2u}	511.37	7.87	E_u	1.0197
4	560.32	0.01	555.40	0.59	B_{2u}	585.85	10.37	E_u	1.0089
5	633.47	5.87	632.04	3.54	B_{2u}	652.85	7.78	E_u	1.0023
6	750.80	67.97	735.93	84.69	B_{2u}	768.00	61.07	E_u	1.0202
7	804.11	2.69	804.12	2.64	B_{2u}	814.13	0.81	E_u	1.0000
8	854.68	0.25	779.19	2.07	B_{2u}	906.01	55.53	E_u	1.0969

9	1029.32	10.98	1029.37	14.31	B_{2u}	1030.03	11.40	E_u	0.9999
10	1068.39	28.79	981.15	88.55	B_{2u}	1111.13	174.45	E_u	1.0889
11	1109.04	217.46	1096.50	111.67	B_{2u}	1084.48	153.67	E_u	1.0114
12	1139.58	133.14	1136.89	51.27	B_{2u}	1138.25	146.17	E_u	1.0024
13	1181.40	2.22	1170.12	31.92	B_{2u}	1190.02	30.39	E_u	1.0096
14	1214.60	29.43	1212.99	0.05	B_{2u}	1210.25	2.10	E_u	1.0013
15	1286.42	19.32	1216.31	60.00	B_{2u}	250.27	5.38	E_u	1.0576
16	1334.09	37.10	1332.63	99.85	B_{2u}	1320.40	49.72	E_u	1.0011
17	1339.90	114.76	122.90	4.73	B_{2u}	1343.80	21.81	E_u	1.0015
18	1370.56	116.07	282.74	8.09	B_{2u}	1436.61	56.00	E_u	1.0003
19	1473.48	96.92	502.48	6.30	B_{2u}	1491.01	32.70	E_u	1.0040
20	1513.99	7.08	564.42	1.59	B_{2u}	1509.13	0.14	E_u	1.0004
21	1529.99	31.61	630.00	41.13	B_{2u}	1511.62	97.41	E_u	1.0006
22	1567.89	8.45	743.13	70.60	B_{2u}	1359.59	233.93	E_u	1.0142
23	1625.98	12.78	796.68	11.85	B_{2u}	1615.53	8.41	E_u	1.0001
24	1646.78	14.96	889.97	67.59	B_{2u}	1641.29	10.73	E_u	1.0001
25	3176.56	6.92	1028.57	1.17	B_{2u}	3173.97	5.98	E_u	1.0000
26	3186.53	33.00	1037.12	660.35	B_{2u}	3187.58	30.09	E_u	1.0000
27	3203.63	47.26	1085.32	0.94	B_{2u}	3204.81	46.69	E_u	1.0000
28	3204.82	9.17	1130.74	71.07	B_{2u}	3201.49	9.71	E_u	1.0000
1	19.90	0.00	19.90	0.00	B_{1u}	22.37	0.00	B_{2u}	1.0000
2	38.47	1.53	38.26	1.50	B_{1u}	31.61	0.57	A_{2u}	1.0055
3	136.17	0.38	136.10	0.40	B_{1u}	134.30	0.00	B_{2u}	1.0005
4	217.25	7.15	214.18	7.83	B_{1u}	249.71	0.02	A_{2u}	1.0143
5	256.63	1.70	255.90	1.58	B_{1u}	249.91	0.00	B_{2u}	1.0029
6	340.23	1.66	340.23	1.66	B_{1u}	352.00	2.18	A_{2u}	1.0000
7	431.00	0.26	430.99	0.22	B_{1u}	433.57	0.00	B_{2u}	1.0000
8	444.31	14.38	443.68	15.75	B_{1u}	446.22	12.41	A_{2u}	1.0014
9	704.03	4.78	704.28	4.03	B_{1u}	715.88	0.00	B_{2u}	0.9997
10	740.49	127.16	746.78	248.74	B_{1u}	748.97	246.81	A_{2u}	0.9916
11	778.36	184.33	566.31	18.00	B_{1u}	122.63	11.08	A_{2u}	1.3744
12	784.63	23.57	784.59	15.03	B_{1u}	788.29	0.00	B_{2u}	1.0000
13	804.01	4.93	795.67	23.91	B_{1u}	797.02	31.45	A_{2u}	1.0105
14	975.37	1.84	975.37	1.88	B_{1u}	978.41	3.74	A_{2u}	1.0000
15	980.94	1.97	980.93	1.82	B_{1u}	977.91	0.00	B_{2u}	1.0000

Table IV.A.2: DFT B3LYP / 6-311++G(2d,2p) computed Raman frequencies (cm^{-1}) and intensities [scattering activities ($Å^4$/amu)] for H_2Pc, D_2Pc and ZnPc. The symmetry labels listed for D_2Pc are also valid for H_2Pc.

	H_2Pc		**D_2Pc**			**ZnPc**			**ν_H / ν_D**
	ν_H	Int	ν_D	Int	Sym	ν_{Zn}	Int	Sym	**Ratio**
1	132.88	32.17	132.66	32.12	A_g	157.58	19.82	B_{1g}	1.0016
2	229.72	74.90	229.34	74.54	A_g	258.37	76.58	A_{1g}	1.0016
3	551.31	38.40	550.28	39.46	A_g	562.60	8.86	B_{1g}	1.0019
4	577.52	49.75	575.39	47.62	A_g	600.07	116.02	A_{1g}	1.0037
5	690.37	377.39	690.31	382.41	A_g	689.90	318.35	A_{1g}	1.0001
6	743.52	1177.46	739.95	1131.63	A_g	764.79	928.75	B_{1g}	1.0048
7	779.27	14.02	778.65	30.22	A_g	788.74	380.92	B_{1g}	1.0008
8	810.69	172.30	805.98	178.69	A_g	851.61	172.77	A_{1g}	1.0058
9	1029.03	242.78	1028.88	255.13	A_g	1029.79	244.29	B_{1g}	1.0001
10	1029.67	562.80	1029.62	553.30	A_g	1030.45	527.33	A_{1g}	1.0000
11	1138.32	1089.91	1135.53	1036.39	A_g	1146.80	1266.13	A_{1g}	1.0025
12	1164.00	2523.97	1162.81	2528.87	A_g	1164.30	2844.76	B_{1g}	1.0010
13	1185.19	352.54	1185.16	348.43	A_g	1186.33	409.97	A_{1g}	1.0000
14	1203.96	998.66	1200.75	665.94	A_g	1202.09	1319.63	B_{1g}	1.0027
15	1327.29	5525.98	1323.34	5987.30	A_g	1323.12	5181.51	B_{1g}	1.0030
16	1360.92	2581.95	1355.50	2828.61	A_g	1363.78	2102.53	A_{1g}	1.0040
17	1373.33	2815.23	1373.11	2646.15	A_g	1368.90	1713.40	B_{1g}	1.0002
18	1422.37	479.56	1419.24	371.63	A_g	1421.41	588.56	A_{1g}	1.0022
19	1460.91	490.84	1460.85	477.32	A_g	1455.62	478.64	A_{1g}	1.0000
20	1481.64	1758.49	1481.63	1759.71	A_g	1478.71	2000.23	B_{1g}	1.0000
21	1541.07	1810.91	1541.07	1815.39	A_g	1529.73	689.94	A_{1g}	1.0000
22	1582.92	18943.34	1582.77	18899.00	A_g	1557.23	19777.07	B_{1g}	1.0001
23	1611.42	108.35	1611.42	108.39	A_g	1614.66	85.11	B_{1g}	1.0000
24	1626.52	39.91	1626.51	40.21	A_g	1617.53	121.12	A_{1g}	1.0000
25	3186.54	633.00	3186.54	633.07	A_g	3187.54	674.71	B_{1g}	1.0000
26	3190.08	678.73	3190.08	678.62	A_g	3187.64	626.18	A_{1g}	1.0000
27	3203.69	717.09	3203.69	717.21	A_g	3204.75	97.81	B_{1g}	1.0000
28	3207.86	785.98	3207.86	786.17	A_g	3204.99	1444.68	A_{1g}	1.0000
29	3612.04	13.17	2649.28	35.98	A_g				1.3634
1	56.85	0.09	56.85	0.09	B_{3g}	60.13	0.15	E_g	1.0000
2	126.40	5.39	126.40	5.39	B_{3g}	125.24	5.12	E_g	1.0000
3	232.80	1.96	232.80	1.96	B_{3g}	235.35	2.24	E_g	1.0000
4	287.33	0.07	287.33	0.07	B_{3g}	288.36	0.04	E_g	1.0000
5	430.59	0.02	430.59	0.02	B_{3g}	433.50	0.00	E_g	1.0000
6	503.88	0.01	503.88	0.01	B_{3g}	508.73	0.03	E_g	1.0000
7	648.09	0.01	648.09	0.01	B_{3g}	659.12	0.03	E_g	1.0000

8	740.37	0.42	740.37	0.42	B_{3g}	739.11	0.40	E_g	1.0000
9	793.08	16.26	793.08	16.26	B_{3g}	792.07	16.68	E_g	1.0000
10	802.06	6.87	802.06	6.87	B_{3g}	809.00	2.40	E_g	1.0000
11	896.46	0.48	896.46	0.48	B_{3g}	897.77	0.40	E_g	1.0000
12	975.36	0.02	975.36	0.02	B_{3g}	978.15	0.26	E_g	1.0000
13	1008.46	0.44	1008.46	0.44	B_{3g}	1006.68	0.21	E_g	1.0000
1	52.87	0.15	52.47	0.16	B_{2g}	60.13	0.15	E_g	1.0075
2	116.84	4.44	116.46	4.38	B_{2g}	125.24	5.12	E_g	1.0032
3	220.35	2.67	214.42	2.64	B_{2g}	235.35	2.24	E_g	1.0276
4	271.88	0.02	271.83	0.03	B_{2g}	288.36	0.04	E_g	1.0002
5	431.40	0.07	430.37	0.09	B_{2g}	433.50	0.00	E_g	1.0024
6	505.86	0.02	511.42	0.00	B_{2g}	508.73	0.03	E_g	0.9891
7	657.47	0.16	659.10	0.18	B_{2g}	659.12	0.03	E_g	0.9975
8	680.33	0.04	495.23	0.03	B_{2g}				1.3738
9	730.47	1.60	729.66	1.62	B_{2g}	739.11	0.40	E_g	1.0011
10	786.56	15.21	786.54	15.19	B_{2g}	792.07	16.68	E_g	1.0000
11	810.37	0.90	810.28	0.87	B_{2g}	809.00	2.40	E_g	1.0001
12	898.03	0.30	898.03	0.30	B_{2g}	897.77	0.40	E_g	1.0000
13	980.86	0.72	980.85	0.71	B_{2g}	978.15	0.26	E_g	1.0000
14	1004.59	0.12	1004.59	0.12	B_{2g}	1006.68	0.21	E_g	1.0000
1	84.78	5.07	84.24	4.93	B_{1g}	112.54	12.92	B_{2g}	1.0064
2	181.25	28.90	179.15	28.05	B_{1g}	231.86	31.49	B_{2g}	1.0117
3	211.90	1.34	211.68	1.69	B_{1g}	213.89	0.00	A_{2g}	1.0011
4	487.58	134.53	486.28	138.50	B_{1g}	489.67	115.86	B_{2g}	1.0027
5	580.49	1.99	563.31	1.81	B_{1g}	588.59	0.00	A_{2g}	1.0305
6	612.25	0.58	599.53	0.01	B_{1g}	629.19	0.00	A_{2g}	1.0212
7	699.34	3.15	696.47	2.36	B_{1g}	701.63	4.69	B_{2g}	1.0041
8	841.82	1.14	762.54	5.27	B_{1g}				1.1040
9	907.44	1.12	880.30	0.00	B_{1g}	864.41	0.00	A_{2g}	1.0308
10	1049.73	227.80	1007.27	134.25	B_{1g}	1056.58	115.99	B_{2g}	1.0422
11	1106.98	43.02	1068.51	65.13	B_{1g}	963.56	42.27	B_{2g}	1.0360
12	1121.65	0.12	1117.37	29.74	B_{1g}	1116.17	0.00	A_{2g}	1.0038
13	1132.51	411.86	1132.15	424.96	B_{1g}	1131.91	375.42	B_{2g}	1.0003
14	1211.42	271.33	1211.42	260.77	B_{1g}	1208.88	0.00	A_{2g}	1.0000
15	1223.56	520.38	1191.40	58.66	B_{1g}	1157.23	0.00	A_{2g}	1.0270
16	1258.70	73.14	1237.35	535.53	B_{1g}	1232.04	741.76	B_{2g}	1.0173
17	1322.50	156.25	1322.34	145.67	B_{1g}	1325.10	0.00	A_{2g}	1.0001
18	1339.32	336.17	1339.09	353.25	B_{1g}	1331.44	454.81	B_{2g}	1.0002
19	1458.98	554.95	1452.44	568.44	B_{1g}	1457.03	323.28	B_{2g}	1.0045
20	1504.73	81.21	1504.73	82.33	B_{1g}	1507.69	0.00	A_{2g}	1.0000
21	1515.01	167.52	1514.97	161.82	B_{1g}	1509.64	222.51	B_{2g}	1.0000

22	1565.84	3.16	1549.62	13.84	B_{1g}	1484.87	0.00	A_{2g}	1.0105
23	1639.07	0.05	1638.96	0.12	B_{1g}	1640.17	0.00	A_{2g}	1.0001
24	1646.82	71.75	1646.71	71.82	B_{1g}	1642.50	31.02	B_{2g}	1.0001
25	3172.80	189.65	3172.80	189.66	B_{1g}	3173.95	0.00	A_{2g}	1.0000
26	3176.57	219.98	3176.57	219.98	B_{1g}	3173.99	400.78	B_{2g}	1.0000
27	3200.16	164.45	3200.16	164.45	B_{1g}	3201.40	0.00	A_{2g}	1.0000
28	3204.82	170.82	3204.82	170.78	B_{1g}	3201.57	344.47	B_{2g}	1.0000

Appendix IV.B: MgPc, AlPc+ and ClAlPc DFT Results

IV.B.1 Introduction

This appendix will present the optimised geometries and vibrational analysis of magnesium, aluminium and chloro-aluminium phthalocyanine (MgPc, $AlPc^+$ and ClAlPc respectively) calculated using density functional theory. All calculations were made using the B3LYP hybrid functional and the 6-311++G(2d,2p) basis set. The calculated geometries of these phthalocyanines (a neutral s-block metal complex, a cationic p-block metal complex and its chlorinated salt) will be given in Section IV.B.2 and compared to the x-ray and gas phase structure. The tabulated infra-red and Raman active vibrational frequencies will be presented in Section IV.B.3 along with the calculated IR absorption and Raman scattering intensities.

Two of these molecules, MgPc and $AlPc^+$, were found to be planar with an inversion centre. Like the case of ZnPc, these 57 atom D_{4h} molecules will have 165 vibrational modes, 68 Raman active (14 A_{1g}, 14 B_{1g}, 14 B_{2g} and 26 E_g) , 40 IR active (8 A_{2u} and 32 E_u) and 33 optically silent modes (6 A_{1u}, 7 B_{1u}, 7B_{2u} and 13 A_{2g}). With 58 atoms ClAlPc has 168 normal vibrational modes. Due to its lower C_{4v} symmetry, ClAlPc has 23 A_1 and 84 E symmetry modes that are both IR and Raman active. 21 B_1 and 21 B_2 modes are also Raman active with 19 A_2 inactive modes. The following correlations may be made between the C_{4v} and D_{4h} symmetries: $A_1 \rightarrow A_{2u}$ and A_{1g}, $A_2 \rightarrow A_{1u}$ and A_{2g}, $B_1 \rightarrow B_{2u}$ and B_{1g}, $B_2 \rightarrow B_{1u}$ and B_{2g} and $E \rightarrow E_g$ and E_u. Table V.B.2 contains the IR active modes of $AlPc^+$ and MgPc and the equivalent IR and Raman modes of ClAlPc correlated by first symmetry then by comparison of the displacement diagrams. Table V.B.3 contains the Raman active modes of $AlPc^+$ and MgPc again with the equivalent ClAlPc modes. Where ClAlPc Raman modes of B_1 and B_2 symmetry correlate with an inactive mode of $AlPc^+$ and MgPc, these are also given. The extra Cl stretch of A_1 symmetry and degenerate pair of Cl bends of E symmetry are duplicated in both tables and are highlighted in bold. To save space and simplify the table, only one each of the degenerate pairs of E, E_g and E_u modes are shown.

IV.B.2 Optimised Geometries

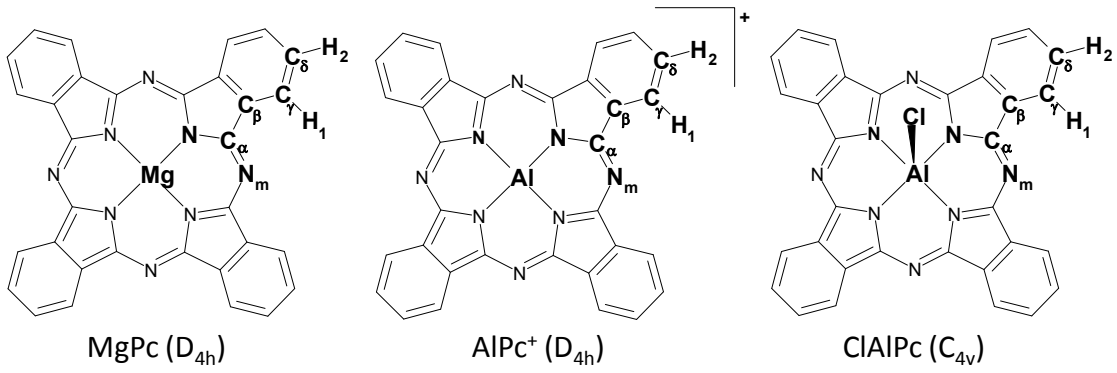

Figure V.B.1: The structures of magnesium, aluminium and chloro-aluminium phthalocyanine. Using DFT calculations MgPc and $AlPc^+$ were found to have square planar geometries, with a point group symmetry D_{4h}. The chlorinated salt of $AlPc^+$, ClAlPc, was found to be non-planar, with a slight 'bowling' of the Pc ring structure and the Al and Cl atoms above the ring (see Figure V.B.2). ClAlPc therefore has a point group symmetry of C_{4v}. The atom labelling used in these calculations is indicated and the structural parameters determined are provided in Table V.B.1.

The geometry optimised structures of MgPc, $AlPc_+$ and ClAlPc were determined by DFT using the B3LYP functional and the 6-311++G(2d,2p) basis set. MgPc was found to have a planar structure with D_{4h} symmetry. In the x-ray crystal data, this molecule is found to have a pyramidal structure where the Mg atoms complexes not only to the four pyrrole N atoms in the ring but also to a meso N atom of another MgPc molecule directly above or below. The Mg ion is said therefore to have a 4+1 coordination structure[1]. As the calculations presented here represent the molecule in the gas phase, inter-molecular interactions would not occur for the monomeric molecule and the molecule would be expected to be planar. The calculated geometric parameters have, none-the-less, been compare to the average of their equivalents in the pseudo-C_{4v} structures found by x-ray crystallography in Table V.B.1.

The DFT optimised structure for ClAlPc was found to have C_{4v} symmetry. Figure V.B.1 clearly shows that not only is the Cl^- anion above the plane of the molecule, as presumed from the start of the calculation, but also the Al atom is significantly (0.450 Å) above the plane formed by the four pyrrole N atoms with a noticeable 'bowling' of the phthalocyanine ring. This geometry (Table V.B.1). is consistent with the structural data found using gas electron diffraction (GED)[2]. Also given in Table V.B.1 are the structural parameters for the cation $AlPc^+$. This species exists in solution when ClAlPc is dissolved in a polar solvent. Its structure was found to be

D_{4h}, like MgPc and ZnPc, and was used to compare the C_{4v} ClAlPc ground state properties with those of the planar Pcs.

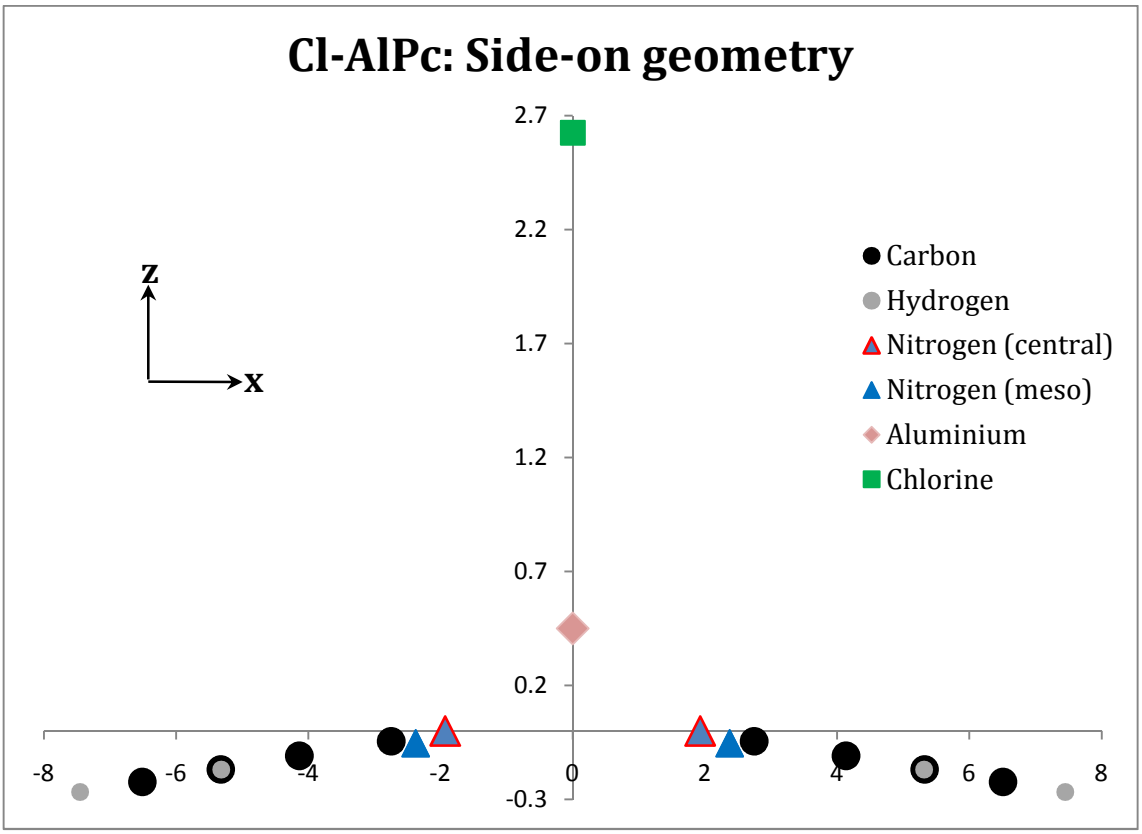

Figure V.B.3: Plot of the atomic positions calculated using DFT of ClAlPc projected onto the zx axis illustrating the loss of planarity of the Pc ring. Distances are in shown Å units and the atomic positions on the vertical axis are plotted relative to the 4 central N atoms. The atoms of the two isoindole fragments along the y axis have been removed for clarity.

Table V.B.1: Selected structural parameters obtained using the B3LYP/6-311++G(2d,2p) method for MgPc, $AlPc^+$ and ClAlPc. Note the experimental parameters for MgPc are taken from x-ray diffraction data of a solid crystal, where the molecule has a pyramidal shape ($\sim C_{4v}$) due to inter-molecular interactions. The z-axis positions of the atoms in ClAlPc are also given and the values are relative to the plane of the central N atoms.

	MgPc		**$AlPc^+$**	**ClAlPc**	
Lengths (Å)	**Exp(C_{4v})[1]**	**B3LYP(D_{4h})**	**B3LYP**	**Exp[2]**	**B3LYP**
N-M	2.047	2.002	1.915	1.976	1.981
N-C_α	1.369	1.369	1.395	1.395	1.379
C_α-N_m	1.351	1.329	1.313	1.326	1.317
C_α- C_β	1.461	1.460	1.441	1.458	1.450
C_β- C_β	1.411	1.408	1.401	1.393	1.399
C_β- C_γ	1.382	1.391	1.394	1.387	1.393
C_γ- C_δ	1.392	1.389	1.386	1.383	1.388
C_δ- C_δ	1.410	1.403	1.407	1.400	1.406
C_γ- H_1	0.950	1.080	1.080	1.111	1.080
C_δ- H_2	0.950	1.081	1.081	1.112	1.081
Al-Cl	N/A	N/A	N/A	2.145	2.175
Bond Angles (deg)					
M-N-C_α	123.609	125.077	126.701	124.2	125.689
N-C_α- N_m	127.491	127.373	126.868	127.5	127.413
C_α-N-C_α	107.920	109.846	106.598	105.8	107.535
N-C_α-C_β	108.665	108.491	109.830	110.6	109.840
C_α-C_β-C_β	106.564	106.586	106.871	106.6	106.482
C_β-C_β-C_γ	120.991	120.993	121.309	121.1	121.248
C_β-C_γ-C_δ	118.087	117.864	117.324	117.7	117.532
C_γ-C_δ-C_δ	120.898	121.142	121.366	121.2	121.220
C_β-C_γ-H_1	120.956	120.690	121.061	120.8	120.855
C_γ-C_δ-H_2	119.534	119.640	119.595	119.6	119.639
ClAlPc – B3LYP					
Atom	**Cl**	**Al**	**N**	**C_α**	**N_m**
Z-Position (Å)	2.625	0.450	0	-0.045	-0.053
Atom	**C_β**	**C_γ**	**H_1**	**C_δ**	**H_2**
Z-Position (Å)	-0.109	-0.169	-0.169	-0.224	-0.267

IV.B.3 IR and Raman DFT vibrational frequencies

Table V.B.2: DFT B3LYP / 6-311++G(2d,2p) computed Infra-red frequencies (ν, cm^{-1}) and intensities (km/mole) of $AlPc^+$ and MgPc with the frequencies and IR and Raman intensities [scattering activities ($Å^4$/amu)] of the equivalent modes of ClAlPc. The symmetry samples are the same for $AlPc^+$ and MgPc.

	ClAlPc				$AlPc_+$		MgPc		
	Sym	ν	IR Int	Ram Int	ν	Int	ν	Int	Sym
1	A_1	40.98	2.16	0.74	45.43	1.69	31.80	0.27	A_{2u}
2	A_1	172.26	5.44	0.21	200.83	19.81	150.63	28.64	A_{2u}
3	A_1	293.97	0.01	3.13	307.89	9.24	263.95	5.20	A_{2u}
4	A_1	359.43	6.51	5.41	373.22	5.90	354.20	0.57	A_{2u}
5	A_1	443.16	26.91	0.27	444.76	11.45	447.11	11.56	A_{2u}
6	**A_1**	**483.16**	**91.08**	**7.10**					
7	A_1	753.76	281.31	0.01	756.85	244.49	751.07	263.56	A_{2u}
8	A_1	802.24	11.92	1.16	805.19	29.28	799.08	21.80	A_{2u}
9	A_1	980.23	2.73	0.04	991.33	2.03	978.82	3.71	A_{2u}
1	**E**	**93.88**	**1.12**	**3.80**					
2	E	135.09	0.08	2.86	125.53	3.87	122.43	4.28	E_u
3	E	311.82	3.58	0.42	311.43	4.78	290.89	5.88	E_u
4	E	391.41	4.29	0.05	431.69	1.15	427.77	0.02	E_u
5	E	527.84	11.42	0.00	536.89	12.42	514.87	8.07	E_u
6	E	587.27	7.01	0.05	590.26	2.82	589.81	11.88	E_u
7	E	659.17	4.84	0.06	667.62	0.62	663.02	4.25	E_u
8	E	773.62	58.12	0.72	776.91	19.72	770.73	62.06	E_u
9	E	818.09	1.42	0.85	827.27	6.48	820.19	1.08	E_u
10	E	921.18	58.48	0.09	926.05	62.69	909.64	61.04	E_u
11	E	1028.69	12.57	0.43	1029.52	2.70	1030.04	11.02	E_u
12	E	1087.16	136.92	1.19	1065.19	45.59	1082.69	204.08	E_u
13	E	1096.60	132.95	0.61	1104.93	116.95	1102.73	150.99	E_u
14	E	1142.98	159.63	0.54	1147.14	128.59	1137.85	127.66	E_u
15	E	1190.04	24.20	0.37	1195.79	8.74	1188.86	20.59	E_u
16	E	1220.68	0.16	0.73	1224.52	3.45	1209.70	1.53	E_u
17	E	1324.98	46.96	0.01	1328.39	36.50	1319.05	48.88	E_u
18	E	1350.26	35.91	3.86	1333.80	137.04	1346.02	6.36	E_u
19	E	1365.62	227.49	0.92	1368.15	343.25	1359.78	250.51	E_u
20	E	1456.69	83.08	0.08	1460.46	77.09	1432.51	37.49	E_u
21	E	1508.56	23.80	0.00	1513.58	21.82	1486.33	32.44	E_u
22	E	1520.34	1.64	0.24	1527.32	0.61	1504.52	104.09	E_u
23	E	1546.11	50.64	1.50	1550.93	3.94	1508.90	2.29	E_u
24	E	1622.01	7.80	0.67	1618.93	0.33	1614.60	6.95	E_u
25	E	1642.69	13.72	0.03	1638.52	12.46	1641.07	10.48	E_u

26	E	3176.18	6.52	0.23	3188.38	2.93	3173.75	6.15	E_u
27	E	3189.88	29.97	2.03	3199.95	5.77	3187.36	30.20	E_u
28	E	3205.33	6.83	0.10	3212.73	0.72	3201.20	9.95	E_u
29	E	3208.21	38.50	0.74	3215.52	13.14	3204.55	47.40	E_u

Table V.B.3: DFT B3LYP / 6-311++G(2d,2p) computed Raman frequencies (cm^{-1}) and intensities [scattering activities ($Å^4$/amu)] for $AlPc^+$ and MgPc with the frequencies and Raman and IR intensities (km/mole) of the equivalent modes of ClAlPc. The symmetry samples are the same for $AlPc^+$ and MgPc.

	ClAlPc				$AlPc^+$		MgPc		
	Sym	ν	IR Int	Ram Int	ν	Int	ν	Int	Sym
1	A_1	255.58	0.25	70.68	264.93	102.08	254.76	72.25	A_{1g}
2	**A_1**	**483.16**	**91.08**	**7.10**					
3	A_1	601.41	1.05	63.80	604.49	61.53	598.01	100.49	A_{1g}
4	A_1	695.31	0.01	320.44	688.76	445.64	690.02	337.39	A_{1g}
5	A_1	850.46	4.41	226.48	857.45	218.66	846.87	197.70	A_{1g}
6	A_1	1029.09	0.24	505.28	1029.90	488.64	1030.33	529.35	A_{1g}
7	A_1	1155.59	0.61	727.46	1159.42	798.84	1145.22	1255.56	A_{1g}
8	A_1	1189.96	0.40	582.47	1196.76	718.64	1186.11	401.16	A_{1g}
9	A_1	1367.76	1.75	2733.99	1367.47	3025.30	1363.79	2184.95	A_{1g}
10	A_1	1429.87	8.14	532.55	1420.45	82.79	1422.67	577.00	A_{1g}
11	A_1	1469.50	0.02	210.73	1472.21	285.28	1453.13	608.82	A_{1g}
12	A_1	1565.98	0.00	785.28	1577.82	871.82	1524.53	630.87	A_{1g}
13	A_1	1624.27	0.25	170.24	1620.79	2.26	1616.50	109.09	A_{1g}
14	A_1	3189.94	0.07	743.12	3200.00	687.97	3187.42	617.36	A_{1g}
15	A_1	3208.38	0.14	1327.42	3215.65	1450.80	3204.73	1454.40	A_{1g}
1	B_1	218.27	0.00	0.08	180.59	10.24	182.16	15.69	B_{1g}
2	B_1	526.94	0.00	0.97	571.14	0.18	569.72	5.35	B_{1g}
3	B_1	705.25	0.00	5.60	768.19	872.75	764.20	870.24	B_{1g}
4	B_1	896.62	0.00	0.01	798.42	329.41	797.37	513.21	B_{1g}
5	B_1	1008.36	0.00	0.01	1029.14	312.07	1029.82	253.23	B_{1g}
6	B_1	1064.23	0.00	224.81	1170.18	2980.21	1164.87	2998.29	B_{1g}
7	B_1	1128.87	0.00	486.10	1197.31	373.05	1204.83	1762.34	B_{1g}
8	B_1	1223.74	0.00	619.93	1316.59	5368.45	1332.12	4872.03	B_{1g}
9	B_1	1334.48	0.00	484.86	1381.21	1136.44	1369.01	1976.77	B_{1g}
10	B_1	1486.76	0.00	324.76	1486.63	2359.03	1477.92	2095.35	B_{1g}
11	B_1	1516.27	0.00	167.63	1600.21	21410.53	1548.39	20262.60	B_{1g}
12	B_1	1643.91	0.00	89.04	1620.15	1458.58	1613.59	145.94	B_{1g}
13	B_1	3176.21	0.00	423.36	3199.92	694.16	3187.32	671.83	B_{1g}
14	B_1	3205.43	0.00	321.30	3215.42	96.05	3204.49	101.05	B_{1g}
1	B_2	133.42	0.00	4.22	120.04	12.62	111.21	12.98	B_{2g}

2	B_2	296.83	0.00	1.03	265.54	38.72	225.54	29.61	B_{2g}
3	B_2	434.24	0.00	0.48	498.43	113.03	489.33	122.55	B_{2g}
4	B_2	770.10	0.00	1009.37	703.97	8.51	701.34	4.61	B_{2g}
5	B_2	979.64	0.00	0.06	978.38	75.68	960.32	32.65	B_{2g}
6	B_2	1167.30	0.00	2161.73	1055.12	478.43	1052.98	146.97	B_{2g}
7	B_2	1206.62	0.00	1302.10	1124.34	542.62	1130.93	420.14	B_{2g}
8	B_2	1333.66	0.00	5299.85	1214.11	507.67	1230.35	814.29	B_{2g}
9	B_2	1375.12	0.00	1393.48	1336.80	492.56	1330.69	496.65	B_{2g}
10	B_2	1485.90	0.00	2027.59	1491.66	402.06	1446.66	282.39	B_{2g}
11	B_2	1596.95	0.00	9915.46	1525.48	122.81	1509.45	248.54	B_{2g}
12	B_2	1622.21	0.00	184.91	1638.44	100.15	1642.18	52.00	B_{2g}
13	B_2	3189.85	0.00	697.72	3188.40	393.04	3173.77	404.01	B_{2g}
14	B_2	3208.13	0.00	70.36	3212.86	348.56	3201.27	346.27	B_{2g}
1	E	57.34	0.33	1.92	65.60	0.10	59.59	0.17	E_g
2	**E**	**93.88**	**1.12**	**3.80**					
3	E	124.72	3.75	0.04	122.77	5.86	126.08	5.16	E_g
4	E	255.32	0.14	0.89	249.86	0.94	236.62	2.08	E_g
5	E	301.08	0.98	0.44	294.71	0.58	289.67	0.03	E_g
6	E	434.82	0.03	0.00	433.89	0.00	434.43	0.00	E_g
7	E	501.44	0.67	0.01	493.14	0.00	509.75	0.03	E_g
8	E	652.38	3.62	0.19	648.15	0.03	660.50	0.03	E_g
9	E	743.09	0.34	0.21	746.24	0.72	741.83	0.29	E_g
10	E	793.89	0.89	12.20	798.57	6.34	793.58	17.28	E_g
11	E	805.50	0.12	4.55	805.55	8.44	809.29	2.73	E_g
12	E	896.60	0.01	0.33	903.33	0.29	898.32	0.39	E_g
13	E	979.92	0.02	0.40	991.04	0.18	978.62	0.27	E_g
14	E	1008.24	0.00	0.35	1022.53	0.56	1006.87	0.25	E_g

IV.B.1 References

(1) Janczak, J.; Kubiak, R. *Polyhedron* **2001**, *20*, 2901.
(2) Strenalyuk, T.; Samdal, S.; Volden, H. V. *The Journal of Physical Chemistry A* **2008**, *112*, 9075.

Chapter V: Visible spectroscopy of H_2Pc and ZnPc isolated in cryogenic matrices

V.1 Introduction

In this chapter, a description of the study of the absorption and luminescence spectra of ZnPc and H_2Pc isolated in rare gas and molecular matrices in the region of the Q band will be given. Very strong similarities were noted in Chapter IV between the vibrational structure in Raman and the vibronic emission spectra. A key aspect of the present work is the exploitation of vibrational analysis of Raman spectra, obtained by large basis set DFT calculations, to obtain vibrational assignments for the emission bands and then for excitation bands for matrix-isolated phthalocyanines (Pcs). Due to the strong mirror symmetry between emission and excitation spectra, an opportunity is thereby at hand to achieve vibrational assignments for the multiple lines present in the excitation and emission spectroscopy of these important molecules. Moreover this comparison between fluorescence and Raman data will allow the identification of the vibrational mode coupling the higher energy Q_y state to the lower Q_x seen in excitation.

In light of the success of density functional methods to predict the ground state properties of H_2Pc and ZnPc, the ability of time dependent DFT (TD-DFT) was assessed with regard to the prediction of the vertical electronic transition energies to the Q states. Large basis sets and molecular geometries calculated at a high level of theory were used. Porphyrins and their derivatives have been extensively studied using TD-DFT. Baerends *et al.*[1] presented an analysis of TD-DFT calculations using the Statistical Averaging of different Orbital dependent model Potentials (SAOP) method for Mg, Zn and Ni porphyrin and tetraazaporphyrin (TAP, which was referred to by the authors as porphyrazine). They concentrated on the origin of the excitation energies and absorption intensities for these molecules by considering the Kohn-Sham (KS) orbitals of the pyrrole, methine and aza fragments, as well as the metallic KS orbitals that make up the metallo-P/

metallo-TAP molecules. Nguyen and Pachter[2] reported TD-DFT results for the metallo-porphyrins ZnP, ZnTBP (zinc tetrabenzoporphyrin), ZnPc and ZnTAP, using the B3LYP functional and 6-31G(d) basis set. They reported all the allowed transitions predicted for the four porphyrins up to the vacuum UV (~200 nm) and compared the excitation and oscillator strengths calculated for ZnP using the 6-31G(d), 6-31+G(d) and 6-311+G(d) basis sets. The lowest energy transitions of H_2P, H_2TBP, H_2Pc and H_2TAP predicted using the TD-DFT method and B3LYP/6-31G(d) functional and basis set have been reported by Song *et al.*[3] while the higher energy transitions of H_2Pc and its multiple protonated analogues, $H_{2+n}Pc^{n+}$, have been calculated at the same level by Lu *et al.*[4]. The Q bands of both H_2Pc and ZnPc and various derivatives have been calculated by Quartarolo et al.[5] with TD-DFT at the PBE0/SVP level of calculation.

The outline of this chapter is as follows. After a brief note on the experimental procedures used, the results for the visible absorption spectra recorded will be given in Part V.3.I. This will be followed in Part V.3.II by the emission results using pulsed laser excitation and monitoring with a time-gated iCCD detector for H_2Pc and ZnPc in various low-temperature matrices. In Part V.3.III the time-resolved emission results will be given. The excitation spectra will be reported in Part V.3.IV. In Part V.3.V the results from linear-response TD-DFT calculations will be given and compared to experiment. The TD-DFT and fluorescence lifetime results will be discussed in Parts V.4.I and V.4.II. The vibronic structures of H_2Pc and ZnPc in emission will be analysed in Part V.4.III and the vibrations assigned by comparison with the ground state Raman spectra and the vibrations calculated using DFT. In Part V.4.IV the excitation and emission spectra of both molecules will be compared and assignments, where possible, made. A brief discussion of the possible resonance mechanism coupling the vibrations of the two lowest allowed excited states of H_2Pc and site structures observed in the electronic spectra of matrix-isolated H_2Pc and ZnPc will be given in Parts V.4.V and V.4.VI.

V.2 Experimental

Experimental results for H_2Pc and ZnPc in Ar, Kr, Xe and N_2 matrices were recorded in Maynooth using the apparatus described in Chapter II. Spectroscopic results for both these molecules in neon were obtained in Orsay in collaboration with the group of Dr. Claudine Crépin, L'Institut des Sciences Moléculaires d'Orsay

(ISMO) at l'Université Paris-Sud. Their cryogenic set-up[6] had a base temperature of 7 K allowing the formation of Ne matrices which would be unattainable using the set-up in Maynooth with a base temperature ~12.5 K. The optical set-up at ISMO was also different with a home built dye laser[6] and a higher resolution 0.6 m Jobin-Yvon emission monochromator. Emission was recorded using the same model Andor DH720 iCCD detector (the spectra recorded in Orsay had to be calibrated *post hoc* due to the lack of suitable calibration curves being included with the Andor software for the Jobin-Yvon monochromator).

V.3 Results

V.3.I Visible absorption

The absorption spectra of ZnPc in all matrices are dominated, as shown on the left panel in Figure V.1, by the intense 0-0 transition of the Q band. The band maximum of this transition has been observed in the gas phase under static cell conditions[7] at 15128 cm^{-1} while the band origin has been identified at 15766 cm^{-1} under free jet conditions[8]. The latter value is indicated by the dashed vertical line in Figure V.1. The 0-0 transition of the Q band is situated at 15574, 15328, 15309, 15182 and 15035 cm^{-1} in Ne, N_2, Ar, Kr and Xe respectively. These bands are all red-shifted from the gas phase position and the energy of the transition decreases from Ne to Xe as the interaction with the matrix gets stronger. Thus the largest shift from the gas phase has been observed in Xe with a value of 731 cm^{-1} while the smallest is 192 cm^{-1} in neon. Other vibronic bands of lower intensity are evident in the region from 15500 to 17000 cm^{-1}. The Ne and N_2 spectra in Figure V.1 have been recorded at 7 K and these matrices, especially N_2, exhibit resolved site structure. The absorption spectra in Ar, Kr and Xe were recorded at a higher temperature (13 K) and while the bands are broader, they do show resolved features in laser excitation scans.

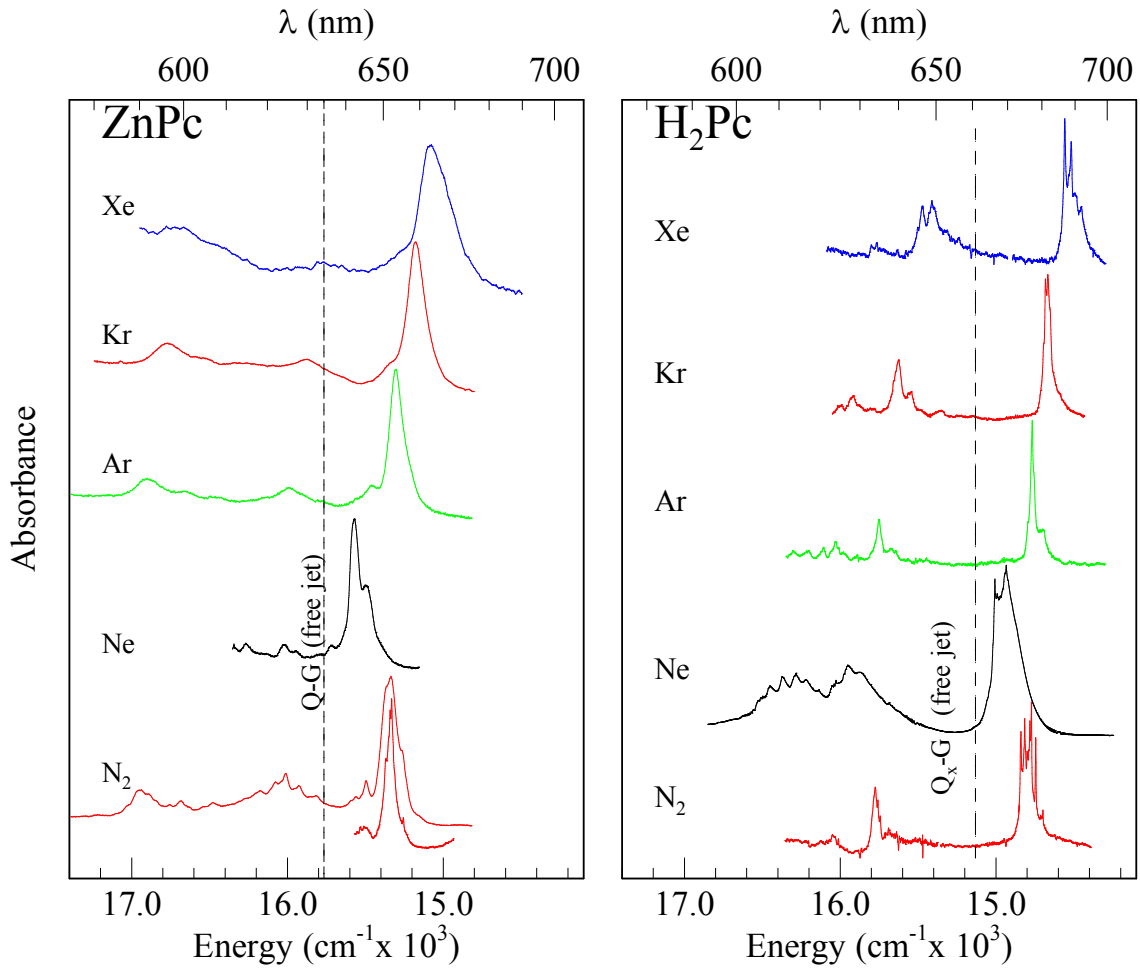

Figure V.1: Absorption spectra of ZnPc (left panel) and H_2Pc (right panel) trapped in Ne, N_2, Ar, Kr and Xe solids. All the spectra were recorded at 7 K except for ZnPc in Ar, Kr and Xe which were recorded at 13 K. The locations of the gas phase band origins are indicated by the dashed vertical lines.

The absorption spectra of H_2Pc, shown on the right of Figure V.1, recorded at 7 K, appears more structured than for ZnPc. In addition, two intense features are evident in the spectra, recorded in all samples, corresponding to absorptions of the Q_x and Q_y states. The band origin of the $Q_X \leftarrow G$ transition in the gas phase is known from laser excitation spectroscopy[9] to be 15132 cm^{-1}. As indicated in Figure V.1 a red-shift exists in all matrices – it is smallest in Ne (193 cm^{-1}) and largest in Xe (615 cm^{-1}). Even under free-jet conditions, the region of the band origin of the $Q_y \leftarrow G$ is spectrally congested and the bands are broader. This is due to the mixing of the band origin of Q_y excited electronic state with the excited vibrational levels of the Q_x excited state[10]. Because of this coupling, the exact position of the band origin of the Q_y state is still unknown in the gas phase. The absorption values recorded in all the matrices studied are collected in Table V.1 as well as the matrix shifts.

Table V.1: Absorption values in wavenumbers (cm^{-1}) units for the 0_0^0 transition in ZnPc (Q band) and H_2Pc (Q_x and Q_y bands) in different matrices. The gas phase band origins are from the published data of Fitch et al.[10] for H_2Pc and of Plows and Jones[8] for ZnPc. In determining the matrix shift, the highest energy component of the Q_y band was used in all hosts (except Ar) where multiple features were present. This component was also used to calculate the splitting of the Q_x and Q_y matrix bands – values which are only indicators in the absence of detailed analysis. The helium droplet data is from the work of Lehning *et al.* [11] while the Shpol'skii data is that of Huang et al.[12].

	H_2Pc				ZnPc	
	Q_X	Matrix shift, Δ	Q_Y	Q_Y - Q_X Splitting	Q	Matrix shift, Δ
Free jet	15132	-	~16680	~1548	15766	-
Ne	15007.2	-115	15950.9	943.7	15574	-192
N_2	14840.1	-292	15775	935	15328	-428
Ar	14767.9	-364	15753.2	985.3	15309	-457
Kr	14685.1 14670	-447	15655 15624	970	15182	-584
Xe	14558.6 14517.7	-573	15474.5 15411.6	916	15035	-731
He droplets	15089	-43	~16500	~1400	15703	-63
Shpol'skii	14475	-657	15332	857	14914	-852
	14411	-721	15275	864	14885	-881

In contrast to ZnPc, the shapes of the H_2Pc bands differ markedly from one solid to another with a highly structured band present in N_2 and a broad but structured band in Ne. Ar presents the simplest absorption spectrum with a single dominating feature. However, as revealed in laser excitation spectroscopy, the widths of the bands in all matrices arise from occupancy of the H_2Pc or ZnPc molecules in multiple sites. However, in the case of H_2Pc/N_2, the resolved lines of the structured absorption band are very narrow and could correspond to distinct sites. Their linewidths (4 to 5 cm^{-1}) are close to the resolving power of the recording instruments, ~2 cm^{-1} in this case.

V.3.II Emission Spectra

Only emission corresponding to transitions from ν'=0 in the first excited state ($Q(S_1)$ or $Q_x(S_1)$ in the case of ZnPc or H_2Pc respectively) to various vibrational levels ν" in the ground $G(S_0)$ electronic state was observed. Thus in both cases vibrationally relaxed emission occurs. In particular, emission with similar lifetimes was observed with laser excitation in the Q_x or Q_y states of H_2Pc. This fact

shows that the relaxation from Q_y to Q_x is much faster than the time scale of the experiment (~1 ns).

Figure V.2 provides a comparison of the emission spectra recorded for ZnPc and H_2Pc in an Ar matrix. Both molecules show a well-resolved vibronic structure extending from 0 to 1600 cm^{-1} from the origin of the electronic transition. It is evident that the emission spectra of the two molecules exhibit many similarities, especially the vibronic progression consisting of three dominant bands in the red part of the spectrum. The frequencies of the emission vibronic bands of ZnPc recorded in different solids are collected in Table V.2, while those for H_2Pc in the same solids are given in Table V.3. For each species, the fluorescence intensity distribution of the vibronic structure is the same in all the matrices (and all the families of sites). It is also evident in Figure V.2 that the 0-0 transition dominates the emission intensity by more than a factor of 10. This is consistent with the results of measurements made in low temperature molecular beams in which the 0-0 transition was found to carry most of the Franck-Condon intensity.

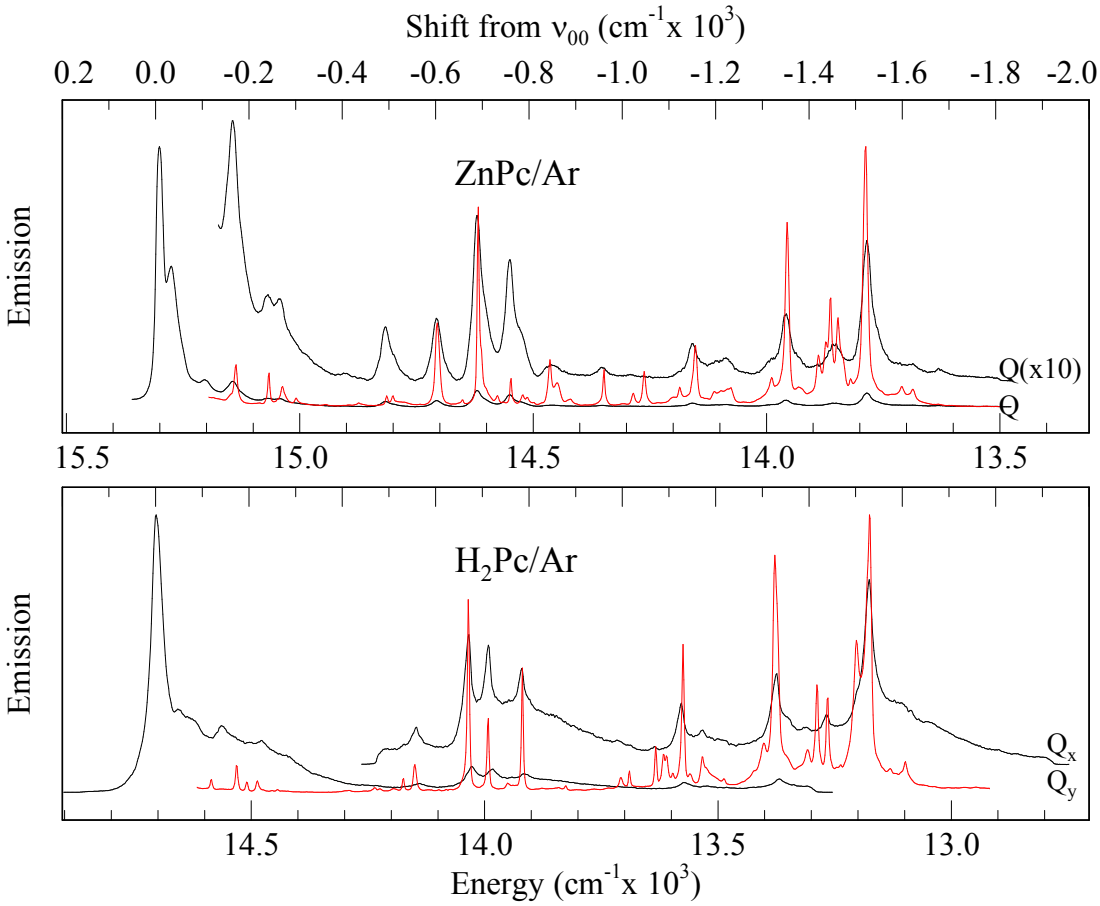

Figure V.2: A comparison of the fluorescence and Raman spectra of the ZnPc (upper panel) and H_2Pc (lower panel) revealing the very strong similarities between the emission and Raman spectra. Emission spectra of ZnPc/Ar (excited in the Q band, λ=647.2 nm) and H_2Pc/Ar (excited in Q_y) and H_2Pc (excited in Q_x). The scale on the top of both plots shows the emission energies as a shift from the position of the 0-0 transition. Raman spectra of ZnPc and H_2Pc in KBr pellets are given in red.

When the laser excitation frequency is tuned inside the 0-0 band of the first excited state, the emission spectra show slight changes in terms of frequency shift and shape of the vibronic bands. This is due to multiple site occupancy. Nevertheless, the fluorescence line narrowing effect is not strong because of a non negligible coupling with the lattice phonons. In the case of ZnPc, two or three main families of sites are thus detected in all the matrices. Similarly, very few sites were also observed for H_2Pc, except in solid nitrogen where the number of clearly distinct matrix environments is higher. However, while the Q_x state provides good site selective excitation, with narrow emission bands, Q_y excitation yields a much poorer site selection, as evident in emission by a broadening of bands in Ar (see Figure V.2) or additional structures involving multiple sites in nitrogen. This effect arises as a result of the spectral overlap of the absorption bands of the two electronic states in H_2Pc. Moreover site selectivity upon excitation in Q_y might be different from the site selectivity upon excitation in the Q_x state.

Table V.2: Frequencies (in cm^{-1}) of the vibronic bands of $G(S_0)$ of ZnPc measured in emission for different matrices. The Shpol'skii data is from Huang et al.[12]. The symmetries of the bands were determined using assignments made using DFT calculations presented in Chapter 4.

N_2	Ar	Kr	Xe		Shpolskii	Raman	Sym
-	9	11		w			
21	34	79		w			
104	102	104	102	w	125	110	B_{2g}
163	165	167	161	m		157	B_{1g}
227	240	237		w	232	228	B_{2g}
262	267	260	265	w		257	A_{1g}
488	490	491	488	m	482	480	B_{2g}
					536	551	B_{1g}
597	600	598		m	592	558	A_{1g}
683	689	688		s	681	677	A_{1g}
752	759	756		s	750	747	B_{1g}
					815		
					836	830	A_{1g}
845	847	854		m	852		
945	947	931	954	w	950	946	B_{2g}
-	-	958					
1147	1150	1149	1152	m	1143	1142	B_{1g}
					1183	1183	B_{2g}
1215	1221	1221	1223	w		1210	B_{2g}
1346	1349	1347	1350	s	1342	1338	A_{1g}
1448	1454	1446	1452	m		1447	B_{1g}
1525	1522	1524	1522	s	1518	1526	B_{1g}
1587	1624	1610	1613	w		1584 1608	A_{1g}/ B_{2g}

Table V.3: Frequencies (in cm^{-1}) of the vibronic bands of $G(S_0)$ of H_2Pc measured in emission for different matrices. The Shpol'skii data is from Huang et al.[12]. The symmetries of the bands were determined using assignments made using DFT calculations presented in Chapter 4.

N_2	Ar	Kr	Xe		Huang	Raman	Sym
--	142	143	--	m	136	130	A_g
--	190	--	--	vw	184	178	B_{1g}
--	239	238	--	vw	232	225	A_g
--	489	494	--	vw	487	478	B_{1g}
--	--	544	--	vw	542	540	A_g
574	579	576	572	w	569	566	A_g
687	688	688	682	s	683	677	A_g
731	730	731	727	s	725	729	A_g
--	--	771	--	vw	769	764	A_g
802	802	802	800	m	801	795	A_g
--	--	--	965	vw	1009	1008	A_g
--	--	1031	1030	vw	1030	1029	B_{1g}
--	--	--	1090	vw	1107	1110	B_{1g}
--	1149	1145	1143	m	1141	1141	A_g
--	--	--	--		1160	1161	A_g
--	1188	1190 (broad sh)	1184	w	1183	1179	A_g
--	--	--	--		1188	1187	B_{1g}
--	--	--	1253	vw	1233	1233	B_{1g}
--	--	--	--		1316	1313	B_{1g}
--	--	--	--		1343	1346	A_g
1356	1351	1351	1350	s	1352		A_g
--	--	--	1376	vw	1372		A_g
1460	1460	1456	1456	w	1453	1452	A_g
--	1523	--	--	vw	1522	1510	A_g
--	--	--	--		1542	1534	B_{1g}
--	--	--	--		1546		A_g
1553	1550	1550	1554	s	1555	1551	A_g

V.3.III Time resolved emission

A summary of the emission decay curves recorded for H_2Pc and ZnPc isolated in different solids (N_2, Ar, Kr and Xe) is given in Figure V.3. The fluorescence decay curves were measured with time-gated iCCD detection and the lifetimes extracted by single exponential fits. The fluorescence lifetimes of H_2Pc are longer than those of ZnPc. Thus the lifetimes of free-base phthalocyanine are 13, 13, 8 and 2.7 ns for N_2, Ar, Kr and Xe respectively, while the lifetimes measured for ZnPc in N_2, Ar and Kr all have very similar values around 3 ns. The recorded lifetimes are all in the nanosecond range, as expected for fully allowed electronic transitions. The shortening of the lifetimes of ZnPc compared to H_2Pc could be due to spin-orbit coupling which had been observed for other porphyrins in the gas phase[13]. The fluorescence lifetimes of H_2Pc and ZnPc are shortest in Xe (~2.8 ns) and may be due to the competitive, non-radiative S_1 - T_1 intersystem crossing - a transition enhanced in this heavy host solid. Attempts to observe the phosphorescence, predicted to occur in the near infrared (NIR), from the triplet states of H_2Pc and ZnPc in Xe with dye laser excitation of the Q state proved unsuccessful using both FT-NIR interferometer and NIR diode array dispersive detection methods.

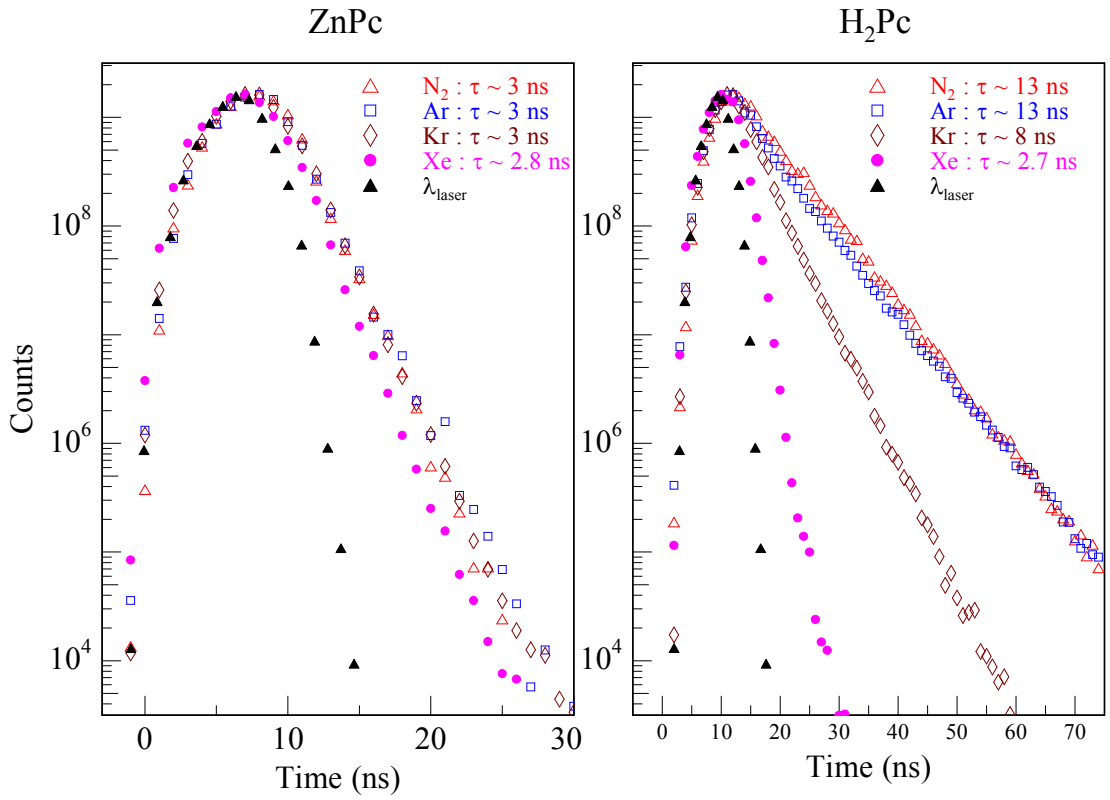

Figure V.3: Semi-log plots of the emission decay curves extracted from Time resolved emission spectra recorded at 13 K for ZnPc and H_2Pc isolated in a variety of low temperature matrices. The shape of the excitation pulse of the laser is also shown.

V.3.IV Excitation spectra

The excitation spectra recorded for H_2Pc isolated in different matrices are shown in Figure V.4. All the spectra presented are shown as the shift from the band origin ($\nu_{0\text{-}0}$) of the Q_x state to facilitate easy comparison of the spectra in different environments. The spectra are the same in all matrices up to ~900 cm^{-1}, but differences appear at higher wavenumbers. The reason for this is the fact that the Q_y band of H_2Pc, located around 1000 cm^{-1} from $\nu_{0\text{-}0}$ of Q_x, can induce a vibronic analogue of Fermi resonance with the vibronic transitions of Q_x. Since the Q_x-Q_y splitting depends on the matrix (cf. Table V.1) the vibronic resonance will couple different vibrational modes of Q_x with those of Q_y for different matrices. The energies of the less complicated modes of ZnPc for the major sites in Ar, Kr, Xe and N_2 (calculated as the shift from the 0-0 transitions) are collected in Table V.4 and compared with Shpol'skii matrix and gas phase data. The energies of the different vibronic modes observed for H_2Pc are collected in Table V. 5 and compared with Shpol'skii matrix[12] and data in Ar published previously[14].

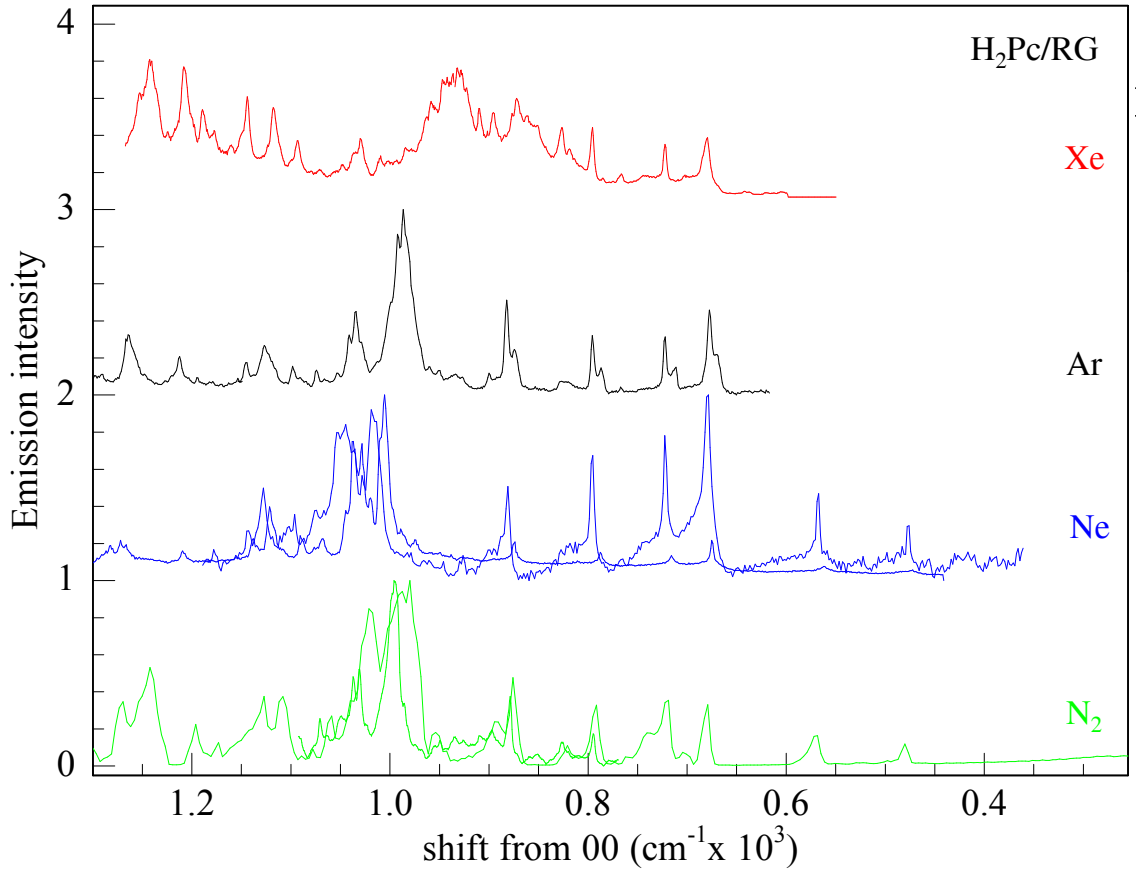

Figure V.4: A comparison of the fluorescence excitation spectra of H_2Pc isolated in Ne, N_2, Ar and Xe at T=7 K recorded by monitoring the vibronic band at 1550 cm^{-1}. Particularly noteworthy in this plot is the similarity of the vibronic structure up to about 950 cm^{-1} from the band origin and the irregular nature of the structure present at higher energies.

Table V.4: Wavenumbers of vibronic transitions in excitation spectra of ZnPc trapped in N_2, Ar, Kr and Xe matrix. The gas phase values were published by Plows and Jones[8] while the Shpol'skii data is from Huang et al.[12]. The symmetries were determined by comparison with DFT Raman results.

N_2	Ar	Kr	Xe	gas phase	Shpol'skii	Sym
				33		
	87			103		B_{2g}
				131		
164	154	155	155	153		A_g
229	225	224	227	226		B_{3g}
259	252	253	255	256		A_g
	314	315	314	306		
	356			324		
	412	410	410	419		
	439			430		
					450w/456w/466vw	
479	478	476	479	482	477vs	B_{3g}
					520w	
				565	568w	B_{1g}
					577w	
593	586	587	586	589	587vs	A_g
					659w	
676	675	675	671		673vs	A_g
744	742	742	737		742s	A_g
					803w/820vw/824w	
832	837	838	837		832m/839m	A_g
846	851				851w	
					889w/899w	
	940	942			937w	A_g

Table V. 5: Wavenumbers of vibronic transitions in excitation spectra of H_2Pc trapped in different matrices. The Shpol'skii data is from Huang et al.[12] and the Ar data is from Bondybey[14].

Huang Shpol'skii	Bondybey Ar	Ar	N_2	Kr	Xe	Ne
		87			86	
136	132	129	131		129	
--	178	175	179		172	
231	231	228	229			
474	475		--			476
565	567		--			568
679	680	677	--		680	680
720	721	722	719		722	722
		768(vw)			766(vw) 784(vw)	
779	--		763			
799	795	795	794	795	795	796
809	--		--	811		
818	--		--		819	
828	827	828(vw)	825	825(vw)	827	
				876(s)	861-872	
890	880	882	878		895	881
900	899	900	896		910	
933	--	933(vw)	935		928-932	926(vw)
	951	949(vw)	947-963	946	946	
--		960(vw)		956	958	
982	985	987-991	982		983	
1009	990	1009(vw)	993-1000	1013	1016	1013-1019
1025	--		--			1028
1028	1034	1034	1030	1033	1030	1035
1036	1039	1041	1036	1044	1048	1044
--	1051	1052	1049	1064		1054
		1065(vw)				
1083	1071	1074	1070	1081	1070	1076
1109	1095	1098	1094	1111	1094	1096
1115	1113	1126	1119	1128	1118	1128
1142	1141	1144	1142	1150	1143	1143
1156				1176	1161(vw)	1178(vw)
1180		1194(vw)			1189	
		1212		1213	1207	
		1264		1251	1243	
		1291-1297		1285		
		1336		1353		
				1451		

V.3.V TDDFT

Electronic excitation energies and oscillator strengths were calculated using linear response time-dependent density functional theory (TD-DFT)[15-17]. The TD-DFT calculations were carried out with Gaussian 03[18] utilising the B3LYP[19-23] functional and the 6-311++G(2d,2p) basis set using geometries calculated in the ground state at the same level of theory. Both spin allowed singlet and forbidden triplet excitation energies were calculated. Calculations of the D_{2h} point group symmetry molecule H_2Pc were carried out with the principal z-axis collinear with the two N-H bond and the x-axis perpendicular to the molecular plane. To facilitate correlation and comparison to the D_{4h} symmetry ZnPc molecule, the x and z axes were exchanged.

The vertical excitation energies and oscillator strengths for zinc and free-base porphyrin, tetrabenzoporphyrin, phthalocyanine and tetraazaporphyrin were also calculated using time-dependent DFT with same functional and basis set. These structurally similar molecules were used to give a more general assessment of the transition energies calculated for H_2Pc and ZnPc. The ground state geometries calculated at the same level (see Chapters IV and VI) were used for the TD-DFT calculations on all eight porphyrin derivatives. The addition of diffuse functions, an extra d polarization function on the heavier atoms (i.e. C, N and Zn atoms) and p polarization functions on the H atoms to the basis set were found to improve the ground state characterisation of these molecules and was used in the current excited state calculations. The selection of the B3LYP functional allowed comparison with previously reported results. Despite its relative old age (1994 - Stephens *et al.*[22,23]), B3LYP is one of the better performing hybrid functionals used in time-dependent studies when compared to experimental results, in particular when applied to heterocyclic aromatic molecules[24].

The results for the lowest allowed singlet transitions ('Q' bands) for both zinc and free-base forms are given in Table V.6 and Table V.7. The lowest energy, spin forbidden triplet transitions are also given. These triplet states are not only important as a competitive relaxation path from the $^1S_1$ excited state to the $^1S_0$ ground state via phosphorescence but are important in the production of singlet oxygen as a reactive species in photodynamic therapy. The experimental results, where available, are also presented in Table V.6 and Table V.7. An extensive

analysis of the orbital contributions to the transition energies and oscillator strengths is given in Appendix V.A.

Table V.6: TD-B3LYP/6-311++G(2d,2p) and experimental results for the singlet 'Q' and corresponding triplet transitions of H_2 and Zn-TAP and H_2 and Zn-Pc aza-porphyrins. The main KS orbital coefficients are also given. Note: the orbital coefficients for each degenerate orbital involved the E_u symmetry transitions are given.

Transition Symmetry	Excitation Energy eV (cm^{-1}) {nm}	f	Orbitals	Coefficients	Experimental Energy eV (cm^{-1}) {nm}	Transition Symmetry	Excitation Energy eV (cm^{-1}) {nm}	f	Orbitals	Coefficients	Experimental Energy eV (cm^{-1}) {nm}
H_2TAP						ZnTAP					
$^1B_{3u}$	2.363 (19058.87) {524.68}	0.1472	$4b_{1u}$-$4b_{2g}$ $5b_{1u}$-$4b_{2g}$ $2a_u$-$4b_{3g}$	-0.16848 -0.36517 0.56609	2.05 (16537) {604.7} Ar[25]	^1E_u	2.4386 (19668.63) {508.43}	0.1683	$5a_{2u}$-$5e_g$ $5a_{2u}$-$5e_g$ $1a_{1u}$-$5e_g$ $1a_{1u}$-$5e_g$	0.26074 -0.22209 0.38060 0.44684	2.13 (17178) {582.1} $CHCl_3/CH_3OH$[26]
$^1B_{2u}$	2.4951 (20124.33) {496.91}	0.1441	$4b_{1u}$-$4b_{3g}$ $5b_{1u}$-$4b_{3g}$ $2a_u$-$4b_{2g}$	0.20293 0.30863 0.57472	2.35 (18978) {526.9} Ar[25]	^1E_u	2.4386 (19668.63) {508.43}	0.1683	$5a_{2u}$-$5e_g$ $5a_{2u}$-$5e_g$ $1a_{1u}$-$5e_g$ $1a_{1u}$-$5e_g$	0.22209 0.26074 -0.44684 0.38060	
$^3B_{3u}$	1.4617 (11789.40) {848.21}		$2a_u$-$4b_{3g}$	0.80933		^3E_u	1.466 (11824.08) {845.73}		$1a_{1u}$-$5e_g$ $1a_{1u}$-$5e_g$	0.46691 0.66652	
$^3B_{2u}$	1.4285 (11521.62) {867.96}		$5b_{1u}$-$4b_{3g}$ $2a_u$-$4b_{2g}$	0.22581 0.81793		^3E_u	1.466 (11824.08) {845.73}		$1a_{1u}$-$5e_g$ $1a_{1u}$-$5e_g$	-0.66652 0.46691	
H_2Pc						ZnPc					
$^1B_{3u}$	2.0331 (16398.05) {609.83}	0.4079	$6b_{1u}$-$6b_{2g}$ $7b_{1u}$-$6b_{2g}$ $4a_u$-$6b_{3g}$	0.21433 -0.14924 0.60042	1.88 (15132) {660.9} Gas[10]	^1E_u	2.0536 (16563.40) {603.74}	0.432	$6a_{2u}$-$7e_g$ $6a_{2u}$-$7e_g$ $2a_{1u}$-$7e_g$ $2a_{1u}$-$7e_g$	0.13954 -0.15158 0.44482 0.4095	1.95 (15766) {634.3} Gas[8]
$^1B_{2u}$	2.051 (16542.42) {604.5}	0.4497	$6b_{1u}$-$6b_{3g}$ $7b_{1u}$-$6b_{3g}$ $4a_u$-$6b_{2g}$	-0.19235 0.10005 0.59866	~2.07 (~16680) {~600} Gas[10]	^1E_u	2.0536 (16563.40) {603.74}	0.432	$6a_{2u}$-$7e_g$ $6a_{2u}$-$7e_g$ $2a_{1u}$-$7e_g$ $2a_{1u}$-$7e_g$	0.15158 0.13954 -0.4095 0.44482	
$^3B_{2u}$	1.0095 (8142.16) {1228.12}		$4a_u$-$6b_{2g}$	0.86361		^3E_u	1.1141 (8985.82) {1112.91}		$2a_{1u}$-$7e_g$ $2a_{1u}$-$7e_g$	0.6389 -0.53607	1.13 (9150) {1092.9} 1-chloronaphthalene[27]
$^3B_{3u}$	1.1605 (9360.06) {1068.34}		$4a_u$-$6b_{3g}$	0.81834	1.24 (10001.3) {999.9} 1-chloronaphthalene[28]	^3E_u	1.1141 (8985.82) {1112.91}		$2a_{1u}$-$7e_g$ $2a_{1u}$-$7e_g$	0.53607 0.6389	

Table V.7: TD-B3LYP/6-311++G(2d,2p) and experimental results for the singlet 'Q' and corresponding triplet transitions of H_2 and Zn-TBP and H_2 and Zn-P methine porphyrins. The main KS orbital coefficients are also given. Note, the orbital coefficients for each degenerate orbital involved the E_u symmetry transitions are given.

Transition Symmetry	Excitation Energy eV (cm^{-1}) {nm}	f	Orbitals	Coefficients	Experimental Energy eV (cm^{-1}) {nm}
H_2TBP					
$^1B_{3u}$	2.0865 (16828.75) {594.21}	0.0963	$7b_{1u}$-$6b_{2g}$ $4a_u$-$6b_{3g}$	0.43833 0.57334	1.895 (15284) {654.3} Ar[29]
$^1B_{2u}$	2.1211 (17107.82) {584.53}	0.2177	$7b_{1u}$-$6b_{3g}$ $4a_u$-$6b_{2g}$	0.34953 -0.59456	2.124 (17132) {583.7} Ar[29]
$^3B_{2u}$	1.3176 (10627.16) {941}		$7b_{1u}$-$6b_{3g}$ $4a_u$-$6b_{2g}$	-0.2774 0.79104	
$^3B_{3u}$	1.6169 (13041.17) {766.79}		$7b_{1u}$-$6b_{2g}$ $4a_u$-$6b_{3g}$	0.12528 0.76415	
H_2P					
$^1B_{3u}$	2.2704 (18312.00) {546.1}	0.0001	$2a_u$-$4b_{3g}$ $5b_{1u}$-$4b_{2g}$	-0.48516 -0.54406	1.98 (15969.8) {626.2} Gas[30]
$^1B_{2u}$	2.4162 (19487.96) {513.14}	0.0002	$2a_u$-$4b_{2g}$ $5b_{1u}$-$4b_{3g}$	-0.49226 0.50965	2.42 (19518.6) {512.3} Gas[30]
$^3B_{2u}$	1.5066 (12151.54) {822.97}		$2a_u$-$4b_{2g}$ $5b_{1u}$-$4b_{3g}$	-0.4202 0.76229	
$^3B_{3u}$	1.8321 (14776.88) {676.74}		$2a_u$-$4b_{3g}$ $5b_{1u}$-$4b_{2g}$	0.2576 0.74584	1.58 (12743.6) {784.7} Xe[32]
ZnTBP					
^1E_u	2.1426 (17281.23) {578.65}	0.1803	$6a_{2u}$-$7e_g$ $2a_{1u}$-$7e_g$	-0.36716 0.59788	2.03 (16339.9) {612} Ar[29]
^1E_u	2.1426 (17281.23) {578.65}	0.1805	$6a_{2u}$-$7e_g$ $2a_{1u}$-$7e_g$	-0.36717 -0.59788	
^3E_u	1.4992 (12091.86) {826.98}		$6a_{2u}$-$7e_g$ $6a_{2u}$-$7e_g$ $2a_{1u}$-$7e_g$ $2a_{1u}$-$7e_g$	-0.11188 0.14039 0.60634 0.4832	1.57 (12662.9) {789.7} Ar[29]
^3E_u	1.4992 (12091.86) {826.98}		$6a_{2u}$-$7e_g$ $6a_{2u}$-$7e_g$ $2a_{1u}$-$7e_g$ $2a_{1u}$-$7e_g$	0.14039 0.11188 0.4832 -0.60634	
ZnP					
^1E_u	2.4083 (19424.24) {514.81}	0.0027	$5a_{2u}$-$5e_g$ $5a_{2u}$-$5e_g$ $1a_{1u}$-$5e_g$ $1a_{1u}$-$5e_g$	0.37619 0.3383 0.34179 -0.38008	2.25 (18140) {551} N_2[31]
^1E_u	2.4083 (19424.24) {514.81}	0.0027	$5a_{2u}$-$5e_g$ $5a_{2u}$-$5e_g$ $1a_{1u}$-$5e_g$ $1a_{1u}$-$5e_g$	-0.3383 0.37619 0.38008 0.34179	
^3E_u	1.7735 (14304.24) {699.1}		$5a_{2u}$-$5e_g$ $5a_{2u}$-$5e_g$ $1a_{1u}$-$5e_g$ $1a_{1u}$-$5e_g$	0.64185 0.23879 -0.42560 0.15834	1.84 (14808) {675.3} Xe[31]
^3E_u	1.7735 (14304.24) {699.1}		$5a_{2u}$-$5e_g$ $5a_{2u}$-$5e_g$ $1a_{1u}$-$5e_g$ $1a_{1u}$-$5e_g$	-0.23879 0.64185 0.42560 0.15834	

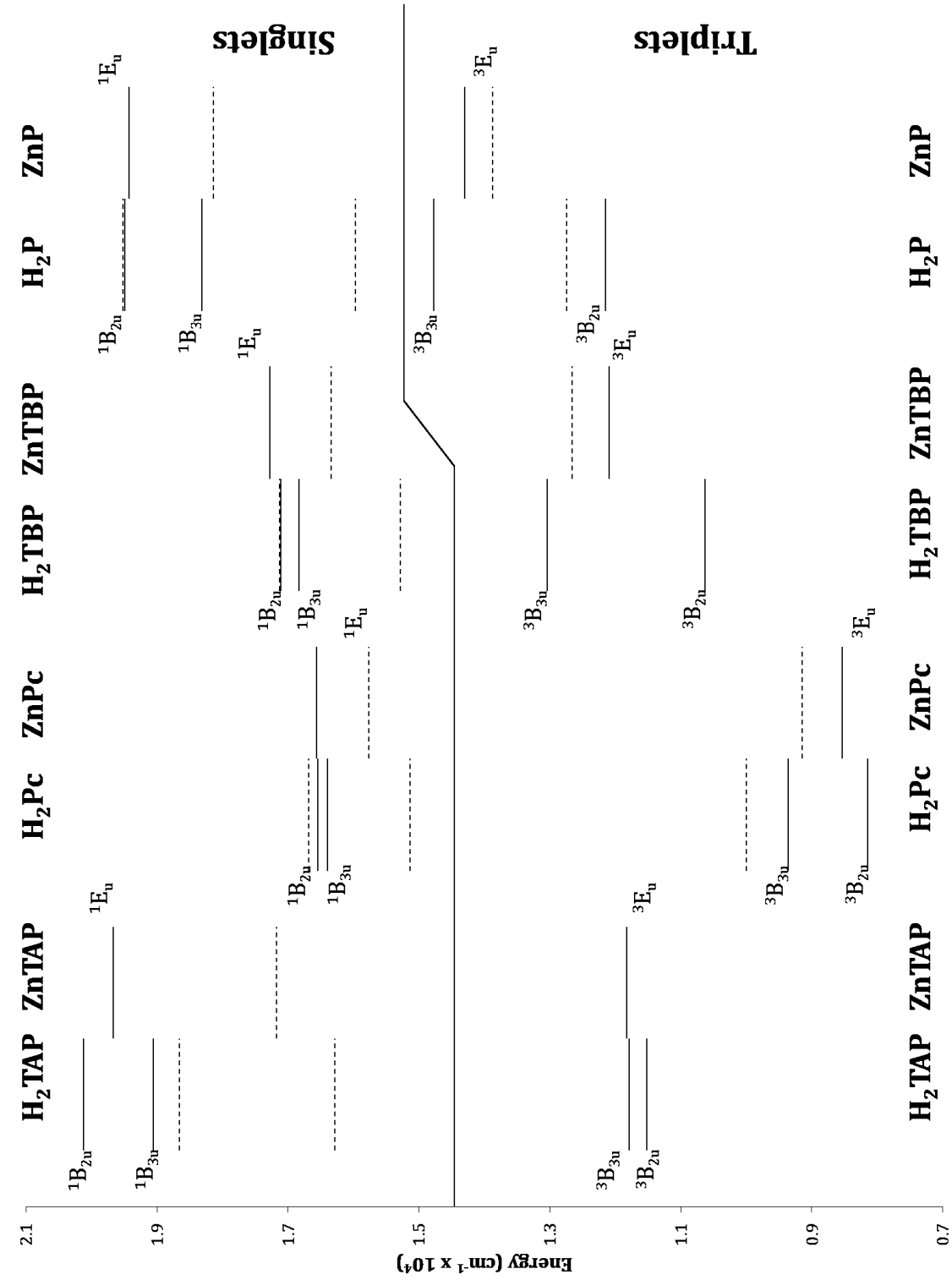

Figure V.5 TD-DFT calculated and experimental transition energies for free-base and zinc porphyrins. TD-DFT results were calculated using the B3LYP/6-311++G(2d,2p) functional and basis set and are indicated by the solid lines. The experimental results are indicated by the dashed lines (see Table V.6 and Table V.7 for values used). Note: there is an excellent match between the experiment and theoretical values for the $^1B_{2u}$ transitions of H_2P and H_2TBP and the lines representing these results overlap.

A plot of the calculated vertical excitation energies compared to the experimental values is given in Figure V.5. The ^1E_u TD-DFT results for ZnPc, ZnTBP and ZnP are between 5.1 – 7.1 % higher than the experimental values while ZnTAP is 14.5 % higher. The closest theoretical results to experiment are for the larger zinc porphyrins where the ^1E_u ZnPc transition is found to be 797 cm^{-1} higher than the gas phase experimental results and ZnTBP 941 cm^{-1} higher than the matrix isolated N_2 results. The ZnP TD-DFT results are 1284 cm^{-1} higher than experimental results also recorded in a N_2 low-temperature solid. The largest difference between theory and experiment for these zinc complexed molecules is for ZnTAP, which is predicted to be 2489 cm^{-1} higher in energy. It should be noted that the experimental results were for ZnTAP in a mixture of dichloromethane and methanol and not in an low-temperature inert solid or in the gas phase.

In general, there is a good match between the experimental and TD-DFT Q_y excitation energies for the free-base molecules. The theoretical $^1B_{2u}$ transition of H_2Pc is 137 cm^{-1} lower than experiment while H_2P and H_2TBP are even closer with the theoretical values only 31 and 24 cm^{-1} lower than experiment. The TD-DFT result for the Q_y transition of H_2TAP is 1145.4 cm^{-1} higher than experiment. Despite the reasonably good match between the theoretical and experimental Q_y transitions of H_2Pc, H_2TBP and H_2P, the same conclusions cannot be made for the lower energy Q_x transitions.

Table V. 8 presents the experimental and TD-DFT results for the Q_y and Q_x transitions of the four free-base porphyrins and the energy gap between them, $\Delta\nu$. In all cases, TD-DFT underestimates the splitting between the transitions. The splitting calculated for the small porphyrins are 44.9 % for H_2TAP and 33.1 % for H_2P of the experimentally determined band difference. The experimental results for H_2TAP were recorded in an Ar matrix and may be affected by its environment, the comparison with the gas phase results of H_2P still shows an underestimation of the Q_x/Q_y energy gap by the TD-DFT method.

While the TD-DFT method underestimated the Q_x/Q_y gap for H_2TAP and H_2P by factors of approximately two and three, for H_2Pc and H_2TBP there is an order of magnitude difference between experiment and theory. The experimental splitting between the Q_y and Q_x transitions are ~1548 cm^{-1} for H_2Pc and 1848 cm^{-1} for H_2TBP (approximately 1.5 to 2 times smaller than their non-benzo analogues).

However, the TD-DFT differences in energy are 144 cm^{-1} for H_2Pc and 279 cm^{-1} for H_2TBP, only 9.3 and 15.1 % respectively of the experimentally determined Δν value and significantly smaller the theoretical splitting calculated for H_2TAP and H_2P. Though small changes to the splitting between Q_x and Q_y in H_2Pc have been seen in different experimental environments (cf. Figure V.4), these shifts are far smaller than the large error between experiment and theory.

Table V. 8: Experimental and theoretical Q_x/Q_y ($^1B_{3u}/^1B_{2u}$) splitting frequencies, Δν, for the free-base porphyrins. Values shown are in cm^{-1} and the experimental conditions are indicated by the superscripts.

	H_2TAP		H_2Pc		H_2TBP		H_2P	
	Exp^{Ar}	TD-DFT	Exp^{gas}	TD-DFT	Exp^{Ar}	TD-DFT	Exp^{gas}	TD-DFT
Q_y	18979	20124	16680	16542	17132	17108	19519	19488
Q_x	16537	19059	15132	16398	15284	16829	15970	18312
Δν	2442	1065	1548	144	1848	279	3549	1176

The calculated oscillator strengths for the zinc porphyrins follow the following trend: ZnPc > ZnTBP ≈ ZnTAP >> ZnP. This trend is found with the experimental values available. For ZnPc the experimental f value of 0.40 is slightly lower than the DFT value of 0.432. The experimental f value of 0.30 for ZnTBP however, is 66 % higher than the f value calculated at 0.1804. For the weakly allowed ^1E_u transition of ZnP the experimental f value of 0.005 is 46 % higher than the calculated value of 0.0027 but proportionally lower than the other fully allowed transitions. No experimentally determined oscillator strengths were available for ZnTAP. For the $^1B_{2u}$ (Q_y) transition oscillator strengths of the free-base porphyrins a similar trend to the zinc porphyrins is seen, with H_2Pc > H_2TBP > H_2TAP >> H_2P. A slightly different trend is found for the oscillator strengths of the $^1B_{3u}$ (Q_x) ← $^1S_0$ transition, H_2Pc > H_2TAP > H_2TBP >> H_2P where the f value calculated for the Q_x of H_2TAP is 53 % higher than the Q_x for H_2TBP. For H_2P and H_2TBP, the higher energy Q_y transitions are experimentally more allowed than the Q_x transitions, with larger absorption strengths consistent with current calculated results. From experiments on the aza bridged porphyrins, the intensities of the states is reversed and the Q_x is more allowed than the Q_y. The TD-DFT results for H_2TAP show the correct f value trend with the Q_x oscillator strength of 0.1472 only 0.0031 larger than the Q_y f value of 0.1441. The calculated oscillator strengths for H_2Pc show the same trend as is apparent for the methine bridged molecule with the Q_y slightly more intense

than the Q_x with f values of 0.4497 and 0.4079 respectively, contrary to the experimental results.

The experimental triplet results are taken from the 0-0 phosphorescent emission bands reported in the literature. The ^3E_u theoretical results for ZnPc and ZnTBP were lower in energy than experimental phosphorescence results by 164 and 571 cm^{-1} respectively. These results represent a 1.8 % and 4.6 % difference. There was a comparable difference between the ZnP results of 432 cm^{-1} (2.9 %) but for this molecule the theoretical triplet excitation energy was higher than the experimental phosphorescence value recorded in a Xe matrix. No phosphorescence data for ZnTAP was found in the literature. For the triplet transitions of the free-base molecules, only emission from one state has been reported experimentally analogous to fluorescence only from the Q_x state. In all free-base molecules, the $^3B_{3u}$ transition, which has been calculated to be higher in energy than $^3B_{2u}$ transition, a reversal of the energy order of the singlet transitions. No phosphorescence for H_2TAP and H_2TBP has been reported. The experimental results for H_2Pc in 1-chloronaphthalene are 641 cm^{-1} higher in energy than the TD-DFT $^3B_{3u}$ calculated at 9360 cm-1. The TD-DFT $^3B_{3u}$ transition is 2033 cm^{-1} higher in energy than the H_2P in Xe result and the calculated $^3B_{2u}$ transition is in fact closer, being only 592 cm^{-1} lower and could be assigned as such. It is interesting to note that the energy difference between the H_2Pc, H_2TBP and H_2P triplet B_{3u} and B_{2u} transitions of 1218, 2414 and 2625 cm^{-1} are closer to the experimental Q_y/Q_x splitting than the corresponding singlet TD-DFT results reported above. The difference between the calculated triplet transitions of H_2TAP is however much smaller at 268 cm^{-1}.

V.4 Discussion

V.4.I TDDFT

The TD-DFT result presented above, calculated using the B3LYP/6-311++G(2d,2p) combination of functional and basis set, are consistent with the theoretical results in the literature with an improvement in the excitation energies when compared to previous work using the same functional but with much smaller basis sets. Despite the improved results, some significant discrepancies still exist between the theoretical and experimental excitation energies. Most pertinent to

the current work, the Q_y/Q_x splitting is grossly underestimated for H_2Pc at only 144 cm^{-1}. This, as well as the incorrect ratio of oscillator strengths of these two states, would limit the ability for use of any direct calculation of the Franck-Condon factors with TD-DFT methods in order to identify the modes coupling between the states. Calculations using the Symmetry Adapted Cluster/Configuration Interaction (SAC-CI) method by Toyota et al.[33] predicted a more accurate Q_y/Q_x splitting of 1694 cm^{-1} with an oscillator strength ratio of 1 : 1.79. However the actual excitation energies they calculated of 1.30 and 1.51 eV (10,485 cm^{-1}, 953.72 nm and 12179 cm^{-1}, 821.1 nm) were much lower than the experimental values and far less accurate than the TD-DFT results presented here.

V.4.II Fluorescence Lifetimes

The fluorescent lifetime (τ) of a transition may be calculated from the oscillator strength (f) and transition wavelength (λ) using the following relationship[34],

$$\tau_0 = \frac{\lambda^2 \varepsilon_0 m_e c}{2\pi e^2 f} \qquad \text{(V.1)}$$

where ε_0 is the vacuum permittivity, c is the speed of light and m_e and e are the mass and charge of an electron respectively. Applying Equation V.1 with λ and f values for the lowest energy Q transitions determined using TD-DFT, the lifetimes calculated for H_2Pc are 16.68 ns and 6.32 ns for ZnPc. Even accepting the weaknesses of the TD-DFT method to predict the excited state transition properties, these lifetimes do reflect the trend seen in experiment where H_2Pc emission was significantly longer lived than ZnPc. It is apparent that the longer lifetime calculated for H_2Pc using Equation V.I is due to its weaker oscillator strength predicted at 0.4076 compared to ZnPc with an oscillator strength of 0.864 (the degenerate Q transitions give f = 2 x 0.432). A simple field correction factor may be applied to f to approximate the apparent oscillator strength f" given as,

$$f"/f = [s(n^2 - 1) + 1]^2/n \qquad \text{(V.1)}$$

where n is the index of refraction of the host material and s is a shape factor for the cavity related to the depolarization factor[35]. Taking into account the experimentally observed matrix shifts Δ (see Table V.1), giving $\lambda = \lambda_{TD\text{-}DFT} + \Delta$, and selecting a suitable s value for a square thin slab (0.5), the lifetimes of H_2Pc and ZnPc in different inert gas solids were determined and are given in Table V.9. For

ZnPc a relatively small variation in the calculated lifetimes in different host materials is observed with longer lifetimes in N_2 compared to Xe, consistent with experimental results. The results for H_2Pc in N_2, Ar and Kr reflect the same trend observed in experiment but the experimentally determined lifetime for Xe is considerably shorter than theory and may indicate phosphorescence due to the heavy atom effect. Temperature studies for H_2Pc and ZnPc in Kr and Xe between 13 and 35 K for showed no change in fluorescence lifetimes.

Table V.9: Theoretically predicted ($\tau_{TD\text{-}DFT}$) and experimental (τ_{exp}) lifetimes of H_2Pc and ZnPc in different host media. Lifetimes are in ns.

		H_2Pc		ZnPc	
	n	$\tau_{TD\text{-}DFT}$	τ_{exp}	$\tau_{TD\text{-}DFT}$	τ_{exp}
Vacuum	1	13.68	-	6.32	-
N_2	1.22	11.17	13	5.25	3
Ar	1.29	10.04	13	4.70	3
Kr	1.428	8.94	8	4.20	3
Xe	1.49	8.44	2.7	3.98	2.8

V.4.III Vibronic structure in Emission

ZnPc and H_2Pc are large molecules exhibiting a lot of vibrational modes but due to their high symmetry (D_{4h} and D_{2h}) these modes can be separated into several symmetry groups. A simplifying consequence is that a limited number of modes are infrared or Raman active. As these molecules have a centre of inversion, there is mutual exclusion behaviour between IR-active modes and Raman active modes, shown by the vibrational representations. Selection rules will also reduce the number of vibrational modes involved in the electronic transitions. The $S_1 \leftrightarrow S_0$ transitions for both ZnPc and H_2Pc are electronic allowed and, depending on the Franck-Condon selection rules, , the totally symmetric A_{1g} /A_g modes as well as vibrational modes of other symmetries of these molecules should also be observable. Accordingly, for the S_1 state of ZnPc which has ^1E_u symmetry, modes that transform as the A_{1g}, A_{2g}, B_{1g} and B_{2g} irreducible representations are predicted to couple to the $S_1 \leftrightarrow S_0$ transitions (where $\nu = 0$ in the initial state and S_0 has A_{1g} symmetry). Similarly, the S_1 (Q_x) state of H_2Pc, which has $^1B_{3u}$ symmetry according to TD-DFT, may couple to A_g and B_{1g} modes. Formally, the E_g modes of ZnPc and B_{2g}

modes of H_2Pc may also couple to these transitions. These modes however would be expected to be extremely weak because they are predicted to transform perpendicular to the main dipole moment of the transitions (which are in the xy plane of the molecule). All these modes, except A_{2g} modes of ZnPc, are Raman active modes. These symmetry arguments are consistent with those made previously by Huang *et al.*[12].

The conventional Raman scattering spectra of ZnPc and H_2Pc recorded in KBr pellets with CW 532 nm excitation are shown in Figure V.2 by the red trace. The vibrational frequencies measured for the Raman active modes of both molecules have been presented and analysed in Chapter IV. What is very evident in Figure V.2 is the strong similarity between the visible emission and the normal Raman spectra in the case of both molecules. Thus while there are some intensity differences between the emission and Raman spectra, the line positions all agree. The significance of this observation is that the mode assignments established with large basis set DFT calculations for the Raman bands can now be used to assign the bands present in the emission spectra.

In Chapter IV, density functional theory (DFT) at the B3LYP /6-311++G(2d,2p) level was used to predict the infrared and Raman frequencies for ZnPc. In these high level calculations it was found that the most stable geometry for the molecule has D_{4h} symmetry with the Zn atom in the plane of the phthalocyanine ring. A key result of the vibrational analysis conducted is that no E_g Raman modes were clearly observed experimentally in KBr pellets. This is the principal reason for the observed similarities between the experimental Raman and fluorescence spectra. The theoretically predicted Raman spectra are compared with experimental data in Figure V.6. The most intense Raman active mode is predicted at 1557 cm^{-1} (1526 cm^{-1} scaled) with B_{1g} symmetry. According to Tackley *et al.*[36] and verified by the current study, this mode corresponds to an out-of-phase stretching of the C-N-C bonds in the tetrapyrrole ring. It is noteworthy that the fluorescence band at 1525 cm^{-1}, which exhibits amplified emission with higher laser intensity (see Chapter VI), is very close to the calculated frequency for the most intense Raman mode.

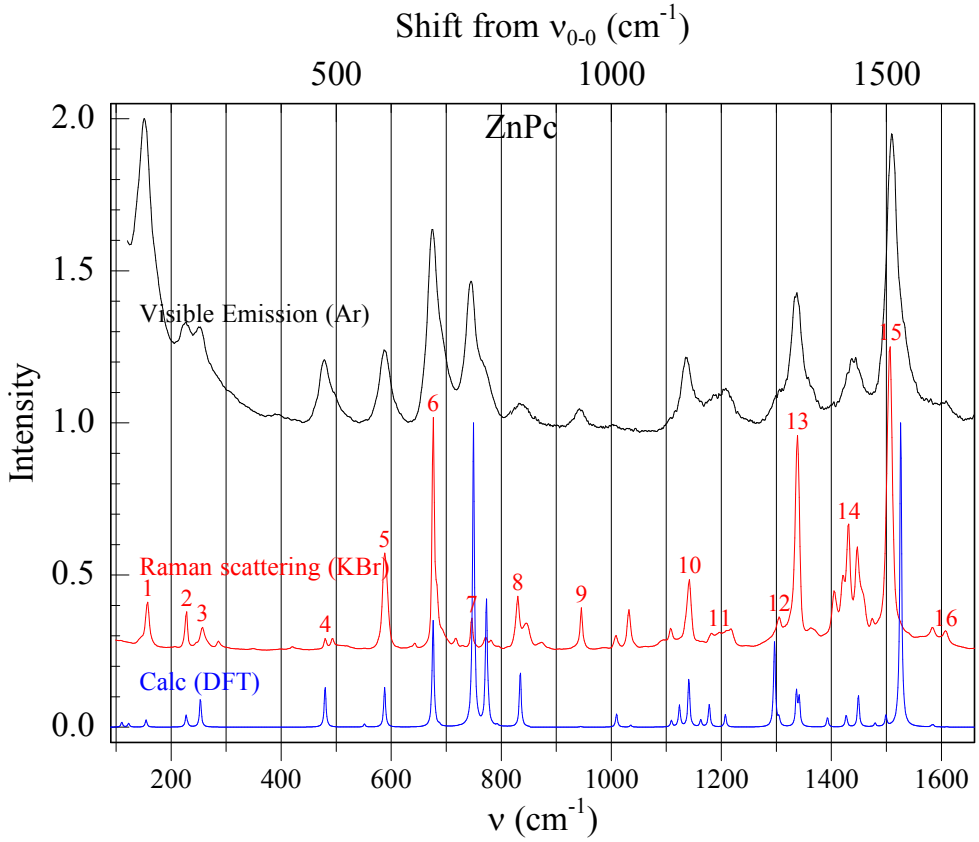

Figure V.6: A detailed comparison of the emission spectra recorded for ZnPc isolated in Ar and the Raman spectra of both experimentally recorded (red trace) and the scaled results of high level DFT predictions (blue trace). The motions of the numbered modes are provided in Table V. 10.

In the same way the Raman spectrum of H_2Pc is very similar to the fluorescence spectrum of H_2Pc in N_2 (Figure V.2). Again fluorescence active modes are also observed in Raman spectroscopy. The most intense Raman band coincides with the band at 1550 cm^{-1} which exhibits amplified emission (AE). Since replacing the two hydrogens by a Zn atom only shifts this mode by 27 cm^{-1}, it is reasonable to assume that the AE mode in H_2Pc will also involve an out-of-phase stretching of the C-N-C bonds in the tetrapyrrole ring. This assumption was confirmed by the DFT calculations performed and presented in Chapter IV. A more comprehensive description of this mode and its role in amplified emission will be given in the chapter following this.

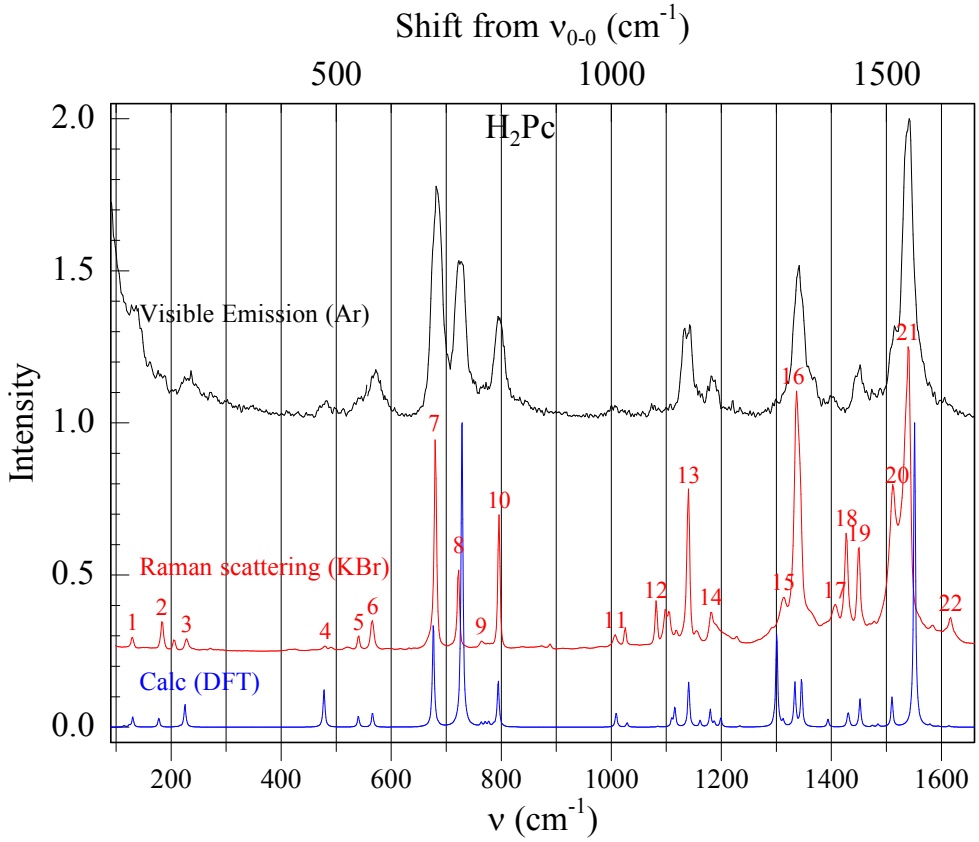

Figure V.7: A detailed comparison of the emission spectra recorded for H_2Pc isolated in Ar and the Raman spectra for both experimentally recorded (red trace) and the scaled results of high level DFT predictions (blue trace). The motions of the numbered modes are provided in Table V.11.

The good agreement between the Raman and fluorescence frequencies was expected because of the similar selection rules, but the observed intensities in Raman and fluorescence spectra are also very similar. This is consistent with the fact that all the vibronic transitions observed in fluorescence are transitions from $\nu'=0$ to $\nu_i''=1$ for different vibrational modes (i.e. no overtones or progressions were observed). Assignment of the vibronic structure of the emission is possible using the ground state Raman results. The most prominent bands in the emission and Raman spectra are numbered in Figure V.7 and Figure V.6 while the mode assignments, taken from the DFT Raman predictions are listed in Table V. 10 and Table V.11 for ZnPc and H_2Pc respectively.

Table V. 10: Characteristic vibrational motions of the most intense bands in the Raman spectra of ZnPc as determined by DFT calculations. The frequencies are given in wavenumber (cm^{-1}) units and all the observed Raman modes involve in-plane motions.

Mode #	Obs.	DFT (unscaled)	Sym	Mode description
1	157.4	157.6	B_{1g}	Bridging C-N-C sym. rocking
2	228.3	231.9	B_{2g}	Bridging C-N-C asym. deformation
3	257.2	258.4	A_{1g}	Bridging C-N-C sym. def.
4	479.9	489.67	B_{2g}	Aryl rocking & central ring def.
5	588.3	600.1	A_{1g}	Aryl deformation/ sym. ring def.
6	676.5	689.9	A_{1g}	Bridging C-N-C sym. def and aryl def
7	746.0	764.8	B_{1g}	Central ring contraction & aryl def..
8	829.9	851.6	A_{1g}	Central ring expansion & pyrrole def..
9	945.8	963.6	B_{2g}	C-H def & aryl C-C str.
10	1141.9	1164.3	B_{1g}	aryl C-C str. and C-H def
11	1197.1	1232.0	B_{2g}	aryl C-C str. and C-H def
12	1304.8	1323.1	B_{1g}	C-H def/aryl def
13	1338.3	1363.8	A_{1g}	aryl C-C str. and C-H def
		1368.9	B_{1g}	aryl C-C str. and C-H def
14	1431.7	1478.7	B_{1g}	C-H def
15	1506.8	1557.2	B_{1g}	Bridging C_α-N_m-C_α asym.str and sym str of the C_α-N_H-C_α bonds
16	1607.6	1642.5	B_{2g}	Pyr C-C str. & aryl C-C str

Table V.11: Characteristic vibrational motions of the most intense bands in the Raman spectra of H_2Pc as determined by DFT calculations. The frequencies are given in wavenumber (cm^{-1}) units and all the observed Raman modes involve in-plane motions.

Mode #	Obs.	DFT (unscaled)	Sym	Mode description
1	129.9	132.9	A_g	Bridging C-N-C sym. rocking
2	182.9	181.2	B_{1g}	Bridging C-N-C asym. deformation
3	228.3	229.7	A_g	Bridging C-N-C sym. def.
4	479.9	487.6	B_{1g}	Aryl rocking & central ring def.
5	541.3	551.3	A_g	Aryl deformation/central ring def
6	565.7	577.5	A_g	Aryl deformation/sym. ring def.
7	679.9	690.4	A_g	Bridging C-N-C sym. def and aryl def
8	722.8	743.5	A_g	Central ring twisting & pyrrole def.
9	763.0	779.3	A_g	Central ring contraction & aryl def..
10	796.1	810.7	A_g	Central ring expansion & pyrrole def..
11	1007.3	1029.3	A_g	C-H def & aryl C-C str.
12	1081.4	1106.9	B_{1g}	N-H IP bending aryl def
13	1140.3	1164.0	A_g	aryl C-C str. and C-H def
14	1180.9	1203.9	A_g	aryl C-C str. and C-H def
15	1312.8	1339.3	B_{1g}	C-H def/aryl def
16	1336.7	1360.9 1373.3	A_g	aryl C-C str. and C-H def
17	1406.5	1422.4	A_g	pyrrole C-C & C-N str.
18	1426.9	1460.9	A_g	C-H def
19	1450.5	1481.6	A_g	aryl C-C str. and C-H def
20	1511.5	1541.0	A_g	Pyr C-N-C str & C-H def.
21	1539.5	1582.9	A_g	Bridging C_α-N_m-C_α asym.str and sym str of the C_α-N_H-C_α bonds
22	1616.8	1646.8	B_{1g}	Pyr C-C str. & aryl C-C str

V.4.IV Comparison of the excitation and emission spectra

Figure V.8 provides a comparison of the excitation and emission spectra recorded for zinc phthalocyanine in Ar. The apparent weak intensity of the 0-0 band is an artefact due to strong re-absorption arising from the overlap between absorption and emission bands. The characteristic most evident in Figure V.8 is the mirror symmetry that exists between the excitation and emission spectra. This is best illustrated in Ar data but the frequencies found for the vibronic modes in excitation and emission in a variety of matrices are listed in Table V.2 and Table V.4 respectively.

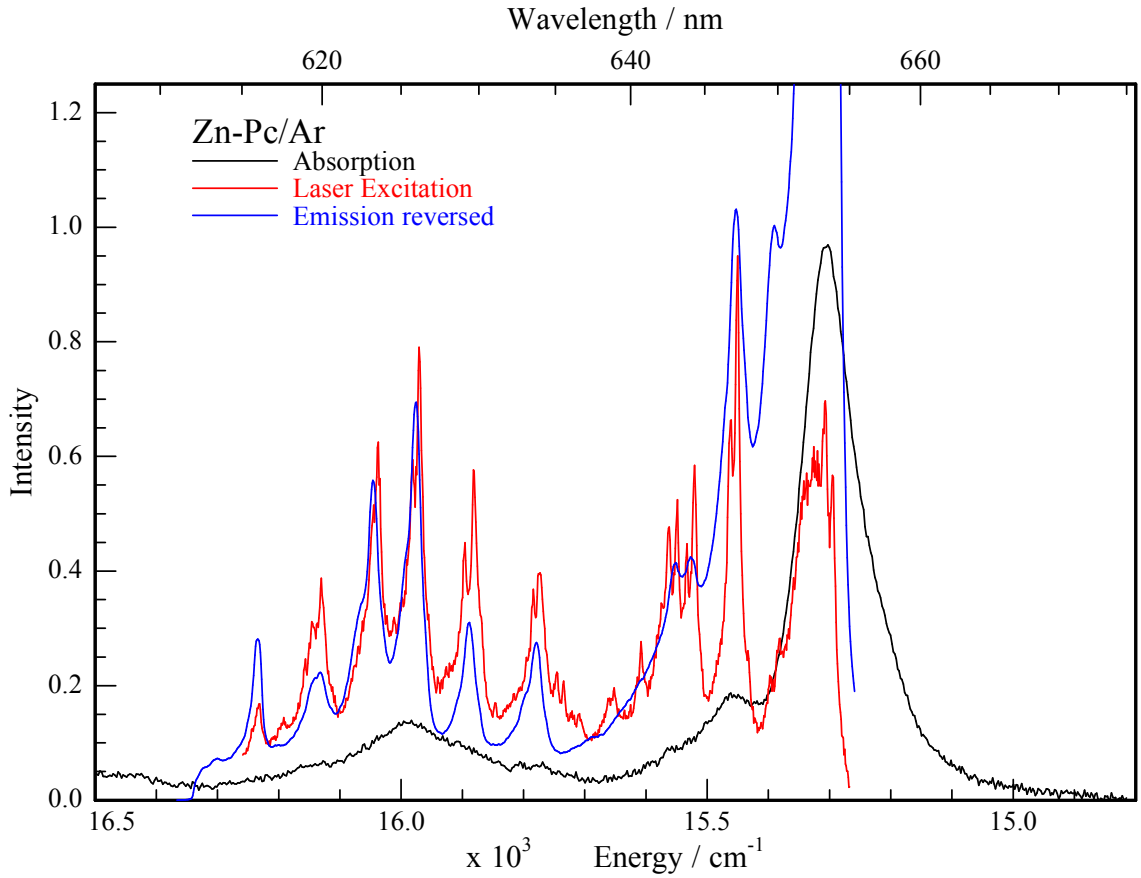

Figure V.8: A comparison of the absorption (black trace), excitation spectra and reversed emission spectra of ZnPc. Very close agreement exists between the excitation and reversed emission indicating very strong mirror symmetry of the two spectra.

The same selection rules exist for vibronic coupling for an electronic transition in both absorption and emission. The similarities in the vibronic intensity distributions in emission and excitation indicate that the molecular geometry in this molecule is not greatly changed when in the first excited electronic state compared to the ground state. This is also confirmed by the fact that the 0-0 band is the most intense band observed in fluorescence spectra. Another key observation which can be made is that positions of the 0-0 transition

in emission and excitation in all matrices agree to within 1 cm^{-1} which is less than the experimental error of the spectroscopic setups. Thus there is no Stokes shift on the Q state emission indicating very similar geometries in the ground and first excited electronic states. The vibrational frequencies of the two electronic states $G(S_0)$ and $Q(S_1)$ of ZnPc isolated in different matrices are in good agreement with those obtained in Shpol'skii matrices as shown in Table V.2 and Table V.4. The current excitation spectra vanish above 1000 cm^{-1} from the 0-0, as those obtained in He droplets[11] also do. The discrepancy from mirror symmetry noticed in Shpol'skii matrices concerned the vibronic structure at higher energy and is not observed in work presented here.

For ZnPc in the gas phase, 13 vibronic bands have been observed in excitation ranging from 33 to 589 cm^{-1} from the band origin. As collected in Table V.4 and shown in Figure V.8, all these modes have been observed for ZnPc in matrices at very similar energies to the gas phase except the modes at 33, 103, 131 and 565 cm^{-1}. The origin of the lowest frequency gas phase mode is unclear as DFT calculations find no vibrational modes less than 22 cm^{-1} making the attribution of the 33 cm^{-1} band to an overtone rather unlikely. On the other hand the 103 and 131 cm^{-1} are present but extremely weak in Raman spectra and most likely correspond to DFT predicted modes at 112.54 and 125.24 cm^{-1}. These modes are probably not observed because they are in the phonon side band of the intense 0-0 band and the mode at 131 cm^{-1} has a very low intensity in the jet experiments. In jet-cooled experiments the most intense band by far was the 0-0, with the band at 153 cm^{-1} being the second most intense in the spectrum. It is also the case in Lehnig's study[11] in helium droplets. In matrices the 0-0 transition is the most intense, but other bands have significant intensities. For example as shown in Figure V.8 the bands at 675 and 153 cm^{-1} are more intense than the 0-0 band. Such intensity ratios will not reproduce the true ratio of the oscillator strengths. This might be due to self absorption phenomena and/or to the fact that the dyes used (DCM and LDS90) are not very intense in the region of the 0-0. The bands between 675 and 938 cm^{-1} may not have been identified in the gas phase because of their low intensity.

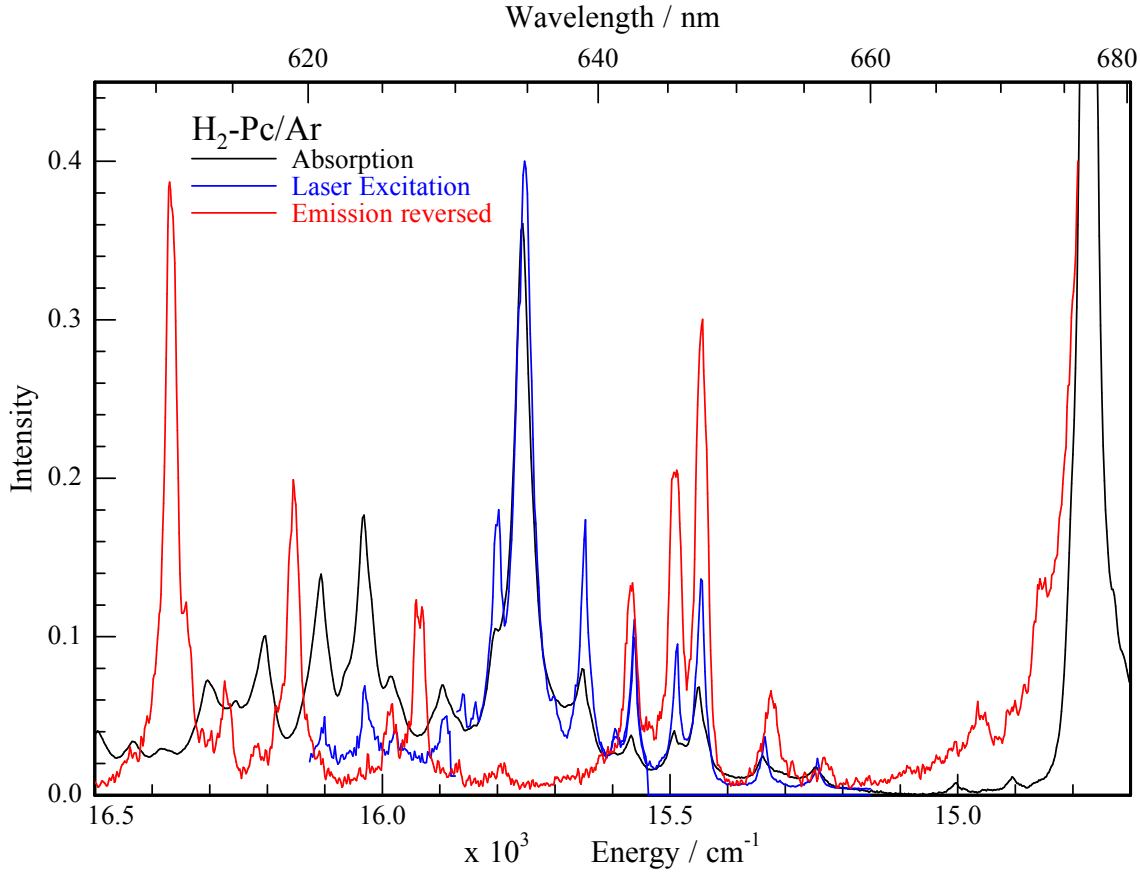

Figure V. 9: A comparison of the absorption (black trace), excitation spectra and reversed emission spectra of H_2Pc. Very close agreement exists between the excitation and reversed emission up to ~950 cm^{-1} from the 0-0 after which the mirror symmetry breaks-down due overlap with the Q_y.

Contrary to ZnPc, for H_2Pc a breakdown of the mirror symmetry occurs in excitation and emission spectra above 1000 cm^{-1} from the 0-0 as shown for the case of H_2Pc in Ar (cf. Figure V. 9). By comparison between the results for emission and excitation of H_2Pc in the other matrices (Table V.3 and Table V. 5 respectively), a similar breakdown of the mirror symmetry is seen. This difference in vibronic structure between emission and excitation is because of the existence of the $Q_y(S_2)$ state at ~1000 cm^{-1} from the $Q_x(S_1)$ state which is not present in ZnPc. The matrix dependence of the position of the Q_y state relative to the 0-0 of the Q_x and subsequent change in structure of this band, indicate coupling between different vibrational modes in the Q_x state depending on the host environment.

From the luminescence study of H_2Pc and D_2Pc in argon reported by Bondybey and English[14], the intense band assigned to the origin of the Q_y electronic transition at 983 cm^{-1} from the 0-0 of the Q_x in H_2Pc was seen to shift by 37 cm^{-1} to 946 cm^{-1} upon deuteration, indicating an isotopic dependence of the vibrational mode coupling the Q_y to the Q_x state. In the current work, a weak feature around 1000 cm^{-1} in emission was correlated to the weak but resolved bands in the experimental Raman spectrum at 1007 and 1025 cm^{-1}. From DFT, the 1025 cm^{-1}

mode has been assigned to an in-plane N-H bending frequency calculated at 1049.7 cm^{-1} (1028.7 cm^{-1} scaled) which shifts by 42.4 cm^{-1} (41.6 cm^{-1}) to 1007.3 cm^{-1} (987.1 cm^{-1}) in D_2Pc.

An intense band found at 882 cm^{-1} in the Ar excitation spectra does not correlate with any feature seen in either emission or Raman spectra. From Bondybey and English, the equivalent excitation band at 880 cm^{-1} in Ar was observed to reduce dramatically in intensity upon deuteration with the growth of a new band at 870 cm^{-1} but with considerably weaker intensity. The closest correlation to these modes in the DFT results were an isotopic pair of B_{1g} modes at 907.44 cm^{-1} (889.29 cm^{-1}) in H_2Pc and at 880.30 cm^{-1} (862.70 cm^{-1}) in D_2Pc, with vanishingly small Raman scattering activities. These modes involve a N-H(D) bending motion coupled to the bridging atoms C-N-C and peripheral aryl C-C-C atoms. Other modes at higher energies than the Q_y were also noticed to shift with deuteration but due to the complex overlap of Q_x and Q_y vibronic bands in this region, they are difficult to assign. No isotopic dependence was seen for the vibronic bands in the excitation spectra up to and including the mode at 795 cm^{-1} from the Q_x 0-0. The excitation spectra of H_2Pc isolated in inert solids also agrees with the results obtained by Plows and Jones[8].

V.4.V Vibronic analogue of the Fermi resonance (H_2Pc)

In contrast to the excitation spectra of ZnPc, which have very similar structures in all solids, the excitation spectra of H_2Pc are quite different to the emission spectra. Moreover, the excitation spectra of H_2Pc depend on both the matrix and on the site that is being monitored. The latter effect can be followed very well in nitrogen matrices which presents many different sites.

The region of the band origin of the $Q_y \leftarrow G$ transition is situated at ~1000 cm^{-1} from the $Q_x \leftarrow G$ transition, so it is expected that vibronic transitions to the excited vibrational states of Q_x will be situated in the same region. The density of vibrational states of Q_x is high in this region and non-adiabatic electronic-vibrational interactions arise between the accidentally degenerate vibronic levels of Q_x and Q_y. As a result, the vibronic lines of the $Q_x \leftarrow G$ transition increase in intensity and are shifted which is analogous to Fermi resonance. The oscillator strength of the $Q_y \leftarrow G$ transition is predicted by TD-DFT to be slightly stronger than that of the $Q_x \leftarrow G$ transition. The enhancement of the weakly allowed vibronic transitions of the Q_x and possible reduction in absorption intensity of the

allowed 0-0 Q_y transition may explain the difference seen between the experimental and theoretical absorption strengths.

In the case of H_2Pc trapped in different solids, the Q_x-Q_y splitting is different. In this way multiple distinct vibronic bands will couple with the Q_y for different matrices. It can also be expected that different sites in the same matrix might have different Q_x-Q_y splittings. This phenomenon has already been observed for other porphyrins (*meso*-tetraazaporphyn, *meso*-tetrapropylporphin and tetrabenzoporphine) in Shpol'skii matrices[37,38]. In the case of H_2Pc the vibrational modes coupled by the "Fermi resonance" are the fundamental modes of Q_x and not the combination modes as observed for *meso*-tetraazaporphyn and *meso*-tetrapropylporphin[38].

V.4.VI Sites of ZnPc and H_2Pc

It has been shown before that both ZnPc and H_2Pc isolated in N_2 show well defined site structures both in absorption and emission. However the number of resolved features is very different for the two molecules with seven observed for H_2Pc and two identified for ZnPc in emission spectra.

The H_2Pc molecule can exist in two different tautomeric forms when isolated in solids depending on the position of the two hydrogen atoms on the inner ring of the phthalocyanine. Because of the interaction with the host matrix, these two tautomers are known to have different absorption frequencies. Thus, where only one band appears in the ZnPc absorption spectrum two bands are expected for H_2Pc. This fact can explain why some of the absorptions peaks of free-base phthalocyanine do not exist in the spectrum of the metal-phthalocyanine, but more experiments are needed in order to identify the correspondence between sites of H_2Pc and ZnPc in N_2.

V.5 Conclusions

The electronic spectra of two tetrapyrrolic molecules isolated in rare gas and molecular matrices namely free-base phthalocyanine and zinc phthalocyanine were investigated. A close comparison was observed between the vibrational bands recorded using Raman spectroscopy and those in emission. This behaviour is explained by the similarities in the selection rules for both types of transitions in these planar molecules. This allowed the use of the Raman active modes calculated

with large basis set density function theory to assign the vibronic modes of the ground state seen in emission for both H_2Pc and ZnPc.

The observed vibronic frequencies in the ground (G) and first excited (Q) states of ZnPc were found to be very similar. This indicated a very similar geometry in the excited state to that in the ground state and allowed the vibrational modes in the Q state to be assigned using the DFT calculated Raman spectra. In the case of H_2Pc the existence of the second exited state Q_y only 1000 cm^{-1} above Q_x is responsible for the observation of a very complicated excitation spectrum due to non-adiabatic coupling between electronic and vibrational states. This made assignment of the modes above the Q_y difficult using the ground state vibrational mode observed in emission or Raman spectra.

The energy difference between the Q_x and Q_y states was found to be dependent on the host matrix, with the largest Q_y-Q_x splitting of 985.3 cm^{-1} found for H_2Pc in Ar and the smallest splitting of 916 cm^{-1} in Xe. An electronic analogy to Fermi resonance has been proposed to explain the coupling of various quasi-degenerate vibronic modes in Q_x to those in Q_y. A tentative assignment of one of these modes 985.3 cm^{-1} from the 0-0 of Q_x in Ar has been made by comparison of the results reported here and those of previous excitation spectra recorded for D_2Pc. Using DFT calculations this mode is identified as a B_{1g} symmetry in-plane deformation mode of the two central N-H bonds. Further analysis, including more extensive experimental analysis and theoretical calculations, is required in order to fully resolve the vibrational modes coupling in both excited states of H_2Pc and in various host environments.

The excitation energies and oscillators strengths of H_2Pc and ZnPc were calculated using linear-response time-dependent DFT. The results from TD-DFT were compared to both experiment and to calculated values for free-base and zinc TAP, TBP and porphine. They were found to be qualitatively useful in identifying and accounting for trends seen in experiment. By examining the KS orbitals described in Appendix V.A, the conjugated π systems contributing to the aromaticity of Pc and TBP were seen to be not only localized to the central ring, as is the case for the smaller P and TAP molecules, but distributed over the fused benzene annulations. This extension of the π system has the effect of perturbing the energies of these orbitals when compared to the non-benzo porphyrins. The

replacement of the CH bridging groups with the more electronegative N atoms lowered the energy of the orbitals with significant coefficients at the meso positions, resulting in the breakdown of Gouterman's four-orbital model for the electronic transitions of porphyrins and their derivatives. Experimentally, the Q band positions are observed at similar wavelengths, between 527-661 nm. This was accounted for by TD-DFT in that despite the changes in the relative orbital energies, the HOMO-LUMO gaps remain similar in all eight molecules theoretically examined.

Unfortunately, the absolute values obtained during the excited state calculations were unreliable, with no systematic error between TD-DFT and experimental transition energies or oscillator strengths. Of particular concern was the considerable underestimation of the Q_y-Q_x splitting. Development of newer functionals adapted for use in time-dependent calculations is ongoing and coupled with the continued increase in computer powers available, may allow TD-DFT to routinely calculate excited state properties with the accuracy and reliability found for many calculations of the ground state properties.

V.6 References

(1) Baerends, E. J.; Ricciardi, G.; Rosa, A.; van Gisbergen, S. J. A. *Coordination Chemistry Reviews* **2002**, *230*, 5.
(2) Nguyen, K. A.; Pachter, R. *Journal of Chemical Physics* **2001**, *114* 10757.
(3) Song, Z. L.; Zhang, F. S.; Chen, X. Q.; Zhao, F. Q. *Acta Physico-Chimica Sinica* **2003**, *19*, 130.
(4) Lu, T.-T.; Xiang, M.; Wang, H.-L.; He, T.-J.; Chen, D.-M. *Journal of Molecular Structure: THEOCHEM* **2008**, *860*, 141.
(5) Quartarolo, A. D.; Lanzo, I.; Sicilia, E.; Russo, N. *Physical Chemistry Chemical Physics* **2009**, *11*, 4586.
(6) Gee, C.; Cuisset, A.; Divay, L.; Crepin, C. *The Journal of Chemical Physics* **2002**, *116*, 4993.
(7) Edwards, L.; Gouterman, M. *Journal of Molecular Spectroscopy* **1970**, *33*, 292.
(8) Plows, F. L.; Jones, A. C. *Journal of Molecular Spectroscopy* **1999**, *194*, 163.
(9) Menapace, J. A.; Bernstein, E. R. *Journal of Chemical Physics* **1987**, *87*, 6877.
(10) Fitch, P. S. H.; Haynam, C. A.; Levy, D. H. *Journal of Chemical Physics* **1981**, *74*, 6612.
(11) Lehnig, R.; Slipchenko, M.; Kuma, S.; Momose, T.; Sartakov, B.; Vilesov, A. *Journal of Chemical Physics* **2004**, *121*, 9396.
(12) Huang, T. H.; Rieckhoff, K. E.; Voigt, E. M. *Journal of Chemical Physics* **1982**, *77*, 3424.
(13) Even, U.; Magen, J.; Jortner, J.; Friedman, J. *The Journal of Chemical Physics* **1982**, *77*, 4384.
(14) Bondybey, V. E.; English, J. H. *Journal of the American Chemical Society* **1979**, *101*, 3446.
(15) Bauernschmitt, R.; Ahlrichs, R. *Chemical Physics Letters* **1996**, *256*, 454.
(16) Casida, M. E.; Jamorski, C.; Casida, K. C.; Salahub, D. R. *The Journal of Chemical Physics* **1998**, *108*, 4439.
(17) Stratmann, R. E.; Scuseria, G. E.; Frisch, M. J. *The Journal of Chemical Physics* **1998**, *109*, 8218.
(18) Gaussian 03, Revision E.01, M. J. Frisch, G. W. Trucks, H. B. Schlegel, G. E. Scuseria, M. A. Robb, J. R. Cheeseman, J. A. Montgomery, Jr., T. Vreven, K. N. Kudin, J. C. Burant, J. M. Millam, S. S. Iyengar, J. Tomasi, V. Barone, B. Mennucci, M. Cossi, G. Scalmani, N. Rega, G. A. Petersson, H. Nakatsuji, M. Hada, M. Ehara, K. Toyota, R. Fukuda, J. Hasegawa, M. Ishida, T. Nakajima, Y. Honda, O. Kitao, H. Nakai, M. Klene, X. Li, J. E. Knox, H. P. Hratchian, J. B. Cross, V. Bakken, C. Adamo, J. Jaramillo, R. Gomperts, R. E. Stratmann, O. Yazyev, A. J. Austin, R. Cammi, C. Pomelli, J. W. Ochterski, P. Y. Ayala, K. Morokuma, G. A. Voth, P. Salvador, J. J. Dannenberg, V. G. Zakrzewski, S. Dapprich, A. D. Daniels, M. C. Strain, O. Farkas, D. K. Malick, A. D. Rabuck, K. Raghavachari, J. B. Foresman, J. V. Ortiz, Q. Cui, A. G. Baboul, S. Clifford, J. Cioslowski, B. B. Stefanov, G. Liu, A. Liashenko, P. Piskorz, I. Komaromi, R. L. Martin, D. J. Fox, T. Keith, M. A. Al-Laham, C. Y. Peng, A. Nanayakkara, M. Challacombe, P. M. W. Gill, B. Johnson, W. Chen, M. W. Wong, C. Gonzalez, and J. A. Pople, Gaussian, Inc., Wallingford CT, 2004.
(19) Becke, A. D. *Physical Review A* **1988**, *38*, 3098.
(20) Becke, A. D. *The Journal of Chemical Physics* **1993**, *98*, 5648.
(21) Lee, C. T.; Yang, W. T.; Parr, R. G. *Physical Review B* **1988**, *37*, 785.
(22) Stephens, P. J.; Devlin, F. J.; Ashvar, C. S.; Chabalowski, C. F.; Frisch, M. J. *Faraday Discussions* **1994**, 103.

(23) Stephens, P. J.; Devlin, F. J.; Chabalowski, C. F.; Frisch, M. J. *Journal of Physical Chemistry* **1994**, *98*, 11623.
(24) Caricato, M.; Trucks, G. W.; Frisch, M. J.; Wiberg, K. B. *Journal of Chemical Theory and Computation* **2010**, *6*, 370.
(25) Crépin, C. and co-workers, Unpublished results; L'Institut des Sciences Moléculaires d'Orsay (ISMO) CNRS – Université Paris-Sud, Orsay, France, 2010.
(26) Dvornikov, S. S.; Knyukshto, V. N.; Kuzmitsky, V. A.; Shulga, A. M.; Solovyov, K. N. *Journal of Luminescence* **1981**, *23*, 373.
(27) Vincett, P. S.; Voigt, E. M.; Rieckhoff, K. E. *The Journal of Chemical Physics* **1971**, *55*, 4131.
(28) Nguyen, K. A.; Kennel, J.; Pachter, R. *The Journal of Chemical Physics* **2002**, *117*, 7128.
(29) Crépin, C.; Shafizadeh, N.; Chin, W.; Galaup, J. P.; McCaffrey, J. G.; Arabei, S. M. *Low Temperature Physics* **2010**, *36*, 451.
(30) Edwards, L.; Dolphin, D. H.; Gouterman, M.; Adler, A. D. *Journal of Molecular Spectroscopy* **1971**, *38*, 16.
(31) Starukhin, A.; Shulga, A.; Waluk, J. *Chemical Physics Letters* **1997**, *272*, 405.
(32) Radziszewski, J. G.; Waluk, J.; Nepras, M.; Michl, J. *Journal of Physical Chemistry* **1991**, *95*, 1963.
(33) Toyota, K.; Hasegawa, J.-Y.; Nakatsuji, H. *The Journal of Physical Chemistry A* **1997**, *101*, 446.
(34) Quimby, R. S. *Photonics and Lasers: An Introduction*; John Wiley & Sons: Hoboken, NJ, 2006.
(35) Shibuya, T. *Journal of Chemical Physics* **1983**, *78*, 5175.
(36) Tackley, D. R.; Dent, G.; Smith, W. E. *Physical Chemistry Chemical Physics* **2000**, *2*, 3949.
(37) Arabei, S. M.; Solovev, K. N.; Shkirman, S. F. *Optika I Spektroskopiya* **1992**, *72*, 359.
(38) Arabei, S. M.; Kuzmitsky, V. A.; Solovyov, K. N. *Optics & Spectroscopy* **2007**, *102*, 692.

Appendix V.A: KS-MO contributions to TD-DFT transitions of porphyrins

V.A.1 Introduction

In the following appendix, a detailed description will be given of lowest energy transitions predicted using TD-DFT of eight structurally related porphyrins. All calculations discussed were calculated at the B3LYP/6-311++G(2d,2p) level of theory. The TD-DFT results for these molecules (zinc and free-base tetraazaporphyrin, phthalocyanine, tetrabenzoporphyrin and porphine) have been tabulated in Table V.6 and V.7 of Chapter V and will be referenced throughout. In this chapter, particular attention will be paid to the Kohn-Sham (KS) orbitals of the single electron transitions predicted to have the largest contributions to the overall electronic state transitions and the effect of the different molecular structures have on the equivalent KS orbital energies of each molecule. These KS orbitals are mathematical constructs used in the determination of the electron density, describing the energy properties of the molecule, and are therefore important in the calculation of transition energies using TD-DFT.

The results for the zinc molecules will be given in Part V.A.2, starting with the methine bridged porphyrins, porphine (P) and tetrabenzoporphyrin (TBP), followed by the aza bridged analogues, phthalocyanine (Pc) and tetraazaporphyrin (TAP). The similarities and differences between the orbital contributions for the different systems will be discussed. A short description of the correlation between the D_{4h} symmetry metallo- and D_{2h} symmetry free-base porphyrins will be given in Part V.A.3 using ZnPc and H_2Pc as examples. In Part V.A.4, the results for the free-base molecules will be described and compared in the same order as for the Zn molecules (that is to say H_2P, H_2TBP, H_2Pc and H_2P).

V.A.2 TD-DFT – zinc porphyrins

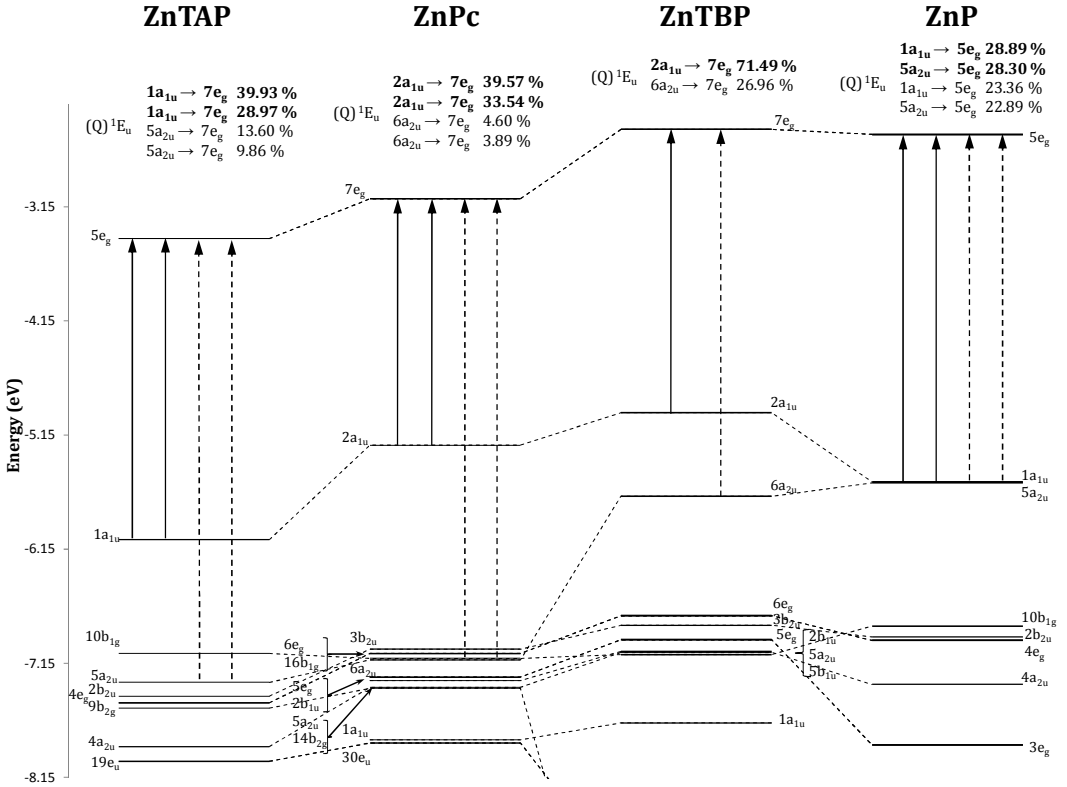

Figure V.A.1: Energy level correlation diagram of the valence Kohn-Sham orbitals of ZnTAP, ZnPc, ZnTBP and ZnP. The major orbital contributions for the Q band transitions are indication by the solid arrow and the significant minor contributions by the dashed arrows.

The TD-DFT results for the two lowest energy singlet and triplet vertical transitions of zinc aza bridged porphyrins are tabulated on right-hand side of Table V.6 while those of the methine bridged porphyrins are given on right-hand side of Table V.7. Considering ZnP first, the Q band ^1E_u transition is predicted to originate primarily from an almost equal "plus" combination of the one electron excitations from the quasi-degenerate $1a_{1u}$ and $5a_{2u}$ HOMO and HOMO-1 to the degenerate $5e_g$ LUMO orbitals with an excitation energy of 2.4083 eV (19424.24 cm^{-1}, 514.81 nm). As the $1a_{1u}$, $5a_{2u}$ and the degenerate $5e_g$ orbitals have a node through the plane of the molecule, they may be described as π orbitals. As shown in Figure V.A.1, there is a large energy gap between the LUMO and HOMO orbitals with a significant gap between the HOMO orbitals and lower energy occupied orbital. This explanation of the origin of the Q transitions is consistent with the four-orbital model proposed by Gouterman in the 1960s[1].

The coefficients for the $5a_{2u}$ orbital are mostly localised to the meso C and pyrrole N atoms with contributions also from the C_β atoms on the pyrrole ring (Figure V.A.5). The $1a_{1u}$ orbital coefficients are localised between the C_α and C_β atoms of the pyrrole rings with nodal plains going through the meso methine groups and pyrrole N atoms. The degenerate pair of LUMO orbitals have coefficients localised between the C_α and C_β atoms along one axis and between the C_α and C_m atoms, pyrrole N atoms and between the C_β atoms on the other axis. Though individually both $1a_{1u} \rightarrow 5e_g$ and $5a_{2u} \rightarrow 5e_g$ are allowed with large transition dipole matrix elements[2], in the plus combination, they have opposite directions and in effect cancel each other out, leading to a low intensity (f=0.0027). The higher energy B band has a minus combination of the same orbital transitions with parallel transition dipoles and hence have a large intensity (predicted using TD-B3LYP/6-311++G(2d,2p) at 3.4816 eV with f=0.9392).

The corresponding triplet ^3E_u transitions involve the same orbitals but with a larger contributions from the $5a_{2u} \rightarrow 5e_g$ orbitals than the $1a_{1u} \rightarrow 5e_g$. The coefficients for the $5a_{2u} \rightarrow 5e_g$ transitions shown in Table V.7 make up 41.2 and 5.7 % of the transition with the $1a_{1u} \rightarrow 5e_g$ transition making up only 18.1 and 2.5 %. This 2.3:1 ratio between the orbital contributions means that the ^3E_u electronic transition may be thought of as a simple $5a_{2u} \rightarrow 5e_g$ transitions with small $1a_{1u} \rightarrow 5e_g$ contributions. It should be noted that whereas the coefficients for the contributions to the singlet transitions are normalised to 0.5, the coefficients for the triplet contributions are normalised to 1. The predicted excitation energy is 1.7735 eV (14,304.24 cm^{-1}, 699.1 nm), red-shifted by 0.6348 eV (5120 cm^{-1}) compared to the singlet transition.

Looking now at ZnTBP, the lowest degenerate ^1E_u symmetry transition predicted at 2.1426 eV (17281.23 cm^{-1}, 578.65 nm) involves the equivalent KS orbitals seen in ZnP but the addition of the benzo annulations has a noticeable effect on the energies of some of these orbitals (Figure V.A.1) and their contribution to the transition. The $6a_{2u}$ orbital is very similar to the $5a_{2u}$ orbital of ZnP, that is, the orbitals are localized to the C_m, pyrrole N and C_β atoms with only a very small coefficient on the C_δ atoms of the benzene rings. This results in a small reduction in the energy of this orbital. The coefficients for the $2a_{1u}$ orbital are affected by the addition of the benzene rings. Like the equivalent $1a_{1u}$ orbital of

ZnP, there are large coefficients between the C_α and C_β of the pyrrole rings but there are now also large coefficients between the C_γ and C_δ atoms on the benzo annulations. As a consequence of the addition of π orbital contributions from the benzene rings, the energy of the $2a_{1u}$ orbital in ZnTBP is raised considerably compared to the $1a_{1u}$ orbital of ZnP. The LUMO $7e_g$ orbital like the $2a_{1u}$ orbital has significant contributions from the π orbitals of the benzo groups. As well as the C_α and C_β coefficients along one axis seen in the ZnP $5e_g$ orbitals, there are large orbital coefficients between the C_γ and C_δ along the same axis. Along the other axis, the orbitals are more similar with coefficients between the C_α and C_m atoms and on the pyrrole N atom and only small contributions on the C_β and C_δ atoms. Despite these extra benzo coefficients only a small rise in the energy of the $7e_g$ orbital was calculated.

The effect of the benzo annulations on the energy of the orbitals, in particular, on the raising of the energy of the $2a_{1u}$ orbital, removes the quasi-degeneracy of the two HOMOs. Though Gouterman's four-orbital model is strained, there is still a large enough energy gap between the $6a_{2u}$ orbital and the other orbitals of the molecule to make it still applicable but the spectroscopic properties predicted are now significantly different from those of ZnP. The smaller energy gap between the $2a_{1u}$ and $7e_g$ orbitals leads to a lower excitation energy of 2.1426 eV (17281.23 cm^{-1}, 578.65 nm) and to a larger contribution from the $2a_{1u} \rightarrow 7e_g$ transition (71.49 %) compared to the $6a_{2u} \rightarrow 7e_g$ transition (26.96 %). This increase in the contribution from one orbital transition has an effect on the absorption strength, allowing one dipole moment contribution to dominate and raising the oscillator strength to 0.1803. The corresponding triplet transition was calculated to have an excitation energy of 1.4992 eV (12091.86 cm^{-1}, 826.98 nm) involving similar orbital transition contributions to the singlet and red-shifted by 0.6434 eV (5189.37 cm^{-1}).

The exchange of the meso C_m-H_m group for the more electronegative N_m in ZnPc has a dramatic effect on the KS orbitals and consequentially on the spectroscopic properties predicted using TD-DFT. The HOMO $2a_{1u}$ orbitals in ZnPc and ZnTBP are almost identical due to negligible coefficients on the bridging meso groups and only a relatively small reduction in energy was seen between this orbital in ZnPc and ZnTBP. There was, however, a major effect on the energy of the

$6a_{2u}$ orbital. Comparably large orbital coefficients are now seen between the C_α atoms and C_γ atoms of the benzene rings with a reduction of the coefficients on the pyrrole N but the most important orbital component in terms of the energy difference between ZnTBP and ZnPc is the continuing presence of a large coefficient at the meso position. The electronegativity of the N atom has the effect of lowering the energy of this orbital greatly, shifting it into a more complicated energy region with other π and σ orbitals (Figure V.A.1). The $7e_g$ LUMOs of ZnPc and ZnTBP have almost indistinguishable orbital coefficients but, like the $6a_{2u}$ orbital, there is large reduction in the energy of these orbitals due to the electronegative N_m atoms but a significant HOMO-LUMO gap still exists.

The lowering of the $6a_{2u}$ orbital from HOMO-1 to HOMO-4 below the $3b_{2u}$, $6e_g$ and $16b_{1g}$ orbitals cause a breakdown of the simple four-orbital model used to describe the Q transitions of porphyrins. The mixing of the single electron contributions from the $2a_{1u} \rightarrow 7e_g$ and $6a_{2u} \rightarrow 7e_g$ orbital transitions is further reduced compared to ZnTBP and ZnP, with the $2a_{1u} \rightarrow 7e_g$ transition with a total contribution of 73.11 % versus only 8.49 % for the $6a_{2u} \rightarrow 7e_g$ transition. The lower energy transition of 2.0536 eV (16,563.40 cm^{-1}, 603.74 nm) and increased oscillator strength of f=0.432 is a consequence of lowering the energy gap between the HOMO and LUMO (which is now the primary contributor to the transition by a factor of 8.61). The triplet transition is now predicted to consist of only $2a_{1u} \rightarrow 7e_g$ components above 1 % (i.e. coefficients above 0.1) with an excitation energy of 1.1141 eV (8985.82 cm^{-1}, 1112.91 nm), red-shifted by 0.9395 eV (7,577.58 cm^{-1}) compared to the singlet.

Removing the benzo annulations of ZnPc to produce ZnTAP has the overall effect of lowering the energy of KS orbitals. The coefficients for these orbitals resemble the general description of those found for ZnP but with different energies. The coefficients on the meso N_m atom significantly lower the energy of the $5a_{2u}$ orbital of ZnTAP compared to the same orbital in ZnP. The removal of the benzo groups also reduces its energy relative ZnPc. The removal of the benzene rings also has the large effect on the HOMO $1a_{1u}$ of lowering its energy significantly relative the $2a_{1u}$ orbital of ZnPc. Also due to the negligible orbital coefficients on the meso atoms, this orbital is somewhat lower in energy than the corresponding KS orbital in ZnP. The energy of the LUMO $5e_g$ is also reduced relative to ZnPc and

is now much lower than the LUMOs in ZnP but with a comparable HOMO-LUMO gap due to the lower HOMO in ZnTAP

The overall effect of these orbital energy changes is that the excitation energy for the Q transition is calculated to be 2.4386 (19,668.63 cm^{-1}, 508.43 nm) only 0.0303 eV (244.43 cm^{-1}) higher than the corresponding transition in ZnP but with a much larger oscillator strength of 0.1683. Like ZnPc and ZnTBP, the higher oscillator strength is due to the reduction in the mixing of the $1a_{1u} \rightarrow 7e_g$ and $5a_{2u} \rightarrow 7e_g$ transitions. The lowering of the $5a_{2u}$ orbital from HOMO-1 to HOMO-2 causes a breakdown of the four-orbital model and mixing of the orbital transitions. The $1a_{1u} \rightarrow 7e_g$ transitions make up the greater percentage of the components to the excitation transition with 39.93 % and 28.97 % (total of 68.90 %) against those from the $5a_{2u} \rightarrow 7e_g$ transition with 13.60 % and 9.86 % (total of 23.46 %). Though the energy of the triplet transition of ZnTAP of 1.466 eV (11,824.08 cm^{-1}, 845.73 nm) are comparable to those of the ZnP, the orbital transition contribution are similar to those of ZnPc, with 66.24 % coming from the $1a_{1u} \rightarrow 7e_g$ transitions.

V.A.3 The correlation between D_{4h} and D_{2h} symmetry orbitals - ZnPc versus H_2Pc

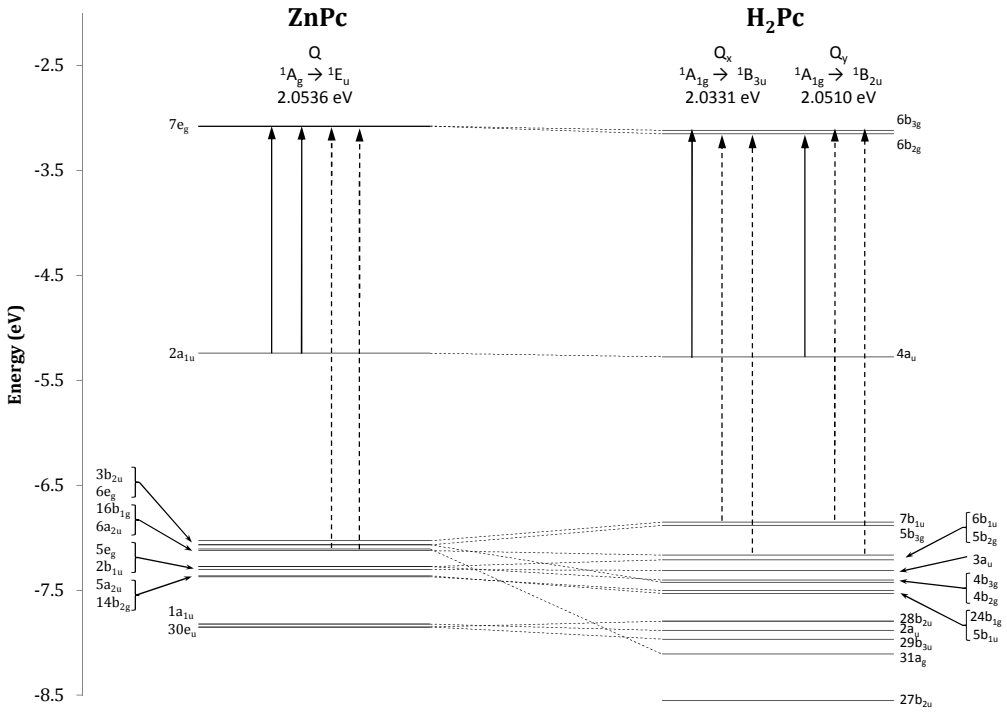

Figure V.A.2: Correlation between the KS orbitals of the D_{4h} symmetry ZnPc and D_{2h} symmetry H_2Pc.

When comparing the results from the D_{4h} point symmetry Zn porphyrins with their D_{2h} point symmetry free-base analogues, important correlations may be made using group theory. The D_{4h} A_{2u} and B_{2u} representations correlate with the B_{1u} representation of D_{2h}. Likewise, A_{1g} and B_{1g} correlate with A_g, A_{2g} and B_{2g} correlate with the D_{2h} B_{1g} representation and A_{1u} correlates with A_u. Of significance to the current study, the doubly degenerate E_u and E_g representations of D_{4h} group symmetry, split into B_{2u}/B_{3u} and B_{2g}/B_{3g} representations, respectively, of the lower symmetry D_{2h} group symmetry. The consequences of the change in symmetry may be seen in Figure V.A.2. For example, the degenerate $30e_u$ orbital of ZnPc (lowest lying orbital of ZnPc shown in Figure V.A.2) correlates with the slightly higher energy $28b_{2u}$ and lower energy $29b_{3u}$ orbitals of H_2Pc. Changes in energy are also apparent in other orbitals, in part due to the slightly different geometries of the Zn and H_2 analogues and the spatial arrangement of the orbital components around those geometries raising or lower the energy. The 3d orbitals from the central zinc atom were found to be very low lying and did not contribute to valence orbitals involved in the visible transitions. The most important difference between ZnPc and H_2Pc, in terms of the visible spectroscopic properties of these molecules, is the

loss of the degeneracy of the $7e_g$ lowest unoccupied molecular orbitals. These orbitals correlate in H_2Pc with the non-degenerate $6b_{2g}$ and $6b_{3g}$ orbitals. The splitting of these orbitals leads to a splitting of the Q transitions of ^1E_u symmetry in ZnPc into Q_y and Q_x transitions of $^1B_{2u}$ and $^1B_{3u}$ symmetry.

V.A.4 TD-DFT – free-base porphyrins

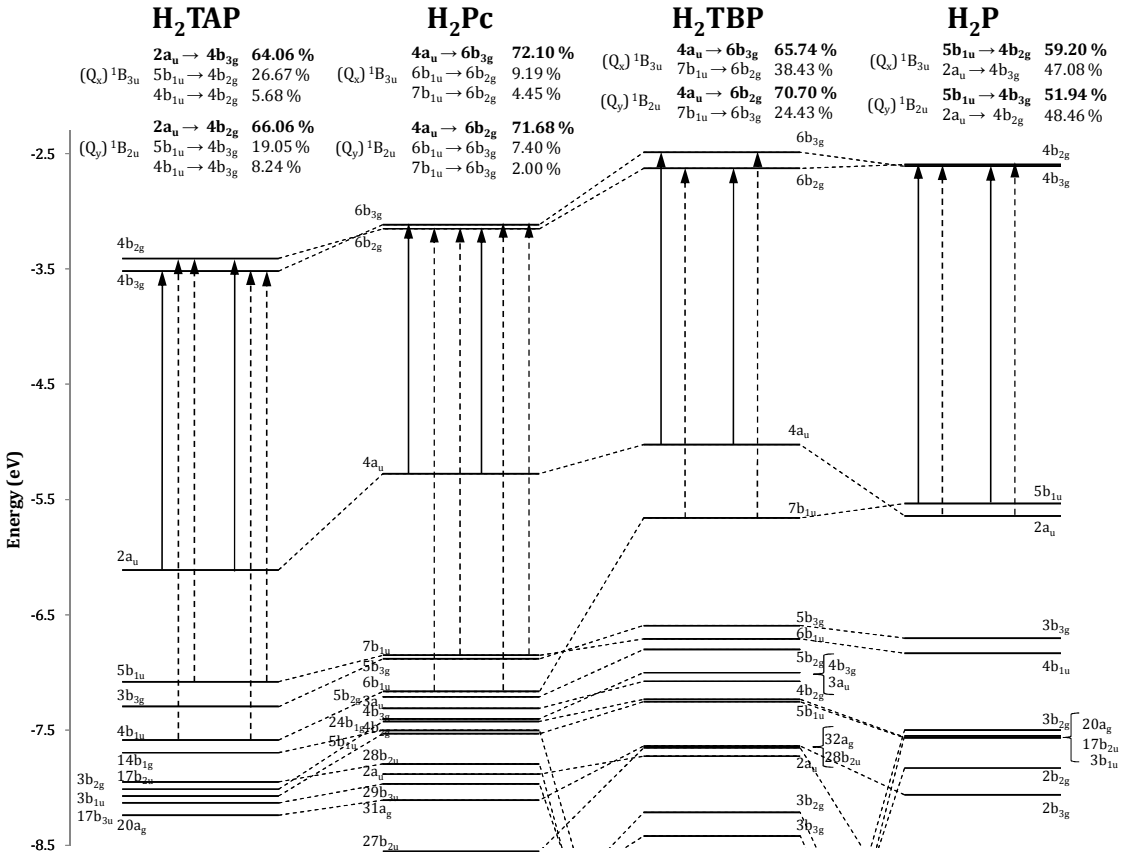

Figure V.A.3: Energy level correlation diagram of the valence Kohn-Sham orbitals of H_2TAP, H_2Pc, H_2TBP and H_2P. The major orbital contributions for the Q_x and Q_y transitions are indication by the solid arrow and the significant minor contributions by the dashed arrows.

The TD-DFT results for the two lowest energy singlet and triplet vertical transitions of free-base aza bridged porphyrins are tabulated on left-hand side of Table V.6 while those of the methine bridged porphyrins are given on left-hand side of Table V.7. An energy correlation diagram of the KS orbitals involved in the transitions is presented in Figure V.A.3 and pictorial representations of the orbital coefficients of the main MOs contributing to the transitions are given in Figure V.A.5. Like the zinc porphyrins, a description of the orbital contributions to the Q transitions of free-base porphyrin (H_2P) will be given first, followed by free-base

tetrabenzoporphyrin (H_2TBP), phthalocyanine (H_2Pc) and tetraazaporphyrin (H_2TAP).

The Q band transitions of H_2P predicted by TD-DFT, like those of ZnP, are consistent with the Gouterman four-orbital model. The lower energy Q_x transition is calculated at 2.2704 eV (18,312 cm^{-1}, 546.1 nm) with $^1B_{3u}$ symmetry while the higher energy Q_y transition is calculated at 2.4162 eV (19,488 cm^{-1}, 513.14 nm) with $^1B_{2u}$ symmetry with a splitting of 0.1458 eV (1,176 cm^{-1}) between them. The largest contribution of the $^1B_{3u}$ excitation is the $5b_{1u} \rightarrow 4b_{2g}$ transition with a slightly smaller contribution from the $2a_u \rightarrow 4b_{3g}$ transition. In the $^1B_{2u}$ transition, the upper orbitals are reversed and the main contribution is from the $5b_{1u} \rightarrow 4b_{3g}$ orbital transition and the minor contribution from the $2a_u \rightarrow 4b_{2g}$ transition. Comparing the orbital coefficients of the occupied orbitals of H_2P and ZnP, the $2a_u$ orbital of H_2P correlates with the $1a_{1u}$ orbital of ZnP and the $5b_{1u}$ orbital of H_2P correlates with the $5a_{2u}$ orbital of ZnP but due to the difference in charge now between the H bonded N atom and N' atom on the alternative pyrrole rings, the $5b_{1u}$ orbital is higher in energy than the $2a_u$ orbital.

The $5e_g$ lowest unoccupied orbitals in ZnP lose their degeneracy and split into a lower energy $4b_{3g}$ LUMO and higher energy $4b_{2g}$ LUMO+1. The coefficients of the $4b_{3g}$ orbital are localized between the C_α and C_β atoms of the pyrrole rings along the x-axis (i.e. the pyrrole rings bonded to the central hydrogens) with orbital coefficients on the N' atoms and between the C_α' and meso C_m atoms and to a lesser extent between the C_β' atoms on the other pyrroles. The $4b_{2g}$ orbital has the orbital coefficient pattern for $4b_{3g}$ rotated by 90°, with coefficients localized between the C_α' and C_β' atoms of the pyrrole rings along the y-axis and on the N_H atoms and between the C_α and meso C_m atoms and the C_β atoms along the x-axis. The nearly 50:50 mixing of the contributions has the effect, again like ZnP, of cancelling the dipole moments leading to a small oscillator strength for both $^1B_{3u}$ and $^1B_{2u}$ transitions, 0.0001 and 0.0002 respectively. The $^3B_{2u}$ triplet transition is predicted at 1.5066 eV (12,152 cm^{-1}, 822.97 nm) with 58.11 % from $5b_{1u} \rightarrow 4b_{3g}$ and 17.66 % from $2a_u \rightarrow 4b_{2g}$ while the higher energy $^3B_{3u}$ transition at 1.8321 eV (14,777 cm^{-1}, 676.74 nm) consists of 55.63 % from $5b_{1u} \rightarrow 4b_{2g}$ and 6.64 % from $2a_u \rightarrow 4b_{3g}$.

For H_2TBP, the excitation energy calculated for the Q_x transition of $^1B_{3u}$ symmetry is 2.0865 eV (16,829 cm^{-1}, 594.21 nm) and for the Q_y transition of $^1B_{2u}$ symmetry, 2.1211 eV (17,108 cm^{-1}, 584.53 nm). The difference between these two excitation values of 0.0346 eV (279.07 cm^{-1}) is more than four times smaller than the splitting between the Q_x and Q_y transitions calculated for ZnP. The equivalent orbitals that were involved in the Q_x and Q_y transitions of H_2P contribute to the H_2TBP transitions with the $^1B_{3u}$ transition consisting of 68.74 % $4a_u \rightarrow 6b_{3g}$ and 38.43 % $7b_{1u} \rightarrow 6b_{2g}$ contributions and the $^1B_{2u}$ transition of 70.70 % $4a_u \rightarrow 6b_{2g}$ and 24.43 % $7b_{1u} \rightarrow 6b_{3g}$ contributions. Analogous to ZnTBP, the benzene annulations have an effect on the energies of these orbitals, moving the $7b_{1u}$ orbital to slightly lower energy and the $4a_u$ orbital to higher energy. The increase in the energy gap between the HOMO levels reduces the mixing of the contributions, leading to one dominant single orbital transition and larger oscillator strengths ($^1B_{3u}$: f=0.0963 and $^1B_{2u}$: f=0.2177).

The addition of the benzo groups has the effect of increasing the energy splitting and reversing the energy order between the LUMOs with the $6b_{3g}$ orbital now higher in energy than the $6b_{2g}$ orbital. Looking the orbital diagrams in Figure V.A.5 a clear difference in orbital distributions is apparent. Orbital coefficients are found for the $6b_{2g}$ orbital on the central ring and benzene rings along the y-axis with smaller contributions on the alternative y-axis benzenes but for $6b_{3g}$, they are found almost exclusively on the central ring and isoindole ring along the x-axis. The main contribution to the lower energy $^1B_{3u}$ transition, counter-intuitively, comes from a transition from the HOMO to the higher energy $6b_{3g}$ orbital and for the higher energy $^1B_{3u}$ transition, from the same HOMO to the lower energy $6b_{2g}$ orbital. The $^3B_{2u}$ triplet transition is predicted at 1.3176 eV (10,627 cm^{-1}, 941 nm) with 62.57 % from $4a_u \rightarrow 6b_{2g}$ and 7.66 % from $7b_{1u} \rightarrow 6b_{3g}$ while the higher energy $^3B_{3u}$ transition at 1.6169 eV (13,041 cm^{-1}, 766.79 nm) consists of 58.39 % from $4a_u \rightarrow 6b_{3g}$ and only 1.57 % from $7b_{1u} \rightarrow 6b_{2g}$ a reversal in the percentage of equivalent contributions seen in ZnP.

The $^1B_{3u}$ Q_x transition of H_2Pc was calculated at 2.0331 eV (16,398 cm^{-1}, 609.83 nm) and the $^1B_{2u}$ Q_y transition at 2.0510 eV (16,542 cm^{-1}, 604.5 nm) with a small splitting of 0.0179 eV (144.37 cm^{-1}) between the two excitations. As seen in the relationship between ZnTBP and ZnPc, replacing the methine bridging group in

H_2TBP with a more electronegative N_m atom in H_2Pc reduces the energies of most of the orbitals, in particular the HOMO-1 $7b_{1u}$ in H_2TBP to the HOMO-3 $6b_{1u}$ orbital. The $6b_{3g}$ and $6b_{2g}$ LUMOs were also lowered in energy, though the difference between the orbitals is reduced, the energy order remains the same relative to H_2TBP. The contributions to the transitions reflect the changes in orbital energy. The $^1B_{3u}$ transition is composed primarily of 72.10 % $4a_u \rightarrow 6b_{3g}$ with lesser coefficients from $6b_{1u} \rightarrow 6b_{2g}$ (9.19 %) consistent with ZnPc but now also with 4.45 % from $7b_{1u} \rightarrow 6b_{2g}$. Likewise the $^1B_{2u}$ transition is predominantly formed of 71.68 % $4a_u \rightarrow 6b_{2g}$ with 7.40 % from $6b_{1u} \rightarrow 6b_{3g}$ and 2.00 % from $7b_{1u} \rightarrow 6b_{3g}$. The addition of lower energy orbital transitions from the $7b_{1u}$ π orbital which was not seen in any of the zinc molecules or free-base methine bridged porphyrins is indicative of the breakdown of the 4 orbital model and results in the large oscillator strengths of 0.4079 for $^1B_{3u}$ and 0.4497 for $^1B_{2u}$ transitions. The triplet transitions are predicted to be predominantly single orbital transitions with the $^3B_{2u}$ transition at 1.0095 eV (8142 cm^{-1}, 1228.12 nm) consisting of 74.58 % $4a_u$-$6b_{2g}$ and the $^3B_{3u}$ transition at 1.1605 eV (9360 cm^{-1}, 1068.34 nm) consisting of 66.97 % $4a_u$-$6b_{3g}$.

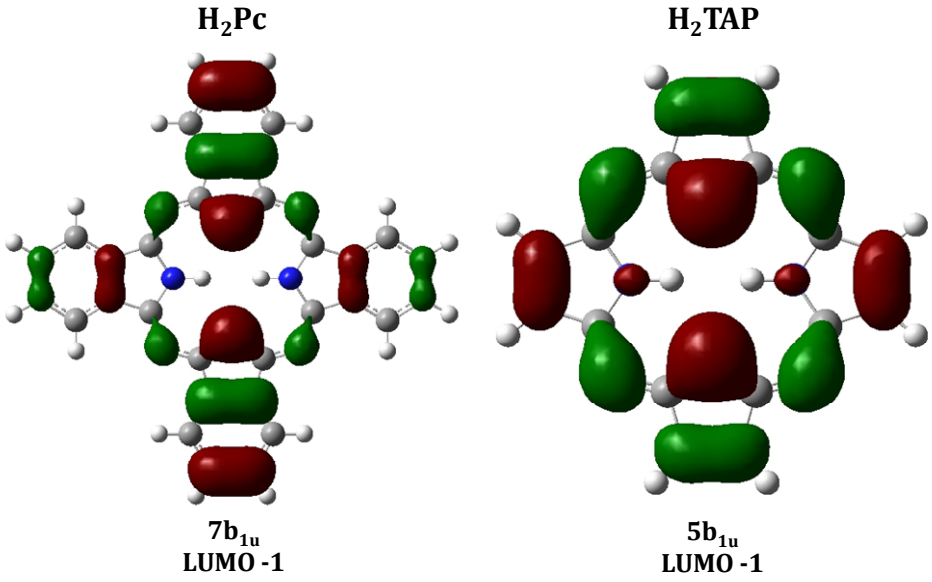

Figure V.A.4: The $7b_{1u}$ and $5b_{1u}$ π orbitals of involved in the Q_x and Q_y transitions of H_2Pc and H_2TAP. Contributions above 1 % of transitions involving the equivalents of these orbitals were not apparent for H_2P and H_2TBP or any of the zinc porphyrins.

The H_2TAP results like the three previous free-base molecules reflect the same changes in orbital energies seen in the zinc molecules and the effect these changes have on the spectroscopic properties calculated. There is a significant lowering in energy of the HOMO $2a_u$ orbital with a smaller reduction in the energy of the $5b_{1u}$ and $4b_{1u}$ orbitals. In the case of the LUMOs, the $4b_{2g}$ and $4b_{3g}$ orbitals have been further reduced relative to H_2Pc but the energy ordering of these orbitals has reversed to match the order seen in H_2P. The $^1B_{3u}$ Q_x transition is predicted to have an excitation energy of 2.363 eV (19,059 cm^{-1}, 524.68 nm) with a 64.06 % contribution from the $2a_u \rightarrow 4b_{3g}$ transition, 26.67 % from $5b_{1u} \rightarrow 4b_{2g}$ and, like H_2Pc, a small 5.68 % contribution from the $6b_{1u} \rightarrow 4b_{2g}$ transition. The higher energy $^1B_{2u}$ Q_y transition, predicted at 2.4951 eV (20,124 cm^{-1}, 496.91 nm), consists of 66.06 % contribution from the $2a_u \rightarrow 4b_{2g}$ transition, 19.05 % from $5b_{1u} \rightarrow 4b_{3g}$ and again a small 8.24 % contribution from the $6b_{1u} \rightarrow 4b_{3g}$ transition. A splitting of 0.1321 eV (1065.46 cm^{-1}) is predicted, comparable to the difference between the Q_x and Q_y transitions in H_2P. The reduction of the mixing from contributions from the lower lying orbitals means that these transitions are predicted to be more allowed than those of H_2P, with oscillator strengths of 0.1472 for $^1B_{3u}$ and 0.1441 for $^1B_{2u}$. Finally the triplet transitions are predicted at 1.4617 eV (1,1789 cm^{-1}, 848.21 nm) for the $^3B_{3u}$ transition and at lower energy the $^3B_{2u}$ transition at 1.4285 eV (1,1522 cm^{-1}, 867.96 nm).

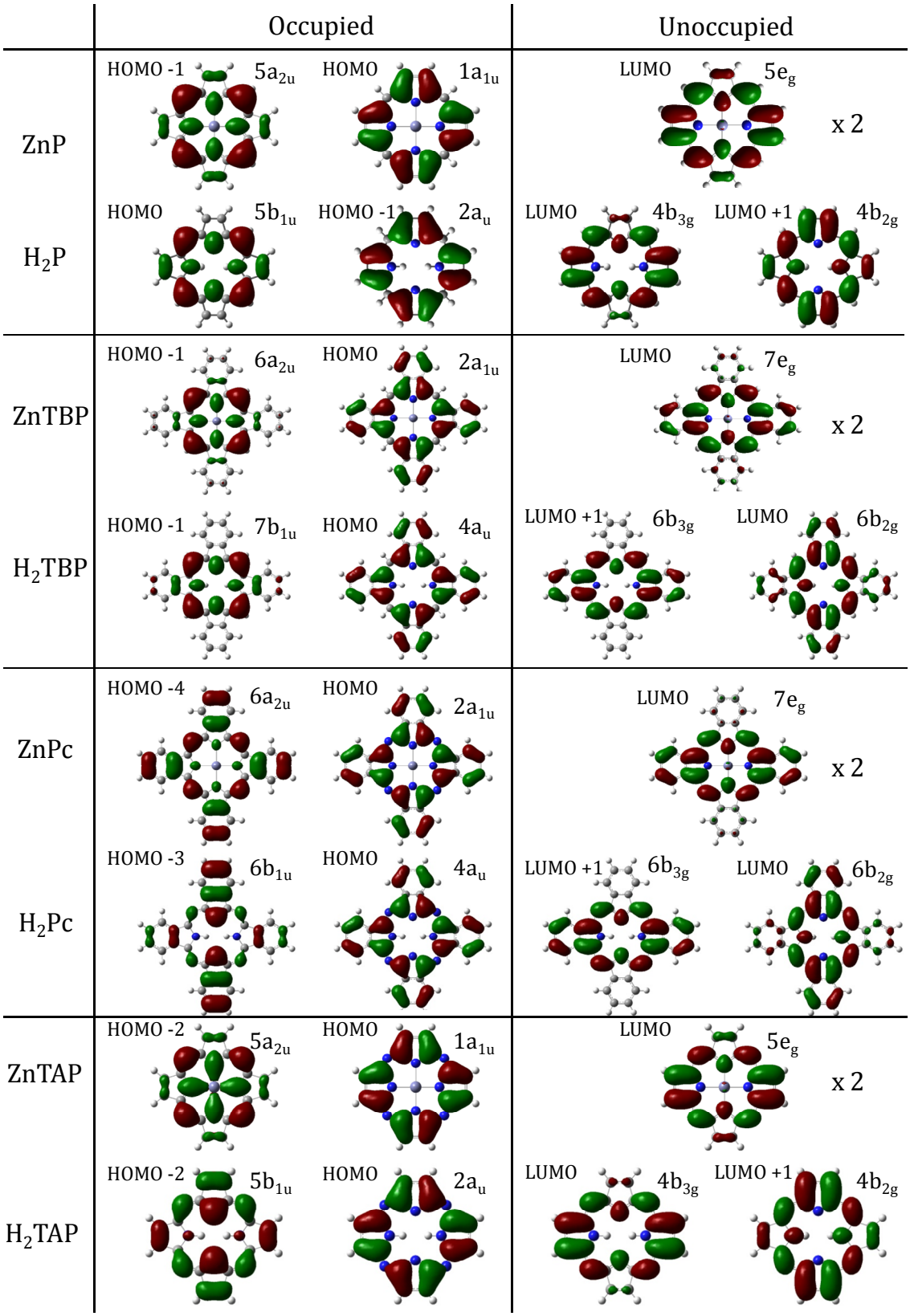

Figure V.A.5: The major Kohn-Sham orbitals involved in Q band and lowest energy triplet transitions. The LUMO e_g orbitals of the Zn porphyrins are degenerate (as indicated by the "x 2").

V.A.5 References

(1) Gouterman, M. *Journal of Molecular Spectroscopy* **1961**, *6*, 138.
(2) Baerends, E. J.; Ricciardi, G.; Rosa, A.; van Gisbergen, S. J. A. *Coordination Chemistry Reviews* **2002**, *230*, 5.

Chapter VI: Amplified emission of phthalocyanines isolated in cryogenic matrices

VI.1 Introduction

Laser-induced fluorescence is very well suited for studies of phthalocyanine due to the close match between their strong absorptions in the visible spectral region and the output of tuneable dye lasers. While undertaking such a spectroscopic study of matrix-isolated free-base phthalocyanine (H_2Pc) and zinc phthalocyanine (ZnPc), by means of emission–excitation spectra using pulsed dye lasers for excitation, a vibronic band was observed to increase in intensity non-linearly with slightly increased laser powers. It is noteworthy that two previous matrix luminescence studies on the phthalocyanines, one by Bondybey and English[1] on H_2Pc and another by Williamson and coworkers[2] on ZnPc in Ar matrices, did not report such a novel solid state effect. In contrast, stimulated emission has been reported by Sorokin and co-workers[3,4] for the closely related molecule chloroaluminium phthalocyanine in solution. Significantly, this was achieved with pulsed ruby laser excitation and within a resonator cavity.

In this chapter, the unusual emission recorded for matrix-isolated H_2Pc and ZnPc will be presented. The possible reasons for the different results of the previous laser matrix studies and the present observations will also be discussed. DFT calculated Raman frequencies and intensities of other aromatic tetrapyrroles, in particular tetraazaporphyrins (TAP), tetrabenzoporphyrins (TBP) and porphines, will be presented and discussed to assess their potential for exhibiting the same unusual emission behaviour.

VI.2 Results

The absorption, emission and excitation spectra of ZnPc and H_2Pc in various low-temperature solids were previously presented and discussed in Chapter V. Figure VI.1 shows typical emission spectra of ZnPc and H_2Pc resulting from excitation to the S_1 (Q) state of ZnPc and to both the S_1 (Q_x) and S_2 (Q_y) states of H_2Pc. These

emission bands were assigned to transitions from v'=0 in the first excited state (Q or Q_x) to various vibrational levels v'' in the ground electronic state, S_0. In the spectra of both molecules, the 0-0 transition dominates the emission with other much weaker vibronic transitions seen at longer wavelengths. As discussed in Chapters IV and V, the vibronic progression of both ZnPc and H_2Pc corresponds to the Raman vibrational modes and was assigned with the assistance of DFT calculated frequencies.

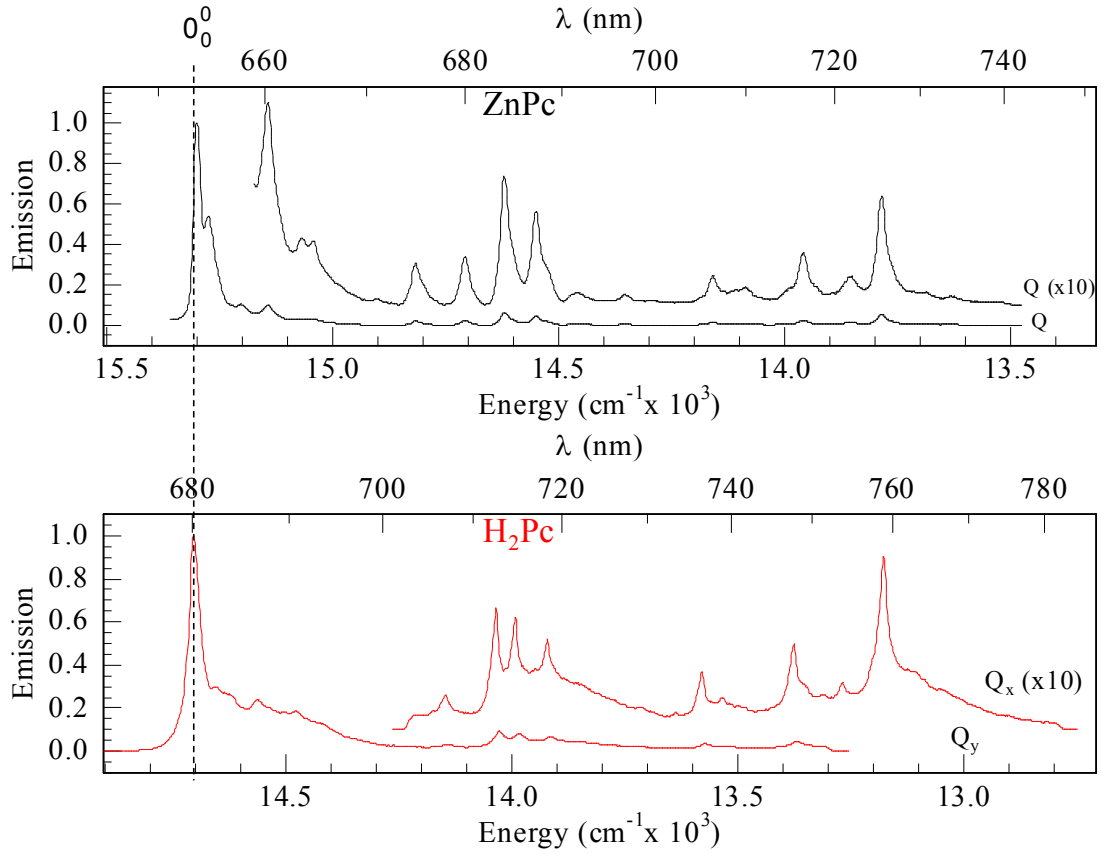

Figure VI.1: Visible emission bands of ZnPc and H_2Pc in Ar. These results were recorded with low intensity laser excitation. The intense 0-0 transition is identified using the dashed line.

VI.2.I Amplified Emission

While optimising the emission signal with the iCCD camera operating in real time, the intensity of the exciting laser was increased with a quite unexpected result. To illustrate the observed effect, a summary of the changes that were recorded for H_2Pc in solid N_2 is presented in Figure VI.2. In this Figure the normal fluorescence, described in the previous section, is shown by the lower, black trace. Shown above this, by the solid trace, is the emission recorded by increasing the laser power from tens of J/pulse to hundreds of J/pulse. It is very evident that the strongest (other than the 0–0 band) emission band at 755.5 nm has gained enormously in intensity

while the others have remained unchanged or diminished slightly. Moreover, it is immediately evident that the linewidth of this emission band reduces considerably when its intensity increases as shown on the upper right panel of Figure VI.2. Under this condition the width of the band approaches that of the exciting laser, decreasing from approximately 8 cm^{-1} to 2 cm^{-1} and thereby reaching the resolving limit of the emission monochromator.

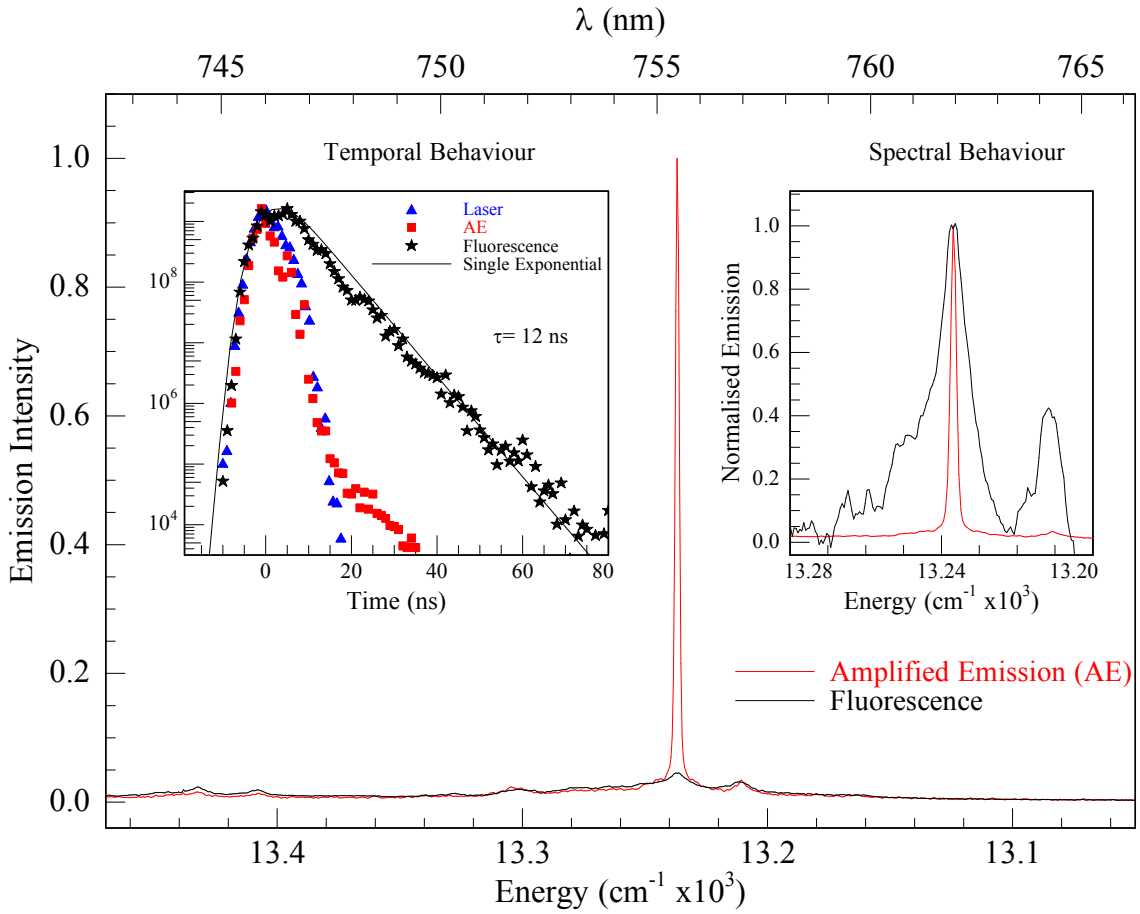

Figure VI.2: Variations in the emission characteristics of the 755.5 nm emission of H_2Pc/N_2 system with laser intensity. The lower trace presents the normal emission (fluorescence) produced with lower laser power (10 J/pulse). The upper trace shows the dramatic increase in the intensity of the 755.5 nm emission with the use of approximately 100 J/pulse. The inset on the right shows details of the lineshape changes on the 755.5 nm band under both low and high pulse energies. Temporal profiles of the 755.5 nm emission decay curves are shown in the inset on the left hand side.

Shown in the inset on the left of Figure VI.2 are the emission decay curves recorded for the 755.5 nm emission band using selected laser excitation intensities. With low laser power, the long-lived decay (stars) is found to have a lifetime of around 12 ns. With higher laser power the intense emission (squares) clearly follows the temporal profile of the laser pulse (triangles). From the spectral and temporal behaviour observed on this band, it is concluded that the 755.5 nm emission is being amplified when the excitation laser intensity exceeds a certain value. It corresponds to reaching a threshold value in the population inversion

between $\nu' = 0$ of the excited (Q_X) electronic state and $\nu'' = 1$ of a specific vibrational mode in the ground electronic state. For the mode involved, spontaneous emission is amplified by stimulated emission once the threshold value is exceeded. This process will be referred to in a general way as amplified emission (AE).

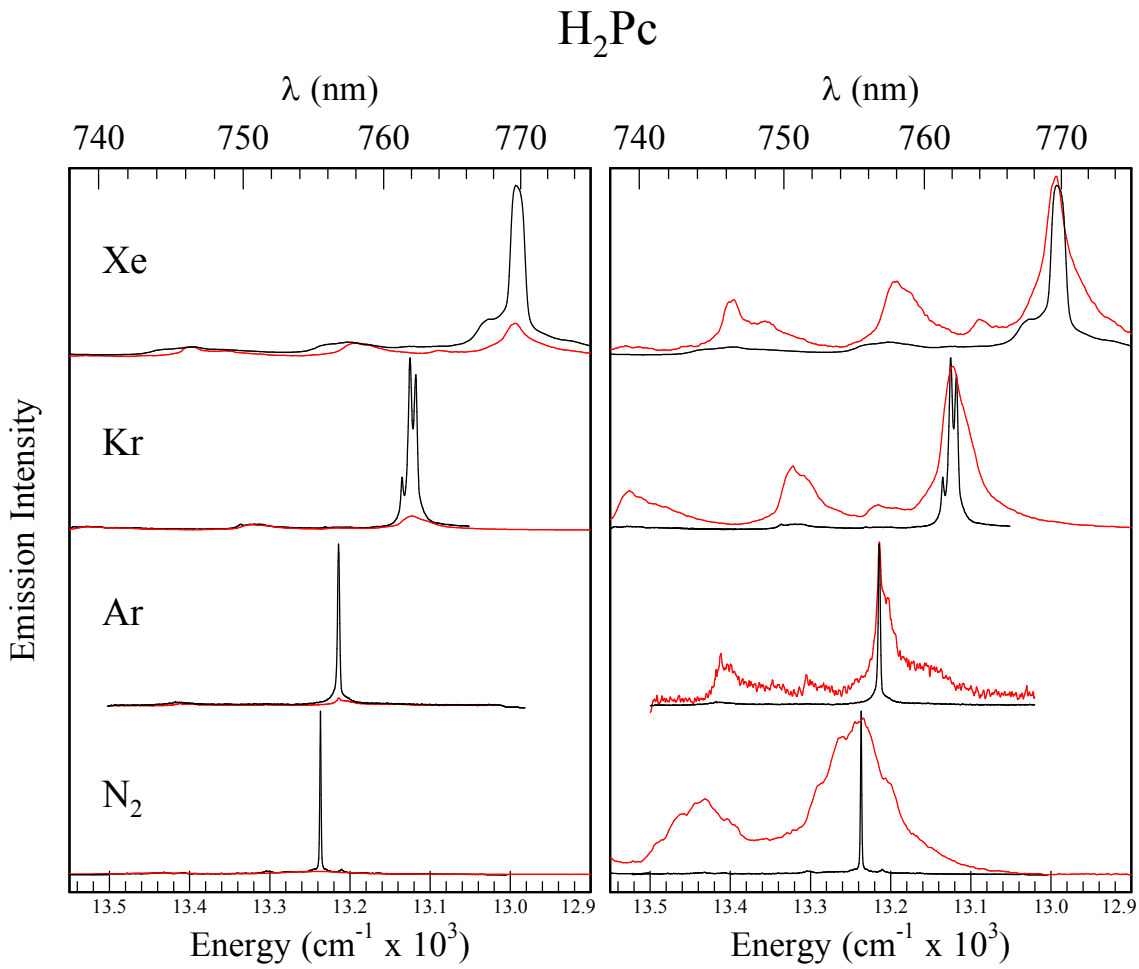

Figure VI.3: A comparison of amplified emission (black trace) and normal fluorescence (red trace) of H_2Pc in Xe, Kr, Ar and N_2 low-temperature solids. The left hand panel shows the significant increase in intensity of the vibronic band found at 1550 cm^{-1} from the 0-0 transition with moderate increases in laser intensity. The right hand panel shows details of the line shapes. A general narrowing of the lines is seen with the relatively broad band widths in Xe due to the use of a lower resolution 0.3 m monochromator. In Kr, the multiple resolved lines of the AE band are due to sites of isolation.

Amplified emission was also observed for H_2Pc isolated in Ne, Ar, Kr and Xe hosts matrices. When observed, AE always appears on the same vibronic transition involving a vibrational mode around 1550 cm^{-1} (see Figure VI.3). In xenon, the conditions for amplified emission were difficult to achieve and it had been reported previously as not occurring at all[5]. It has been determined that the normal fluorescence decay time in xenon is considerably shorter than in the other hosts, indicating that an efficient nonradiative decay mechanism may be present in

this solid. The likely origin of this effect lies in the external heavy atom effect which increases the probability of intersystem crossing from the excited singlet S_1 state to the lower lying spin triplet state, T_1 state. Thus another relaxation mechanism may be competing for the fluorescence and thereby reducing the chance of the excited singlet state population reaching the threshold condition. Attempts to record near-IR phosphorescence from the T_1 state of H_2Pc in Xe were unsuccessful. In the case of H_2Pc/Ne, a very efficient hole-burning phenomenon is observed in the 0–0 $Q_X \leftarrow S_0$ absorption band with even weak dye laser excitation [data not shown]. As the excited family of sites disappears during excitation, AE is not sustainable for long periods in this solid.

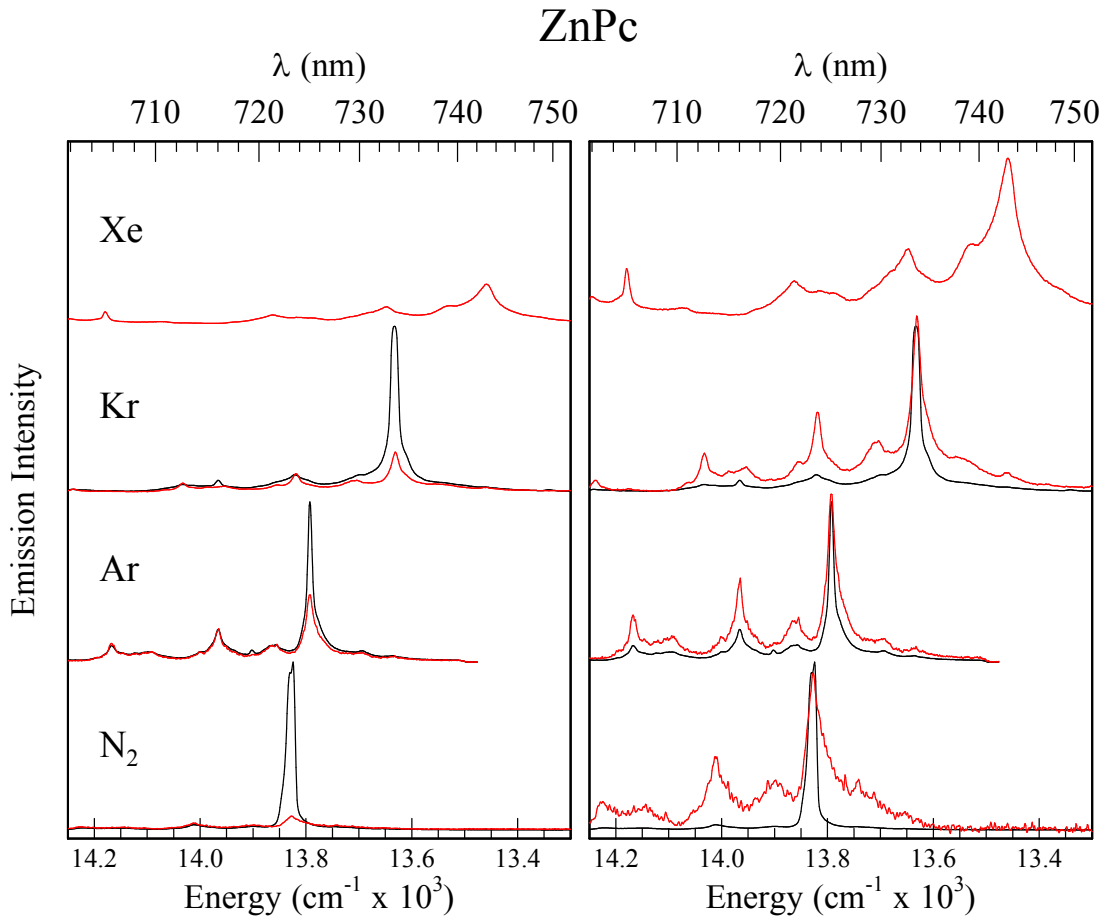

Figure VI.4: A comparison of amplified emission (black trace) and normal fluorescence (red trace) of H_2Pc in Xe, Kr, Ar and N_2 low-temperature solids. The left hand panel shows the significant increase in intensity of the vibronic band found at 1525 cm^{-1} from the 0-0 transition with moderate increases in laser intensity. The right hand panel shows details of the line shapes. A general narrowing of the lines is seen and is limited by the resolution of the monochromator used. No amplified emission was observed for ZnPc in Xe.

The results obtained in the ZnPc systems closely mirror those for the free-base systems (see Figure VI.4). Thus, a single mode is amplified in ZnPc at 1525 cm^{-1} equivalent to the 1550 cm^{-1} mode of H_2Pc. AE was observed for ZnPc in all the solids studied except xenon. Even though the emission lifetimes for ZnPc in all

hosts were similar (3 ns for ZnPc in Ar, Kr and N_2 and 2.8 ns in Xe), an external heavy atom effect similar to that described above for H_2Pc in Xe may exist for ZnPc in Xe. This again may result in non-radiative decay mechanism to the T_1 state, competing with fluorescence from the S_1 state. Attempts to record the near-IR phosphorescence from the T_1 state of ZnPc in Xe were also unsuccessful. An alternative reason why AE may not have been observed in the present study may be due to the weak laser powers available using DCM (which has a range of 615 – 660 nm) and LDS 698 (which has a range of 665 – 730 nm) laser dyes in the region of the Q band of ZnPc at 665 nm.

VI.2.II Excitation spectra and improved site resolution with amplified emission

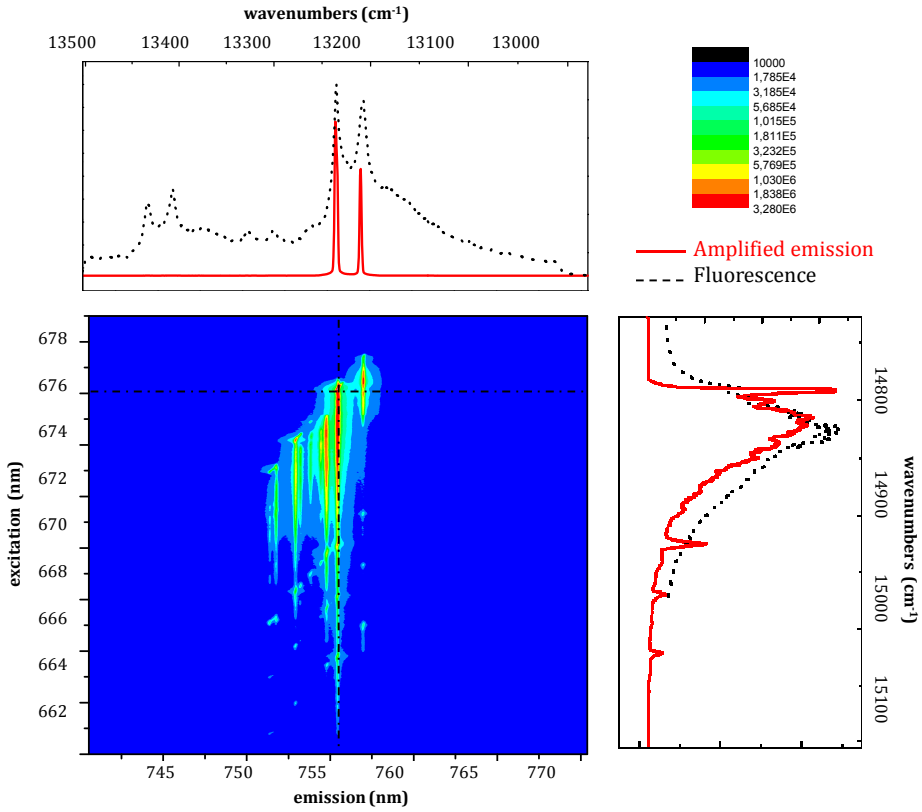

Figure VI.5: 2-D excitation/emission plots of the AE observed for free-base phthalocyanine (H_2Pc) isolated in solid N_2. The data were recorded by monitoring emission with iCCD detection while scanning the tunable dye laser used for excitation at high intensity. The variety of sites is indicated in the central portion of the plot. Characteristic excitation and emission slices are shown on the right hand side and on the upper parts of the figure respectively, corresponding to the positions in emission and excitation given by the black dots on the 2-D plot. Particularly noteworthy is the improved resolution of the AE excitation/emission scans compared with that recorded from the conventional fluorescence signal shown by the dotted lines at the same emission/excitation wavelengths.

Figure VI.5 shows an example of a two-dimensional (2-D) excitation/emission plot of the AE observed for free-base phthalocyanine (H_2Pc) isolated in solid N_2. The plot depicts the variety of sites detected with excitation in the 0–0 region of the $Q_X \leftarrow S_0$ transition while monitoring the AE band centred around 755 nm. Shown on the right hand side and on the upper part of the figure are characteristic excitation and emission slices recorded for normal fluorescence (dotted lines) and under AE conditions. The increased resolution on an individual site is evident in both emission and excitation spectra. However, it is especially evident in the excitation scans shown on the right hand side where the lineshapes change from a featureless band (dotted line) to a highly structured band (solid trace) exhibiting what appears to be a sharp zero-phonon line and a structured side-band. Other examples of excitation spectra recorded for H_2Pc/N_2 under AE conditions are depicted by traces b–e in Figure VI.6 and compared with normal fluorescence excitation scans recorded with the pump laser intensity below threshold (a). Clearly excitation spectra recorded for the AE signal provide greatly enhanced spectroscopic information over what can be extracted from either conventional fluorescence excitation or absorption spectroscopy.

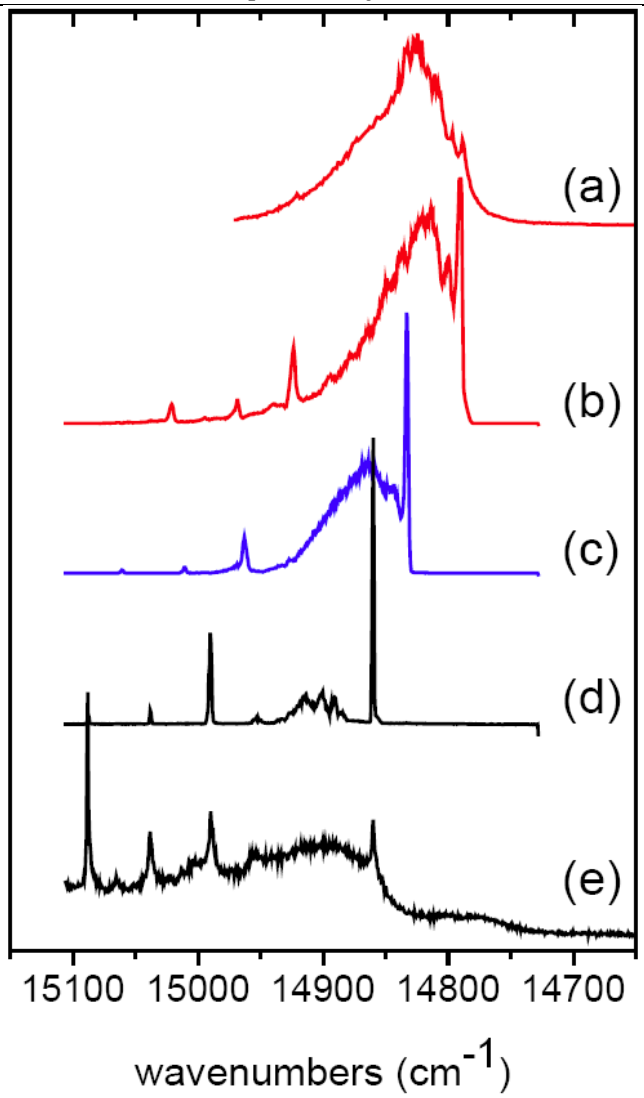

Figure VI.6: A selection of laser excitation scans recorded with AE, involving the 1550 cm^{-1} (b-d) and the 730 cm^{-1} (e) modes, for a variety of sites occupied by H_2Pc isolated in solid N_2. The emission bands monitored are at 13236 cm^{-1} (a-b), 13279 cm^{-1} (c), 13302 cm^{-1} (d) and 14126 cm^{-1} (e). For the purpose of comparison a conventional fluorescence excitation scan is shown in (a). The spectra recorded range from a site with moderate electron-phonon coupling (b) to one with vanishing small coupling (d). The sharp features evident in the four AE scans (b) – (e), correspond to the low frequency vibrational modes in the Q_X excited state.

The sharp, resolved lines present in the AE excitation scan in N_2 are shifted by 130, 178 and 228 cm^{-1}, as shown in Figure VI.6, from the 0–0 transition. They correspond to a vibronic progression on the $Q_X \leftarrow S_0$ transition that has been identified in the excitation scans of the molecule in low temperature matrices[1] and molecular beams[6]. The AE excitation spectra (b–e) shown in Figure VI.6 depict the range of behaviour exhibited by the different sites for the Q_X state of H_2Pc in N_2. The most representative is trace (b) which exhibits a clearly identifiable zero-phonon line (ZPL) for the 0–0 transition with a more intense phonon sideband (PSB). Due to the strength and the width of the latter bands, excitation of the ZPL of a blue site simultaneously excites the PSBs of the red sites. As a result, AE is then

observed in all the sites as shown in Figure VI.5. Strong phonon sidebands are also observed in the excitation spectra recorded in Ar and Kr matrices. Indeed for some sites the ZPL can even be absent. In solid Ar, AE appears mainly at only one frequency assigned to a vibronic transition of the molecule occupying the main site: the threshold of AE is much easier to reach for this specific site which can be efficiently populated in the excited state through the phonon band. In contrast, excitation spectra of AE in solid Ne are dominated by the 0–0 transition line. There is a continuum of equally occupied sites and the AE frequency follows the excitation frequency all along the excitation in the broad absorption band. It seems that in this ‘‘soft’’ solid there is no preferential site geometry—a possible reason for the unusual behaviour sometimes observed[7] with the use of neon as a host material. Thus, the observation of AE should be useful to determine the number of main families of sites in a given host and to underline the differences between the sites occupied in these hosts.

VI.2.III Threshold for amplified emission

A threshold in the dependence of the intensity of the amplified emission on the excitation laser intensity is clearly observed under both Q_X and Q_Y excitation. Threshold data is shown inn Figure VI.7 for the dominant site emission in H_2Pc/N_2 (755.5 nm) produced with excitation at 634 nm (Q_Y excitation). The band exhibiting amplification at 755.5 nm is represented in Figure VI.7 by the filled stars. For comparison, normal fluorescence from the same site is shown in Figure VI.7 by the emission bands at 744.4 and 676.3 nm (the 0–0 band) which were not observed to be amplified. As shown in the lower portion of the plot, the growth in the intensities of these two emission bands track the 755.5 nm band up to a specific value of the exciting laser intensity. Beyond this value, the intensity of 755.5 nm band rapidly increases while the fluorescence intensity remains unchanged on the scale shown. To identify the point beyond which amplified emission takes over from fluorescence, the three sets of data are shown on a larger scale in the upper portion of the plot. The threshold value is indicated in Figure VI.7 by the vertical dashed line at approximately 0.95 mW (95 J/pulse). The intensity of non-amplified emission follows the same behaviour as the amplified band before the threshold, but the slope slightly decreases beyond this point. When the amplification of one vibronic emission occurs, the corresponding specific transition becomes a preferential relaxation path (open stars).

The threshold condition for amplified emission is given[8] by the expression,

$$\frac{N_{th}}{V} = \frac{8\pi\tau\Delta\nu}{\lambda^2\phi l} n^2 \qquad \text{(VI.1)}$$

in terms of the number density of the excited state molecules per cubic centimetre. In this equation τ is the radiative lifetime of the excited S_1 (Q_X) state (assumed to be equal to the measured lifetime, 12 ns), $\Delta\nu$ is the emission linewidth (8 cm^{-1}, 240 GHz), λ is the wavelength (755.5 nm) and ϕ is the emission quantum yield of this vibronic transition (f = 0.05). l is the sample pathlength (0.025 cm) and n is the index of refraction (1.22) of the medium. Making substitutions for the photophysical parameters measured for the H_2Pc/N_2 transition, given in parenthesis, we obtain a threshold value of $2x10^{16} cm^{-3}$. While this is a very large value for gas phase conditions, it is at least 2 orders of magnitude less than the concentration of the ground state molecules isolated in the solid. Accordingly, it has been observed that AE does not occur in very dilute samples in which this threshold cannot be reached with similar excitation powers. In contrast, AE is easily observed for slightly higher concentration, as shown in the example of Figure VI.5 where AE has been recorded on most of the families of sites in N_2.

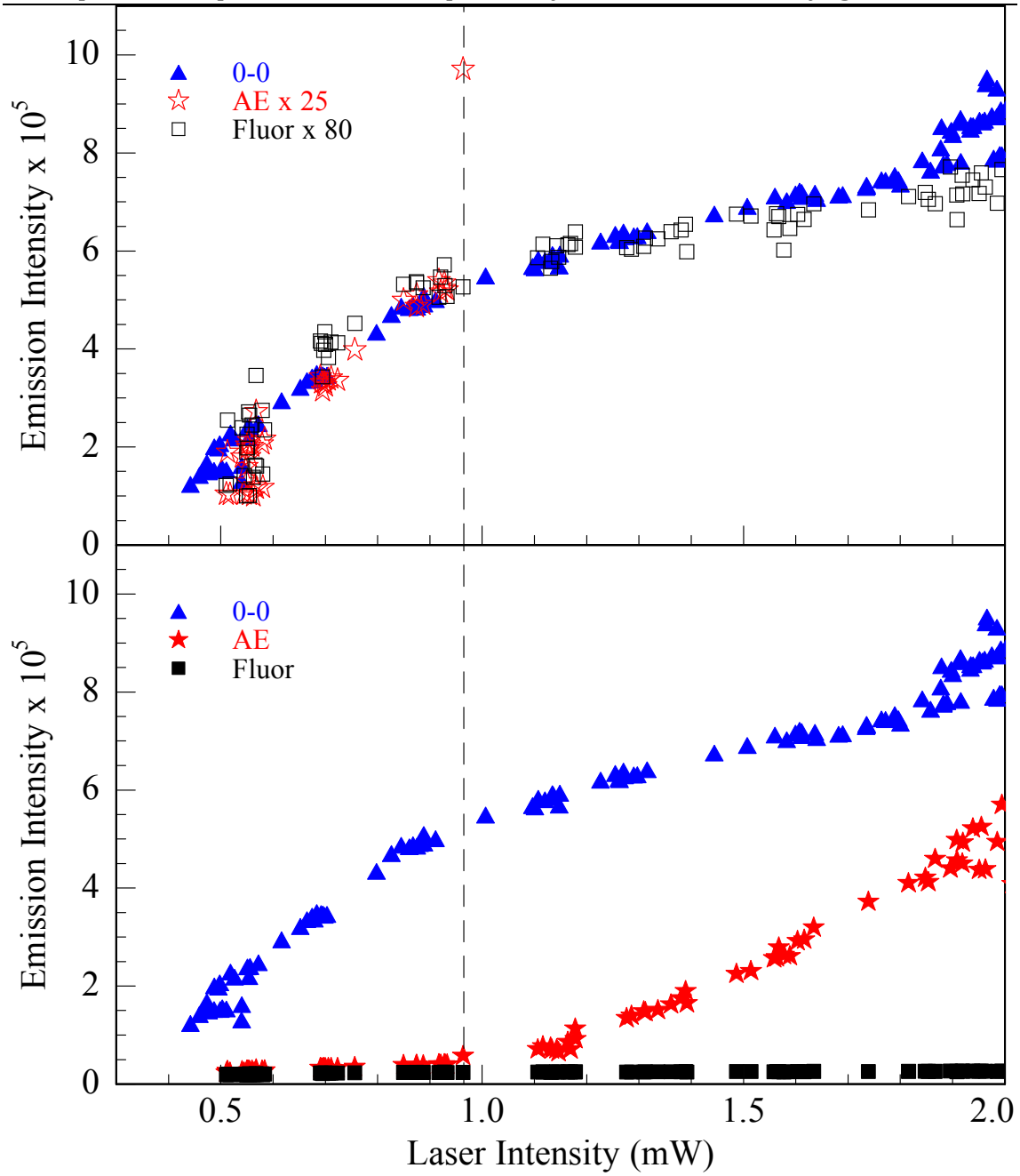

Figure VI.7: Threshold curves measured for the dominant site emission of H_2Pc isolated in solid N_2. The data was recorded by monitoring the intensities of emission at the indicated wavelengths while varying the laser excitation intensity at 634 nm. The wavelengths selected 676.3, 744.4 and 755.5 nm correspond to 0-0 emission of the $Q_X \leftarrow S_0$ transition at 14787 cm^{-1} (0-0), fluorescence of a vibronic band at 13433 cm^{-1} (Flour) and the amplified emission band at 13236 cm^{-1} (AE) respectively. The change in slope, depicted by the dashed vertical line, indicates the onset of AE from normal fluorescence. This point reveals the threshold for the generation of AE on the 13236 cm^{-1} band which is 1551 cm^{-1} from the band origin. The open symbols correspond to full symbols at a scale enlarged by a factor of 25 or 80 depending on the band; it shows that before the threshold all the emission bands follow the same intensity dependence.

VI.2.IV Ground State DFT Geometries

The ground state geometries and vibrational spectra of ZnPc and H_2Pc were compared to six other related porphyrins. Free-base porphyrin (or porphine) is regarded as the parent molecule for the porphyrins. It consists of four pyrrole sub-groups connected via a CH methine bridge to produce an aromatic, macrocyclic ring. Tetrabenzoporphyrin is a benzo annulation of porphyrin where a benzene rings have been attached to the pyrrole rings, producing isoindole sub-groups. The methine bridges may be substituted with aza groups producing tetraazaporphyrin from porphyrin and phthalocyanine from tetrabenzoporphyrin. All four of these porphyrins may act as ligands (with a 2- charge) to form complexes with metals in the central cavity of the macrocycle. Without metallation, two hydrogen atoms bind to the central nitrogens to form free-base porphyrins.

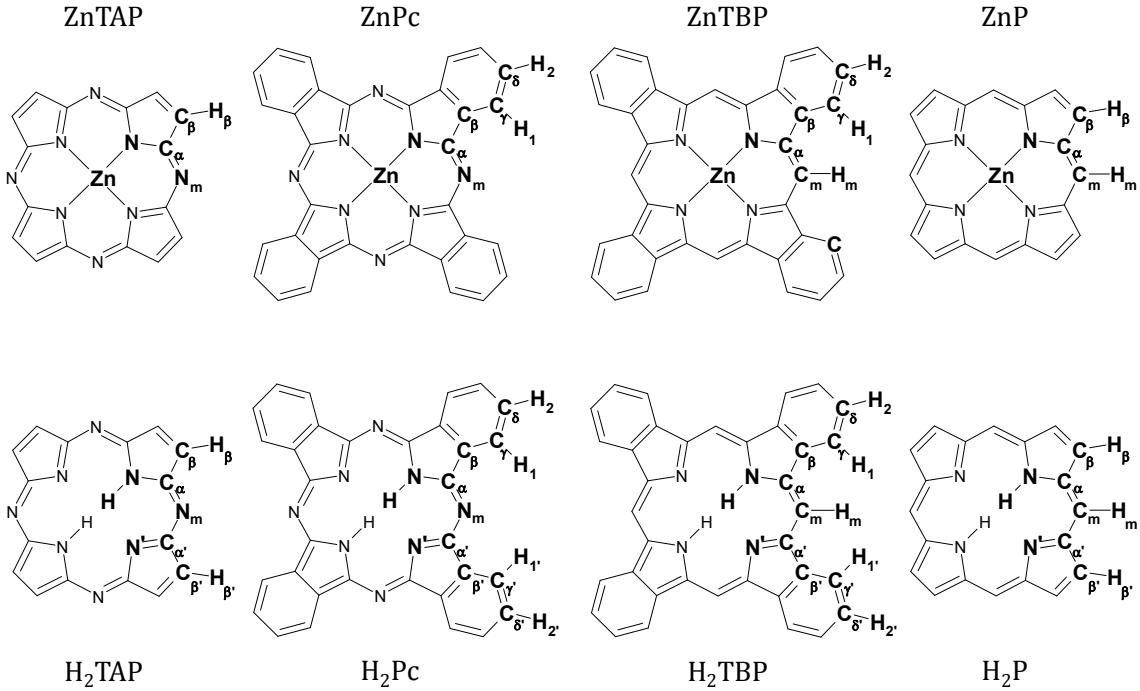

Figure VI.8: Molecular structures of the zinc (Zn) and free-base (H_2) derivatives of tetraazaporphyrin (TAP), phthalocyanine (Pc), tetrabenzoporphyrin (TBP) and porphine (P). The Zn porphyrins (top row) were all found to have D_{4h} symmetry while the H_2 porphyrins (bottom row) were found to have D_{2h} symmetry. The atoms in bold represent the atomic labeling used in this work.

The ground state geometries of porphine (H_2P), tetraazaporphyrin (H_2TAP) and tetrabenzoporphyrin (H_2TBP) as well as their zinc (II) metallo-porphyrin derivatives (ZnP, ZnTAP and ZnTBP) were optimised using DFT calculations with the B3LYP hybrid functional and large Pople basis set 6-311++G(2d,2p). The geometries of H_2Pc and ZnPc were also calculated at the same level of theory (Chapter VI). The molecular structures determined are shown in Figure VI.8. All minimised structures were found to be planar, with the Zn porphyrins having the square planar D_{4h} point group symmetry and, due to the presence of two hydrogens in binding to N atoms on opposite isoindole subgroups, the free-base molecules have a D_{2h} point group. From calculations of the vibrational frequencies, where the energy second derivative Hessian matrix was calculated, no imaginary frequencies were found and the geometry parameters shown in Table VI.1 may be regarded as minima for the current level of calculation.

Table VI.1: Bond lengths and angles determined from DFT calculations for H_2TAP, H_2Pc, H_2TBP and H_2P and ZnTAP, ZnPc, ZnTBP and ZnP. The atom labelling system used is provided in Figure VI.8.

	H_2TAP	H_2Pc	H_2TBP	H_2P	ZnTAP	ZnPc	ZnTBP	ZnP
Lengths (Å)								
N-H(Zn)	1.008	1.009	1.011	1.010	1.977	1.998	2.074	2.051
N-C_α	1.370	1.375	1.371	1.369	1.365	1.369	1.370	1.369
C_α-N(C)$_m$	1.320	1.313	1.384	1.390	1.332	1.327	1.388	1.393
C_α- C_β	1.444	1.450	1.445	1.432	1.457	1.459	1.452	1.443
C_β- C_β	1.362	1.409	1.413	1.368	1.356	1.407	1.406	1.360
C_β- C_γ(H_β)	1.076	1.394	1.399	1.077	1.077	1.391	1.397	1.078
C_γ- C_δ		1.386	1.383			1.390	1.386	
C_δ- C_δ		1.406	1.407			1.403	1.405	
C_γ- H_1		1.080	1.081			1.080	1.082	
C_δ- H_2		1.081	1.081			1.081	1.081	
C_m- H_m			1.081	1.081			1.081	1.081
N'-$C_{\alpha'}$	1.360	1.362	1.360	1.360				
$C_{\alpha'}$- N(C)$_m$	1.334	1.332	1.395	1.396				
$C_{\alpha'}$- $C_{\beta'}$	1.466	1.465	1.463	1.457				
$C_{\beta'}$- $C_{\beta'}$	1.347	1.400	1.404	1.352				
$C_{\beta'}$- $C_{\gamma'}$($H_{\beta'}$)	1.077	1.389	1.393	1.078				
$C_{\gamma'}$- $C_{\delta'}$		1.392	1.389					
$C_{\delta'}$- $C_{\delta'}$		1.401	1.401					
$C_{\gamma'}$- $H_{1'}$		1.081	1.082					
$C_{\delta'}$- $H_{2'}$		1.081	1.081					
Angles (deg)								
H(Zn)-N-C_α	124.59	123.74	123.65	124.57	125.69	125.06	125.71	126.43
N-C_α- N(C)$_m$	127.75	128.10	126.13	125.65	127.25	127.46	125.47	125.14
C_α-N-C_α	110.81	112.53	112.71	110.86	108.62	109.89	108.58	107.14
N-C_α-C_β	106.55	106.14	106.14	106.53	108.52	108.45	109.33	109.44
C_α-C_β-C_β	108.04	107.60	107.51	108.04	107.16	106.61	106.39	107.00
C_β-C_β-C_γ(H_β)	128.62	120.96	120.50	127.58	128.71	121.02	120.65	127.97
C_β-C_γ-C_δ		117.83	118.48			117.84	118.40	
C_γ-C_δ-C_δ		121.21	121.02			121.14	120.95	
C_β-C_γ-H_1		120.59	121.15			120.71	121.35	
C_γ-C_δ-H_2		119.62	119.70			119.64	119.73	
C_α-C_m-H_m			116.18	115.91			115.34	116.57
N'-$C_{\alpha'}$- N(C)$_m$	127.56	121.69	125.70	125.52				
$C_{\alpha'}$-N'-$C_{\alpha'}$	105.53	107.23	107.61	105.76				
N'-$C_{\alpha'}$-$C_{\beta'}$	111.04	110.70	110.52	110.85				
$C_{\alpha'}$-$C_{\beta'}$-$C_{\beta'}$	106.20	105.69	105.68	106.28				
$C_{\beta'}$-$C_{\beta'}$-$C_{\gamma'}$($H_{\beta'}$)	129.57	121.22	120.73	128.28				
$C_{\beta'}$-$C_{\gamma'}$-$C_{\delta'}$		117.67	118.40					
$C_{\gamma'}$-$C_{\delta'}$-$C_{\delta'}$		121.11	120.88					
$C_{\beta'}$-$C_{\gamma'}$-$H_{1'}$		120.93	121.49					
$C_{\gamma'}$-$C_{\delta'}$-$H_{2'}$		119.64	119.72					

There are many similarities between the equivalent geometric parameters for these porphyrins but there are some notable differences. The N-H bond lengths for the free-base molecules are quite similar with the methine bridged molecule's N-H bond lengths only 0.002 Å longer than their aza counterparts. There is a larger difference between the Zn-N bond lengths calculated. The Zn-N bond in ZnP is greater than that in ZnTAP by 0.074 Å and similarly for the benzo annulated pair, the Zn-N bond of ZnTBP is greater than ZnPc by 0.076 Å. A similar trend exists between the distances of opposite pairs of central nitrogens (N-N and N'-N') in the free-base molecules with H_2P greater than H_2TAP by 0.238 Å (H_2P: 4.221 and 4.062 Å versus H_2TAP 3.983 and 3.825 Å) and H_2TBP greater than H_2Pc by 0.239 Å (H_2TBP: 4.284 and 4.140 Å versus H_2Pc: 4.045 and 3.901 Å). This difference in cavity size is primarily due to the longer C_α-C_m bond in the non-aza substituted porphyrins, 0.061 Å for the zinc molecules and ~0.07 Å (C_α-C_m) and ~0.063 Å ($C_{\alpha'}$-C_m) for the free-base ones. There is also a compression of the pyrrole rings with the C_α-N-C_α ~2° smaller in the non-aza substituted forms.

VI.2.V DFT calculated harmonic frequencies

The vibrational frequencies, infrared intensities and Raman scattering activities for the eight porphyrins were calculated using the geometries optimised using the B3LYP/6-311++G(2d,2p) method and at the same level of theory. H_2TAP, H_2Pc, H_2TBP and H_2P have 34, 58, 62 and 38 atoms respectively giving a total of 96, 168, 180 and 108 vibrational normal modes. According to group theory, 48, 84, 90 and 54 modes are Raman active, 41, 71, 76 and 46 are IR active while 7, 13, 14 and 8 are optically inactive modes of A_u symmetry. Table VI.2 lists the number of modes of each symmetry for the four D_{2h} molecules. The metallo-porphyrins of D_{4h} symmetry have one less atom than their free-base equivalents and therefore three less vibrational modes. Of these modes, ZnTAP, ZnPc, ZnTBP and ZnP have 38, 68, 73 and 43 Raman active modes, 37, 64, 69 and 42 IR active modes and 18, 33, 35 and 20 inactive modes respectively. A full break-down of the symmetries of these modes is given in Table VI.3.

Table VI.2: Number and symmetry of the vibrational modes of the D_{2h} symmetry molecules H_2TAP, H_2Pc, H_2TBP and H_2P. Also tabulated are the total number of Raman (Ram), infrared (IR) and inactive (IA) modes. The z-axes have been re-oriented perpendicular to the molecule plane to ease the comparison with the D_{4h} Zn porphyrins.

	A_g	B_{1g}	B_{2g}	B_{3g}	Total Ram	B_{1u}	B_{2u}	B_{3u}	Total IR	A_u IA	Total Modes
H_2TAP	17	16	8	7	48	9	16	16	41	7	96
H_2Pc	29	28	14	13	84	15	28	28	71	13	168
H_2TBP	31	30	15	14	90	16	30	30	76	14	180
H_2P	19	18	9	8	54	10	18	18	46	8	108

Table VI.3: Number and symmetry of the vibrational modes of the D_{4h} symmetry molecules ZnTAP, ZnPc, ZnTBP and ZnP. Also tabulated are the total number of Raman (Ram), infrared (IR) and inactive (IA) modes.

	A_{1g}	B_{1g}	B_{2g}	E_g	Total Ram	A_{2u}	E_u	Total IR	A_{1u}	A_{2g}	B_{1u}	B_{2u}	Total IA	Total Modes
ZnTAP	8	8	8	14	38	5	32	37	3	7	4	4	18	93
ZnPc	14	14	14	26	68	8	56	64	6	13	7	7	33	165
ZnTBP	15	15	15	28	73	9	60	69	6	14	8	7	35	177
ZnP	9	9	9	16	43	6	36	42	3	8	5	4	20	105

All IR and Raman vibrational frequencies and intensities for both zinc and free-base porphyrin, tetraazaporphyrin and tetrabenzoporphyrin are tabulated in the appendix to this chapter (Appendix VI.A). A full vibrational analysis of ZnPc and H_2Pc has already been presented in Chapter IV. Considering the Franck-Condon factors governing the vibronic selection rules, emission from an E_u electronic state of a D_{4h} molecule will relax to the Raman active A_{1g}, A_{2g}, B_{1g}, B_{2g} and E_g symmetry modes in the ground state and emission from a B_{3u} electronic state of a D_{2h} molecule will relax to Raman active A_g, B_{1g} and B_{2g} symmetry modes. B_{3g} Raman active modes of D_{2h} molecules are predicted to be vibronically forbidden in emission from a B_{3u} excited electronic state (see Chapter III for vibronic selection rules). In all the systems considered in this work, Raman modes of B_{3g} symmetry were found to be very weak and were not seen in the experimental spectra.

Due to vibronic selection rules and similarities seen between intensities of the Raman scattering spectra and fluorescence spectra of H_2Pc and ZnPc (calculated Raman frequencies and intensities shown in Figure VI.9), particular attention will be paid to the calculated Raman frequencies and intensities. The following sections

will review important results from the DFT calculated Raman spectra including the similarities/differences between the zinc and free-base spectra and identification of the most intense modes. The spectra of the four porphyrins (both zinc and free-base) will be compared.

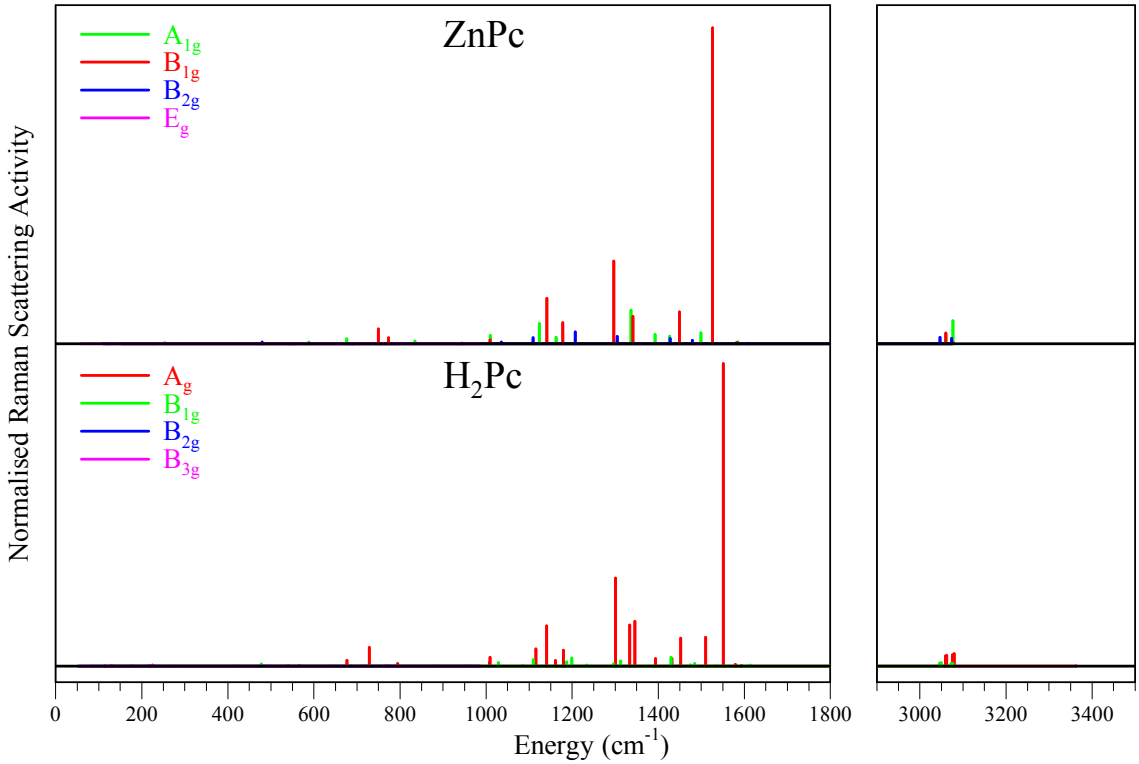

Figure VI.9: DFT calculated Raman spectra of zinc (upper plot) and free-base phthalocyanine (lower plot). The symmetry of each mode is indicated by the colour coding shown on the figure. The frequencies <2000 cm^{-1} have been scaled by a factor of 0.98 and the C-H and N-H stretches have been scaled by 0.96 and 0.931 respectively. The intensities have been normalized and the same scale is used in both spectral regions.

VI.2.V.a ZnP and H_2P

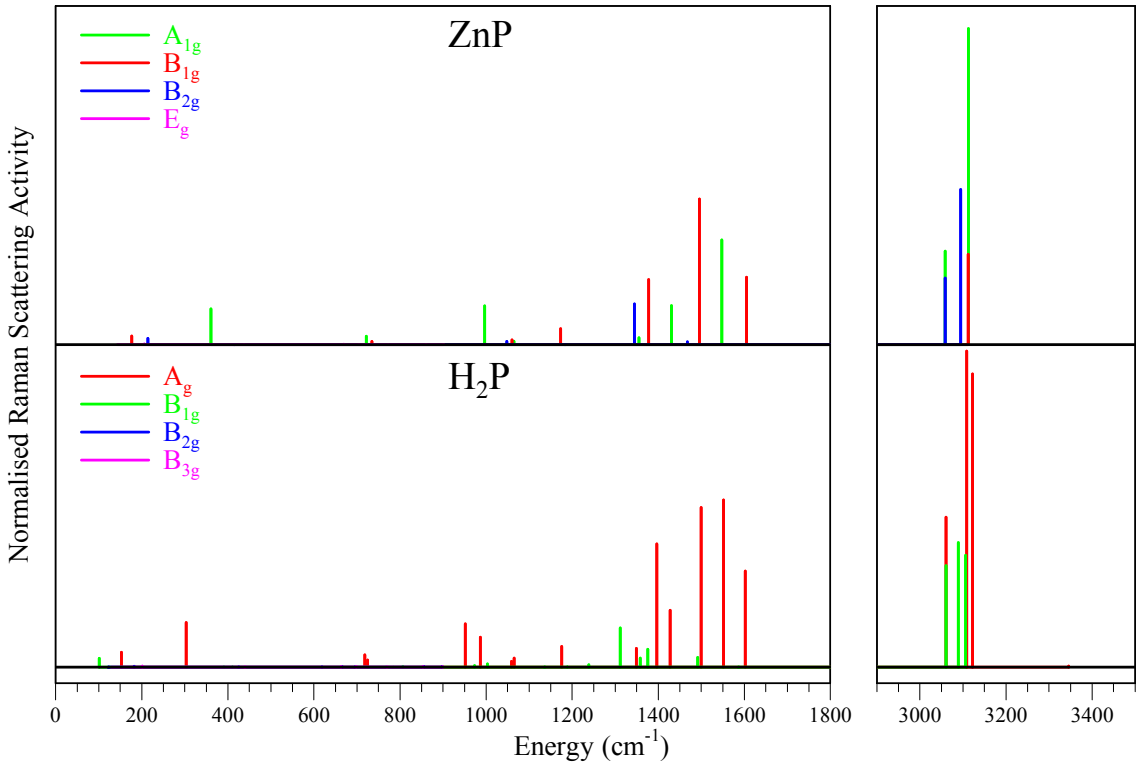

Figure VI.10: DFT calculated Raman spectra of zinc (upper plot) and free-base porphyrin (lower plot). The symmetry of each mode is indicated by the colour coding shown on the figure. The frequencies <2000 cm^{-1} have been scaled by a factor of 0.98 and the C-H and N-H stretches have been scaled by 0.96 and 0.931 respectively. The intensities have been normalized and the same scale is used in both spectral regions.

The scaled DFT vibrational frequencies and intensities of the Raman active mode of ZnP and H_2P are shown in Figure VI.10. Both spectra are very similar, dominated by the A_{1g} and B_{1g} vibrations in ZnP and the equivalent A_g vibrations in H_2P. There are also a small number of B_{2g} modes visible in the ZnP plot as well as their B_{1g} equivalents in H_2P plot. The E_g modes in ZnP and B_{2g} and B_{3g} modes in H_2P have been calculated to have very weak intensities and cannot be seen in plots shown. The most intense bands predicted are in the C-H stretching region between 3000 and 3200 cm^{-1}. The lower frequency modes in this region have been assigned to the stretching vibrations of the meso C_m-H_m atoms with the higher frequency modes to the pyrrole C_β-H_β modes. The structure of the pyrrole C-H bands predicted in H2P is slightly more complicated than that seen in ZnP due to the reduction in symmetry but as seen in the experimental Raman spectra of H_2Pc and ZnPc, these bands would be expected to be difficult to resolve. The weak N-H stretching A_g symmetry mode of H_2P is only just visible at 3345.5 cm^{-1}.

The four most intense modes predicted below 1800 cm^{-1} in ZnP at 1378, 1496, 1548 and 1605 cm^{-1} and in H_2P at 1397, 1500, 1552 and 1602 cm^{-1} have been

found to be equivalent. The 1378/1397cm^{-1} (Zn/H_2P) mode is primarily a C-H bending mode of the bridging meso group while the 1496/1500 cm^{-1} mode in both molecules is the most intense mode in this region and is a bending motion of the C-H bonds on the pyrrole rings with some coupling to the other bonds of the ring. The mode at 1548 cm^{-1} in ZnP and 1552 cm^{-1} in H_2P may be described as an expansion of the distance between the C_α atoms in each pyrrole ring coupled to a contraction of the C_β- C_β bonds. Finally the mode at 1605/1602 cm^{-1} is a ring mode involving stretching motions of the C_m-C_α bonds. This mode is equivalent the most intense mode identified in ZnPc and H_2Pc but is the 3rd most intense ZnP mode and 4th most intense H_2P mode <1800 cm^{-1} and are both predicted to be less intense the C-H stretch modes. The DFT calculated frequencies and intensities of all the IR and Raman active vibrational modes of H_2P and ZnP are tabulated in Appendix IV.A, Tables IV.A.1 and IV.A.2.

VI.2.V.b ZnTAP and ZnTAP

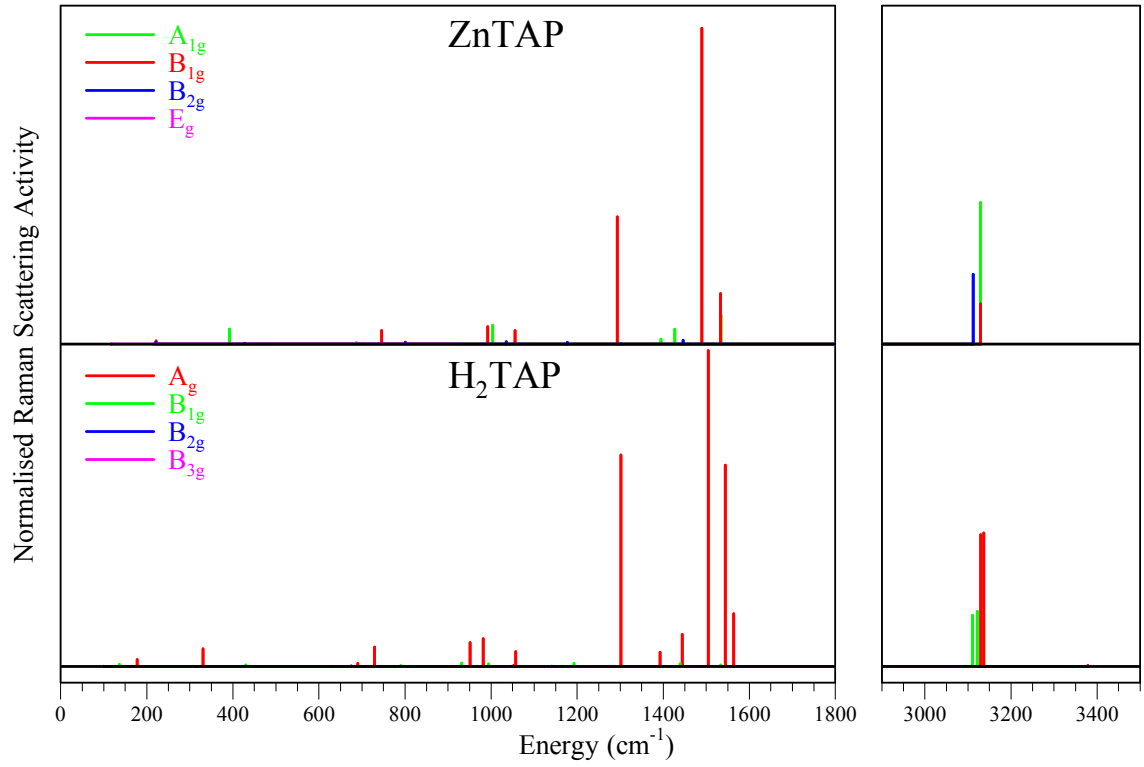

Figure VI.11: DFT calculated Raman spectra of zinc (upper plot) and free-base tetraazaporphyrin (lower plot). The symmetry of each mode is indicated by the colour coding shown on the figure. The frequencies <2000 cm^{-1} have been scaled by a factor of 0.98 and the C-H and N-H stretches have been scaled by 0.96 and 0.931 respectively. The intensities have been normalized and the same scale is used in both spectral regions.

The Raman spectra predicted for ZnTAP and H_2TAP are qualitatively different from those predicted for Zn and H_2-porphyrin. As shown in Figure VI.11, the most intense modes are now predicted below 1800 cm^{-1} with the C-H stretching modes

having relatively lower but still significant intensity. The most intense modes are still of B_{1g} and A_{1g} symmetry in ZnTAP and A_g symmetry in H_2TAP and the only modes of B_{2g} (ZnTAP) and B_{1g} (H_2TAP) now with noteworthy intensity being the asymmetric C-H stretches at ~3110 cm^{-1}. Replacing the methine bridge with an aza bridge in the porphyrin ring leads to a simpler band structure in C-H stretching region but the lower symmetry free-base TAP is still more complicated than the zinc TAP.

The most intense bands predicted in ZnTAP and H_2TAP are of B_{1g} and A_g symmetry respectively and are to be found in the spectral region 1290-1570 cm^{-1}. The ratios of the intensities of the three most intense bands are approximately 2.5:6.2:1 for ZnTAP and 1:1.5:1.1 for H_2TAP. The existence of one dominant band in ZnTAP is similar to the very intense band found in ZnPc and H_2Pc through which amplified emission occurred but the nature of this vibration is very different. In both ZnTAP and H_2TAP the most intense mode at 1489.9 cm^{-1} and 1504.9 cm^{-1} consist of a N-C_α-C_β bending motion coupled to a C_β-C_β stretch and C_b-H_b bend. These vibrations are equivalent to the modes found at 1548 cm^{-1} in ZnP and 1552 cm^{-1} in H_2P. The second most intense modes found in ZnTAP at 1293.3 cm^{-1} and in H_2TAP at 1301.5 cm^{-1} are equivalent, consisting of alternating C_α-N-C_α bends around the TAP ring moving the central N atoms in and out from the centre of the molecule. Interestingly, a similar motion was found for the second most intense modes in ZnPc at 1296.7 cm^{-1} and H_2Pc at 1300.8 cm^{-1} with very similar frequencies. The DFT calculated frequencies and intensities of all the IR and Raman active vibrational modes of H_2TAP and ZnTAP are tabulated in Appendix IV.A, Tables IV.A.3 and IV.A.4.

VI.2.V.c ZnTBP and H_2TBP

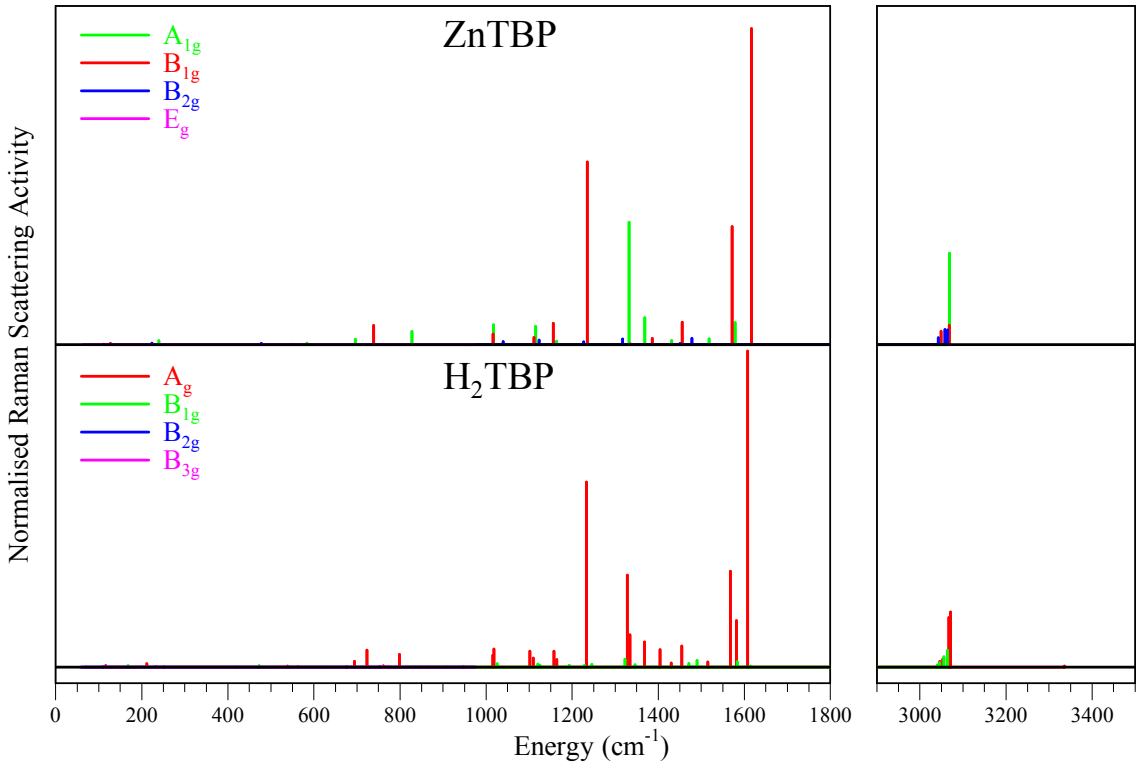

Figure VI.12: DFT calculated Raman spectra of zinc (upper plot) and free-base tetrabenzoporphyrin (lower plot). The symmetry of each mode is indicated by the colour coding shown on the figure. The frequencies <2000 cm^{-1} have been scaled by a factor of 0.98 and the C-H and N-H stretches have been scaled by 0.96 and 0.931 respectively. The intensities have been normalized and the same scale is used in both spectral regions.

The Raman spectra predicted for ZnTBP and H_2TBP are qualitatively different from for the corresponding spectra of ZnP and H_2P and are more similar to their aza bridged analogues, ZnPc and H_2Pc. As shown in Figure VI.12, the higher frequency C-H and N-H stretches are relatively weak with the most intense modes in the 1200-1700 cm^{-1} region. The C-H modes are noteworthy in that the most intense of these, of A_{1g} symmetry in ZnTBP and A_g symmetry in H_2TBP, involve a coupling of the benzo $C_{\gamma(\delta)}$-$H_{1(2)}$ and meso C_m-H_m bonds, a coupling not seen in the smaller porphyrine molecules between the pyrrole C_β-H_β and meso C_m-H_m bonds. Like all the molecules seen so far, the inner hydrogen stretch frequency calculated at 3335.96 cm^{-1} (3583.21 cm^{-1} unscaled) is predicted to have an extremely low Raman scattering intensity.

The most intense modes in ZnTBP and H_2TBP, predicted at 1616.69 and 1607.83 cm^{-1} (scaled) respectively, correspond to the intense modes which exhibited amplified emission in ZnPc and H_2Pc, predicted at 1526.09 and 1551.26 cm^{-1} (scaled). The intensities of this mode in tetrabenzoporphyrin relative to the other vibrations are lower than that seen in DFT calculations of the

phthalocyanines. The ratios of this mode and the second most intense mode (1235.21 cm^{-1} in ZnTBP and 1233.29 cm^{-1} in H_2TBP) are 1.73:1 and 1.71:1 for ZnTBP and H_2TBP versus 3.82:1 and 3.43:1 for ZnPc and H_2Pc. The reason for this lowering in Raman scattering activity is probably due to coupling of the C_m-C_α stretches which make up this mode in both TBP and Pc molecules with a C_m-H_m bending motion seen for the TBP molecules which obviously do not occur in the aza bridged Pc molecules. The second most intense modes predicted at 1235.21 cm^{-1} in ZnTBP and 1233.29 cm^{-1} in H_2TBP consist of a bending vibration of all C-H bonds coupled to stretches of the C_α-C_β bonds. The other two intense bands seen in the spectra in Figure VI.12 at 1332.04 and 1571.63 cm^{-1} in ZnTBP and 1328.24 and 1567.60 cm^{-1} in H_2TBP consist of a bending of the C-N-C atoms coupled to an antisymmetric stretching of the C_β-C_β and C_δ-C_δ bonds in the lower energy vibration and a symmetric stretch of the C_β-C_β and C_δ-C_δ bonds in the higher energy vibration distorting the size of the benzo annulations. The 1332.04/1328.24 cm^{-1} vibrations correspond to the second most intense modes seen in ZnPc and H_2Pc. The DFT calculated frequencies and intensities of all the IR and Raman active vibrational modes of H_2TBP and ZnTBP are tabulated in Appendix IV.A, Tables IV.A.5 and IV.A.6.

VI.2.V.d Comparison of DFT Raman spectra

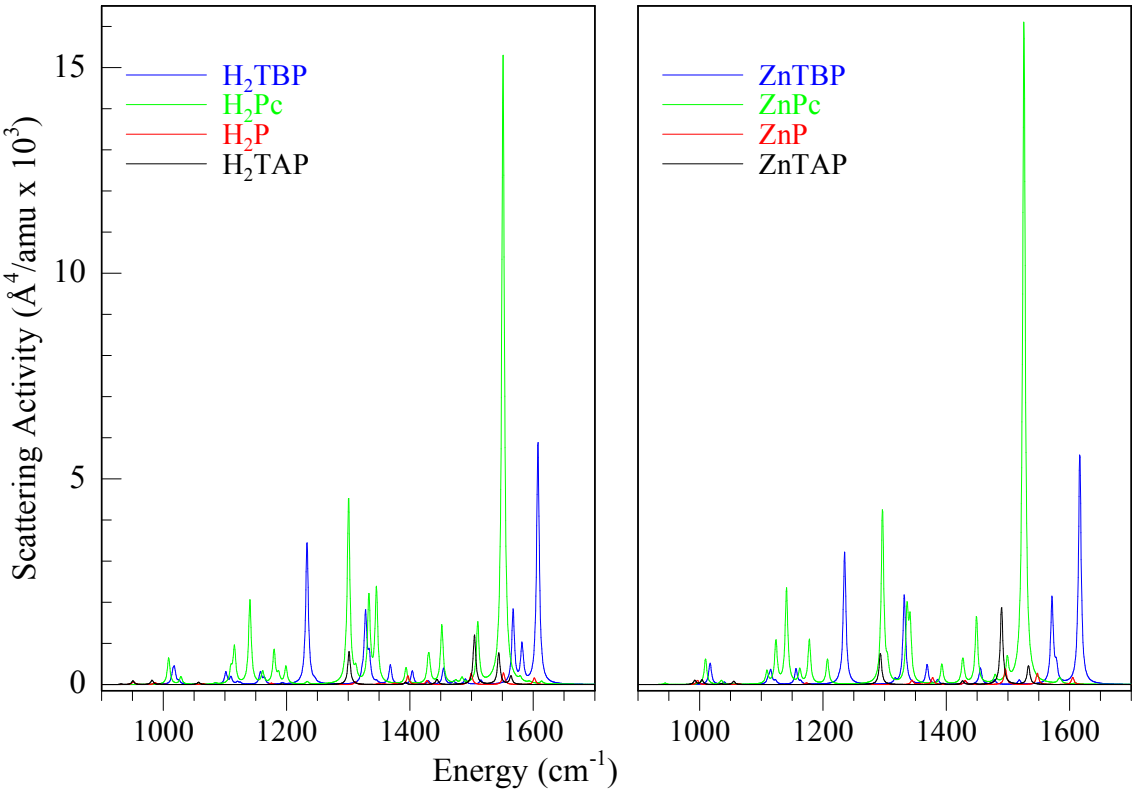

Figure VI.13: Absolute Raman scattering activity of H_2TAP, H_2P, H_2Pc and H_2TBP (left panel) and ZnTAP, ZnP, ZnPc and ZnTBP (right panel). The intensities are given in Å⁴/amu and both panels use the same scale. The larger Pc and TBP molecules have significantly larger intensities than the smaller TAP and P molecules. The larger intensity seen for the aza bridged porphyrins on certain modes is due to coupling of motions from the meso C-H in the methine bridged molecules.

The spectra shown above in Figure VI.9, Figure VI.10, Figure VI.11 and Figure VI.12 have been presented with normalized intensities. Looking at the absolute intensities calculated by Gaussian 03 in units of Å⁴/amu, a large difference in intensity is seen. As shown in Figure VI.13, the larger phthalocyanines and tetrabenzoporphyrins are calculated to have a much greater scattering intensity than the smaller tetraazaporphyrins and porphyrins. The maximum intensity value calculated for ZnPc and H_2Pc are 2.73 and 2.75 times more intense than the maximum values for ZnTBP and H_2TBP but this difference in intensity may be explained due to coupling of the C_m-H_m bonds in this particular vibration. As can be seen in Figure VI.13, most of the other vibrational modes are predicted to have comparable intensities. The Raman active modes of ZnTAP and H_2TAP are generally much less intense than those calculated for the Pc and TBP molecules with the ZnP and H_2P modes weaker again. The addition of aromatic rings to a molecule, increasing its size, has been seen to increase the Raman activity of particular modes in polycyclic aromatic hydrocarbons (PAHs)[9], molecules with many similarities to porphyrins and phthalocyanines. The differences between the

intensities found for TAP and porphyrin molecules (like the difference found between Pc and TBP) are primarily due to the presence of C_m-H_m contributions in certain modes, reducing the components of the polarizability tensor which determines the Raman scattering activity.

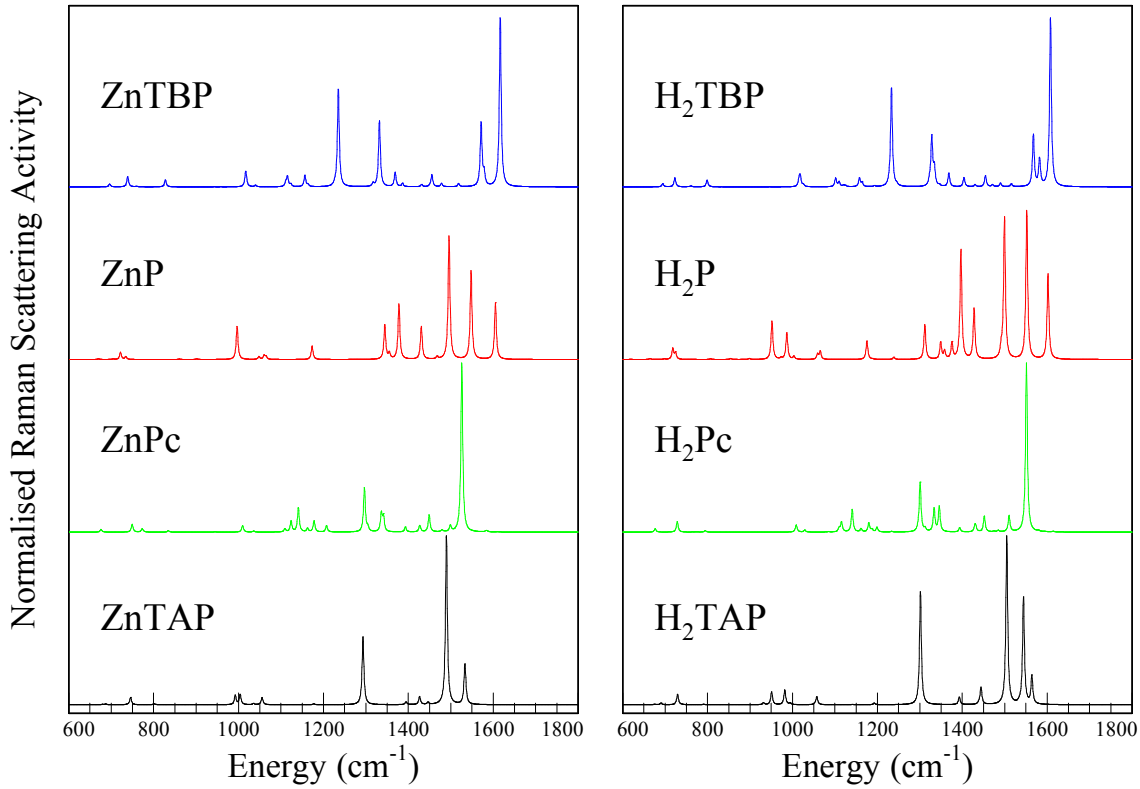

Figure VI.14: Frequencies and normalized Raman scattering intensities of zinc and free-base TBP, P, Pc and TAP calculated using DFT. The plots shown have been convoluted with a 5 cm^{-1} Lorentzian line-shape.

Comparing the frequencies calculated for the eight porphyrins, a greater similarity is apparent between the aza bridged derivatives and methine bridged derivatives than between the benzo annulations and non-benzo annulations. A good example of these similarities and differences is the most intense mode in ZnTBP and H_2TBP and ZnPc and H_2Pc (Figure VI.14). The unscaled vibrational frequencies calculated for ZnTBP and H_2TBP were 1640.64 and 1649.69 cm^{-1} and are a close match to the equivalent modes found in ZnP and H_2P at 1638.02 and 1634.71 cm^{-1}. Likewise, the unscaled vibration frequencies calculated for ZnPc and H_2Pc were shifted to lower frequencies of 1557.23 and 1582.92 cm^{-1} and are a close match to ZnTAP and H_2TAP at 1564.32 and 1595.96 cm^{-1}. There is however a disparity between the relative intensity of this mode and the other Raman active modes of the molecules. While in the larger molecules this is the most intense mode, in the smaller molecules this mode is comparatively minor, particularly in ZnTAP and H_2TAP. As the TAP molecules are thought to be good candidates for AE, the reason for this lower intensity was further investigated.

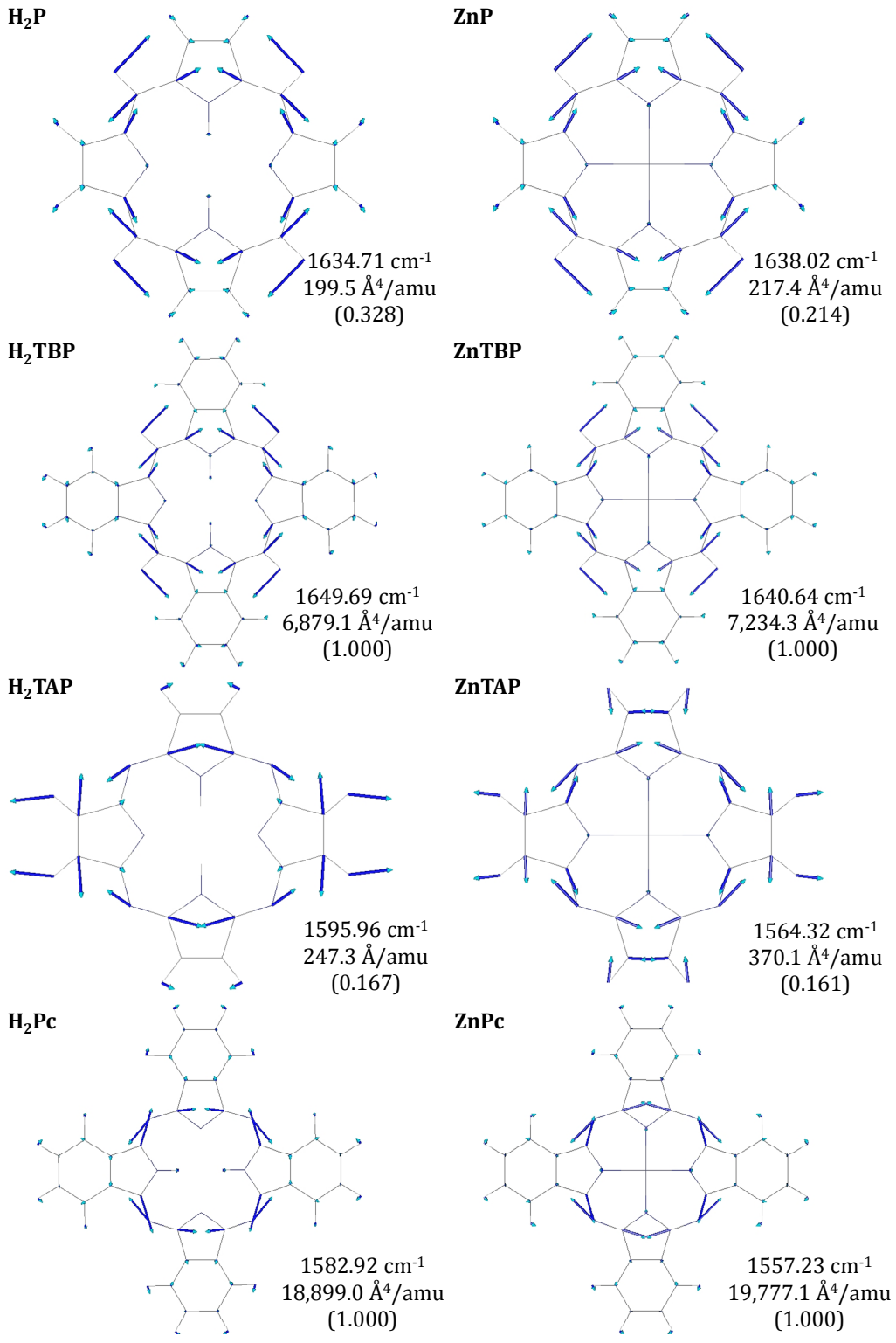

Figure VI.15: Displacement vector diagrams of the most intense Raman vibrations in TBP and Pc molecules and the corresponding modes in P and TAP. The values given are the un-scaled frequencies, absolute intensities and relative intensities calculated using the B3LYP/6-311++G(2d,2p) method.

Examining the atomic displacements of the vibration calculated at 1582.92 cm^{-1} in H_2Pc, most of the motion involves an asymmetric stretching of the C_α-N_m bonds making up the ring of the phthalocyanine. Though there is some coupling to the C-H bonds of the benzene rings, their contribution is very minor and the vibration

may be regarded as a 'pure' ring mode. Considering the corresponding vibration in H_2TAP, a similar stretching of the C_α-N_m bonds is evident but there is also a significant contribution from bending of the C_β-H_β bonds. An attempt to demonstrate the effect of decoupling C_β-H_β was made by calculating the vibrational frequencies and Raman intensities of H_2TAP with very large H_β masses. Figure VI.16 shows the results of these calculations with H_β masses up to 20 amu. The vibrational frequencies of modes involving significant H_β contributions show a large reduction in energy. The mode originating at 1595.96 cm^{-1} however, displayed a relatively small decrease of 31.09 cm^{-1} to 1564.87 cm^{-1} with a H_β mass of 20 amu. As shown in the vector displacement diagrams in Figure VI.16, the larger mass of the H_β atoms has decoupled the contributions of the C-H motions, leaving an almost pure ring mode like that seen in H_2Pc.

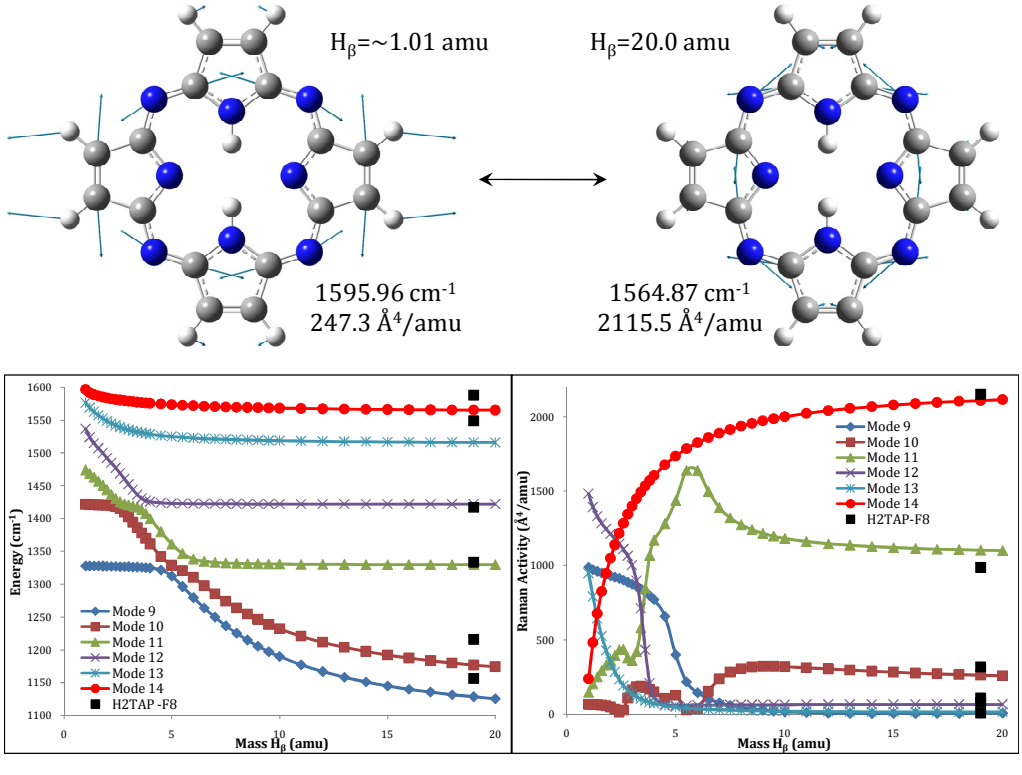

Figure VI.16: Change in intensity of selected A_g symmetry modes of H_2TAP with increasing H_β mass. The plots in the lower half of the figure show change of frequency (un-scaled) and change in Raman scattering activity with increasing mass of the outer pyrrole hydrogen atoms, H_β. The red circles represent the values for the equivalent mode in H_2TAP (vector displacement diagrams shown in upper half of figure) found to exhibit amplified emission in H_2Pc. The black squares represent the values determined for H_2TAP's fluoridated analogue H_2TAP-F_8.

What is also evident is the dramatic increase in intensity of this mode from the fourth most intense mode in the normal proton H_2TAP with a calculated Raman activity of 247.3 $Å^4$/amu to the most intense mode in the 20 amu proton form, with a calculated activity of 2115.5 $Å^4$/amu. Analysis of the effect on the other A_g modes is made more complicated by a series of non-crossing events as the mass of the H_β

atoms increase. The vibrational modes numbered 12 and 11 are assigned to modes 10 and 9 respectively in the heavier isotopomer, reducing in both frequency and intensity. Mode 9 has been assigned to mode 11 with a slight increase in intensity and frequency (due to originating in a higher frequency mode) and remains the second most intense vibrational mode. Similarly, mode 10 has been assigned to mode 12 with a small change in frequency and intensity. The results for the same isotopic substitutions for ZnTAP are shown in Figure VI.17 with similar effects as seen for H_2TAP. In particular, the vibrational frequency at 1564.32 cm^{-1}, corresponding to the mode calculated at 1595.96 cm^{-1} in H_2TAP, decreases to 1535.97 cm^{-1} (a difference of 28.35 cm^{-1}) with a large increase in Raman scattering intensity from 370.1 to 2246.3 $Å^4$/amu.

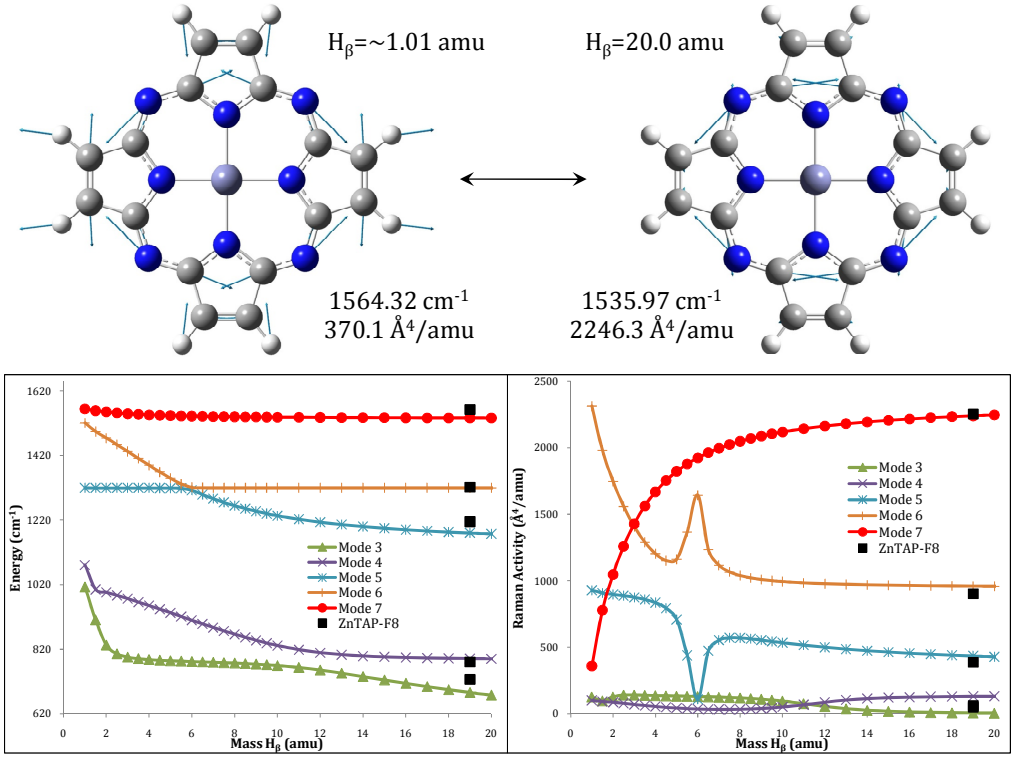

Figure VI.17: Change in intensity of selected B_{1g} symmetry modes of ZnTAP with increasing H_β mass. The plots in the lower half of the figure show change of frequency (un-scaled) and change in Raman scattering activity with increasing mass of the outer pyrrole hydrogen atoms, H_β. The red circles represent the values for the equivalent mode in ZnTAP (vector displacement diagrams shown in upper half of figure) found to exhibit amplified emission in ZnPc. The black squares represent the values determined for the fluoridated analogue ZnTAP-F_8.

Decoupling the C_β-H_β motion by increasing the H_β atomic masses clearly increases the intensity calculated for the corresponding vibrational modes in ZnTAP and H_2TAP that were seen to exhibit amplified emission in ZnPc and H_2Pc, resulting in a simpler predicted Raman spectrum, dominated by one vibrational mode. A mass greater than three amu is of course unrealistic for hydrogen. A more experimentally viable model would be to replace the H atoms with a heavier mono-

valence atom. The optimised geometries and vibrational frequencies and intensities for the fluoridated analogues of ZnTAP and H_2TAP, ZnTAP-F_8 and H_2TAP-F_8 were calculated using the same B3LYP/6-311++G(2d,2p) DFT method. The frequencies and intensities calculated compare favourably to those calculated for the H_β mass approximately equal to the mass of fluorine, i.e. 19 amu, as indicated by the black squares in Figure VI.16 and Figure VI.17. The optimised geometeries and DFT calculated frequencies and intensities of all the IR and Raman active vibrational modes of H_2TAP-F_8 and ZnTAP-F_8 are presented in Appendix IV.B.

VI.3 Discussion

The essentials of the AE observed in this work can be described with the energy level scheme shown in Figure VI.18. It comprises the ground state [Level 1, S_0 ($\nu'' = 0$)], which is the only one populated at cryogenic temperatures before laser excitation, the pumped state, the upper level of the AE [Level 2, in H_2Pc Q_X ($\nu' = 0$) or in ZnPc Q] and the lower level of AE [Level 3, S_0 ($\nu'' = 0$ of a specific mode)] i.e. in H_2Pc at 1550 cm^{-1} and in ZnPc at 1525 cm^{-1} above the vibrationless ground state. In general we have a 4-level scheme because a Level 2' is usually involved. As indicated in Figure VI.18, this is either a vibrationally excited level of Q_X or the Q_Y electronic state. For AE to occur, an efficient route for populating Level 2 is required. This is provided by very efficient pumping with pulsed laser excitation of an electronic transition having a huge extinction coefficient—ε= 162 000 cm^{-1}/M at 698.5 nm for H_2Pc in chloronaphthalene[10]. For indirect excitation in H_2Pc via the Q_Y state (Level 2') an efficient relaxation to Level 2 is required. This is indeed the case, because the only emission that has been observed with Q_Y is relaxed, originating from $\nu' = 0$ in the Q_X state. For the main sites of H_2Pc and ZnPc in the low temperature solids studied, no Stokes shift on the 0–0 $Q_X \leftrightarrow S_0$ transition was observed so with direct pumping of $\nu' = 0$ in the Q_X or Q states, there is only a single Level 2. Consistent with this, AE in H_2Pc seems easier to reach by pumping Q_X than Q_Y. Finally, Level 3 corresponds to a non-thermally populated level at 1550 or 1525 cm^{-1} so that the inversion population on the (2)→(3) transition is easily obtained.

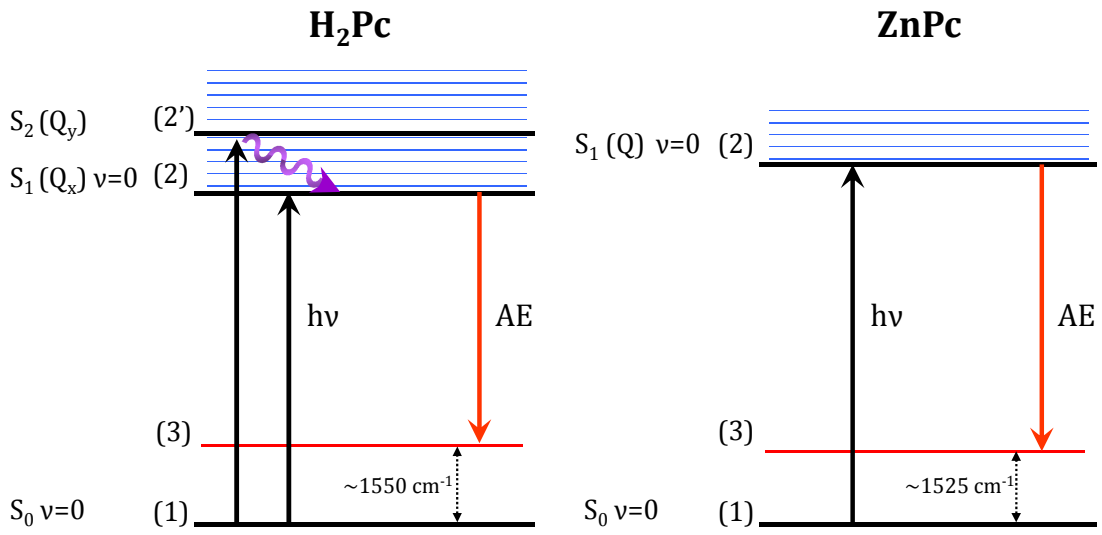

Figure VI.18: A schematic energy level diagram of the states involved in the amplified emission of the phthalocyanines. The effect of AE can be produced with 0-0 excitation (2) or with higher energy excitation (2').

In order to maintain the population inversion during the course of the 10 ns laser pump pulse, the vibrational Level 3 must rapidly relax to vibrational levels of lower energy. Level 2 of H_2Pc has observed lifetimes of 13, 13, 8 and 2.7 ns in N_2, Ar, Kr and Xe solids while ZnPc has lifetimes of 3 ns in N_2, Ar and Kr and 2.7 ns in and Xe, indicating that Level 3 must decay more quickly than this. From DFT calculations on ZnPc, the 1525 cm^{-1} vibrational mode (equivalent to 1550 cm^{-1} mode in H_2Pc) involves out-of-phase stretching of the C–N–C bridges on the inner ring of Pc. Thus it is expected that this mode can relax very quickly towards low frequency modes. Indeed the measured fluorescence bandwidth of a few wavenumbers (cm^{-1}) is consistent with typical vibrational lifetimes in the picosecond range.

As already mentioned, a large population can be very efficiently pumped into the available Levels 2 with pulsed laser excitation of phthalocyanines. These dye materials were examined by Sorokin[3,4] as good candidates to generate stimulated emission around 750 nm. With this characteristic, H_2Pc and ZnPc seem ideal molecules to observe the AE process in low temperature matrices. From Equation VI.1 it is evident that threshold will be reached most easily for strongly allowed transitions (short τ) with narrow linewidths (small $\Delta\nu$) and for high fluorescence quantum yields. All of the parameters in the threshold equation, except the pathlength, are favoured in the case of H_2Pc and ZnPc emission in low temperature

matrices. Especially favourable is the narrow emission linewidth (~8 cm^{-1}) on a fully allowed electronic transition. Arising from these observations, we predict that AE should also be possible for these dye molecules isolated in Shpol'skii matrices when excited with short pulse lasers.

Another key factor in generating amplified emission is the nature of the laser excitation. Thus to achieve the threshold population in the excited state, it is essential that a temporally compact excitation is used such as that provided by the nanosecond pulse of a Q-switched Nd:YAG laser. In this regard, when we used a low intensity laser pulse, only normal fluorescence was observed. Similarly, if a cw laser is used, the threshold condition will not be attained. We surmise that it was for these reasons that AE emission was not observed in any of the previous laser studies of the matrix-isolated phthalocyanines. Thus, Bondybey and English[1] used a low power pulsed nitrogen laser, while in the more recent study of Williamson and co-workers[2], a dye laser pumped by a cw Ar^+ laser was employed. The detailed spectroscopic work that has been done on free-base and metallo-phthalocyanines, by Huang *et al.*[11], also utilised a dye laser pumped by a cw Ar^+ laser. With cw excitation the threshold population will not be reached and only normal fluorescence will be observed. An additional parameter that renders this effect difficult to observe in low temperature matrices is the short path length (l= 250 m) of these thin film samples. In comparison, production of amplified emission in the gas phase[12-14] requires the use of cells whose length are typically tens of centimetres.

The next question that must be addressed in the observations presented in this article is why does only a single mode exhibit amplification? The answer to this question is also to be found in Equation VI.1. Thus for molecular emission involving several vibrational transitions, the threshold will be reached most easily for the mode with the largest Franck–Condon factor in order to optimise ϕ. In other words, it is to be expected that the most intense emission band will reach threshold first. It will be remembered as shown in Figure VI.1, the 0–0 band (around 676 nm) is much stronger than the vibronic band around 755 nm which becomes amplified. However, there is extensive spectral overlap of absorption and emission bands for the 0–0 transition. Hence, this transition will suffer from competitive absorption and accordingly will not reach threshold. Moreover, the threshold in this specific case is much higher than that given by Equation VI.1

because of the large population in the lower level, i.e., the vibrationless ground state.

In the previous studies of phthalocyanine in solution[3,4], isolated in organic solids[11,15] or matrices[1,2] the transition involving the vibrational mode around 1550 cm^{-1} is always either one of the more intense bands or the most intense band in emission spectra. The stimulated emission observed by Sorokin *et al.*[3,4] for AlPc in ethanol was also on this vibronic transition. Other vibrational modes appear in the emission spectrum with intensities similar to the 1550 cm^{-1} mode (Figure VI.1). In fact, some experiments done on quite concentrated H_2Pc samples with high laser intensities have shown that AE is also possible on other vibronic transitions. Thus AE has been observed in N_2 solid, when exciting specific sites involving modes at 687 and 730 cm^{-1} (a related excitation spectrum is shown in Figure VI.6e).

For other systems to demonstrate AE, they must exhibit strongly allowed transitions with short lifetimes and high fluorescence quantum yields in order to meet the threshold conditions described in Equation VI.1.The visible Q band absorption strengths of free-base and zinc porphine are very weakly allowed[16,17] with low fluorescence quantum yields and competitive triplet phosphorescence in inert host solids[17,18]. This means that even though the vibronic structures determined from the Raman spectra may be sufficient to create vibronic bands with high quantum yields compared to the 0-0, the overall fluorescence quantum yield and competitive emission pathway offered by phosphorescence will make AE unlikely. Alternatively, the visible transitions of tetraazaporphyrins and tetrabenzoporphyrins are more fully allowed and would be expected to fulfil the short lifetime and longer wavelength requirements of Equation VI.1.

As with H_2Pc and ZnPc, the AE threshold will be most easily reached for the vibronic mode with the largest Franck-Condon factor in emission. For H_2Pc and ZnPc the intense mode in emission that exhibited AE corresponded to the most intense Raman modes predicted at 1551.26 and 1526.09 cm^{-1} (scaled). Due to the similarities between the in-plane motion of the Raman allowed modes in H_2/ZnPc and those predicted for H_2/ZnTAP and H_2/ZnTBP, a correlation between the Raman intensity and vibronic intensity would be expected. The dominant Raman mode predicted for ZnTAP at 1489.9 cm^{-1} (with scaling) would be expected to exhibit a larger fluorescence quantum yield and reach the threshold criteria more

easily than the other vibronic modes, analogous to ZnPc. Unlike ZnTAP, no single mode is expected to dominate the vibronic structure H_2TAP in emission. AE would therefore be predicted to be more difficult to achieve. However, if the AE population threshold conditions were met for H_2TAP, the similar intensities predicted for the most intense Raman modes may allow AE to occur through multiple vibronic bands at 1504.9, 1301.5 and 1544.3 cm^{-1} from the 0-0 origin.

As has already been noted, the Raman spectra predicted for H_2TBP and ZnTBP show many similarities to those of H_2Pc and ZnPc. It is therefore expected that the vibronic structure of the emission bands will also be similar. The most intense Raman bands calculated at 1607.8 cm^{-1} for H_2TBP and 1616.7 cm^{-1} for ZnTBP (both frequencies scaled by 0.98) are predicted to exhibit AE. This prediction has recently been confirmed by Crépin et al.[19], where the most intense vibronic band of H_2TBP observed at 1620 cm^{-1} from the 0-0 exhibited AE in Ar and N_2 low temperature solids but, like ZnPc, not in Xe. They also presented emission spectra of ZnTBP where the most intense vibronic band was located at 1636 cm^{-1} from the 0-0. Despite the similarities in the fluorescence spectra of H_2TBP and ZnTBP no AE was seen for ZnTBP but competitive phosphorescence was observed below 12,500 cm^{-1}.

VI.4 Conclusions

The luminescence spectroscopy of phthalocyanines embedded in low temperature solids has revealed the phenomenon of amplified emission under modest conditions of pulsed laser excitation. The possibility an iCCD camera provides of very efficiently collecting high resolution 2-D excitation/emission scans has been central to the discovery of this unexpected phenomenon. In addition to the huge increase in intensity, the lineshape of the AE band narrows and its decay time shortens so that it matches the Q-switch laser used for excitation. The photophysical characteristics conducive to this effect are analysed and it is concluded the key conditions are (1) the large absorption strengths of these dye materials, (2) the spectrally narrow emission lines that these molecules exhibit and (3) the use of a Q-switched excitation laser. Accordingly, AE should also be observable for these molecules isolated in other solid materials that produce narrow linewidths such as Shpol'skii matrices.

DFT calculations not only allowed assignment of the vibronic modes of H_2Pc and ZnPc but also allowed predictions of the characteristics of the Raman and emission spectra of other similar molecules and if AE can be observed. H_2TBP has already been shown to exhibit AE and future study of the TAP molecules may be warranted to confirm if AE is possible or will competitive relaxation paths and small quantum yields impede this unusual phenomenon occurring as occurred in the case of ZnTBP. It will also be interesting to see that if AE does occur, will it be through one mode as predicted for ZnTAP and for the fluoridated molecules $H_2TAP\text{-}F_8$ and $ZnTAP\text{-}F_8$ (at 1533.6 and 1505.3 cm^{-1} respectively) or through multiple modes as predicted for H_2TAP. If the fluoridated molecules can be synthesised, the addition of the highly electronegative fluorine atoms may detrimentally affect the absorption and fluorescent properties of the molecules but the results presented for $H_2TAP\text{-}F_8$ and $ZnTAP\text{-}F_8$ may act as a model for other tetraazaporphyrins with heavy atoms or groups attached to the β carbons.

Excitation scans recorded for the AE mode yield greatly enhanced site selectivity compared to what is obtained in normal fluorescence excitation scans. This behaviour stems from the increased resolution of individual sites whose lineshape change from featureless fluorescence excitation bands to a highly structured AE excitation band. The very well-resolved spectra available in AE excitation scans allows detailed exploration of site occupancies in a given solid and from one solid to another. Differences in matrix sites have been observed and analysed by Waluk and co-workers[20] in the case of porphyrins and porphycenes which are very similar molecules. The observations of AE, made in the present study with only moderate laser excitation intensities, should allow new insights into site effects and site selectivity in future studies of solid state spectroscopy.

VI.5 References

(1) Bondybey, V. E.; English, J. H. *Journal of the American Chemical Society* **1979**, *101*, 3446.
(2) Prince, B. J.; Williamson, B. E.; Reeves, R. J. *Journal of Luminescence* **2001**, *93*, 293.
(3) Sorokin, P. P.; Lankard, J. R. *IBM Journal of Research and Development* **1966**, *10*, 162.
(4) Sorokin, P. P.; Lankard, J. R.; Hammond, E. C.; Moruzzi, V. L. *IBM Journal of Research and Development* **1967**, *11*, 130.
(5) Dozova, N.; Murray, C.; McCaffrey, J. G.; Shafizadeh, N.; Crepin, C. *Physical Chemistry Chemical Physics* **2008**, *10*, 2167.
(6) Plows, F. L.; Jones, A. C. *Journal of Molecular Spectroscopy* **1999**, *194*, 163.
(7) Deperasinska, I.; Kozankiewicz, B.; Biktchantaev, I.; Sepiol, J. *Journal of Physical Chemistry A* **2001**, *105*, 810.
(8) Allen, L.; Peters, G. I. *Physical Review A* **1973**, *8*, 2031.
(9) Rigolio, M.; Castiglioni, C.; Zerbi, G.; Negri, F. *Journal of Molecular Structure* **2001**, *563-564*, 79.
(10) Du, H.; Fuh, R. C. A.; Li, J. Z.; Corkan, L. A.; Lindsey, J. S. *Photochemistry and Photobiology* **1998**, *68*, 141.
(11) Huang, T. H.; Rieckhoff, K. E.; Voigt, E. M. *Journal of Chemical Physics* **1982**, *77*, 3424.
(12) Alekseev, V. A. *Optics and Spectroscopy* **2002**, *93*, 334.
(13) Alekseev, V. A.; Ridley, T.; Lawley, K. P.; Donovan, R. J. *Chemical Physics Letters* **2007**, *443*, 34.
(14) Glessner, J. W.; Davis, S. J. *Journal of Applied Physics* **1993**, *73*, 2672.
(15) Hala, J.; Pelant, I.; Parma, L.; Vacek, K. *Czechoslovak Journal of Physics* **1982**, *32*, 705.
(16) Edwards, L.; Dolphin, D. H.; Gouterman, M.; Adler, A. D. *Journal of Molecular Spectroscopy* **1971**, *38*, 16.
(17) Starukhin, A.; Shulga, A.; Waluk, J. *Chemical Physics Letters* **1997**, *272*, 405.
(18) Radziszewski, J. G.; Waluk, J.; Nepras, M.; Michl, J. *Journal of Physical Chemistry* **1991**, *95*, 1963.
(19) Crépin, C.; Shafizadeh, N.; Chin, W.; Galaup, J. P.; McCaffrey, J. G.; Arabei, S. M. *Low Temperature Physics* **2010**, *36*, 451.
(20) Kyrychenko, A.; Waluk, J. *Journal of Chemical Physics* **2005**, *123*.

Appendix VI.A: DFT vibrational frequencies of free-base and zinc porphyrins

VI.A.1 Introduction

In this appendix the vibrational frequencies, infra-red absorption and Raman scattering intensities of free-base and zinc porphyrin (H_2P and ZnP), tetraazaporphyrin (H_2TAP and ZnTAP) and tetrabenzoporphyrin (H_2TBP and ZnTBP) calculated using DFT will be presented. All optimized geometries were found to be planar with the H_2 molecules having D_{2h} symmetry and the Zn molecules having D_{4h} symmetry. By convention the D_{2h} symmetry labels of the normal modes the free-base molecules produced by the Gaussian-03 computational software package have the primary z-axis aligned along the axis containing the most atoms, that is the axis containing the N-H bonds in the molecular plane. In contrast, it has the z-axis aligned with the highest order axis (C_4 axis), perpendicular to the plane of the molecule for the D_{4h} symmetry of ZnPc. For ease of comparison of the vibrational modes of the free-base and metallo molecules it is advantageous to re-orient the z-axis of the D_{2h} molecules perpendicular to the molecule plane. This has the effect of interchanging the 1 and 3 subscript labels of the Mulliken symmetry symbols.

Parts VI.A.2, VI.A.3 and VI.A.4 contain tables of the infra-red vibrational frequencies and intensities and Raman active vibrational frequencies and intensities. The IR active B_{2u} and B_{1u} symmetry modes of the D_{2h} molecules correlate to the degenerate E_u modes of the D_{4h} molecules. The IR active B_{3u} modes of the D_{2h} molecules however correlated with the IR active D_{4h} A_{2u} modes and optically silent B_{2u} modes. The A_g modes of the D_{2h} molecules correlate with the A_{1g} and B_{1g} modes of the D_{4h} molecules. The B_{3g} and B_{2g} symmetry modes the D_{2h} molecules correlate with the degenerate E_g modes of the D_{4h} molecules. The Raman active B_{1g} modes of the D_{2h} molecules correlate with the Raman active B_{2g} and optically silent A_{2g} modes of the D_{4h} molecules.

In order to compensate for the approximations made when calculated the vibrational frequencies, in particular the lack of anharmonicity, scaling factors have been applied to the calculated vibrational frequencies. For frequencies below 1800 cm^{-1}, a scaling factor of 0.98 was found to give a good match with experiment while factor of 0.96 for C-H stretches and 0.931 for N-H stretches were found to be suitable for these higher energy, more anharmonic modes. Part VI.A.2 presents the IR (Table IV.A.1) and Raman (Table IV.A.2) results for H_2P and ZnP. All the optically active modes for these two molecules have been correlated by comparison of the displacement vector diagrams of the vibrations. Part VI.A.3 presents the IR (Table VI.A.3) and Raman (Table VI.A.4) results for H_2TAP and ZnTAP while Part VI.A.4 presents the IR (Table VI.A.5) and Raman (Table VI.A.6) results for H_2TBP and ZnTBP. Like H_2P and ZnP, the optically active modes for the free-base form of these molecules have been correlated with those of the metallo form. All vibrational frequencies presented were determined using the B3LYP DFT hybrid functional with the 6-311++G(2d,2p) basis set using the geometries optimized using tight convergence criteria and determined using the same level of theory.

VI.A.2 H_2P and ZnP DFT vibrational frequencies

Table IV.A.1: DFT B3LYP/6-311++G(2d,2p) computed Infra-red frequencies (ν, cm^{-1}) and intensities (km/mole) for H_2P and ZnP. The scaled calculated frequencies (ν_{scaled}, cm^{-1}) are also given using the factors described in the introduction to this appendix.

	H_2P				**ZnP**			
	ν	ν_{scaled}	IR Int	Sym	ν	ν_{scaled}	IR Int	Sym
1	318.23	311.86	2.59	B_{3u}	358.83	351.65	7.15	E_u
2	357.54	350.39	8.91	B_{3u}	390.25	382.44	10.02	E_u
3	737.62	722.87	33.57	B_{3u}	753.06	738.00	27.91	E_u
4	798.64	782.66	2.09	B_{3u}	811.93	795.69	5.63	E_u
5	988.76	968.98	55.49	B_{3u}	1011.26	991.04	105.12	E_u
6	1016.57	996.24	0.26	B_{3u}	1036.96	1016.22	0.49	E_u
7	1070.16	1048.76	41.03	B_{3u}	1077.66	1056.10	58.13	E_u
8	1160.42	1137.21	26.01	B_{3u}	1174.32	1150.84	8.73	E_u
9	1218.15	1193.78	1.74	B_{3u}	1265.50	1240.19	0.13	E_u
10	1312.83	1286.57	1.16	B_{3u}	1323.01	1296.55	11.64	E_u
11	1427.03	1398.49	32.59	B_{3u}	1412.86	1384.60	10.37	E_u
12	1433.08	1404.42	6.74	B_{3u}	1462.47	1433.22	3.88	E_u
13	1537.00	1506.26	0.00	B_{3u}	1548.44	1517.47	14.55	E_u
14	1552.74	1521.68	9.40	B_{3u}	1578.55	1546.98	12.76	E_u
15	3188.21	3060.68	7.63	B_{3u}	3186.22	3058.77	8.77	E_u
16	3217.70	3089.00	5.57	B_{3u}	3223.36	3094.43	3.80	E_u
17	3252.37	3122.28	7.34	B_{3u}	3242.12	3112.43	19.34	E_u
18	3552.33	3027.96	79.78	B_{3u}	226.29	221.76	0.96	E_u
1	293.57	287.70	0.19	B_{2u}	358.83	351.65	7.15	E_u
2	357.89	350.74	11.62	B_{2u}	390.25	382.44	10.02	E_u
3	757.61	742.46	31.56	B_{2u}	753.06	738.00	27.91	E_u
4	796.36	780.43	0.09	B_{2u}	811.93	795.69	5.63	E_u
5	967.16	947.82	95.02	B_{2u}	1011.26	991.04	105.12	E_u
6	1003.52	983.45	6.75	B_{2u}	1036.96	1016.22	0.49	E_u
7	1077.45	1055.90	39.96	B_{2u}	1077.66	1056.10	58.13	E_u
8	1179.32	1155.73	0.01	B_{2u}	1174.32	1150.84	8.73	E_u
9	1260.59	1235.38	52.74	B_{2u}	226.29	221.76	0.96	E_u
10	1274.48	1248.99	2.09	B_{2u}	1265.50	1240.19	0.13	E_u
11	1377.86	1350.30	2.96	B_{2u}	1323.01	1296.55	11.64	E_u
12	1435.09	1406.39	16.91	B_{2u}	1412.86	1384.60	10.37	E_u
13	1522.05	1491.61	3.52	B_{2u}	1462.47	1433.22	3.88	E_u
14	1571.16	1539.74	32.77	B_{2u}	1548.44	1517.47	14.55	E_u
15	1623.24	1590.77	25.96	B_{2u}	1578.55	1546.98	12.76	E_u
16	3188.20	3060.67	5.78	B_{2u}	3186.22	3058.77	8.77	E_u

17	3235.61	3106.19	1.22	B_{2u}	3223.36	3094.43	3.80	E_u
18	3238.00	3108.48	27.74	B_{2u}	3242.12	3112.43	19.34	E_u
1	55.62	54.50	0.00	B_{1u}	56.97	55.83	0.00	B_{2u}
2	92.76	90.90	9.75	B_{1u}	74.22	72.74	2.09	A_{2u}
3	207.83	203.68	1.89	B_{1u}	208.72	204.55	0.00	B_{2u}
4	336.16	329.44	5.66	B_{1u}	349.31	342.33	8.68	A_{2u}
5	651.38	638.35	0.08	B_{1u}	678.56	664.99	0.00	B_{2u}
6	709.52	695.33	57.21	B_{1u}	721.12	706.69	69.19	A_{2u}
7	739.89	725.09	6.60	B_{1u}	190.92	187.11	23.48	A_{2u}
8	788.37	772.60	112.23	B_{1u}	776.84	761.30	51.04	A_{2u}
9	794.53	778.64	25.45	B_{1u}	798.02	782.06	0.00	B_{2u}
10	880.12	862.52	142.60	B_{1u}	887.82	870.06	131.00	A_{2u}

Table IV.A.2: DFT B3LYP / 6-311++G(2d,2p) computed Raman frequencies (ν, cm^{-1}) and scattering activities ($Å^4$/amu) for H_2P and ZnP. The scaled calculated frequencies (ν_{scaled}, cm^{-1}) are also given using the factors described in the introduction to this appendix.

	H_2P				ZnP			
	ν	ν_{scaled}	Act	Sym	ν	ν_{scaled}	Act	Sym
1	155.90	152.78	31.13	A_g	180.15	176.54	27.68	B_{1g}
2	309.60	303.41	92.84	A_g	367.97	360.61	115.15	A_{1g}
3	732.79	718.14	25.43	A_g	736.73	721.99	27.41	A_{1g}
4	739.31	724.53	14.97	A_g	749.48	734.49	10.93	B_{1g}
5	971.20	951.77	90.12	A_g	1017.02	996.68	125.32	A_{1g}
6	1006.87	986.73	62.49	A_g	1018.50	998.13	1.86	B_{1g}
7	1080.73	1059.12	12.30	A_g	1081.86	1060.23	15.40	B_{1g}
8	1087.22	1065.48	19.05	A_g	1086.67	1064.94	11.40	A_{1g}
9	1199.47	1175.48	43.39	A_g	1197.37	1173.43	51.85	B_{1g}
10	1376.75	1349.21	39.32	A_g	1383.04	1355.38	22.38	A_{1g}
11	1425.42	1396.91	256.28	A_g	1406.14	1378.01	209.93	B_{1g}
12	1457.03	1427.89	118.44	A_g	1459.94	1430.74	125.64	A_{1g}
13	1530.15	1499.55	331.45	A_g	1526.53	1495.99	469.58	B_{1g}
14	1583.67	1551.99	347.35	A_g	1579.54	1547.95	337.48	A_{1g}
15	1634.71	1602.01	199.54	A_g	1638.02	1605.26	217.44	B_{1g}
16	3188.35	3124.59	311.49	A_g	3186.36	3122.63	301.17	A_{1g}
17	3238.05	3108.53	656.34	A_g	3241.97	3112.29	290.88	B_{1g}
18	3252.39	3122.30	609.16	A_g	3242.36	3112.67	1018.40	A_{1g}
19	3593.46	3027.98	2.27	A_g				
1	131.65	129.02	0.05	B_{3g}	145.91	142.99	0.06	E_g
2	205.64	201.53	2.32	B_{3g}	210.09	205.89	2.32	E_g
3	447.43	438.48	0.13	B_{3g}	446.49	437.56	0.05	E_g
4	676.89	663.35	1.21	B_{3g}	683.46	669.79	1.29	E_g

5	712.47	698.22	1.27	B_{3g}	718.54	704.17	1.04	E_g
6	784.70	769.01	0.37	B_{3g}	787.96	772.20	0.00	E_g
7	870.59	853.18	1.27	B_{3g}	878.37	860.80	1.02	E_g
8	917.40	899.05	0.91	B_{3g}	919.80	901.41	1.20	E_g
1	124.48	121.99	0.31	B_{2g}	145.91	142.99	0.06	E_g
2	185.94	182.22	1.94	B_{2g}	210.09	205.89	2.32	E_g
3	432.78	424.12	0.14	B_{2g}	446.49	437.56	0.05	E_g
4	631.22	618.60	0.64	B_{2g}				
5	679.19	665.60	1.22	B_{2g}	683.46	669.79	1.29	E_g
6	708.36	694.20	0.17	B_{2g}	718.54	704.17	1.04	E_g
7	783.58	767.91	0.06	B_{2g}	787.96	772.20	0.00	E_g
8	872.73	855.27	1.34	B_{2g}	878.37	860.80	1.02	E_g
9	916.20	897.88	1.48	B_{2g}	919.80	901.41	1.20	E_g
1	103.42	101.36	18.50	B_{1g}	218.86	214.48	20.09	B_{2g}
2	397.91	389.95	0.07	B_{1g}	418.59	410.22	0.00	A_{2g}
3	419.11	410.73	0.41	B_{1g}	422.00	413.56	0.46	B_{2g}
4	800.34	784.33	0.01	B_{1g}	811.11	794.88	0.00	A_{2g}
5	823.27	806.81	1.73	B_{1g}	838.92	822.15	0.03	B_{2g}
6	992.92	973.06	3.18	B_{1g}	1019.18	998.80	0.00	A_{2g}
7	1023.96	1003.48	7.05	B_{1g}	1069.62	1048.22	10.72	B_{2g}
8	1158.29	1135.13	0.12	B_{1g}	1170.46	1147.05	0.00	A_{2g}
9	1213.11	1188.85	0.76	B_{1g}	1206.25	1182.12	0.12	B_{2g}
10	1264.10	1238.81	5.19	B_{1g}				
11	1338.64	1311.86	81.63	B_{1g}	1342.71	1315.86	0.00	A_{2g}
12	1386.10	1358.38	18.91	B_{1g}	1383.13	1355.47	0.00	A_{2g}
13	1403.78	1375.71	37.56	B_{1g}	1372.09	1344.64	131.45	B_{2g}
14	1522.16	1491.71	20.25	B_{1g}	1497.75	1467.79	9.26	B_{2g}
15	1618.18	1585.82	0.11	B_{1g}	1591.05	1559.23	0.00	A_{2g}
16	3188.22	3060.69	210.95	B_{1g}	3186.23	3058.78	214.61	B_{2g}
17	3217.69	3088.98	258.55	B_{1g}	3223.16	3094.23	0.00	A_{2g}
18	3235.63	2995.67	232.33	B_{1g}	3223.54	3000.76	500.22	B_{2g}

VI.A.3 H_2TAP and ZnTAP DFT vibrational frequencies

Table VI.A.3: DFT B3LYP / 6-311++G(2d,2p) computed Infra-red frequencies (ν, cm^{-1}) and intensities (km/mole) for H_2TAP and ZnTAP. The scaled calculated frequencies (ν_{scaled}, cm^{-1}) are also given using the factors described in the introduction to this appendix

	H_2TAP				ZnTAP			
	ν	ν_{scaled}	Int	Sym	ν	ν_{scaled}	Int	Sym
1	369.14	361.76	26.90	B_{3u}	388.18	380.42	33.14	E_u
2	376.00	368.48	8.30	B_{3u}	435.28	426.57	0.69	E_u
3	727.65	713.10	94.57	B_{3u}	742.54	727.69	39.78	E_u
4	775.83	760.31	13.28	B_{3u}	795.01	779.11	7.22	E_u
5	950.94	931.92	232.49	B_{3u}	995.30	975.40	204.21	E_u
6	1002.45	982.41	0.57	B_{3u}	1027.69	1007.14	4.55	E_u
7	1063.06	1041.79	71.00	B_{3u}	1070.28	1048.87	80.44	E_u
8	1139.55	1116.76	4.88	B_{3u}	1193.97	1170.09	0.44	E_u
9	1254.82	1229.72	33.23	B_{3u}	1273.63	1248.16	11.51	E_u
10	1356.87	1329.73	1.40	B_{3u}	1353.59	1326.51	10.74	E_u
11	1442.76	1413.91	3.55	B_{3u}	1449.69	1420.70	0.04	E_u
12	1510.34	1480.13	39.85	B_{3u}	1490.55	1460.74	34.32	E_u
13	1542.38	1511.54	83.83	B_{3u}	1551.27	1520.25	90.56	E_u
14	3240.45	3110.83	0.23	B_{3u}	3241.77	3112.10	0.16	E_u
15	3267.65	3136.94	0.03	B_{3u}	3259.57	3129.19	3.78	E_u
16	3565.39	3319.37	111.63	B_{3u}	252.27	247.22	0.23	E_u
1	343.36	336.49	5.88	B_{2u}	388.18	380.42	33.14	E_u
2	377.44	369.89	7.35	B_{2u}	435.28	426.57	0.69	E_u
3	748.85	733.87	50.48	B_{2u}	742.54	727.69	39.78	E_u
4	776.51	760.98	0.09	B_{2u}	795.01	779.11	7.22	E_u
5	957.24	938.09	124.64	B_{2u}	995.30	975.40	204.21	E_u
6	970.33	950.92	39.56	B_{2u}	1027.69	1007.14	4.55	E_u
7	1069.60	1048.21	38.86	B_{2u}	1070.28	1048.87	80.44	E_u
8	1198.73	1174.76	19.22	B_{2u}	1193.97	1170.09	0.44	E_u
9	1266.18	1240.86	28.14	B_{2u}	252.27	247.22	0.23	E_u
10	1313.93	1287.65	2.89	B_{2u}	1273.63	1248.16	11.51	E_u
11	1367.02	1339.68	3.29	B_{2u}	1353.59	1326.51	10.74	E_u
12	1517.65	1487.29	7.89	B_{2u}	1490.55	1460.74	34.32	E_u
13	1543.66	1512.79	10.31	B_{2u}	1449.69	1420.70	0.04	E_u
14	1596.03	1564.11	114.20	B_{2u}	1551.27	1520.25	90.56	E_u
15	3251.54	3121.48	0.00	B_{2u}	3241.77	3112.10	0.16	E_u
16	3260.14	3129.74	5.29	B_{2u}	3259.57	3129.19	3.78	E_u
1	54.23	53.15	0.02	B_{1u}	62.40	61.15	0.00	B_{2u}
2	89.27	87.49	3.19	B_{1u}	52.04	50.99	0.17	A_{2u}

3	196.51	192.58	3.17	B_{1u}	178.51	174.94	0.00	B_{2u}
4	349.79	342.80	7.51	B_{1u}	365.30	357.99	7.44	A_{2u}
5	656.65	643.52	1.26	B_{1u}	679.35	665.76	0.00	B_{2u}
6	722.50	708.05	33.10	B_{1u}	732.03	717.39	44.08	A_{2u}
7	760.83	745.61	18.63	B_{1u}	171.43	168.00	17.73	A_{2u}
8	820.78	804.36	0.08	B_{1u}	822.82	806.36	0.00	B_{2u}
9	832.20	815.56	248.11	B_{1u}	826.10	809.58	169.61	A_{2u}

Table VI.A.4: DFT B3LYP / 6-311++G(2d,2p) computed Raman frequencies (ν, cm^{-1}) and scattering activities ($Å^4$/amu) for H_2TAP and ZnTAP. The scaled calculated frequencies (ν_{scaled}, cm^{-1}) are also given using the factors described in the introduction to this appendix.

	H_2TAP				ZnTAP			
	ν	ν_{scaled}	Act	Sym	ν	ν_{scaled}	Act	Sym
1	181.26	177.63	33.04	A_g	226.17	221.65	24.22	B_{1g}
2	337.65	330.90	83.27	A_g	400.31	392.31	110.01	A_{1g}
3	704.23	690.15	14.82	A_g	701.09	687.07	10.92	A_{1g}
4	744.26	729.37	90.68	A_g	760.99	745.77	99.15	B_{1g}
5	970.35	950.95	112.47	A_g	1024.45	1003.96	137.80	A_{1g}
6	1002.01	981.97	130.30	A_g	1012.59	992.34	127.24	B_{1g}
7	1074.19	1052.71	5.57	A_g	1081.96	1060.32	0.14	A_{1g}
8	1079.00	1057.42	69.65	A_g	1077.06	1055.52	99.29	B_{1g}
9	1328.06	1301.50	990.00	A_g	1319.68	1293.28	928.67	B_{1g}
10	1421.44	1393.01	66.46	A_g	1423.14	1394.68	37.29	A_{1g}
11	1473.69	1444.21	150.21	A_g	1455.76	1426.64	108.32	A_{1g}
12	1535.62	1504.91	1478.59	A_g	1520.22	1489.81	2305.02	B_{1g}
13	1575.80	1544.29	942.52	A_g	1565.60	1534.28	212.44	A_{1g}
14	1595.96	1564.04	247.34	A_g	1564.32	1533.03	370.10	B_{1g}
15	3260.16	3129.76	617.55	A_g	3259.49	3129.11	294.39	B_{1g}
16	3267.65	3136.94	625.71	A_g	3259.69	3129.30	1033.47	A_{1g}
17	3629.13	3483.97	5.82	A_g				
1	122.16	119.72	0.81	B_{1g}	119.89	117.49	1.22	E_g
2	218.93	214.55	0.45	B_{1g}	219.72	215.32	0.27	E_g
3	464.22	454.94	0.49	B_{1g}	461.22	452.00	0.73	E_g
4	687.71	673.96	2.31	B_{1g}	693.20	679.33	2.76	E_g
5	740.80	725.98	1.82	B_{1g}	752.20	737.16	1.47	E_g
6	824.25	807.76	1.33	B_{1g}	823.60	807.13	0.49	E_g
7	939.85	921.05	0.01	B_{1g}	940.60	921.79	0.11	E_g
1	102.16	100.11	1.12	B_{2g}	119.89	117.49	1.22	E_g
2	194.26	190.37	0.13	B_{2g}	219.72	215.32	0.27	E_g
3	439.58	430.79	0.62	B_{2g}	461.22	452.00	0.73	E_g
4	641.40	628.58	1.56	B_{2g}				

5	689.42	675.63	2.44	B_{2g}	693.20	679.33	2.76	E_g
6	755.09	739.99	1.17	B_{2g}	752.20	737.16	1.47	E_g
7	823.17	806.71	0.13	B_{2g}	823.60	807.13	0.49	E_g
8	940.53	921.72	0.26	B_{2g}	940.60	921.79	0.11	E_g
1	138.79	136.01	10.55	B_{3g}	225.87	221.35	14.14	B_{2g}
2	439.15	430.37	7.29	B_{3g}	436.09	427.37	6.12	B_{2g}
3	453.35	444.28	0.00	B_{3g}	475.38	465.87	0.00	A_{2g}
4	778.95	763.37	1.20	B_{3g}	795.13	779.23	0.00	A_{2g}
5	806.65	790.52	4.40	B_{3g}	817.21	800.86	14.02	B_{2g}
6	950.62	931.60	16.71	B_{3g}	1007.03	986.89	0.00	A_{2g}
7	1014.76	994.47	12.81	B_{3g}	1056.36	1035.24	17.18	B_{2g}
8	1164.36	1141.07	2.86	B_{3g}				
9	1216.82	1192.48	14.47	B_{3g}	1201.48	1177.45	12.46	B_{2g}
10	1250.89	1225.87	0.12	B_{3g}	1220.75	1196.34	0.00	A_{2g}
11	1334.27	1307.59	0.14	B_{3g}	1328.62	1302.05	1.54	B_{2g}
12	1364.27	1336.99	0.50	B_{3g}	1342.33	1315.48	0.00	A_{2g}
13	1468.73	1439.36	12.15	B_{3g}	1478.16	1448.59	0.00	A_{2g}
14	1565.33	1534.02	7.99	B_{3g}	1475.86	1446.34	28.14	B_{2g}
15	3240.44	3110.82	240.63	B_{3g}	3241.64	3111.97	0.00	A_{2g}
16	3251.54	3121.48	258.76	B_{3g}	3241.86	3112.18	509.61	B_{2g}

VI.A.4 H_2TBP and ZnTBP DFT vibrational frequencies

Table VI.A.5: DFT B3LYP / 6-311++G(2d,2p) computed Infra-red frequencies (ν, cm^{-1}) and intensities (km/mole) for H_2TBP and ZnTBP. The scaled calculated frequencies (ν_{scaled}, cm^{-1}) are also given using the factors described in the introduction to this appendix.

	H_2TBP				ZnTBP			
	N	ν_{scaled}	Int	Sym	ν	ν_{scaled}	Int	Sym
1	123.51	121.04	1.58	B_{3u}	122.00	119.56	0.98	E_u
2	263.26	258.00	1.35	B_{3u}	287.78	282.02	0.16	E_u
3	491.44	481.61	2.43	B_{3u}	505.34	495.24	3.15	E_u
4	560.10	548.89	0.28	B_{3u}	577.22	565.67	0.85	E_u
5	628.29	615.72	24.90	B_{3u}	640.18	627.38	18.36	E_u
6	740.51	725.69	73.87	B_{3u}	755.01	739.91	87.66	E_u
7	798.31	782.35	13.65	B_{3u}	809.11	792.93	1.84	E_u
8	896.13	878.21	16.07	B_{3u}	910.78	892.56	31.33	E_u
9	1036.06	1015.34	36.16	B_{3u}	1037.52	1016.77	33.94	E_u
10	1066.99	1045.65	116.79	B_{3u}	1079.37	1057.79	82.78	E_u
11	1107.46	1085.31	64.05	B_{3u}	1134.04	1111.36	103.68	E_u
12	1137.61	1114.85	42.08	B_{3u}	1143.99	1121.11	71.01	E_u
13	1184.70	1161.01	15.13	B_{3u}	1186.17	1162.44	0.08	E_u
14	1197.63	1173.68	26.48	B_{3u}	1220.41	1196.00	29.04	E_u
15	1253.07	1228.01	56.45	B_{3u}	1266.22	1240.89	71.06	E_u
16	1319.73	1293.34	4.54	B_{3u}	1329.53	1302.94	32.11	E_u
17	1358.69	1331.52	8.98	B_{3u}	1359.07	1331.89	39.07	E_u
18	1406.73	1378.60	2.80	B_{3u}	1407.06	1378.92	0.88	E_u
19	1447.87	1418.91	52.95	B_{3u}	1450.22	1421.22	57.48	E_u
20	1500.15	1470.14	7.25	B_{3u}	1505.39	1475.28	4.11	E_u
21	1510.21	1480.00	54.07	B_{3u}	1519.97	1489.57	57.46	E_u
22	1558.73	1527.56	13.52	B_{3u}	1581.81	1550.18	25.05	E_u
23	1602.95	1570.89	0.81	B_{3u}	1610.31	1578.11	2.92	E_u
24	1636.56	1603.83	5.19	B_{3u}	1640.36	1607.55	5.59	E_u
25	3167.02	3040.34	0.79	B_{3u}	3169.36	3042.59	0.02	E_u
26	3180.65	3053.43	2.90	B_{3u}	3176.43	3049.37	2.79	E_u
27	3183.19	3055.86	32.66	B_{3u}	3185.76	3058.33	24.82	E_u
28	3190.89	3063.26	6.53	B_{3u}	3191.29	3063.64	7.35	E_u
29	3199.18	3071.21	64.38	B_{3u}	3196.42	3068.56	80.01	E_u
30	3546.66	3301.94	100.63	B_{3u}	220.88	216.46	6.17	E_u
1	122.60	120.15	1.15	B_{2u}	122.00	119.56	0.98	E_u
2	252.74	247.68	1.32	B_{2u}	287.78	282.02	0.16	E_u
3	490.27	480.46	0.05	B_{2u}	505.34	495.24	3.15	E_u
4	555.44	544.33	1.62	B_{2u}	577.22	565.67	0.85	E_u

5	627.24	614.70	13.52	B_{2u}	640.18	627.38	18.36	E_u
6	743.34	728.47	83.59	B_{2u}	755.01	739.91	87.66	E_u
7	805.49	789.38	6.59	B_{2u}	809.11	792.93	1.84	E_u
8	875.37	857.87	1.64	B_{2u}	910.78	892.56	31.33	E_u
9	1038.52	1017.75	30.36	B_{2u}	1037.52	1016.77	33.94	E_u
10	1067.70	1046.35	5.54	B_{2u}	1079.37	1057.79	82.78	E_u
11	1117.54	1095.19	239.00	B_{2u}	1134.04	1111.36	103.68	E_u
12	1145.28	1122.37	9.00	B_{2u}	1143.99	1121.11	71.01	E_u
13	1181.27	1157.64	2.34	B_{2u}	1186.17	1162.44	0.08	E_u
14	1231.67	1207.04	31.03	B_{2u}	1220.41	1196.00	29.04	E_u
15	1262.91	1237.66	78.67	B_{2u}	1266.22	1240.89	71.06	E_u
16	1295.17	1269.27	9.67	B_{2u}	220.88	216.46	6.17	E_u
17	1346.22	1319.29	39.55	B_{2u}	1329.53	1302.94	32.11	E_u
18	1357.78	1330.63	73.55	B_{2u}	1359.07	1331.89	39.07	E_u
19	1438.66	1409.88	21.58	B_{2u}	1407.06	1378.92	0.88	E_u
20	1478.22	1448.65	90.31	B_{2u}	1450.22	1421.22	57.48	E_u
21	1513.53	1483.26	0.01	B_{2u}	1505.39	1475.28	4.11	E_u
22	1553.03	1521.97	39.33	B_{2u}	1519.97	1489.57	57.46	E_u
23	1609.86	1577.67	10.00	B_{2u}	1581.81	1550.18	25.05	E_u
24	1619.63	1587.24	0.92	B_{2u}	1610.31	1578.11	2.92	E_u
25	1647.71	1614.75	9.36	B_{2u}	1640.36	1607.55	5.59	E_u
26	3172.86	3045.94	0.45	B_{2u}	3169.36	3042.59	0.02	E_u
27	3173.27	3046.34	2.08	B_{2u}	3176.43	3049.37	2.79	E_u
28	3188.81	3061.26	7.97	B_{2u}	3185.76	3058.33	24.82	E_u
29	3191.82	3064.15	13.12	B_{2u}	3191.29	3063.64	7.35	E_u
30	3194.85	3067.06	91.12	B_{2u}	3196.42	3068.56	80.01	E_u
1	19.94	19.54	0.00	B_{1u}	20.21	19.81	0.00	B_{2u}
2	39.20	38.41	1.66	B_{1u}	37.54	36.79	0.90	A_{2u}
3	131.87	129.24	0.29	B_{1u}	128.14	125.58	0.00	B_{2u}
4	218.60	214.22	0.48	B_{1u}	260.67	255.45	1.58	A_{2u}
5	267.59	262.23	0.79	B_{1u}	277.01	271.47	0.00	B_{2u}
6	319.60	313.21	5.79	B_{1u}	328.73	322.15	6.97	A_{2u}
7	432.24	423.59	0.15	B_{1u}	436.14	427.41	0.00	B_{2u}
8	442.76	433.90	21.24	B_{1u}	443.74	434.87	18.28	A_{2u}
9	684.58	670.88	3.97	B_{1u}	704.04	689.96	0.00	B_{2u}
10	713.22	698.96	28.14	B_{1u}	723.37	708.91	96.42	A_{2u}
11	766.77	751.43	303.21	B_{1u}	774.80	759.30	166.14	A_{2u}
12	770.33	754.92	0.34	B_{1u}	775.19	759.68	0.00	B_{2u}
13	786.72	770.99	2.39	B_{1u}	136.96	134.22	6.49	A_{2u}
14	862.28	845.04	37.00	B_{1u}	871.02	853.60	41.21	A_{2u}
15	958.81	939.64	1.28	B_{1u}	962.10	942.86	0.00	B_{2u}

16	965.54	946.23	1.19	B_{1u}	962.81	943.55	2.22	A_{2u}

Table VI.A.6: DFT B3LYP / 6-311++G(2d,2p) computed Raman frequencies (ν, cm^{-1}) and scattering activities ($Å^4$/amu) for H_2TBP and ZnTBP. The scaled calculated frequencies (ν_{scaled}, cm^{-1}) are also given using the factors described in the introduction to this appendix.

	H_2TBP				ZnTBP			
	N	ν_{scaled}	Act	Sym	ν	ν_{scaled}	Act	Sym
1	118.41	116.04	38.29	A_g	129.75	127.15	31.68	B_{1g}
2	216.24	211.91	80.47	A_g	244.88	239.98	85.95	A_{1g}
3	549.60	538.61	27.89	A_g	557.76	546.61	11.94	B_{1g}
4	574.36	562.88	12.46	A_g	595.74	583.82	34.17	A_{1g}
5	708.62	694.45	135.04	A_g	710.60	696.39	115.97	A_{1g}
6	737.78	723.03	392.03	A_g	754.06	738.98	419.91	B_{1g}
7	776.68	761.15	28.86	A_g	779.60	764.01	1.63	B_{1g}
8	815.19	798.89	292.15	A_g	844.62	827.73	287.67	A_{1g}
9	1036.30	1015.57	271.01	A_g	1037.16	1016.42	231.06	B_{1g}
10	1039.07	1018.29	414.65	A_g	1038.26	1017.49	431.36	A_{1g}
11	1124.16	1101.68	367.16	A_g	1138.14	1115.38	401.02	A_{1g}
12	1132.54	1109.89	208.56	A_g	1134.06	1111.38	154.56	B_{1g}
13	1181.42	1157.79	365.05	A_g	1179.99	1156.39	464.49	B_{1g}
14	1187.89	1164.13	173.86	A_g	1187.69	1163.94	77.49	A_{1g}
15	1258.46	1233.29	4239.71	A_g	1260.42	1235.21	3975.63	B_{1g}
16	1355.35	1328.24	2106.49	A_g	1359.22	1332.04	2666.04	A_{1g}
17	1361.55	1334.31	742.96	A_g	1362.82	1335.56	13.52	B_{1g}
18	1396.37	1368.44	580.03	A_g	1396.98	1369.04	586.44	A_{1g}
19	1432.73	1404.07	399.15	A_g	1414.59	1386.29	135.23	B_{1g}
20	1459.28	1430.10	96.94	A_g	1460.47	1431.26	89.15	A_{1g}
21	1484.36	1454.67	485.53	A_g	1485.30	1455.59	488.83	B_{1g}
22	1546.25	1515.33	120.58	A_g	1549.42	1518.44	129.50	A_{1g}
23	1599.59	1567.60	2197.67	A_g	1603.71	1571.63	2571.81	B_{1g}
24	1614.18	1581.90	1064.37	A_g	1610.93	1578.71	479.75	A_{1g}
25	1640.64	1607.83	7234.25	A_g	1649.69	1616.69	6879.05	B_{1g}
26	3173.28	3046.34	128.02	A_g	3176.30	3049.25	12.81	A_{1g}
27	3180.67	3053.44	185.14	A_g	3176.56	3049.50	294.24	B_{1g}
28	3190.68	3063.05	6.00	A_g	3190.95	3063.31	13.93	A_{1g}
29	3194.92	3067.13	1137.66	A_g	3196.22	3068.37	418.11	B_{1g}
30	3199.26	3071.29	1263.92	A_g	3196.77	3068.90	1990.84	A_{1g}
31	3583.21	3335.96	27.69	A_g				
1	58.55	57.38	0.02	B_{3g}	64.02	62.74	0.03	E_g
2	119.54	117.15	5.88	B_{3g}	118.31	115.94	5.91	E_g
3	238.64	233.86	2.57	B_{3g}	248.77	243.79	2.59	E_g

4	267.89	262.53	0.15	B_{3g}	274.10	268.62	0.00	E_g
5	427.34	418.79	0.01	B_{3g}	430.90	422.28	0.09	E_g
6	487.71	477.96	0.04	B_{3g}	493.27	483.41	0.03	E_g
7	627.18	614.64	0.00	B_{3g}	636.78	624.04	0.01	E_g
8	719.09	704.71	0.32	B_{3g}	717.60	703.25	0.13	E_g
9	775.19	759.69	11.81	B_{3g}	774.68	759.18	9.84	E_g
10	785.26	769.55	1.84	B_{3g}	789.68	773.88	0.45	E_g
11	864.27	846.99	0.05	B_{3g}	869.68	852.29	0.02	E_g
12	880.01	862.41	0.42	B_{3g}	883.90	866.22	0.26	E_g
13	958.78	939.60	0.61	B_{3g}	962.39	943.14	1.62	E_g
14	997.40	977.45	0.21	B_{3g}	995.39	975.48	0.08	E_g
1	60.20	59.00	0.01	B_{2g}	64.02	62.74	0.03	E_g
2	111.86	109.62	5.68	B_{2g}	118.31	115.94	5.91	E_g
3	235.93	231.21	1.58	B_{2g}	274.10	268.62	0.00	E_g
4	255.22	250.11	1.59	B_{2g}	248.77	243.79	2.59	E_g
5	428.22	419.65	0.26	B_{2g}	430.90	422.28	0.09	E_g
6	493.73	483.85	0.07	B_{2g}	493.27	483.41	0.03	E_g
7	637.72	624.96	0.07	B_{2g}	636.78	624.04	0.01	E_g
8	689.25	675.46	0.72	B_{2g}				
9	711.66	697.43	0.13	B_{2g}	717.60	703.25	0.13	E_g
10	768.57	753.19	7.92	B_{2g}	774.68	759.18	9.84	E_g
11	787.61	771.86	0.29	B_{2g}	789.68	773.88	0.45	E_g
12	864.26	846.98	0.07	B_{2g}	869.68	852.29	0.02	E_g
13	881.82	864.18	0.14	B_{2g}	883.90	866.22	0.26	E_g
14	965.45	946.14	2.31	B_{2g}	962.39	943.14	1.62	E_g
15	993.24	973.37	0.03	B_{2g}	995.39	975.48	0.08	E_g
1	69.10	67.71	0.80	B_{1g}	113.88	111.61	9.49	B_{2g}
2	171.46	168.03	34.61	B_{1g}	228.33	223.77	32.44	B_{2g}
3	213.09	208.83	1.07	B_{1g}	217.62	213.27	0.00	A_{2g}
4	482.46	472.81	37.96	B_{1g}	487.68	477.92	31.58	B_{2g}
5	555.44	544.33	0.21	B_{1g}	574.52	563.03	0.00	A_{2g}
6	590.16	578.36	0.10	B_{1g}	591.27	579.44	0.00	A_{2g}
7	689.69	675.89	4.80	B_{1g}	693.22	679.36	5.94	B_{2g}
8	849.78	832.79	1.42	B_{1g}	864.31	847.02	0.00	A_{2g}
9	927.18	908.64	1.74	B_{1g}	977.83	958.27	2.18	B_{2g}
10	1046.68	1025.75	81.74	B_{1g}	1061.17	1039.95	66.94	B_{2g}
11	1106.48	1084.35	0.20	B_{1g}	1115.75	1093.44	0.00	A_{2g}
12	1143.31	1120.44	68.38	B_{1g}	1146.09	1123.17	98.32	B_{2g}
13	1148.14	1125.18	43.84	B_{1g}	1149.72	1126.73	0.00	A_{2g}
14	1217.56	1193.21	41.19	B_{1g}	1218.08	1193.72	0.00	A_{2g}
15	1253.59	1228.52	42.22	B_{1g}	1251.77	1226.74	61.90	B_{2g}

16	1271.40	1245.98	67.29	B_{1g}				
17	1316.56	1290.23	0.15	B_{1g}	1316.58	1290.25	0.00	A_{2g}
18	1349.77	1322.78	182.89	B_{1g}	1343.88	1317.01	124.56	B_{2g}
19	1373.57	1346.09	56.33	B_{1g}	1356.45	1329.32	0.00	A_{2g}
20	1501.18	1471.16	87.49	B_{1g}	1506.14	1476.02	0.00	A_{2g}
21	1509.17	1478.99	3.85	B_{1g}	1508.48	1478.31	138.30	B_{2g}
22	1520.45	1490.04	156.14	B_{1g}	1480.18	1450.58	25.94	B_{2g}
23	1616.30	1583.98	124.93	B_{1g}	1594.40	1562.51	0.00	A_{2g}
24	1636.51	1603.78	5.93	B_{1g}	1639.06	1606.28	0.00	A_{2g}
25	1647.14	1614.20	26.97	B_{1g}	1641.41	1608.59	0.16	B_{2g}
26	3167.02	3040.34	51.73	B_{1g}	3169.36	3042.58	149.69	B_{2g}
27	3172.87	3045.96	100.93	B_{1g}	3169.36	3042.59	0.00	A_{2g}
28	3183.16	3055.83	240.43	B_{1g}	3185.44	3058.03	331.05	B_{2g}
29	3188.94	3061.39	13.51	B_{1g}	3186.08	3058.63	0.00	A_{2g}
30	3192.10	3064.42	388.31	B_{1g}	3191.77	3064.10	319.02	B_{2g}

Appendix VI.B: DFT geometries and vibrational frequencies of H_2TAP-F_8 and $ZnTAP-F_8$

VI.B.1 Introduction

In the following appendix the DFT optimised geometries and vibrational frequencies and intensities of H_2TAP-F_8 and $ZnTAP-F_8$ will be presented. All calculations were completed using the B3LYP hybrid functional and 6-311++G(2d,2p) basis set. In Part VI.B.2 the optimised geometries for of H_2TAP-F_8 and $ZnTAP-F_8$ will be presented. In Part VI.B.3 the calculated vibrational frequencies and intensities for the infrared and Raman active modes of H_2TAP-F_8 and $ZnTAP-F_8$ will be presented. The vibrational frequencies presented were calculated using the geometries presented in Part VI.B.3. As with the results of the other D_{2h} molecules presented so far in this work, the x and z axis have been exchanged for H_2TAP-F_8 resulting in the z-axis orientated perpendicular to the plane of the molecule. Consequentially the 1 and 3 Mulliken symmetry labels have also been exchanged.

VI.B.2 Optimised geometries

The molecular structure for H_2TAP-F_8 and $ZnTAP-F_8$ shown in Figure VI.B.1, were found to be plane with D_{2h} and D_{4h} point symmetries respectively. The geometric parameters for H_2TAP-F_8 and $ZnTAP-F_8$ have been tabulated in Table VI.B.1 alongside the DFT results for H_2TAP and $ZnTAP$ calculated at the same level of theory. A favourable comparison can be made between the pairs of structures with the largest difference being the $C_\beta-H_\beta$ and $C_\beta-F_\beta$ bond lengths.

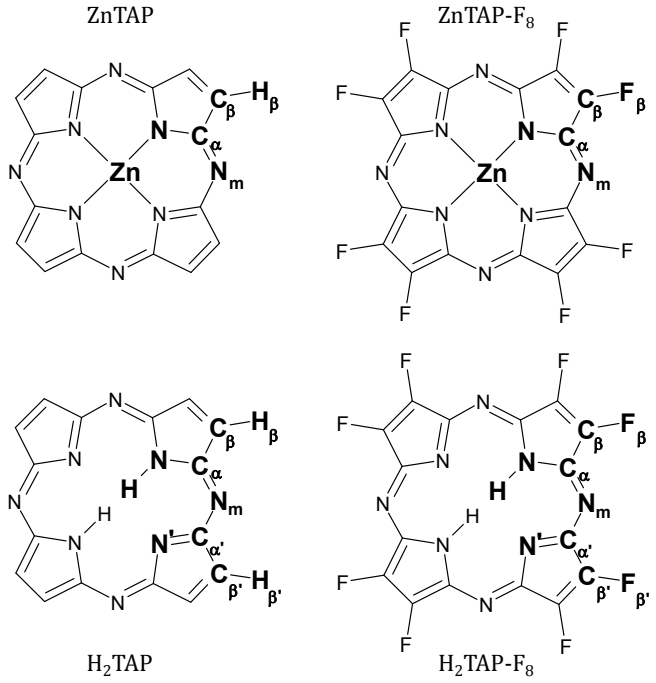

Figure VI.B.1: Molecular structures and atom labeling for ZnTAP, ZnTAP-F_8, H_2TAP and H_2TAP-F_8.

Table VI.B.1: Bond lengths and angles determined from DFT calculations for H_2TAP-F_8, and ZnTAP-F_8 with H_2TAP and ZnTAP. The atom labelling system used is provided in Figure VI.B.1.

	H_2TAP	**H_2TAP-F_8**	**ZnTAP**	**ZnTAP-F_8**
Lengths (Å)				
N-H(Zn)	1.008	1.007	1.977	1.980
N-C_α	1.370	1.371	1.365	1.366
C_α-N_m	1.320	1.313	1.332	1.325
C_α-C_β	1.444	1.445	1.457	1.455
C_β-C_β	1.362	1.361	1.356	1.356
C_β- H_β(F_β)	1.076	1.318	1.077	1.321
N'-C_α'	1.360	1.360		
C_α'- N_m	1.334	1.328		
C_α'- C_β'	1.466	1.463		
C_β'- C_β'	1.347	1.346		
C_β'- H_β'(F_β)'	1.077	1.322		
Angles (deg)				
H(Zn)-N-C_α	124.59	124.15	125.69	125.27
N-C_α- N_m	127.75	128.41	127.25	127.84
C_α-N-C_α	110.81	111.70	108.62	109.46
N-C_α-C_β	106.55	105.83	108.52	107.79
C_α-C_β-C_β	108.04	108.32	107.16	107.48
C_β-C_β-H_β(F_β)	128.62	127.59	128.71	127.70
N'-C_α'- N_m	127.56	128.09		
C_α'-N'-C_α'	105.53	106.32		
N'-C_α'-C_β'	111.04	110.36		
C_α'-C_β'-C_β'	106.20	106.48		
C_β'-C_β'-H_β'(F_β)'	129.57	128.72		

VI.B.3 H_2TAP-F_8 and ZnTAP-F_8 DFT vibrational frequencies

Table VI.B.2: DFT B3LYP/6-311++G(2d,2p) computed Infra-red frequencies (ν, cm^{-1}) and intensities (km/mole) for H_2TAP-F_8 and ZnTAP-F_8. The scaled frequencies, ν_{scaled}, have been multiplied by a factor of 0.98.

	H_2TAP-F_8				ZnTAP-F_8			
	ν	ν_{scaled}	IR Int	Sym	ν	ν_{scaled}	Act	Sym
1	168.99	165.61	1.82	B_{3u}	163.59	160.31	0.82	E_u
2	246.61	241.68	1.06	B_{3u}	249.32	244.33	1.31	E_u
3	330.31	323.71	8.20	B_{3u}	363.24	355.97	1.73	E_u
4	518.04	507.68	1.39	B_{3u}	528.41	517.84	3.04	E_u
5	642.17	629.32	135.28	B_{3u}	652.76	639.70	115.88	E_u
6	725.56	711.05	3.74	B_{3u}	784.10	768.42	0.05	E_u
7	847.60	830.65	18.37	B_{3u}	860.29	843.09	12.34	E_u
8	983.12	963.46	198.03	B_{3u}	1014.33	994.04	88.31	E_u
9	1066.00	1044.68	61.71	B_{3u}	1134.41	1111.72	130.90	E_u
10	1183.44	1159.77	711.66	B_{3u}	1184.93	1161.23	786.81	E_u
11	1322.94	1296.48	25.93	B_{3u}	1332.40	1305.76	80.45	E_u
12	1393.96	1366.09	129.49	B_{3u}	1404.25	1376.17	95.57	E_u
13	1456.26	1427.13	100.90	B_{3u}	1467.55	1438.20	89.10	E_u
14	1530.31	1499.70	174.14	B_{3u}	1513.88	1483.60	192.19	E_u
15	1680.36	1646.76	796.90	B_{3u}	1690.10	1656.29	652.39	E_u
16	3569.90	3498.50	125.94	B_{3u}	261.84	256.61	7.41	E_u
1	167.42	164.07	0.77	B_{2u}	163.59	160.31	0.82	E_u
2	241.69	236.86	7.75	B_{2u}	249.32	244.33	1.31	E_u
3	326.66	320.12	1.06	B_{2u}	363.24	355.97	1.73	E_u
4	526.92	516.39	2.54	B_{2u}	528.41	517.84	3.04	E_u
5	638.09	625.33	55.78	B_{2u}	652.76	639.70	115.88	E_u
6	726.73	712.19	1.27	B_{2u}	784.10	768.42	0.05	E_u
7	824.55	808.06	50.25	B_{2u}	860.29	843.09	12.34	E_u
8	996.35	976.43	5.35	B_{2u}	1014.33	994.04	88.31	E_u
9	1126.69	1104.16	513.10	B_{2u}	1134.41	1111.72	130.90	E_u
10	1182.73	1159.08	532.90	B_{2u}	1184.93	1161.23	786.81	E_u
11	1278.67	1253.10	21.24	B_{2u}	261.84	256.61	7.41	E_u
12	1336.74	1310.00	18.92	B_{2u}	1332.40	1305.76	80.45	E_u
13	1445.70	1416.79	118.36	B_{2u}	1404.25	1376.17	95.57	E_u
14	1540.66	1509.85	40.17	B_{2u}	1467.55	1438.20	89.10	E_u
15	1572.00	1540.56	210.68	B_{2u}	1513.88	1483.60	192.19	E_u
16	1725.36	1690.85	494.00	B_{2u}	1690.10	1656.29	652.39	E_u
1	29.27	28.68	0.00	B_{1u}	34.72	34.03	1.65	A_{2u}
2	50.15	49.15	1.19	B_{1u}	65.39	64.08	0.00	B_{3u}
3	165.33	162.02	0.84	B_{1u}	134.43	131.74	3.24	A_{2u}

4	292.73	286.87	0.01	B_{1u}	236.63	231.90	0.00	B_{3u}
5	342.58	335.73	0.33	B_{1u}	321.34	314.91	0.50	A_{2u}
6	396.76	388.82	9.29	B_{1u}	402.74	394.68	11.94	A_{2u}
7	683.19	669.53	54.10	B_{1u}	623.35	610.88	0.00	B_{3u}
8	720.95	706.53	3.98	B_{1u}	764.78	749.48	0.00	B_{3u}
9	770.96	755.54	43.25	B_{1u}	773.52	758.05	25.95	A_{2u}

Table VI.B.3: DFT B3LYP / 6-311++G(2d,2p) computed Raman frequencies (ν, cm^{-1}) and scattering activities ($Å^4$/amu) for H_2TAP-F_8 and $ZnTAP-F_8$. The scaled frequencies, ν_{scaled}, have been multiplied by a factor of 0.98.

	H_2TAP-F_8				$ZnTAP-F_8$			
	ν	ν_{scaled}	Act	Sym	ν	ν_{scaled}	Act	Sym
1	139.60	136.81	18.13	A_g	169.51	166.12	13.52	B_{1g}
2	212.91	208.65	20.68	A_g	228.66	224.09	15.61	A_{1g}
3	275.60	270.08	0.21	A_g	277.02	271.48	0.26	B_{1g}
4	332.03	325.39	36.85	A_g	355.99	348.87	55.14	A_{1g}
5	654.58	641.49	16.97	A_g	656.79	643.65	35.05	A_{1g}
6	728.37	713.81	0.68	A_g	726.56	712.03	50.10	B_{1g}
7	735.74	721.02	99.44	A_g	780.91	765.29	63.30	B_{1g}
8	808.54	792.37	126.01	A_g	860.93	843.71	88.88	A_{1g}
9	1156.71	1133.58	8.43	A_g	1169.75	1146.36	11.27	A_{1g}
10	1215.72	1191.40	317.19	A_g	1215.18	1190.88	388.74	B_{1g}
11	1333.56	1306.89	987.18	A_g	1321.50	1295.07	903.74	B_{1g}
12	1416.67	1388.33	108.66	A_g	1417.08	1388.73	97.14	A_{1g}
13	1548.75	1517.78	80.08	A_g	1529.26	1498.68	65.54	A_{1g}
14	1587.62	1555.87	2150.97	A_g	1562.58	1531.33	2254.59	B_{1g}
15	1685.22	1651.51	103.27	A_g	1691.01	1657.19	25.69	B_{1g}
16	1727.13	1692.59	95.56	A_g	1694.47	1660.58	183.91	A_{1g}
17	3634.03	3561.35	13.54	A_g				
1	72.75	71.30	1.61	B_{3g}	73.84	72.36	1.65	E_g
2	134.15	131.47	0.82	B_{3g}	129.53	126.94	0.66	E_g
3	294.79	288.90	0.49	B_{3g}	295.58	289.67	0.86	E_g
4	345.28	338.37	3.90	B_{3g}	351.09	344.07	3.89	E_g
5	553.65	542.58	1.42	B_{3g}	563.30	552.03	1.99	E_g
6	746.36	731.43	1.59	B_{3g}	747.33	732.38	1.71	E_g
7	770.52	755.11	1.00	B_{3g}	771.83	756.40	0.18	E_g
1	47.60	46.65	1.88	B_{2g}	73.84	72.36	1.65	E_g
2	111.66	109.43	0.14	B_{2g}	129.53	126.94	0.66	E_g

3	266.05	260.73	2.19	B_{2g}	295.58	289.67	0.86	E_g
4	342.49	335.64	3.75	B_{2g}	351.09	344.07	3.89	E_g
5	488.71	478.94	0.08	B_{2g}				
6	559.40	548.21	2.53	B_{2g}	563.30	552.03	1.99	E_g
7	729.80	715.20	2.07	B_{2g}	747.33	732.38	1.71	E_g
8	767.86	752.50	0.00	B_{2g}	771.83	756.40	0.18	E_g
1	109.68	107.48	5.43	B_{1g}	159.83	156.64	1.38	B_{2g}
2	207.38	203.24	7.15	B_{1g}	233.40	228.73	15.07	B_{2g}
3	254.80	249.71	0.33	B_{1g}	258.87	253.69	0.00	A_{2g}
4	496.54	486.60	4.02	B_{1g}	498.44	488.47	3.54	B_{2g}
5	581.23	569.61	0.15	B_{1g}	579.31	567.73	0.00	A_{2g}
6	646.29	633.36	0.57	B_{1g}	680.49	666.88	0.00	A_{2g}
7	830.10	813.49	0.01	B_{1g}	856.99	839.85	3.40	B_{2g}
8	950.71	931.69	18.09	B_{1g}	1003.64	983.57	7.90	B_{2g}
9	1070.97	1049.55	0.04	B_{1g}	1085.47	1063.76	0.00	A_{2g}
10	1143.81	1120.94	0.05	B_{1g}	1176.24	1152.72	0.00	A_{2g}
11	1192.57	1168.72	10.79	B_{1g}	1195.26	1171.35	6.86	B_{2g}
12	1247.53	1222.58	0.00	B_{1g}				
13	1397.63	1369.68	0.73	B_{1g}	1408.97	1380.79	5.40	B_{2g}
14	1443.50	1414.63	4.54	B_{1g}	1413.46	1385.19	0.00	A_{2g}
15	1482.70	1453.04	15.00	B_{1g}	1490.52	1460.71	34.23	B_{2g}
16	1579.20	1547.61	12.17	B_{1g}	1493.57	1463.70	0.00	A_{2g}

Chapter VII: Conclusions

VII.1 IR and Raman spectra of H_2Pc and ZnPc

The use of the matrix-isolation as a sample preparation technique provided IR spectra of ZnPc, H_2Pc and of its isopotomers with narrow, well resolved lines that were relatively free from aggregates. The Raman spectra of the phthalocyanines in KBr were recorded and were found to have broader line-widths than those in the matrix IR and bands due to aggregates. Historically, vibrational spectra of samples prepared in halide salt disks at room-temperature display broad line-shapes with additional peaks due to aggregate species and "hot-bands" from thermally populated excited states. The deuteration of free-base phthalocyanine not only produced samples containing D_2Pc but also the partially deuterated species HDPc. The use of difference spectra of the IR results allowed the band positions of the deuterium/hydrogen vibrations to be resolved for the three isotopomers, H_2Pc, D_2Pc and HDPc.

VII.2 Vibrational Analysis

The DFT calculated vibrational frequencies and intensities were found to be essential in the assignment of the spectral features observed in both IR and Raman. Calculation of the optimised geometries and vibrations of the various Pcs using the B3LYP functional with the large 6-311++G(2d,2p) basis set, resulted in an excellent match with the experimental spectra. Notably, the combination of the high level theoretical calculations and matrix IR spectra with narrow, weakly shifted lines, transitions from $\nu'' = 0$ only and few peaks due to aggregates, allowed an unambiguous assignment of the vibrations. Using the IR and Raman experimental results and accurate DFT computational data, a comprehensive overview of the vibrational behaviour of phthalocyanines was made, with a specific emphasis on the NH motion of free-base phthalocyanine.

Except for vibrational frequencies assigned to the higher energy NH/D stretching modes, relatively small shifts upon deuteration were seen for the vibrations involving in-plane and out-of-plane bending motions. The reason for the relatively low ν_H/ν_D ratios was due to coupling the NH motion to other atomic displacements that were clearly seen by inspection of the normal modes calculated

using DFT. Another interesting observation was the small differences apparent between the Raman spectra of H_2Pc and D_2Pc. This was again explained by the DFT calculations where the Raman active modes involving NH motion are predicted to be very weak. From careful analysis of the experimental and theoretical data, the following assignments of the important NH vibrations observed in both IR and Raman spectra were made:

NH Stretching

- IR – H_2Pc: 3310 cm^{-1}, D_2Pc: 2480 cm^{-1}, HDPc: (NH) 3337 cm^{-1}, (ND) 2500 cm^{-1}
- Raman – H_2Pc: 3363 cm^{-1}, D_2Pc: 2505 cm^{-1}

NH Out-of-plane bending

- IR – H_2Pc: 722 cm^{-1}, D_2Pc: 730 cm^{-1}, HDPc: (ND) 719 cm^{-1}
- H_2Pc: 765 cm^{-1}, D_2Pc: 555 cm^{-1}, HDPc: (NH) 743 cm^{-1}
- Raman – Not observed (DFT H_2Pc: 680 cm^{-1}, D_2Pc: 495 cm^{-1} with 0 intensity)

NH In-Plane bending

- IR – H_2Pc: 737 cm^{-1}, D_2Pc: 722 cm^{-1}, HDPc: (ND) 728 cm^{-1}
  H_2Pc: 1046 cm^{-1}, D_2Pc: 964 cm^{-1}, HDPc: (NH) 1034 cm^{-1} (ND) 978 cm^{-1}
  H_2Pc: 1096 cm^{-1}, D_2Pc: 1080 cm^{-1}, HDPc: (NH) 1091 cm^{-1} (ND) 1066 cm^{-1}
  H_2Pc: 1251 cm^{-1}, D_2Pc: 1189 cm^{-1}, HDPc: (NH) 1240 cm^{-1} (ND) 1176 cm^{-1}
- Raman – H_2Pc: 1026 cm^{-1}, D_2Pc: 986 cm^{-1}
  H_2Pc: 1081 cm^{-1}, D_2Pc: 1044 cm^{-1}
  H_2Pc: 1228 cm^{-1}, D_2Pc: 1220 cm^{-1}

Several of the NH bending modes calculated using DFT were found to exhibit the peculiar behaviour of $\nu_H > \nu_D$. Most of the modes exhibiting positive H to D frequency shifts were either too weak to be seen in the experimental spectra or were difficult to resolve. However, an out-of-plane bend observed in the IR spectra at 722 cm^{-1} in H_2Pc was assigned using the theoretical results to a band at 730 cm^{-1} in D_2Pc, a small positive shift of 8 cm^{-1} that is easily distinguishable in low-temperature matrices. This unexpected behaviour of the ν_H/ν_D ratios was analysed through the examination of the continuous evolution of the frequencies calculated with sub-amu increments (atomic mass units of 0.05) for the central NH protons. This frequency increase in the heavier isotopomer was found to be a consequence of the reversal of the direction of the NH motion when going from H_2Pc to D_2Pc and

avoided crossing events between vibrational modes transforming with the same symmetry.

When a comparison was made between the Raman spectra of ZnPc and H_2Pc in KBr and the emission spectra recorded for the same molecules in rare gas and nitrogen matrices, a striking resemblance was found. This correlation between Raman and fluorescence was to become crucial in the analysis of the visible luminescence spectroscopy of H_2Pc and ZnPc. It allowed the assignments made for the Raman spectral bands using ground state DFT vibration calculations to be applied to the vibronic structures observed in not only emission but also excitation.

VII.3 Visible Luminescence

The absorption bands of the lowest allowed transitions of ZnPc and H_2Pc, generally referred to as the 'Q' transitions after their weakly absorbing equivalents in the visible spectra of porphyrins, were observed in Ne, Ar, Kr, Xe and N_2 host matrices. A matrix dependence on the spectral positions of the intense Q band of ZnPc was seen, with shifts to lower energies from the gas phase value of 15,766 cm^{-1} ranging with 192 cm^{-1} for Ne to 731 cm^{-1} for Xe due to increasing interactions with the host material. Two distinct visible absorption bands are observed for H_2Pc, a lower energy Q_x and higher energy Q_y. Compared to the Q band of ZnPc, smaller matrix shifts from the gas phase value of 15,132 cm^{-1} for Q_x of H_2Pc were observed but a broadly similar trend is seen i.e. a red-shift of 155 cm^{-1} for Ne to 573 cm^{-1} for Xe. The same trend of decreasing energy with increasing interaction with the host material is seen for the Q_y transition.

The fluorescence of both Pcs isolated in various host matrices was recorded with pulsed dye laser excitation. Emission was observed exclusively from the Q state of ZnPc and from the lower energy Q_x of H_2Pc with well resolved vibronic structures. As had been noted in the pure vibrational analysis of H_2Pc and ZnPc, a comparison of the fluorescence spectra with Raman spectra in KBr pellets had revealed very strong similarities. This is entirely consistent with the selection rules where the Raman active modes with A_{1g}, B_{1g}, B_{2g} and E_g symmetry as well as the optical silent A_{2g} modes are predicted to couple to the E_u symmetry $Q \leftrightarrow G$ transitions of ZnPc. Similarly for H_2Pc the A_g, B_{1g} and B_{2g} Raman active modes may couple to the B_{3u} symmetry $Q_x \leftrightarrow G$ transitions with the weakly scattering B_{3g} modes predicted not

to couple to this state. This excellent match between fluorescence and Raman also points to the occurrence of only fundamental vibrational transitions in the emission spectra from ν' = 0 in the excited state to those in the ground state. This favourable comparison allowed the vibronic modes of ZnPc and H_2Pc coupling to the electronic emission to be assigned using the DFT calculated vibrational spectra. Emission lifetimes 3 ns for Ar, Kr, and N_2 and 2.8 ns in Xe were determined for ZnPc using time-resolved spectroscopy. The emission recorded for H_2Pc was generally longer lived with lifetimes of 13 ns for Ar and N_2 and 8 ns for Kr. In Xe, the emission lifetime of H_2Pc was found to be significantly shorter lived at only 2.7 ns, comparable with that found for ZnPc in the same host.

The excitation spectra were also recorded for ZnPc and H_2Pc with laser excitation resulting in sharp, site selective vibronic lines. A mirror symmetry between the vibronic structures of ZnPc in emission and excitation was observed. This along with the negligible Stokes shift between the 0-0 transitions seen in emission and excitation, indicated similar geometries in the ground and excited states. The same selection rules exist for the vibronic coupling between both states which allowed the vibrational modes of ZnPc in the excited state to be assigned using the same DFT Raman vibrations determined for the ground state.

For the excitation spectra of H_2Pc, the onset of the higher energy Q_y state absorption created a breakdown after ~950 cm^{-1} of the mirror symmetry with emission. The matrix dependence of Q_x-Q_y energy splitting made identification of the vibrational modes in Q_x coupling to Q_y very difficult. By comparison of the H_2Pc excitation and emission spectra recorded in this work and those previously reported for D_2Pc[1], a tentative assignment of a vibrational mode in the Q_x state coupling to the Q_y in Ar was made. This vibration, at 985.3 cm^{-1} from the 0-0 of the Q_x, was correlated with a weak Raman active vibronic mode which was seen to shift to 946 cm^{-1} upon deuteration. From the normal vibrations predicted by DFT, this B_{1g} symmetry mode consists of an in-plane bending motion of the central N-H bonds.

In order assess the ability of linear-response time-dependent DFT (TD-DFT) as a predictive tool, the vertical excitation energies and oscillator strengths of H_2Pc and ZnPc as well as those of free-base and zinc tetraazaporphyrin (TAP), tetrabenzoporphyrin (TBP) and porphine (P) were calculated utilizing the B3LYP

hybrid functional and 6-311++G(2d,2p) basis set. The theoretical results for the lowest energy transitions were compared to experimental data and were found to correctly predict many of the trends apparent for these molecules. For ZnPc, ZnTBP and ZnP, the error between theory and experiment was between 5.1 and 7.1 % higher than experiment. However, a larger error of 14.5 % was found for ZnTAP. For H_2Pc, H_2TBP and H_2P, the TD-DFT excitation energies of the Q_y were less than 1 % lower than the experimental values while the free-base analogue of ZnTAP, H_2TAP, was again seen to have the largest error of 6.0 %. Significantly, one of the major discrepancies that was identified between the TD-DFT and experimental transition energies was the underestimation of the theoretically determined Q_x-Q_y splitting of all the free-base molecules and in particular H_2Pc. The difference between the TD-DFT Q_x and Q_y states (of B_{3u} and B_{2u} symmetry respectively) was only 144 cm^{-1}, significantly smaller the approximate gas phase value of ~1550 cm^{-1} and of the smallest matrix energy gap determined in this work of 916 cm^{-1} in Xe. The TD-DFT oscillator strengths for the visible transitions of H_2Pc also incorrectly predicted the ratio the absorptions with the Q_y calculated to be more allowed than the Q_x, a reversal of what was observed in experiment.

VII.4 Amplified Emission

The luminescence spectroscopy of H_2Pc and ZnPc embedded in low temperature solids revealed the unusual phenomenon of amplified emission (AE) under conditions of low intensity pulsed laser excitation. For these molecules in Ne, Ar, Kr, N_2 and, with the exception of ZnPc in Xe matrices, a huge increase in the intensity of a one particular emission band was observed when pumping the $S_1 \leftarrow S_0$ transition. The band is located at 1550 and 1525 cm^{-1} from the 0-0 of H_2Pc and ZnPc in emission, respectively and involves a vibrational mode of the ground state. This vibration was assigned in both phthalocyanines using DFT to the most intense Raman active mode involving an out-of-phase stretching of the C-N-C bonds in the tetrapyrrole ring.

Many of the photophysical characteristics of AE are exhibited by this vibronic transition. By analysing the threshold conditions for amplified emission, it was concluded that the main conditions conducive to this non-linear optical effect occurring in these molecules were-

- Their large absorption strengths

- The narrow spectral emission lines that were exhibited
- The use of a Q-switched excitation laser
- And the large population density of excited molecules in the host solids

Another factor permitting this phenomenon to be seen for ZnPc and H_2Pc was the large vibronic intensity of the mode exhibiting AE and its relatively high quantum yield. From the experimental spectra recorded and the scattering activities calculated using DFT, this mode corresponded to the most intense Raman active mode.

With the success of DFT to correctly predict the both the spectral positions and relative intensities of the vibronic band coupling to emission of H_2Pc and ZnPc, via calculation of the Raman active modes, a theoretical vibrational analysis was undertaken in order to assess the potential of other molecules to exhibit AE. The optimized geometries, vibrational frequencies and Raman scattering intensities were calculated for free-base and zinc tetraazaporphyrin (TAP), tetrabenzoporphyrin (TBP) and porphine (P), tetrapyrrolic molecules related to the Pcs. The porphines were immediately disregarded as likely AE candidates because of the weak visible absorptions but they were found useful in comparing the vibrational structures with the other molecules. From the calculated Raman results for H_2TBP and ZnTBP, a very similar vibrational structure to H_2Pc and ZnPc was found with their most intense mode corresponding to the same in-plane ring motion seen for the Pcs. The equivalent ring mode calculated for ZnTAP and H_2TAP was found not to be the most intense and indeed for H_2TAP no one dominant Raman vibration was predicted. The reduction in the intensity of the "AE mode" in the TAPs was due to coupling of the pyrrole CH motions to the in-plane ring motion not seen for the Pcs and TBPs due to the presence of the benzo annulations in the larger tetrapyrroles. By substituting the peripheral hydrogen atoms for a heavier element, for example fluorine, their motion was seen to decouple and the remaining 'pure' ring mode resulted in an increase in Raman intensity, producing a similar spectra to those of TBP and Pc, with one dominant vibration.

Using theoretically calculated Raman frequencies and intensities, AE emission is predicted to occur in the equivalent mode to H_2Pc and ZnPc for H_2TBP and ZnTBP, in one mode of ZnTAP and the fluoridated TAP molecules and possibly in multiple modes of H_2TAP. The predictions made for H_2TBP in low-temperature solids have

already been confirmed by Crépin *et al*[2] where amplified emission was observed at 1620 cm^{-1} close to the mode predicted in this work at 1608 cm^{-1} (scaled by 0.98).

VII.5 Summary

The rich optical spectroscopy displayed by the phthalocyanines and presented in this thesis offered a difficult yet interesting challenge to analyse. With ZnPc and H_2Pc having 57 and 58 atoms respectively, high level theoretical calculations were crucial in the analysis and assignment of their spectroscopic features. Despite the successful assignment of the majority vibrational bands observed in IR, Raman and luminescence, much still remains to be understood about the optical properties of these important molecules. Unambiguous assignment of the vibrational modes coupling the Q_x to Q_y transitions of H_2Pc remains to be resolved. It is hoped that the assignment of the vibrational bands in this work, made possible by the use of matrix-isolated spectroscopy and DFT calculations, will help in this task. It would be beneficial in any future experimental work into the proposed Fermi resonance analogy describing the coupling seen between the Q_x and Q_y that a pure sample of D_2Pc be prepared. This may be possible to do this by treatment of a metallo-phthalcyanine with a deuterated strong mineral acid, replacing the metal cation in the MPc to produce D_2Pc without H_2Pc impurities. Further research may also be warranted into the investigation of amplified emission occurring in other solids such as Shpol'skii matrices or for other molecules with high emissive quantum yields and narrow linewidths.

Finally, it must be noted that the aesthetic beauty of these molecules was not lost on the author, from the brilliant blue colour of the matrix-isolated samples formed to the high symmetry molecular structures determined using high level theoretical calculations.

VII.6 References

(1) Bondybey, V. E.; English, J. H. *Journal of the American Chemical Society* **1979**, *101*, 3446.
(2) Crépin, C.; Shafizadeh, N.; Chin, W.; Galaup, J. P.; McCaffrey, J. G.; Arabei, S. M. *Low Temperature Physics* **2010**, *36*, 451.